Computational Studies of Actinide Complexes with Expanded Porphyrins

Poppy Di Pietro

UCL

PhD in Chemistry

I, Poppy Di Pietro, confirm that the work presented in this thesis is my own. Where information has been derived from other sources, I confirm that this has been indicated in the thesis.

Abstract

Covalency in complexes of the actinides has been identified as the potential driving force behind selective behaviour exhibited by separation ligands of use to the nuclear industry. In this thesis, complexes of actinyls with hexadentate macrocyclic expanded porphyrin ligands are investigated at the density functional level of theory and their electron densities analysed in detail. Initially, strong correlations are established between the vibrational frequencies of the distinctive uranyl stretching modes and covalency in the equatorial bonds of several simple uranyl complexes with monodentate first row ligands, with redshift of the uranyl stretching modes indicating a weakening of the U-O_{yl} interaction as a result of competing interactions in the equatorial plane. Subsequently, strong similarities are established in the U-N and U-O_{yl} bonding character of two multidentate uranyl complexes: UO_2-isoamethyrin(1.0.1.0.0.0) and $[UO_2(\text{bis-triazinyl-pyridine})_2]^{2+}$, where isoamethyrin(1.0.1.0.0.0) is a hexadentate macrocyclic expanded porphyrin ligand and bis-trizinyl-pyridine (BTP) is a tridentate ligand which has shown selectivity for An(III) over Ln(III). A series of uranyl hexaphyrin complexes is then investigated, finding moderate correlations between stability, equatorial covalency and the frequencies of the uranyl stretching modes, which crucially only hold when there is a degree of relative planarity in the ligand. It is found that smaller ligands have greater stability and equatorial covalency. Broadening the study to include neptunyl and plutonyl complexes finds that the isoamethyrin complex shows some evidence for selectivity for uranyl over later actinides in the same oxidation state, but significant spin contamination throws the appropriateness of these methodologies for dealing with open-shell actinide systems into question. Preliminary calculations performed using spin constrained DFT were found to be helpful here, but a full geometry reoptimisation will ultimately be necessary to fully appreciate the effects of spin contamination on the geometry and electronic structure of the neptunyl and plutonyl complexes.

Publications

Work completed during this PhD project has been published in:

First Author: Ligand size dependence of U-N and U-O bond character in a series of uranyl hexaphyrin complexes: quantum chemical simulation and density based analysis, Poppy Di Pietro & Andrew Kerridge, *PCCP*, March 2017

Assessing covalency in equatorial U-N bonds: density based measures of bonding in BTP and isoamethyrin complexes of uranyl, Poppy Di Pietro & Andrew Kerridge, *PCCP*, June 2016

U-Oyl stretching vibrations as a quantitative measure of equatorial bond covalency in uranyl complexes: a quantum chemical investigation, Poppy Di Pietro & Andrew Kerridge, *Inorganic Chemistry*, January 2016

The above publications form a major part of Chapters 3, 4 and 5 of this thesis.

Additionally:

Contributing Author: Neptunyl(VI) centred visible LMCT emission directly observable in the presence of uranyl(VI), Sean D. Woodall, Adam N. Swinburne, Nidhu lal Banik, Andrew Kerridge, Poppy Di Pietro, Christian Adam, Peter Kaden and Louise S. Natrajan, *Chemical Communications*, December 2014

Acknowledgements

My first and greatest thanks must go to my supervisor, Andy Kerridge, without whose help, support, and many good ideas this work would not have been possible. Also, Nik Kaltsoyannis for taking over as 'on paper' supervisor upon Andy's departure and Rob Bell for taking over as 'on paper' supervisor upon Nik's departure. It looks like I've been scaring them away…

I would like to give my thanks to everyone who worked in G19 alongside me, in particular, but not limited to: Joe, Eszter, Abi, Nick, Qian-Rui, Reece, Kieran and Bengt for somehow turning a hot, windowless box into a friendly and supportive working environment. Thanks for lots of interesting conversations (sometimes even about science…!), lots of biscuits and many, many cups of tea.

The support services at legion@ucl and grace@ucl, as well as at the NSCCS for answering my (occasionally silly) questions.

Last but not least, thanks to Rob, whose love and support has been vital.

Contents

Table of Figures

Table of Tables

1. Introduction and Literature review

In this thesis, computational studies using the Density Functional Theory (DFT) and density based analytical tools have been performed on AnO_2^{2+} (An = U, Np, Pu) complexes with ligands from the multidentate macrocyclic expanded porphyrin family. The purpose of this chapter is to introduce the context of the research in this thesis and relevant literature. First, the broad context of this research, the management of spent nuclear fuel, will be introduced.

Then, the computational motivation for this research will be explored. Important literature relating to the effect on actinyls, particularly uranyl, of coordination by relatively simple monodentate ligands will be introduced, and the relevant literature on expanded porphyrins will be summarised, with the intent being to show what is has been possible to synthesise in this field, with f-element complexes of particular interest. Finally, literature exploring what has been achieved computationally with expanded porphyrin complexes with f-block elements is introduced.

1.1. Context: Spent Nuclear Fuel

Worldwide, nuclear fission now accounts for 10.9 % of energy generated[1], with a typical reactor generating about 20 metric tons of spent fuel a year[2], and this is only likely to increase as the world becomes more reliant on fission power in order to meet growing energy demands. Spent nuclear fuel consists mainly of a mixture of uranium and plutonium, with small amounts of the minor actinides neptunium, americium and curium, and fission products including lanthanides and transition metals. An ongoing issue faced by the nuclear power industry is how best to manage the long-lived and highly radiotoxic actinides in this spent fuel. Uranium and plutonium is recovered *via* the liquid-liquid extraction ion-exchange process, Plutonium Uranium Redox EXtraction (PUREX)[3] and various modifications (UREX[4], which extracts only uranium, TRUEX[5], which removes Am/Cm, DIAMEX[6], which is designed to form waste containing only carbon, hydrogen, oxygen and nitrogen and so avoid the formation upon combustion of gases which contribute towards acid rain, and UNEX[7], designed to completely remove Sr and Cs radioisotopes alongside minor actinides). The minor actinides, in particular Am and Cm, whose chemistry is dominated by the trivalent oxidation state[3], present a particular challenge as current practices for their management require efficient separation from the lanthanides, which exhibit very similar chemistry. Once minor actinides are separated from the lanthanides, they can then either be stored more efficiently or transmuted *via* neutron bombardment into shorter-lived species[8]. The Selective ActiNide EXtraction (SANEX) process is proposed as a way to remove the minor actinides from the lanthanides, whose large neutron cross-section[9] would hamper any attempt at transmutation of the minor actinides. For this reason, a significant research effort is currently focussed on the identification of ligands which show selectivity for actinides over lanthanides[10,11].

To this purpose, relatively soft N-donor ligands have been investigated with varying degrees of success[12]. Several, such as ligands from the bis-triazinyl-pyridine (BTP), bis-triazinyl-bipyridine (BTBP) and bis-triazinyl-phenanthroline (BTPhen) families, have exhibited promising selectivity[10,13–17], however the source of this selectivity is not fully understood, and can be destroyed, or greatly enhanced, with small modifications to the ligand[10,16,18–20], albeit not yet in a predictable way. Developing our understanding of the bonding interactions of actinide elements is desirable from both a fundamental and practical perspective. The coordination chemistry of the actinides is a widely researched topic, with coordination by mono- and multi-dentate, as well as macrocyclic, ligands of great fundamental interest[12,21–33]. From a practical perspective, developing an improved characterisation of bonding in actinide complexes may be useful to the nuclear industry for the purposes of designing very sensitive selective separation ligands.

1.2. Context: Computational motivation

Working with actinides is challenging from both an experimental and theoretical perspective. However, there are many advantages. Computational studies allow us to investigate properties which are hard to quantify experimentally. They allow us to explore hypothetical or hard to synthesise complexes[34], or examine in more detail systems for which crystallographic data could not be obtained, of which there are several macrocyclic actinide complexes[35,36]. Computational investigations present a way to investigate the radioactive and toxic actinides while limiting the difficulties and expenses involved in their handling, and in the search for selective ligands, mean that many complexes can be explored simultaneously. However, the challenges involved in modelling actinide complexes are numerous. Strong electron correlation, weak crystal fields and significant relativistic effects mean that the modelling of these complexes is far from trivial[37–42], however there has been success modelling actinide systems using various different methodologies[38,40,43,44]. The challenges involved in modelling actinide complexes will be further explored in the Methodology (Chapter 2).

1.3. Actinyl Complexes

1.3.1. Introduction to Actinide and Actinyl Complexes

There is a growing body of work demonstrating that due to the actinide 5f-shell being relatively diffuse and extended, 5f orbitals have greater chemical availability[24,42,44–47] than the lanthanide 4f orbitals which are contracted and core-like[12,48–51]. Actinides therefore have the potential to form bonds with a greater degree of covalency than lanthanides[11,15,24,45,46,48–56]. The consequence of this is enhanced covalent character in the largely ionic An-N bonds, compared to similar Ln-N bonds, with this covalency conferring additional stability upon the actinide systems. This covalency is predicted to be most pronounced for the early actinides, decreasing across the series[48,49,51–53].

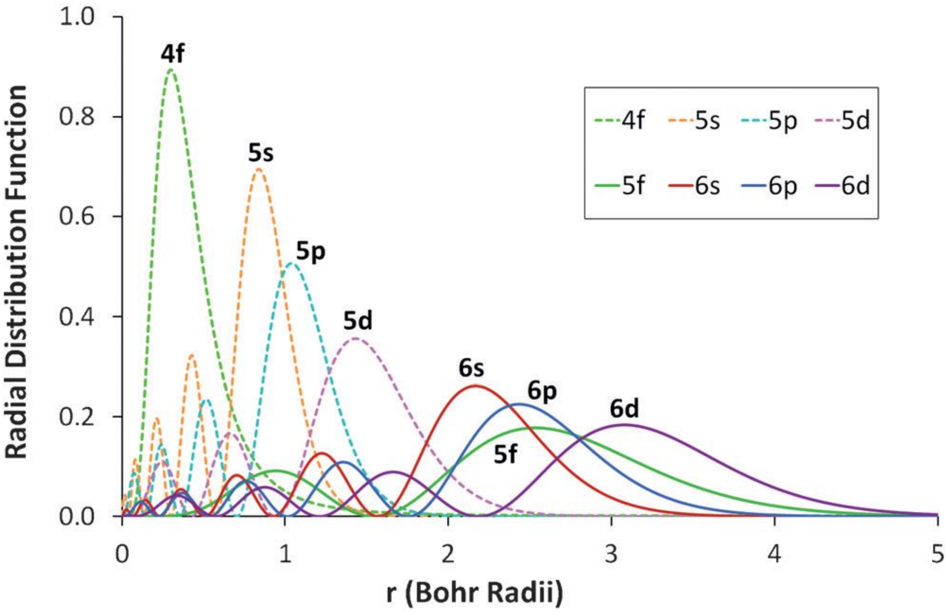

Figure 1.1: Illustrative radial distribution functions for 4f, 5s, 5p, 5d, 5f,6s, 6p, and 6d atomic orbitals. Reproduced from Stephen T. Liddle, The Renaissance of Non-Aqueous Uranium Chemistry, *Angew. Chem. Int. Ed*. **2015**, 54, 8604–8641 (Ref [57]).

The minor actinides Am(III) and Cm(III) behave very similarly to the lanthanides in terms of their bonding interactions[3], hence the need for ligands which are highly selective. Covalency in complexes of the lanthanides and later actinides is weak[49,58], thus any variation in covalent character is commensurately very small[48,53,54,59–61]. Uranium complexes have previously been considered as model systems[16,62–65] in studies of actinide covalency due to the aforementioned magnitude of covalent character in early actinides[48,53,58–60,64], making any variation in covalency more apparent. Developing our understanding of the U-N interaction may therefore shed light on how covalency may be controlled and enhanced[11,12,66].

Consequently, coordination of the actinides is a widely researched topic, with a great many complexes reported, and many in-depth reviews published[21–23,30,43,52,67–74]. Experimentally, radioactivity, toxicity and in some cases, rarity make f-element complexes difficult to work with, while computationally, the strong relativistic effects experienced by the f-elements and their often strongly correlated electronic structure present many challenges. It is vital that theoretical methods are chosen carefully as some methods experience known difficulties with, for example, accurately reproducing electron correlation energy (see Methodology, Chapter 2).

The specific focus of this thesis is complexes of the actinyls. In aqueous U(VI) chemistry, the uranyl dication (UO_2^{2+}) is ubiquitous. For uranium, the 6+ state is the most stable oxidation state to be found in solution. It is also the simplest on which to perform calculations, with its closed shell structure and formally empty 5f shell. Isostructural with the UO_2^{2+} dication are the NpO_2^{2+} and PuO_2^{2+} dications, both open shell, with one and two unpaired 5f electrons, respectively. NpO_2^{2+} and PuO_2^{2+} are more easily reduced than the UO_2^{2+} dication, more commonly being found as NpO_2^{+} and PuO_2^{+}. The electronic structure of uranyl, neptunyl and plutonyl has been well characterised theoretically using various experimental and theoretical methods[33,47,71,75–79].

1.3.2. Relevant Literature Focussing on Actinyl Complexation

In this section, the relevant literature focussing on coordination of actinyls, chiefly uranyl, with monodentate and some multidentate ligands will be introduced. An important starting point when considering the coordination of actinyls is the aquo complex of uranyl, which has been experimentally well-characterised in the aqueous phase by X-ray absorption spectroscopy (XAS)[80–82] as consisting of five coordinating water molecules in the equatorial plane of the uranium atom, perpendicular to the U-

O_{yl} bonds[83]. This complex is well known and has been characterised by X-ray absorption spectroscopy in the aqueous phase, with EXAFS revealing the uranyl aquo complex to have two 1.76 Å U-O_{yl} bonds and five U-O_{eq} bonds at 2.41 Å. In the aqueous phase, uranyl has two distinctive vibrational modes amounting to a symmetric and antisymmetric stretch. These are ν_s = 860-880 cm^{-1} and ν_{as} = 930-960 cm^{-1} for the symmetric and antisymmetric modes, respectively[56,84,85].

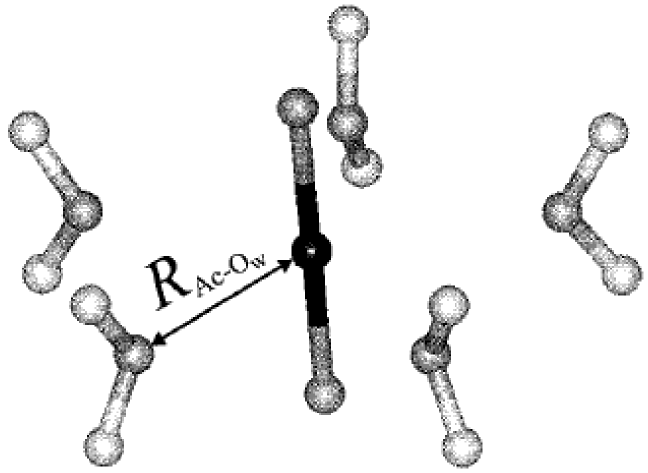

Figure 1.2: The pentagonal bipyramid geometry of $AnO_2^{2+}\cdot 5H_2O$ (An = U, Pu). Reproduced from Spencer, Gagliardi, Handy, Ioannou, Skylaris, and Willetts, "Hydration of UO_2^{2+} and PuO_2^{2+}" *J. Phys. Chem. A* **1999,** *103*, 1831-1837 (Ref [86]).

Replacement of one or more of the coordinated water molecules with organic ligands results in a weakening of the U-O_{yl} bonds, seen as a lengthening of these bonds upon complexation and a red-shift of the distinctive uranyl stretching frequencies[30,56,85]. The oxo-hydroxo complexes of uranyl (Figure 1.3) have been investigated using Raman spectroscopy[87], where the red-shifts of the uranyl stretching frequencies were used to determine the presence of $[UO_2(H_2O)_5]^{2+}$, $(UO_2)_2(OH)_2(H_2O)_6^+$ and $(UO_2)_3O(OH)_3(H_2O)_6^+$ species.

DFT simulations also confirm the 5-coordinate nature of the aquo complex[86,88–90] along with the reduction in coordination observed in more basic environments[81,89,91,92]. The cyano and isocyano complexes of uranyl have also been studied theoretically[91,93,94], where the cyano complex was the most stable, *i.e.* a preference for binding the uranium centre *via* the carbon atom was found.

Raman spectroscopy has also been performed on a series of solvated uranyl complexes with one of the five aquo ligands replaced by an organic or inorganic ligand, (1:1

complexes) with the results showing that the U-O_{yl} bond is weakened by complexation, with the most profound weakening effect given by OH^- and the least by Br^- and NO_3^-, in the order $OH^- > CO_3^{2-} > C_2O_4^{2-} > F^- > SO_4^{2-} > CH_3CO_2^- > Cl^- > Br^-$, NO_3^-.[85,95] Though this weakening of the axial U-O_{yl} bond has been widely observed both experimentally and theoretically[56,89,96,97], there is continuing debate over the causes of this weakening. In a theoretical study of 1:1 uranyl complexes with OH^-, CO_3^{2-}, $C_2O_4^{2-}$, F^-, SO_4^{2-}, $CH_3CO_2^-$ and Cl^- ligands[96] performed by Tsushima, Natural Population Analysis (NPA) was used alongside analysis of molecular orbitals to attribute the weakening to a reduction in covalent character of the U-O_{yl} bond, caused by competition between the uranyl oxygen atom and the ligand for access to the U 6d or U 5f/6p hybrid orbitals. This contrasts with the previous conclusions of Ingram *et al.* who, following a theoretical study on $[UO_2(H_2O)_m(OH)_n]^{2-n}$, ($n + m = 5$), report no evidence of competition for the U 6d or U 5f/6p hybrid orbitals, and conclude that the weakening of the U-O_{yl} bond originates from a reduction of ionic character of the U-O_{yl} bond, related to the amount of charge accumulated on the U atom[89].

Many other equatorial coordination complexes of actinyls with monodentate ligands are known. Several uranyl hydroxo, carbonate and hemicarbonate complexes ($[(UO_2)_2CO_3(OH)_3]^-$, $[UO_2(OH)_4]^{2-}$, $[UO_2(CO)_3]^{2-}$ and $[UO_2(CO_3)_3]^{2-}$) were investigated using Raman spectroscopy and ^{13}C NMR, and the frequency of the uranyl symmetric stretching mode was used to assist in the determination of species[98]. Additionally, a correlation was observed between the frequency of the uranyl symmetric stretching mode and the number and type of ligand[98]. Clark *et al.* subsequently used ^{13}C NMR to characterise the plutonyl and americyl carbonate complexes in aqueous solution[99].

There are several known pseudohalide complexes of uranyl: $[UO_2(OH)_4]^{2-}$, $[UO_2(NCS)_5]^{3-}$ and $[UO_2(CN)_5]^{3-}$ have been synthesised and characterised with Raman and extended X-ray absorption fine structure (EXAFS) spectroscopy, respectively[32,70,81,100]. The pseudohalide complex, $[UO_2(NCS)_5]^{3-}$ is formed in a 15M sodium thiocyanate solution and has been characterised in the solid-state[100], with Raman spectroscopy providing evidence of thiocyanate complexation in the aqueous phase, whereas $[UO_2(CN)_5]^{3-}$ is formed in the reaction of $UO_2(OTf)_2$ with NEt_4CN in acetonitrile[32]. The equatorial coordination number of the hydroxide complex is determined as four[81] in strongly alkaline solution by a combined EXAFS and theoretical study, although there is some debate on the existence of the five-coordinating complex[101]. The coordination number of four for the hydroxo complex is unusual for UO_2^{2+} complexes, but has been supported with EXAFS and theoretical data[81].

The UO_2^{2+} coordination number of four has also been associated with sterically crowded systems, such as $[UO_2(Cl)_4]^{2-}$. For most monodentate ligands, the coordination number for actinyls seems to be fixed at five, although there is some variation where the halides are concerned[56,100,102]. Both of the halide complexes of uranyl, $[UO_2(F)_5]^{3-}$ and $[UO_2(Cl)_4]^{2-}$ have been synthesised and characterised *via* X-ray crystallography and vibrational spectroscopy, as well as theoretically[33,89,92,103]. The fluoride and hydroxide complexes were studied using a combined EXAFS and quantum chemical approach by Vallet *et al.* finding that the fluoride complexes $UO_2F_n(H_2O)_{5-n}^{2-n}$, n = 3, 4, 5 all have a pentagonal bipyramid geometry. Gas phase calculations predict a coordination number of four for both the fluoride and hydroxide Calculations with the inclusion of solvent effects, both implicitly and explicitly, cause the optimal coordination number of the fluoride complex to increase to five, while the hydroxide complex retains a coordination number of four. Takao *et al.* examined uranyl halide complexes in *N*,*N*-dimethylformamide using UV-vis spectroscopy and EXAFS, concluding that the stability of uranyl halide complexes in *N*,*N*-dimethylformamide is consistent with the hardness order of the halides[102], *i.e.* the harder the donor, the more stable the complex, with halides becoming softor donors are one descends the periodic table. These experiments confirmed the limiting coordination number of four for the chloride complex, while for the bromide complex, coordination numbers of one and two were observed. No stable uranyl iodide complex was found.

The chloride complex, characterised using IR spectroscopy as M_2UO_2; M = Rb, Cs, Me_4N, by Schnaars and Wilson, was observed to have uranyl stretching frequencies of $\nu_s = 839$ cm^{-1} and $\nu_{as} = 907$ cm^{-1} (Rb), $\nu_s = 832$ cm^{-1} and $\nu_{as} = 922$ cm^{-1} (Cs), and $\nu_s = 831$ cm^{-1} and $\nu_{as} = 909$ cm^{-1} (Me_4N)[103]. This shift respective to aqueous uranyl[84] indicates a weakening of the U-O_{yl} bonds[96]. A theoretical study by Vallet *et al.* suggested that the U-O_{yl} destabilisation in the $[UO_2(Cl)_4]^{2-}$ complex compared to $[UO_2(H_2O)_5]^{2+}$ is largely due to electrostatic interactions[56].

When considering the uranyl fluoride complex, EXAFS data obtained in a 3M $N(CH_3)_4F$ solution[92] gives a fluoro coordination number of 4.4 ± 0.6, with density functional theory (DFT) simulations finding $UO_2F_5^{3-}$ to be stable in an aqueous environment[92,104]. The neptunyl aquo and chloro complexes, investigated theoretically by Fujii *et al.*, were calculated to have $\nu_s = 887$ cm^{-1} ($[NpO_2(H_2O)_5]^{2+}$), $\nu_s = 863$ cm^{-1} ($[NpO_2Cl(H_2O)_3]^{+}$), $\nu_s = 860$ cm^{-1} ($[NpO_2Cl(H_2O)_4]^{+}$), and $\nu_s = 860$ cm^{-1} ($[NpO_2Cl_2(H_2O)_2]$).

The plutonyl chloro complex has also been characterised in the same manner as the uranyl complex, *via* X-ray crystallography and vibrational spectroscopy[47,103] by Schnaars and Wilson, who observed plutonyl vibrational frequencies of $\nu_s = 810$ cm^{-1} and $\nu_{as} = 932$ cm^{-1} (Rb), $\nu_s = 801$ cm^{-1} and $\nu_{as} = 932$ cm^{-1} (Cs), and $\nu_s = 793$ cm^{-1} and $\nu_{as} = 909$ cm^{-1} (Me_4N)[103], compared to the frequencies of the stretching modes of the Pu-O bond in $[PuO_2(H_2O)_5]^{2+}$ of $\nu_s = 835$[105] cm^{-1} and $\nu_{as} = 962$[84] cm^{-1}. The aquo and chloro complexes of UO_2^{2+} and NpO_2^{+} as well as the complexes of the Np^{4+} and Pu^{3+} ions, have been studied using EXAFS to determine the effect of concentration on coordination number of these systems, finding that as Cl^- concentration in aqueous solution is increased, complexation of Cl^- in the inner coordination sphere results in a lengthening of An-O_{water} bond lengths and a reduction in hydration number[82].

In general, the body of experimental and theoretical data available on actinyl complexes with monodentate ligands leads to the understanding that the behaviour of the actinyl unit is strongly dependent upon the coordination environment. Considering complexes of the actinyls with multidentate ligands, there are many complexes reported in the literature, many beyond the scope of this literature review. Detailed reviews can be found in several published resources[22,23,40,71,106–109].

Many minor actinide complexes with ligands from the BTP/BTBP/BTPhen families have been reported[10,11,14,16,17,19], and there have been many studies on uranyl complexes with the macrocyclic calixarenes[110] , as well as with multidentate Schiff-base ligands[72] and crown ethers[28]. The uranyl complex with two industrially relevant bis-triazinyl-pyridine (BTP) ligands[31] is of particular interest. Of course, the focus of this thesis is actinyl complexes with expanded porphyrin ligands[21,23], and these will be explored in the next section.

1.4.Expanded Porphyrins

1.4.1. Introduction to Expanded Porphyrins

Porphyrins are aromatic macrocyclic molecules consisting of four connected pyrrolic subunits with a standard core size of sixteen atoms. Typically highly pigmented, many porphyrins occur as a part of biological systems, with examples found in nature including haem in red blood cells, which is responsible for the bright red colour of blood and vital to the mechanism by which oxygen transport occurs, and chlorophyll, which is responsible for the green colouring of most plants and vital to the process by which photosynthesis occurs. Because of this, porphyrins have often been referred to as 'the pigments of life'[111–113].

Porphyrins are conjugated systems that obey Hückel's rule for aromaticity, with (4n + 2) π electrons delocalised in the macrocycle. The central cavity of the porphyrin is ideal for forming highly stable complexes with metal ions, and these complexes have been investigated for diverse purposes such as sensing ions[114–117], sensitising photocells[113,118] and drug delivery[119]. Aside from the fact that that porphyrins typically (but not always) coordinate 2+ ions, an unusual oxidation state for Ln/An ions[120], the cavity size of the porphyrin may be ideal for forming various transition metal complexes, but the increased ionic radius of atoms from the f-block mean that in-plane coordination with porphyrins is not possible, although porphyrin sandwich complexes with lanthanides and actinides are of importance in the field of single-molecule magnetism[121–128].

The expanded porphyrins are large synthetic porphyrins with a central core of at least seventeen atoms, usually with five or more pyrrole units[129], although there are several expanded porphyrin-like macrocycles, such as the texaphyrins, which have only three pyrrole units, but five nitrogen donors in total[130,131]. The larger core of these macrocycles compared to standard tetrapyrrolic porphyrins allows for the formation of complexes with a larger range of metals, in terms of differing ionic size and different oxidation states. Expanded porphyrins do not necessarily obey Hückel's rule. Their differing sizes relate to their differing numbers of π–electrons, so they may be aromatic, antiaromatic or non-aromatic. For conjugated macrocyclic systems in general, macrocycles with the correct number of π–electrons for aromaticity tend to be planar, at least for molecules where the macrocycle is small, as a result of the additional aromatic stabilisation energy gained by the system due to overlapping π-orbitals. Larger expanded porphyrins have a tendency towards non-planarity regardless of aromaticity or lack thereof[132]. Their large core size and distinct UV-vis absorption spectra are of particular relevance for applications in the nuclear industry[133,134] and as chemodosimeters as shifts in the UV-vis spectra of macrocycles upon complexation can allow the detection of specific ions[114]. These spectral changes are often accompanied by a colour change of the solution, which may be instantaneous in some cases[35,133].

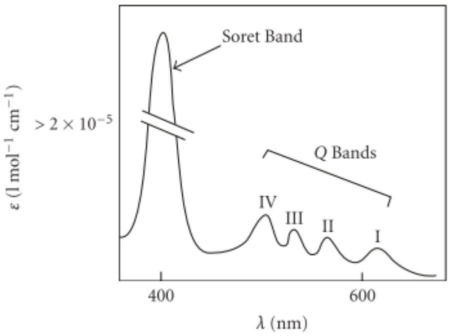

Figure 1.3: A typical absorption spectrum of a porphyrin, reproduced from Josefson and Boyle, “Photodynamic Therapy and the Development of Metal-Based Photosensitisers”, *Metal Based Drugs*, **2008**, 1-24 (Ref[135]).

A typical UV-Vis spectrum of a porphyrin, resulting from excitations between the four frontier molecular orbitals identified by Gouterman[136,137], as seen in Figure 1.3 and Figure 1.4, has a band with high oscillator strength at around 400nm, called the Soret or B band, and a series of transitions with lower oscillator strengths at higher wavelengths called Q bands[138].

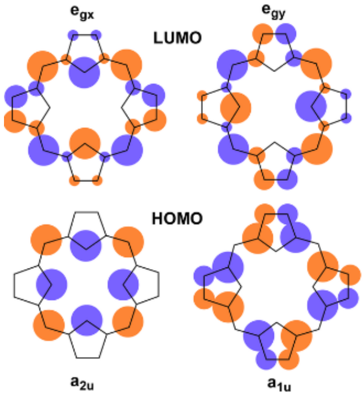

Figure 1.4: The four orbitals involved in Gouterman’s theory. Reproduced from Senge *et al.*, “Chlorophylls, Symmetry, Chirality, and Photosynthesis” Symmetry **2014**, *6*(3), 781-843 (Ref [113]).

The spectra of expanded porphyrins are similar in terms of their key features to the spectra of the naturally-occurring tetrapyrrolic porphyrins, and their bands are referred to as Soret-like and Q-like. Expanded porphyrins have been found to form complexes with many transition metals as well as lanthanides and actinides[21,139–143].

Since the discovery in the 1960's of sapphyrin (reported in 1983), the first expanded porphyrin, by Woodward and Bauer[144], a wide range of expanded porphyrins have been synthesised, ranging in size from five to eighteen pyrrole units, as well as a number of ter- or tetrapyrrolic penta- or hexadentate macrocycles such as texaphyrin[130], alaskaphyrin[145] and grandephyrin[35]. Larger macrocycles possess an inherent flexibility, possibly showing inversion of one or more pyrrole unit[141,146–149]. Pyrrole units may be directly adjacent to one another or they may be separated by one or more meso carbon atoms. In their simplest form, pyrrolic subunits are terminated with hydrogen atoms, but more commonly are synthesised with a range of peripheral substituents[150]. Substitutions at the meso-positions are also common[151,152]. Various hybrid macrocycles are also found in this family, for example the substitution of one or more pyrrole ring with a furan ring[153], pyridine ring[154,155], or similar, and related systems include macrocycles such as texaphyrin[130], which contains only three pyrrole rings but a total of 5 nitrogen donors.

The potential applications for expanded porphyrins and similar molecules are wide and varied. Potential areas of interest include actinide sensing in the nuclear industry[133,134,156] as well as potential use in solvent extraction[66], chemodosimeters for the sensing of metal ions[157,158], medical applications such as MRI contrast agents[159] and photosensitisers for photodynamic thererapies[131,160], models in bioinorganic chemistry[161], and components of non-linear optics materials[162–164].

The general notation used to describe molecules in the expanded porphyrin family is as follows for the example of [n]hexaphyrin(1.1.1.1.1.1). The n in square brackets may be used to indicate, where relevant, the number of π-electrons in the system, the round brackets indicate the number and position of meso carbon atoms, where (1.1.1.1.1.1) signifies the presence of one meso carbon atom in each of the six bridging positions in a six-membered macrocycle. Some example porphyrins and expanded porphyrins are show in Figure 1.5.

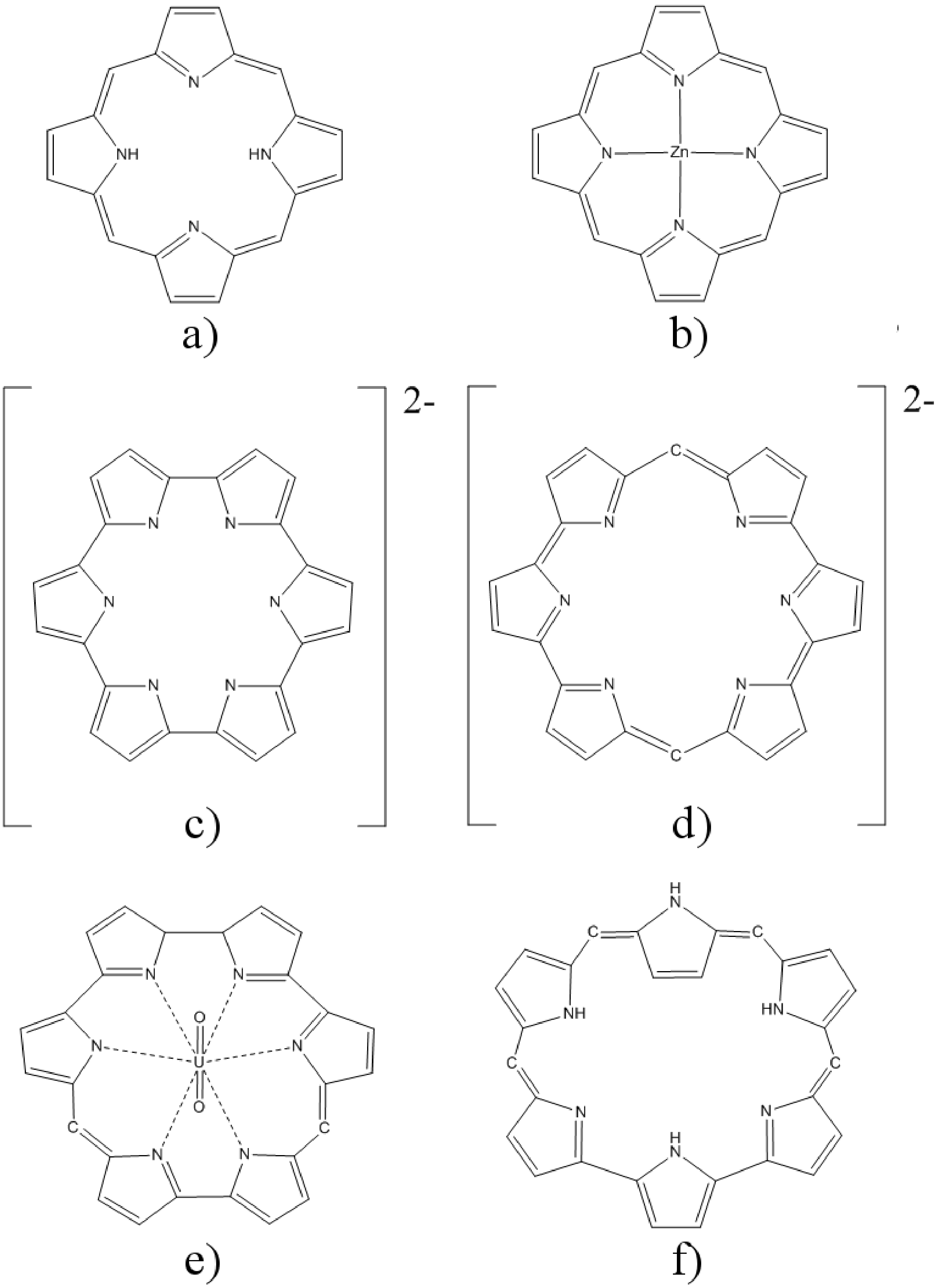

Figure 1.5: Example structures of some porphyrins and expanded porphyrins. a) free-base porphyrin; b) zinc porphyrin; c) [cyclo[6]pyrrole]$^{2-}$; d) [amethyrin(1.0.0.1.0.0)]$^{2-}$; e) UO_2-isoamethyrin(1.0.1.0.0.0); f) free-base rubyrin(1.1.1.1.0.0) showing an inverted pyrrole unit.

1.4.2. Literature Relating to Synthesised Expanded Porphyrins

The field of synthetic expanded porphyrin chemistry has seen massive development since the first synthesis of sapphyrin[144], with many different series of expanded porphyrin and porphyrin like molecules reported. Here the primary focus is on f-block complexes with expanded porphyrins, and detailed synthetic approaches will not be given, as the intention here is simply to report what it has been possible to synthesise. More detail can be found in several recent review articles[21,132,139–141,165–167].

1.4.2.1. Systems with Five Pyrrole Units

Sapphyrin(1.1.1.1.0), so named because of the intense blue colouring of the yield, demonstrates a strong Soret-like band at 458 nm. It was reported some twenty years after its initial accidental synthesis[144] by Woodward and Bauer, who were attempting to synthesise metallocorroles. Free-base di(dipyromethane) underwent a catalytic hydrogenation reaction with platinum oxide in the presence of tetrahydrofuran to give a tetrapyrrolic intermediate. This was treated with hydrobromic and formic acid, followed by iodine, resulting in a blue glass with a sharp Soret-like band at 458 nm in the UV-vis spectrum. This spectrum was markedly different from that of the metallocorroles which had by this point been successfully synthesised[168] and it was concluded that a new complex had been formed. Sapphyrin was formed in a low yield, but Bauer asserts in his 1983 paper, *"that any sapphyrin was formed at all attests to the innate stability of the pentapyrrolic superstructure"*[144]. In the same period, several sapphyrin derivatives were also synthesised, including 25,29-dioxasapphyrin[169], which has two of its pyrrole subunits substituted with furan rings, and 27-thiasapphyrin[170], which has one pyrrolic nitrogen atom substituted with sulphur. The pentapyrrolic macrocycle smaragdyrin(1.1.0.1.0) was also initially reported in this period, as was the similar pentapyrrolic superpthalocyanine, synthesised as a complex of uranyl[144,171,172]. Orangarin(1.1.0.0.0)[173] and isosmaragdyrin(1.1.1.0.0)[155] have also been reported, and [22]dehydropentaphyrin(2.1.0.0.1) and [22]pentaphyrin(1.1.1.1.1) were synthesised by Weghorn *et al*.[174].

Of greater interest to this thesis are uranyl complexes of these ligands. Attempts to synthesise a uranyl complex with sapphyrin were initially reported to have been met with failure, however pentaphyrin was been reported to form a stable uranyl complex[175] which single crystal X-ray crystallography reveals to adopt a saddle-shaped structure with the uranyl cation situated in the centre. This complex is said to resemble the previously reported uranyl superpthalocyanine complex[171], although unlike uranyl superpthalocyanine is said to be soluble in all common solvents and to possess considerably greater stability. The neptunyl and plutonyl complexes with pentaphyrin were also reported by the Sessler group[35], with changes to the UV-vis spectra taken as evidence of complex formation, although neither complex was structurally characterised.

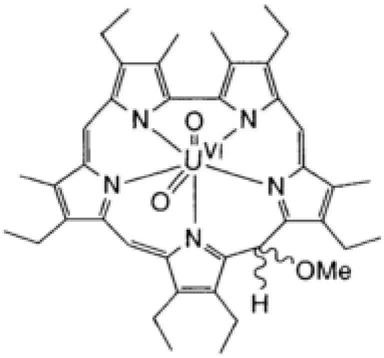

Figure 1.5: Meso-methoxy-substituted iso-sapphyrin complex of uranyl. Reproduced from: Burrell, Cyr, Lynch and Sessler, "Nucleophilic Attack at the *meso*-Position of a Uranyl Sapphyrin Complex", *J. Chem. Soc., Chem. Commun.*, **1991**, 1710 – 1713 (Ref [176]).

Burrell *et al.*, inspired by the ease with which the uranyl pentaphyrin complex was formed, reattempted synthesis of a uranyl sapphyrin complex. It was found that when sapphyrin in its free-base form is reacted with the chloride salt of uranyl in the presence of methanol, pyridine and trimethylamine, a rapid reaction occurs, with the solution changing colour from green to dark red. IR spectroscopy confirmed the presence of the uranyl unit *via* identification of the characteristic uranyl stretching band at 919 cm^{-1}. The complex formed was reported to possess unusual spectral properties, without the typical Soret-like absorption band characteristic to the expanded porphyrins, and two broad bands at 479 and 508 nm. This was explained with the aid of NMR spectroscopy, which revealed that the methanol had become incorporated into the complex during the reaction. This was confirmed with X-ray spectroscopy which showed that the macrocycle had incorporated a methoxide anion at one of the meso positions to form a meso-methoxy-substituted iso-sapphyrin complex of uranyl[176] (see Figure 1.5). Uranyl has also been stabilised by oxasappyrin[177], a ligand in which the 'central' pyrrolic subunit is replaced by a furan subunit[36,156]. The UV-vis spectrum of this complex was more typical of an expanded porphyrin, with a strong Soret-like band at 483 nm as well as three Q-like bands at 624, 647 and 708 nm[177]. Presence of the uranyl unit was confirmed using IR spectroscopy, which revealed a characteristic uranyl stretching band at 936 cm^{-1}.

Pentaphyrin derivatives have also been metallated with lutetium and investigated as potential drugs for photodynamic therapy[178,179]. Ballico *et al*. investigated Lu(III) pentaphyrin complexes as potential photosensitising drugs for photodynamic therapy[178]. The Lu(III) pentaphyrin complex was synthesised and characterised with NMR, which suggested a neutral species. The ideal photosensitising drug has absorption peaks shift into the 650-800 nm region[178] of the UV-vis spectrum, where the human body is most transparent. This increases the ability of radiation therapy to efficiently generate reactive oxygen species and singlet oxygen, causing cell death. Metallation with lutetium(III) results in a fluorescence spectra with broad bands between 300 and 500 nm. When cell cultures were treated with the Lu(III) pentaphyrin and a related Zn(II) pentaphyrin, there was a significantly higher cellular uptake than for the metallated pentaphyrin, and a higher uptake of Lu(III) pentaphyrin compared to Zn(II) pentaphyrin which was explained as being due to the neutral nature of the Lu(III) complex, compared to the cationic Zn(II) complex. When photodynamic properties were tested, a cytotoxic effect was observed proportional to the weight of the metal ion. This is only one of several expanded porphyrin macrocycles to be investigated for possible medicinal use[131,135,159,178–180].

The main differences between the various pentapyrrolic macrocycles lies in the number and position of meso-carbon atoms, but there have been many publications focussing on meso or peripheral substitution[147,150,152,181–184].

1.4.2.2. Systems With Six Pyrrole Units

Comprising six pyrrolic sub-units, the hexaphyrins provide a larger central cavity than the pentaphyrins, and bimetallic transition metal complexes become possible synthetic targets. The larger size, higher potential coordination number, greater flexibility and modifiability of the ligands mean they are also of particular interest for the formation of complexes with actinides. Like the pentaphyrins, hexaphyrins differ from one another mainly in their number of meso carbon atoms and have great potential for further modification *via* substitution at the meso positions and the periphery of the pyrrole units.

The simplest and smallest six member expanded porphyrins is cyclo[6]pyrrole[185,186], comprising six pyrrolic subunits with no meso-carbon atoms. Cyclo[6]pyrrole has been reported as forming a complex with uranyl[187]. The highly planar, stable and antiaromatic complex UO_2-cyclo[6]pyrrole, obtained as a green solid, is formed when cyclo[6]pyrrole in its free-base form is exposed to $UO_2[N(SiMe_3)_2]_2{\cdot}2THF$. Structural characterisation was performed using single-crystal X-ray diffraction. Free-base cyclo[6]pyrrole itself was initially formed as a by-product in a reaction to create the larger cyclo[8]pyrrole and there are several other larger macrocycles in the cyclo[*n*]pyrrole family[186].

Much of the work in the area of synthetic expanded porphyrin chemistry has been done by the Sessler group, who are responsible for the initial synthesis of amethyrin(1.0.0.1.0.0)[188], and its uranyl complex, which is described as extremely labile, demetallating rapidly in only weakly acidic conditions. The existence of the uranyl amethyrin complex was confirmed with mass spectrometry, but a crystal structure was not obtained[173]. The neptunyl(V) complex with amethyrin has also been reported[35], a bright red solution with a Soret-like band at 483 nm and a Q-like band at 843 nm, and a characteristic Np(V) absorption band at 977 nm. Over a number of days, red crystals were observed to precipitate from a gold-coloured solution. The crystals were too small to be characterised using X-Ray crystallography and dissolved again upon the addition of acid to the solution. More stable was the bimetallic complex of copper with amethyrin[189] synthesised by Weghorn *et al.* This complex was characterised using high resolution mass spectrometry and NMR. All six pyrrolic nitrogen atoms were found to act as donors for the copper ions. The complex was formed with two metal ions coordinated side by side, within the plane of the macrocycle.

Sessler *et al*. also reported the synthesis of isoamethyrin(1.0.1.0.0.0)[133,134], as well as the uranyl and neptunyl and plutonyl complexes with isoamethyrin(1.0.1.0.0.0)[133,190]. Sessler suggested the possible use of isoamethyrin(1.0.1.0.0.0) as a highly sensitive actinide sensor, due to the dramatic colour change the macrocycle undergoes on complexation with actinyls, from a yellow bis-hydrochloride salt to a bright pink complex in solution with dichloromethane, as seen in Figure 1.6.

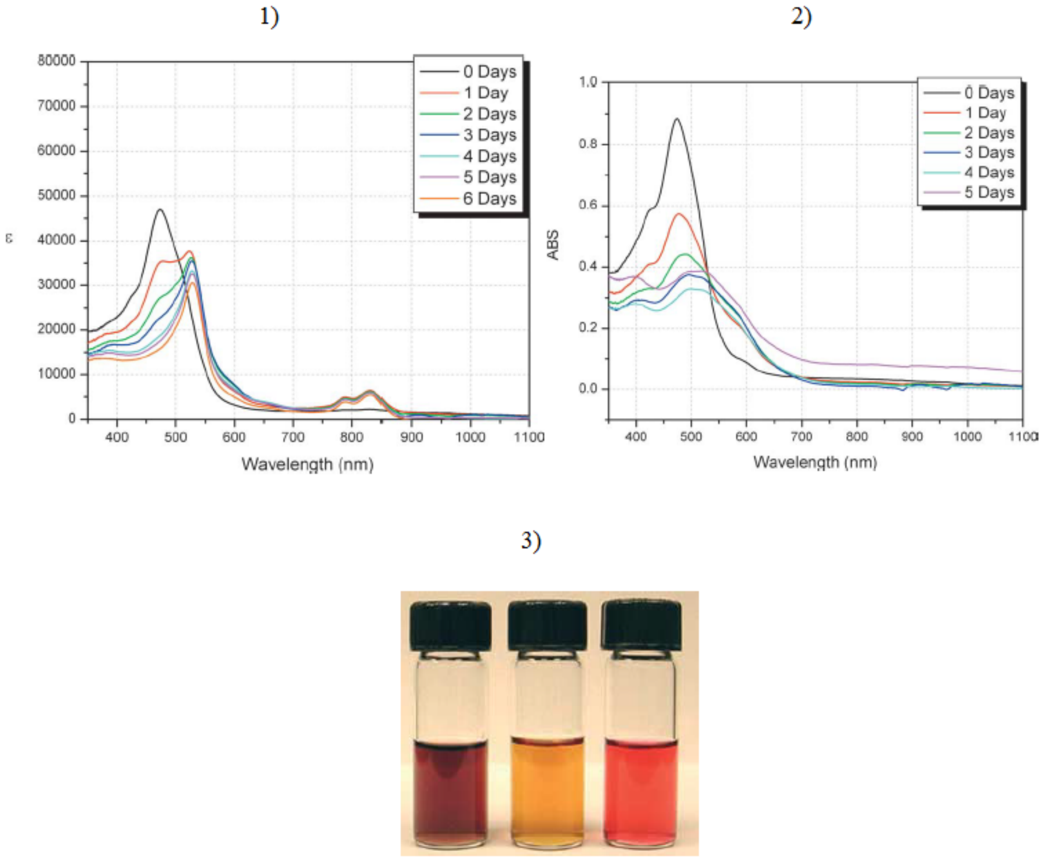

Figure 1.6: 1) Absorption spectra for free-base isoamethyrin(1.0.1.0.0.0) showing spectral changes over a period of six days; 2) solution of isoamethyrin containing 0.5 equiv. uranyl acetate showing spectral changes over a period of six days; 3) Left: acid salt of isoamethyrin; Middle: after addition of 10 equiv. Et3N; Right: UO_2^{2+} complex. All reproduced from: Sessler, Melfi, Seidel, Gorden, Ford, Palmer and Tait, “Hexaphyrin(1.0.1.0.0.0): A New Colorimetric Actinide Sensor” *Tetrahedron,* 60 (2004) 11089–11097 (Ref [133])

These changes are visible to the naked eye when the actinyl is at a concentration of 5.8 parts per million, and with UV spectroscopy with just 28 parts per billion[133]. The uranyl, neptunyl and plutonyl complexes of isoamethyrin have been well characterised with X-ray crystallography and UV-vis spectroscopy[35]. Prior to complexation, the UV-vis spectrum of the acid salt of isoamethyrin has three Soret-like bands at 384nm, 397nm and 597nm[133]. When uranyl is added, isoamethyrin is oxidised, changing the system from antiaromatic to aromatic, and the features of the UV-vis spectrum change, developing one sharp Soret-like band at 530 nm and two smaller Q-like bands at 791 nm and 832 nm. The single Soret-like band has an intensity greater than that of the Soret-like band present in the spectrum of the acid salt of free base isoamethyrin, increased by a factor of five. The uranyl complex required around 24 hours to undergo the changes resulting in a significant colour change, but plutonyl and neptunyl complexes were formed instantly, giving an instantaneous colour change. This has been explained as being due to the reduction of An(VI) to An(V), which happens easily for both neptunyl and plutonyl, as they are stable in the (V) oxidation state. This then simplifies the oxidation of the macrocycle. Uranyl remains in the (VI) oxidation state, and as such, the macrocycle must undergo air-based oxidation, slowing the rate at which the complex can form. All AnO_2-isoamethyrin complexes are a very similar pink-red in colour. Sessler *et al.* also reported the synthesis of an in-plane binuclear copper(II) complex and an oxovanadium(V) complex with isoamethyrin(1 0.1.0.0.0)[191]. Both complexes were characterised using X-ray diffraction and NMR, revealing that in the binuclear copper(II) complex, the macrocycle distorts slightly in order to fit both ions. Formation of the binuclear copper complex occurs as the macrocycle is oxidised and becomes aromatic, while complexation of the oxovanadium cation forms a non-aromatic macrocycle.

Rosarin(1.0.1.0.1.0)[192] is the next largest macrocycle in this family, with three equally spaced meso carbon atoms, and like many of the others in this series, is named for the bright colour of the product of the synthesis. The rubyrins, with four meso carbon atoms, have been reported in three isomeric forms: Rubyrin(1.1.1.1.0.0)[146], rubyrin(1.1.1.0.1.0)[147] and rubyrin(1.1.0.1.1.0)[193], and these complexes demonstrate the inherent flexibility of larger expanded porphyrin macrocycles, with reports of inverted pyrrole units becoming common for free-base systems[146,147,149], such as the macrocycle in Figure 1.5 f). This macrocycle, rubyrin(1.1.1.1.0.0), was synthesised by the Sessler group with a yield of 46% from an acid catalysed condensation reaction[146]. Finally, hexaphyrin(1.1.1.1.1.1) is the largest of the hexaphyrin family, and has been reported both in its free-base form and as a mono- or bimetallic complex with various transition metals[151,194–196], and is reported to act as a chemodosimeter for silver ions[157].

1.4.3.3. Larger Macrocycles and Hybrid Macrocycles

Heptaphyrins and octaphyrins are also frequently reported in the literature, and at this larger size, a new 'figure eight' can be observed[141,197–199]. It is common in the six membered rings to see non-planar macrocycles, with a saddle-like shape or a twisted conformation. In the larger hepta- and octaphyrins, this twisting is often more pronounced, with, in the most extreme cases, the macrocycle being divided into two portions, each with a separate cavity[141,197,199]. Each of these cavities can then complex, for example, a transition metal ion, such as the dicopper and disilver complexes of octaphyrins(1.1.1.1.1.1.1.1) synthesised by Shimizu *et al*[200]. Two copper complexes were synthesised in dichloromethane, one of which with the ligand twisted into a figure-eight conformation with each copper(II) ion bound to four pyrrolic nitrogen atoms, created in a yield of 14%, and the other featuring a hydrolytic ring opening of one of the pyrrolic rings. The copper(II) ions are then bound on one side to four pyrrolic nitrogen atoms, and on the other side to three pyrrolic nitrogens and an oxygen centre, in a yield of 58%. Considering larger ligands, nonaphyrin has been reported as a [40]nonaphyrin(1.1.1.1.1.1.1.1.1) system, with a figure-eight shape, and as the reduced [42]nonaphyrin(1.1.1.1.1.1.1.1.1), with a 'butterfly-like' shape[201] (see Figure 1.7). Both of these nonaphyrin(1.1.1.1.1.1.1.1.1) structures have been reported to form complexes with copper, zinc and palladium[201] with high yields.

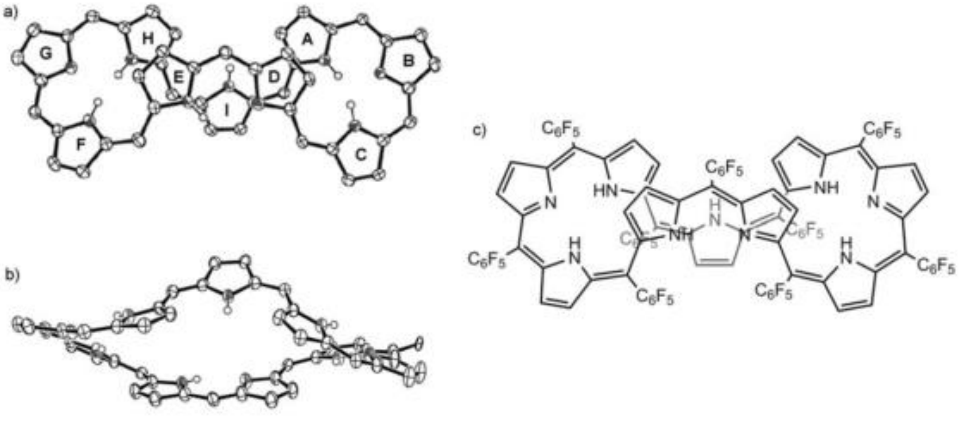

Figure 1.7: X-ray crystal structure of the 'butterfly-like' configuration of [42]nonaphyrin(1.1.1.1.1.1.1.1.1) showing: a) top view; b) side view; c) formal structure. Reproduced from: Kamimura, Shimizu, and Osuka, [40]Nonaphyrin(1.1.1.1.1.1.1.1.1) and Its Heterometallic Complexes with Palladium–Carbon Bonds, *Chem. Eur. J.* **2007**, *13*, 1620 – 1628 (Ref [201]).

The next largest macrocycle is decaphyrin (also known as turcasarin) with ten pyrrole units[199,202], of which a bis-uranyl complex has been synthesised but unfortunately could not be structurally characterised by X-ray spectroscopy[36,202]. Next largest is dodecaphyrin (twelve pyrrole units)[149,203,204], tetradecaphyrin (fourteen pyrrole units)[205], hexadecaphyrin (sixteen pyrrole units)[206,207], and the largest to date, octadecaphyrin, with eighteen pyrrole units[205]. As the ring size increases, the Soret-like absorption band is redshifted by increasing amounts, until hexa- and octadecaphyrin where the effect appears to saturate[205]. Some of these larger expanded porphyrins are shown in Figure 1.8.

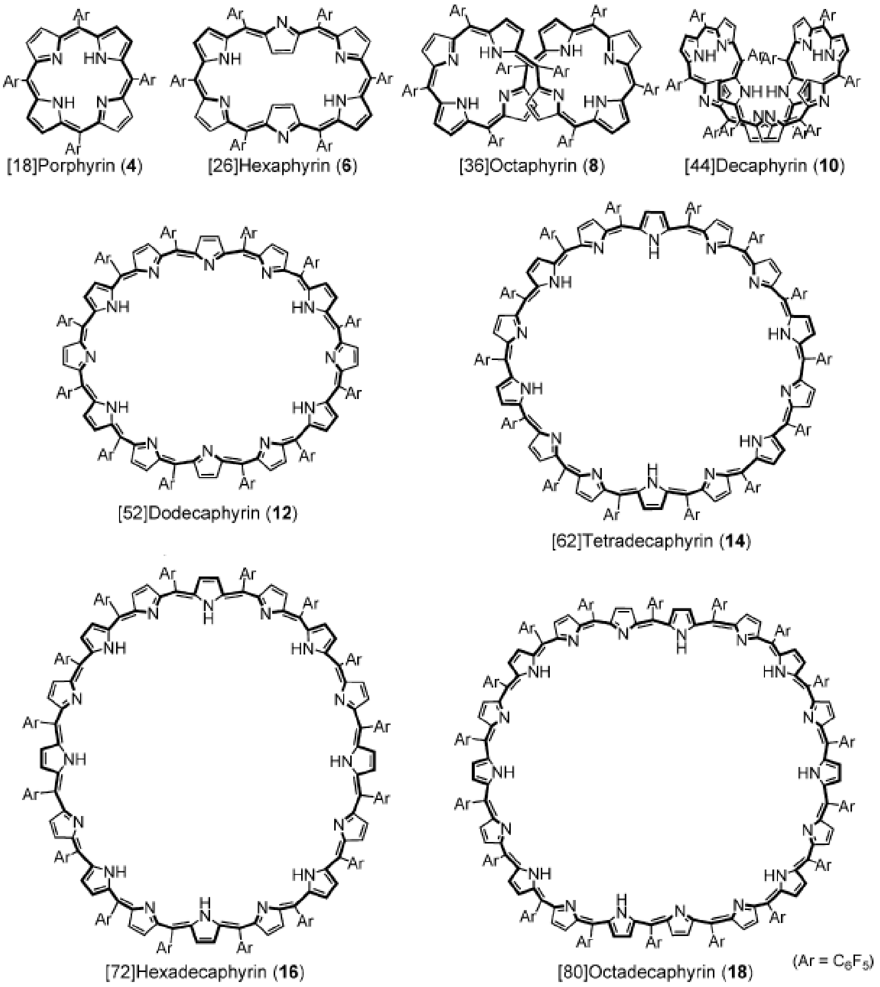

[18]Porphyrin (**4**) [26]Hexaphyrin (**6**) [36]Octaphyrin (**8**) [44]Decaphyrin (**10**)

[52]Dodecaphyrin (**12**) [62]Tetradecaphyrin (**14**)

[72]Hexadecaphyrin (**16**) [80]Octadecaphyrin (**18**) (Ar = C_6F_5)

Figure 1.8: Different sized expanded porphyrins, reproduced from: Tanaka, Shin and Osuka, Facile Synthesis of Large meso-pentafluorophenyl-Substituted Expanded Porphyrins *European Journal of Organic Chemistry*, 2008, 1341-1349 (Ref [205]).

There have also been many hybrid pyrrole-containing macrocycles synthesized, mainly relying on nitrogen donors but occasionally incorporating oxygen donors. Previously mentioned superpthalocyanine is very similar to a pentaphyrin macrocycle with the meso-carbon atoms replaced by nitrogens[172], but many of the hybrid macrocycles in the literature resemble expanded porphyrins only in so much as some of their nitrogen donors are pyrrolic.

Sessler *et al.* synthesised a complexes with Schiff-base oligopyrrolic macrocyles[208]. A 2, 5-diformylpyrrole-derived expanded porphyrin complex with uranyl was analysed using X-ray diffraction, which suggested that the complex had liquid crystalline-like properties. Further analysis with UV-Vis spectroscopy indicated the formation of three different oligopyrrolic complexes with uranyl cations. Further experimentation involved neptunyl and plutonyl cations[208]. When the free base form of a dipyrromethane-derived Schiff-base macrocycle was added to NpO_2^{2+} and PuO_2^{2+} chloride salts, a complex was formed, causing changes in the UV-vis spectra. Addition of Np/PuO_2^{2+} caused the development of a Q-like band at 630nm, and a colour change from pale yellow to blue, with both changes happening instantaneously. These changes are induced by the reduction of the metal centre and oxidation of the macrocycle which occurs upon complexation.

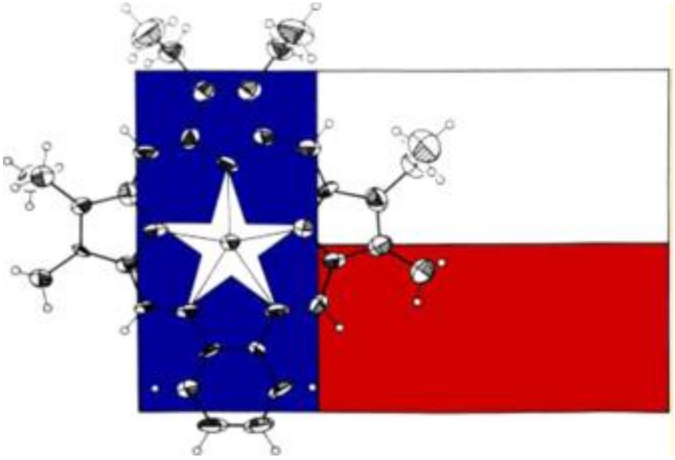

Figure 1.9: A texaphyrin complex. Reproduced from Preihs, Arambula, Magda, Jeong, Yoo, Cheon, Siddik, and Sessler, "Recent Developments in Texaphyrin Chemistry and Drug Discovery" *Inorganic Chemistry*, *52*, **2013**, 12184-12192 (Ref [209]).

The texaphyrins[130,160,209], so named for their apparent resemblance to the state flag of Texas, are terpyrrolic penta-aza macrocycles developed by the Sessler group. The central cavity is larger than a standard porphyrin, large enough to complex transition metals[143] and lanthanides. Lanthanide complexes with ligands from the texaphyrin family (see Figure 1.10) have shown promise as photosensitising agents in photodynamic therapies, with some of these complexes, namely Gd-Texaphyrin (XCYTRIN®) and Lu-Texaphyrin (LUTRIN®) having reached the stage of advanced clinical trials[131,210]. Additionally, the magnetic properties of lanthanides make them good candidates for medical contrast agents.

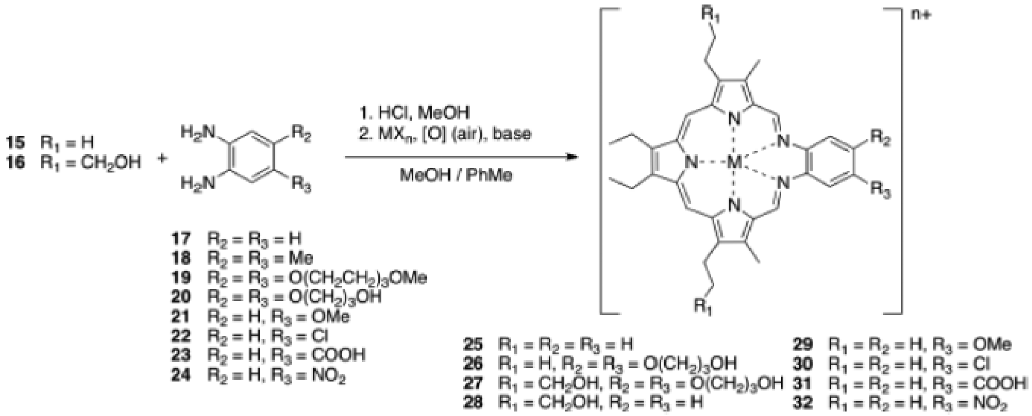

Figure 1.10: Scheme for the general synthesis of a texaphyrin. Reproduced from Preihs, Arambula, Magda, Jeong, Yoo, Cheon, Siddik, and Sessler, “Recent Developments in Texaphyrin Chemistry and Drug Discovery” *Inorganic Chemistry, 52,* **2013**, 12184-12192 (Ref [209]).

A gadolinium texaphyrin complex has also been found to localise in tumour tissue[159], where it acts as a MRI contrast agent. Hannah *et al.* investigated complexes of late first row transition metals with texaphyrin[143]. The synthesis of manganese(II), cobalt(II), nickel(II), zinc(II) and iron(II) complexes with texaphyrin, *via* a simultaneous oxidation/metallation reaction is reported. Structural characterisation was performed using X-ray diffraction.

The texaphyrin macrocycle acts as a tridentate ligand, whereas previous complexes with lanthanides had seen the texaphyrin macrocycle act as a pentadentate ligand, with the lanthanide ion located above the coordination plane. The larger core size of the texaphyrin macrocycle compared to a standard tetrapyrrolic porphyrin is found to be beneficial in the stabilisation of complexes with lower oxidation states. Of the complexes studied by Hannah *et al*., the Mn(II), Co(II) and Fe(II) complexes are found to be sufficiently stable in aqueous solution to suggest their possible future use in pharmaceuticals research.

Grandephyrin is a tetrapyrrolic, hexadentate analogue of texaphyrin. Its uranyl complex has been characterised with NMR and X-ray crystallography[35], with U-N bond lengths ranging from 2.563 to 2.857 Å and U-O bond lengths of 1.76 Å. Similar NMR spectroscopic changes were observed upon exposure to neptunyl and plutonyl, although to date, formation of these complexes has not been confirmed by X-ray crystallography[35]. Alaskaphyrin is related a six nitrogen donor macrocycle containing two pyrrole units, which has also formed stable uranyl complexes[206,208], characterised using X-ray diffraction. IR spectroscopy displayed a sharp band at 897 cm^{-1} attributed to the antisymmetric stretching mode of the uranyl unit.

The hybrid macrocycle cyclo[1]furan[1]pyridine[4]pyrrole has been characterised in its oxidised, dianionic form as a complex with uranyl[154,211] and has been used alongside photoacoustic imaging in animal studies to detect uranyl *in vivo*[212]. Several related macrocycles have also been realised synthetically[213]. The so-called "pac-man" expanded porphyrin-like macrocycles have been widely reported[29,34,214,215], and these macrocycles, with a folded structure, have been reported to complex U^{3+} and uranyl[34,214,216–219], potentially allowing the activation of the uranyl oxygen ion[216–218,220–223].

Ultimately, the field of expanded porphyrin chemistry is wide and varied, with a great many macrocycles synthesised, and many ways in which these can be modified. This characteristic makes the family of expanded porphyrins and similar macrocycles promising candidates for characterising An-N bonding and investigating selectivity, as ligands can be modified in many ways.

1.4.3. Computational Modelling of Expanded Porphyrins and their F-element Complexes

This section outlines major theoretical studies focussing on expanded porphyrins and their f-element complexes. Model chemistries are stated, but computational methodologies will not be explained in detail in this chapter. For more information about computational methodologies, basis sets, *xc*-functionals and treatment of relativistic effects see the Methodology Chapter 2 and several published resources[224–231].

The challenges of modelling f-elements and their complexes are well documented[40–44,69,227,232,233].The large number of electrons in even the smallest actinide complex means that calculations tend to be computationally expensive, even more so when a large ligand is involved. Lanthanide and actinide atoms are known to exhibit strong relativistic effects[37,38,232,234–236], which must be accounted for. In the literature, relativistic effects are most frequently dealt with implicitly, using a relativistic effective core potential (ECP), although for some applications it is necessary to explicitly treat all of the electrons and use a relativistic Hamitonian[233]. The interactions between f-electrons are known to be difficult to model, particularly the unpaired 5f electrons in, for example , a trivalent minor actinide species, which lead to strong static correlation effects, potentially seriously impacting the accuracy of any results obtained, and in several documented cases, single-determinant and density functional based methodologies struggle to accurately describe the electronic structure of many f-element complexes[33,237–241], although computational expense limits the extent to which multiconfigurational methods can be used to address these problems[242].

Difficulties aside, there is much in the literature focussing on density functional based investigations of actinides and actinide-containing systems and theoretical data with good agreement with experimental values has been produced[40,41,43,44,241,243]. The purpose of this section is to briefly introduce how expanded porphyrins, and particularly, the actinide complexes with expanded porphyrins, are dealt with theoretically, and how the literature confronts the aforementioned difficulties.

An important paper which must be considered here is Shamov and Schreckenbach's theoretical investigation of uranyl isoamethyrin[150]. Shamov and Schreckenbach performed scalar relativistic Density Functional Theory (DFT) calculations using the Priroda and ADF codes. Triple-zeta polarised basis sets were used alongside the PBE *xc*-functional. It was reported that the simplification of isoamethyrin by removal of the peripheral alkyl groups present on the synthesised complex, and termination of the pyrrole groups with a single hydrogen atom, as is a common technique for reducing computational expense in computational chemistry, badly overestimates some of the U-N bond lengths and fails to replicate the overall experimental geometry of the complex. This is attributed to steric effects due to the alkyl groups twisting to avoid one another, causing the macrocycle to distort from planarity, shortening the U-N bond lengths in the process. Thus there are two competing factors: shorter, stronger U-N bond lengths caused by distortion of the ligand from planarity, and aromatic stability in the ligand which is at a maximum for planar configurations. The finding that the inclusion of peripheral substituents was essential for reproducing the experimental geometry is an important one and will be considered in later chapters of this thesis.

The uranyl meso-methoxy-substituted iso-sapphyrin complex (Figure 1.5) reported by Burrel *et al*.[176] was investigated theoretically in an attempt to model the possible reaction mechanism between the ligand and the metal centre[244], and understand why meso-methoxy-substituted iso-sapphyrin is able to stabilise uranyl, while regular sapphyrin is not. Shamov performed DFT calculations using the Priroda code. The PBE *xc*-functional was used alongside all-electron basis sets of triple-zeta polarised quality. It was concluded that methanol substitution of the trianionic sapphyrin ligand, acts to reduce it to the dianionic meso-methoxy-substituted iso-sapphyrin, which has an improved affinity for the dicationic uranyl compared to the unsubstituted trianionic sapphyrin.

Pan *et al*. investigated the uranyl and bis-uranyl complexes of a series of three ligands: a hypothetical "pac-man"-like macrocycle consisting of four pyrrolic subunits joined by napthalenyl linkers (L^2) , and two experimentally reported similar macrocycles with phenylenyl (L^1) and anthracenyl (L^3) linkers[34]. The Priroda[245] code was used to perform DFT calculations using the PBE *xc*-functional alongside double-zeta polarised basis sets and the Priroda scalar relativistic all-electron approach for dealing with relativistic effects[246].

The size of the linkers was found to affect the geometry of the complexes: considering the binuclear complexes, phenylenyl (L^1) linkers result in ‘butterfly’ or ‘T’ shaped complexes; the hypothetical napthalenyl-linked (L^2) complexes are predicted to be stable only in the ‘butterfly’ conformation, and the anthracenyl (L^3) complexes adopt a geometry which is distorted to minimise intramolecular interactions between the uranyl oxygen ions (see Figure 1.11). Pan *et al*. conclude that, given strong similarities to known complexes, it should be possible to synthesize the hypothetical bis-uranyl L^2 complex.

In a previous related study using the same computational methodology, Pan *et al*. compared the structures and stabilities of ‘T’ shaped and ‘B’ (butterfly) shaped bis-uranyl expanded porphyrins[217], finding that the ‘B’ complexes are more stable.

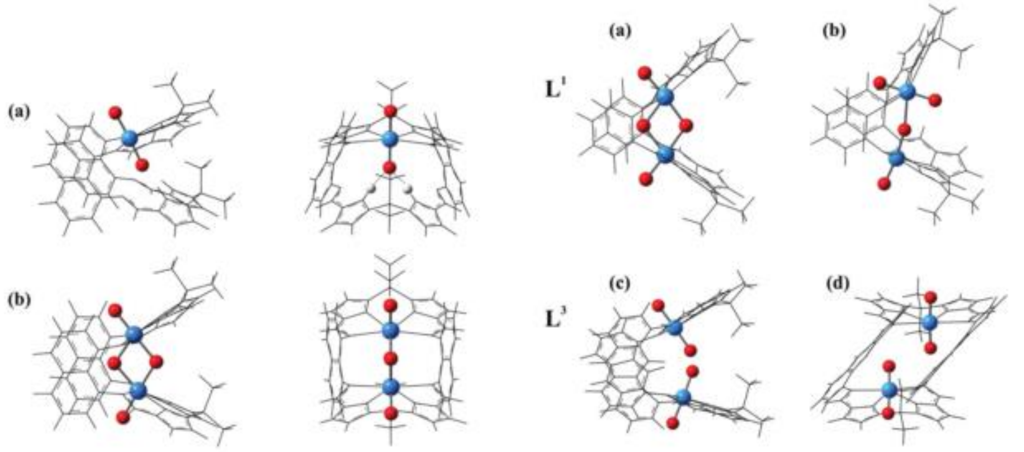

Fig. 1 Structures of (a) mononuclear $[(UO_2)(H_2L^2)]^{n-2}$ and (b) binuclear $[(UO_2)_2(L^2)]^{2n-4}$ (n = 2 for U^{VI}; n = 1 for U^V; left: side-on view, right: face-on view).

Fig. 2 Structures of the binuclear $[(UO_2)_2(L^x)]^{2n-4}$ ($L^x = L^1$ and L^3) complexes, (a) **B**utterfly-like L^1 isomeric complex, (b) **T**-shaped L^1 isomeric complex, (c) L^3 complex, side-on view, (d) L^3 complex, face-on view.

Figure 1.11: Structures of uranyl and bis-uranyl complexes with three Pacman-like ligands. Reproduced from Pan, Odoh, Schreckenbach, Arnold, Love, “Theoretical exploration of uranyl complexes of a designed polypyrrolic macrocycle: structure/property effects of hinge size on Pacman-shaped complexes”, *Dalton Trans*., **2012**, *41*, 8878-8885 (Ref [217]).

The lutetium(III) complex of pentaphyrin(1.1.1.1.1) was investigated by Fortes *et al*[247]. Both the TURBOMOLE and Gaussian 03 quantum chemistry software packages were used to perform a time-dependent density functional theory (TD-DFT) study using four different *xc*-functionals: B3LYP and PBE0 with TURBOMOLE, and *ω*B97X and *ω*B97XD with Gaussian 03. Solvent effects were included using the COnductor-like Screening MOdel (COSMO) with a dielectric constant of ($\varepsilon = 8.93$) to simulate solvation in dichloromethane. For geometry optimisations, the SV(P) Ahlrichs basis set was used, incorporating the Stuttgart pseudopotential, comprising 60 core electrons on the lutetium atom. The def2-SVP Ahlrichs basis set was used for calculation of vertical electron affinities as well as ionisation potentials. Very little structural variation is induced by changing the *xc*-functional. When the excitation energies are calculated, the Q-like band is found at a very low energy: 1501 nm and 1340 nm for the PBE0 and B3LYP *xc*-functionals, respectively. For the ωB97X and ωB97XD *xc*-functionals, these energies are found to correspond to wavelengths of 636 nm and 770 nm, respectively, slightly overestimated in comparison with the experimental value of 814 nm.

Cao and Dolg have performed DFT investigations on lanthanide [La(III), Gd(III), Lu(III)] texaphyrins, using the TURBOMOLE quantum chemistry software package. The B3LYP *xc*-functional was employed alongside scalar-relativistic energy-consistent 4f-in-core lanthanide pseudopotentials, and double and triple zeta basis sets with polarisation. Electron affinities were calculated by subtracting the energy of Ln-Tex^{2+} from Ln-Tex^{+}. The Gd-Tex^{2+} system (the *in vivo* X-ray radiation enhancer XCYTRIN®[131,210]) has been calculated to have a high electron affinity. Its strongly paramagnetic properties mean that it can be easily visualised using MRI, and it has been observed to localise in tumours[131,159,209]. Electron capture in cells by Gd-Tex^{2+} following reactions between X-rays and water result in high concentrations of hydroxyl radicals, leading to cytotoxicity and cell death. High electron affinities in the Ln(III)-Tex^{2+} systems are therefore an important property, that La(III), Gd(III) and Lu(III)-Tex^{2+} were all calculated to possess in this study. Binding energies, calculated in the gas phase and in aqueous solution, were all higher than 10 eV, indicating highly stable complexes. The optical properties were calculated to be very similar for all complexes, with one high energy band at 454-462 nm and a lower energy band at 681-686 nm. Subsequently, Cao *et al*. performed DFT investigations on the actinide [Ac(III), Cm(III) and Lr(III)] complexes with the related motaxafins[248,249] using the same model chemistry as for the previous Ln(III) complexes, with scalar-relativistic energy-consistent 5f-in-core actinide pseudopotentials in place of the 4f-in-core lanthanide pseudopotentials. Actinides were found to be coordinated out of the plane of the macrocycle, accounting for their lower stability compared to the lanthanide complexes, and suggesting that these particular macrocycles may be too small to adequately complex actinides. However, Ac-Motex^{2+}, the most stable of the actinide complexes, was suggested as the most likely synthetic target.

Several other expanded porphyrin-like systems and their complexes with actinides have been investigated theoretically. The $AnO_2^{2+/+}$, An = U, Np, Pu, complexes of the expanded porphyrin-like macrocycle alaskaphyrin and two similar macrocycles have been investigated using density functional methods by Shamov and Schreckenbach[250]. DFT calculations were performed using the Priroda code, applying a scalar four-component relativistic method with the PBE *xc*-functional alongside all-electron double and triple zeta basis sets. Bond lengths and vibrational frequencies compared favourably to experimental data[206], although the overall conformation of the uranyl Alaskaphyrin complex obtained by X-ray crystallography was not reproduced, a discrepancy attributed to crystal packing effects. The affinity of the ligand to the metal centre was calculated to decrease in the order U > Np > Pu, which was attributed to the actinide contraction. A previous study of actinyl (An = U, Np, Pu) complexes with alaskaphyrin by Liao *et al*. used the ADF code to explore the effects on the electronic structure of including or omitting the treatment of relativistic effects[251]. It was found that significant differences in the bond lengths and the ground state configurations of the isolated actinyls and the actinyl complexes are induced by the inclusion of relativistic effects using the quasi-relativistic method compared to non-relativistic calculations. Lan *et al*. investigated the actinyl (An = U(V/VI), Np(V/VI), Pu(V/VI)) complexes of the expanded porphyrin-like hybrid macrocycle cyclo[1]furan[1]pyridine[4]pyrrole using DFT[211]. The Gaussian 09 quantum chemistry package was used with the B3LYP *xc*-functional. Small-core scalar-relativistic ECPs were used alongside a 14s13p10d8f6g valence basis set contracted to 10s9p5d4f3g on the actinides. All other atoms had the polarised all-electron 6-31G(d) basis set applied. For the uranyl complex, good agreement with experimental bond lengths were found. Natural Population Analysis (NPA) reveals that the pyrrolic nitrogen atoms were found in all complexes to be the strongest donors to the actinides, and Mayer bond order analysis suggests that the pyrrolic An-N interactions contain more covalent character than either the interactions between the actinide and the pyridine nitrogen or the furan oxygen atoms. Actinyl(VI) complexes were found to display greater ligand-to-actinyl charge transfer than the actinyl(V) analogues, which was confirmed by charge decomposition analysis. Lan *et al*. conclude that in aqueous solution containing chloride ions, the plutonyl(VI) and uranyl(V) cations possess the highest selectivity for this macrocycle. Su *et al*. performed DFT investigations of the binuclear U^{3+} complexes with various species of a Pacman-like polypyrrolic macrocycle[252] using the Priroda code with a scalar relativistic four-component all-electron approach. Gaussian basis sets of double-zeta polarized quality were used alongside the PBE GGA *xc*-functional. Sixteen stable species were found, characterised by the angle at which the macrocycle was folded, and the angle at which it was twisted. It was concluded that the inherent flexibility of the macrocycle allows wide range of structural conformations and energetic states, as well as diverse U-U bonding. U-U interactions were characterised using Mayer bond order analysis. Dependent on structure, the U-U interaction ranges from no U-U bond being present, to a weak single U-U bond in the ground state conformation, to a U-U triple bond found in one species.

The effect of explicit solvation on a range of actinyl complexes with a polypyrrolic macrocycle was investigated by Qu *et al*[253]. Eighteen complexes with the macrocycle (H_4L) were optimised and studied[253]: $[(Sol)(An^{m}O_2)(H_2L)]^{n-}$, An = U, Np, Pu; m = VI when n = 0; and m = V when n = 1; Sol = vacant, pyridine and tetrahydrofuran. Using the Priroda code using a scalar relativistic all-electron approach, for geometry optimisations and the ADF code using the ZORA method to account for relativistic effects to calculate solvation free energies using the COSMO continuum solvation model. With both quantum chemistry codes, the PBE GGA *xc*-functional was used to approximate the exchange-correlation energy and double-zeta polarised basis sets. Charges and spin densities were found to be only slightly affected by the inclusion of explicit solvation. Explicitly solvated complexes were found to have slight geometric differences from solvent free complexes. There were small effects (within 0.01 Å) on actinyl An-O bond lengths, and differences in the O-An-O angle between unsolvated and explicitly solvated complexes were less than 1˚. Distances between the actinyl oxygen ions and hydrogen atoms associated with the ligand, however, were found to differ more significantly, by up to 0.05 Å.

Yang *et al*. have recently investigated the complexes of $AnO_2^{2+/+}$ with the amethyrin, oxasappyrin and grandephyrin macrocycles[254] (see Figure 1.12). Density functional theory (DFT) calculations were performed using the Gaussian 09 quantum chemistry software package and the range-separated hybrid *xc*-functional CAM-B3LYP. For the actinide atoms, quasi-relativistic 5f-in-valence small-core ECPs were used alongside the optimized segmented basis set for the valence shells, which is contracted as (14s13p10d8f6g)/[10s9p5d4f3g]. The triple-zeta quality 6-311G basis set was applied to the N and O atoms in the first coordination sphere, and for all other atoms, the double-zeta 6-31G(d) basis set was applied. Analysis was performed using the Quantum Theory of Atoms in Molecules (QTAIM) and Natural Population Analysis (NPA), and NMR properties were calculated. Yang *et al.* conclude, based on changes in the free energy, that NpO_2^{2+} and PuO_2^{2+} cations show stronger tendency for binding with these ligands than UO_2^{2+}, UO_2^{+}, NpO_2^{+}, and PuO_2^{+}. It was also found that the oxasapphyrin ligand is a better fit for these cations than H_2-amethyrin and grandephyrin. QTAIM analysis shows that the interactions between actinide ions and ligand donor atoms is ionic, while the An-O_{yl} bonds are covalent.

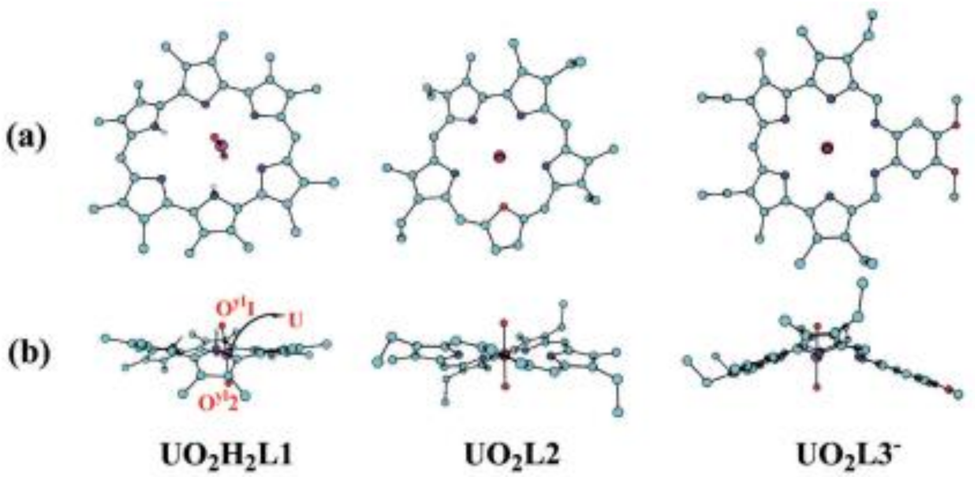

Figure 1.12: The optimised structures seen a) from above and b) from the side of UO_2H_2-amethyrin(1.0.0.1.0.0) (left), UO_2-oxasapphyrin(1.1.1.1.0) (centre) and UO_2-grandephyrin (right). Reproduced from: Yang, Ding, Wang, "Characterization of the binding of six actinyls $AnO_2^{2+/+}$ (An = U/Np/Pu) with three expanded porphyrins by density functional theory", *New J. Chem.*, **2016,** DOI: 10.1039/c6nj01615d (Ref [254]).

Other metal complexes, and the uncoordinated expanded porphyrin macrocycles themselves, have also been the subject of computational studies[164,255–260], with one interesting example being the bis-Zn, bis-Cd and bis-Hg complexes of phenyl-substituted hexaphyrin(1.1.1.1.1.1), investigated using DFT by Sun *et al*[261]. Metallation with Zn(II) and Cd(II) results in dumbbell shaped complexes, while metallation with bis-Hg(II) produces a rectangular complex, possibly due to steric repulsion between two inward pointing meso-phenyl groups in the bis-Hg(II) dumbbell conformer.

Studies using multiconfigurational methods have thus far been restricted to the tetrapyrrolic porphyrins, where a significant amount of work has been done to determine the electronic structure of various porphyrins[262–274], where in general improvements are found compared to TDDFT simulations[257].

An early multiconfigurational study was performed by Merchán *et al.*, who used the complete active space, self-consistent field (CASSCF) and the multiconfigurational second-order perturbation theory (CASPT2) to model the electronic structure of free-base porphyrin, obtaining calculated excitation energies to within 0.3 eV of experimental data, and determining that in order to build an accurate picture of the electronic structure of porphyrin, both σ- and π-electron contributions must be considered. Due to the large size of the porphyrin relative to previous studies, the active space (see Chapter 2.5. Methodology: Multiconfigurational (Post-HF) Methods) could not simply be defined to include all π electrons. This study expanded the active space systematically, including those orbitals with occupation numbers which deviated most from zero or two, showing for the first time the applicability of the CASPT2 methodology to a large system. Subsequently, Serrano-Andrés *et al*. performed CASPT2 calculations on the low-lying optically allowed valence states of free-base porphyrin finding that the wavefunctions of the states considered have a significantly multiconfigurational character, meaning a single-determinant method may struggle to describe them accurately. Choice of basis set and the size of the active space are found to be important, and overall, the CASPT2 results are found to be in agreement with experimental data. Since then, there have been many more multiconfigurational studies on porphyrin systems. CASSCF and CASPT2 studies were performed to determine the electronic structure of the ground state of iron(II) porphine[265,266] by Choe *et al.*

The excitation spectra of free-base and magnesium porphyrin were calculated using both the Symmetry Adapted Cluster-Configuration Interaction (SAC-CI) and CASPT2 methodologies by Šeda *et al*. It was determined that both methodologies reproduced the electronic spectra of free-base porphyrin with a high level of accuracy, although the accuracy achieved with the SAC-CI methodology was determined to be at its current limit, with improvement requiring higher configuration selection thresholds presently impossible (in 2004) for such a large system[263]. The CASPT2 calculations reproduced the experimental spectra of both free base and magnesium porphyrin to a high level of accuracy[263].

The electronic spectrum of magnesium porphyrin was investigated by Rubio *et al*. using CASSCF and CASPT2 methods, finding generally good agreement with experimental spectra, with a consistent underestimation of transition energies of 0.1-0.5 eV[269]. This difference was attributed to several factors, namely the approximate treatment of the dynamical correlation with CASPT2, the limited basis set and the fact that the calculations were performed on an unsubstituted analogue to the substituted experimental structure. Jensen *et al*. studied the porphyrin-based biomolecule oxyheme using CASPT2 methods, reproducing the experimental excitation spectrum with an average error of 0.24 eV[264]. They conclude that the active space selected in this study, 14 electrons in 13 orbitals, comprising all five Fe 3d orbitals, the correlated orbitals for all occupied Fe 3d orbitals, as well as all four O_2 π and π^* orbitals, is sufficient to build an accurate description of the ground state of the oxyheme system.

More recently, Kerridge has applied the Restricted Active Space, Self-Consistent Field (RASSCF) methodology to free base, magnesium and zinc porphyrins[272]. He concludes that placing the Gouterman orbitals in the RAS2 subspace (see Chapter 2.5. Methodology: Multiconfigurational (Post-HF) Methods) *i.e.* considering all excitations involving these orbitals and a limited number of excitations for the remainder of the π-conjugated subsystem in the RAS1 and RAS3 subspaces, furnishes results with a high degree of accuracy at a fraction of the computational cost of the CASSCF method. This finding is particularly useful for the transition metal complexes where the size of the active space necessary to encompass the entire π-conjugated subsystem in addition to the relevant metal orbitals becomes prohibitively expensive for CASSCF methodologies[264,272,273]. Additionally, the practice of placing the Gouterman orbitals alone into RAS2 may be applicable to the expanded porphyrins and possibly even f-block complexes of the expanded porphyrins in the future.

To summarise, there have been several publications where theoretical methods have successfully been used to study f-element complexes with expanded porphyrins and similar systems, either to investigate hypothetical species or in conjunction with experimental data. Where experimental data is available, it can be replicated with good agreement in most cases although care must be taken to minimise the effect of method-dependent errors. Inclusion of at least scalar relativistic effects is vital to obtaining good results.

1.5. Summary

Presently many research groups are using both experimental and theoretical techniques to investigate the many possible uses of expanded porphyrins and their complexes. Further theoretical studies are essential to developing the understanding the nature of bonding in these complexes, and theoretical methods present a way of examining systems that may be difficult to study experimentally.

2. Methodology

2.1. Bra-Ket Notation

At various points in this chapter, where is has been expedient to do so, bra-ket notation has been used, as detailed in equation 2.1.

$$\text{bra: } \langle f| = f^*(x), \quad \text{ket: } |f\rangle = f(x) \qquad (Eq. 2.1)$$

Such that the expectation value of an observable represented by an operator $\hat{A}$ for a physical system in the state $|\psi\rangle$ is:

$$\langle\psi|\hat{A}|\psi\rangle \qquad (Eq. 2.2)$$

2.2. Introduction to Quantum Chemical Calculations

The purpose of this chapter is to give an introduction to quantum chemical calculations, chiefly the density functional and multiconfigurational methods employed in the results chapters of this thesis. It is aimed at introducing the concepts and relevant mathematics important for understanding how these methodologies work. More in-depth information can be found in several resources[38,40,41,224–231,243,275,276].

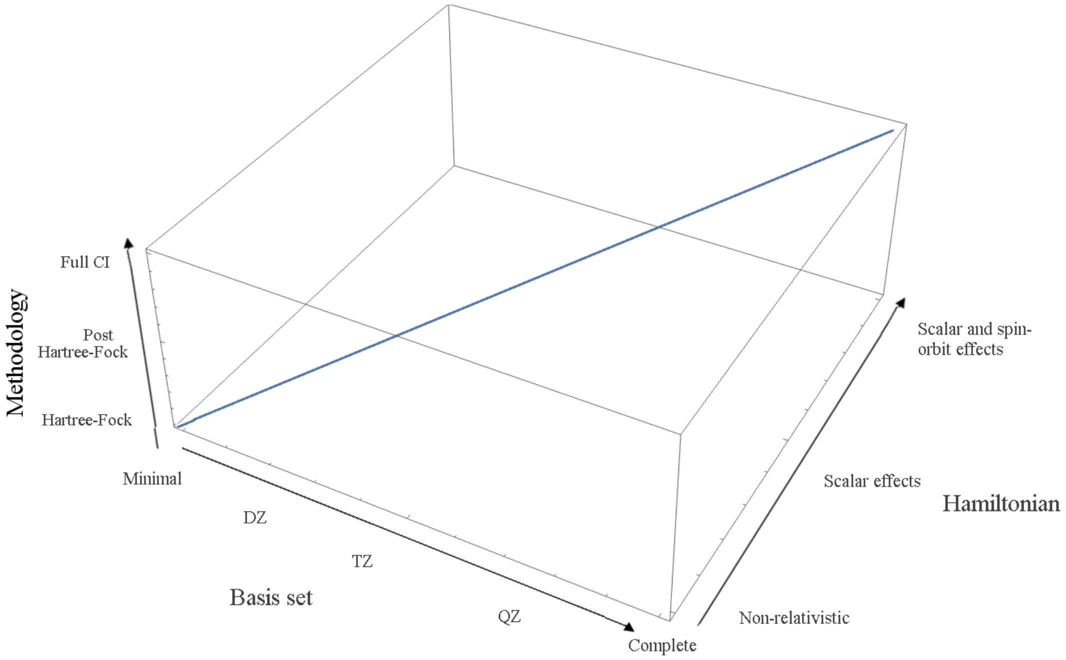

Figure 2.2: 3-dimensional Pople diagram showing how the quality of a quantum chemical calculation depends on methodology, Hamiltonian and basis set choice.

The quality of a quantum chemical calculation depends on three factors: the basic methodology (*i.e.* how electron correlation is modelled), the quality of the basis set, and the treatment of relativistic effects. The treatment of relativistic effects is particularly important for heavy elements. The Pople diagram[277] in Figure 2.1 shows that the quality of the calculation approaches the exact solution as the quality of the basis set is increased, as the Hamiltonian is modified to include relativistic effects, and as the methodology is improved to include electron correlation.

2.3. Basis Sets

A quantum chemical calculation must initially build a description of the molecular orbitals of the system using basis functions. For a molecular calculation, molecular orbitals are built using linear combinations of atomic orbitals, although basis sets in common use for other applications can be based on plane waves. Larger basis sets generally mean higher quality calculations, although computational expense increases with size. The atomic orbitals used can be either Slater-type orbitals (STOs)[278],

$$\chi_{\zeta,n,l,m}(r,\theta,\phi) = \mathrm{N}Y_{l,m}(\theta,\phi)r^{n-1}e^{-\zeta r} \qquad (Eq. 2.3)$$

or Gaussian-type orbitals (GTOs)[279],

$$\chi_{\zeta,n,l,m}(r,\theta,\phi) = \mathrm{N}Y_{l,m}(\theta,\phi)r^{2n-2-l}e^{-\zeta r^2} \qquad (Eq. 2.4)$$

Here, N is a normalisation constant, $Y_{l,m}$ are spherical harmonics, n is the principle quantum number, representing the relative total energy of the orbital, increasing with distance from the nucleus. In general, zeta, ζ, is a parameter used to define the rate of decay of the basis function. In a minimal basis set, this is related to the effective charge of the nucleus and accounts for partial shielding by other electrons.

STOs are able to describe systems with a high level of accuracy, exhibiting exponential decay at long range and a cusp at the atomic nucleus. Radial nodes are modelled using linear combinations of STOs. A less computationally intensive, but less physically accurate, method involves approximating STOs using GTOs[280–282]. The $e^{-\zeta r^2}$ component in GTOs results in reduced accuracy compared to STOs when used for modelling the short- and long-range behaviour of electrons. Approaching the nucleus, GTOs have a zero gradient, and at long-range, they have a steeper gradient than STOs. This means GTOs decay faster, making them less accurate at modelling the long-range behaviour of electrons. Linear combinations of GTOs are needed to build orbitals with a sufficient level of accuracy compared to any given STO (an infinite combination of GTOs is required to give the *same* level of accuracy), although a combination of several GTOs are still computationally cheaper to use than STOs because their integrals are much simpler to solve.

At minimum, a sufficient number of basis functions are necessary to describe all the electrons in an atom. For example, a basis set for a hydrogen atom must contain at a minimum, one 1s function. The simplest basis set, known as a minimal basis set, contains no additional functions. A double zeta (double-ζ or DZ) basis set comprises two sets of functions. For hydrogen, this means a 1s and 1s' function, each with different exponents. A triple zeta (triple-ζ or TZ) basis set comprises three sets of functions, a quadruple zeta (quadruple-ζ or QZ) basis set comprises four, and so on.

The larger the basis set, the higher the quality of the calculation, but also the greater the computational expense. This expense can be reduced by recognising that some electrons, the outermost, are significantly more likely than others to become involved in bonding interactions. Many basis sets increase the number of functions on the valence electrons only, while describing the core region using a minimal basis set. These are known as valence double, triple, quadruple zeta, and so on. An increased number of valence functions will improve the modelling of radial correlation. Additional functions, such as polarisation or diffuse functions, can be added to improve the quality of the basis set.

Polarisation functions can also be added to improve the quality of the basis set. The electron density of an atom in a molecule is influenced by the presence of other nuclei, so a greater level of flexibility in the spatial symmetry of orbitals is useful. Polarisation functions have higher angular momentum than that of the orbital they are added to. They allow a more realistic description of bonding interactions by accounting for the fact that during a bonding interaction, the electron density is distorted in an asymmetrical manner. s orbitals can be polarised by adding p functions, p orbitals by adding d functions, and so on. Diffuse functions have a small exponent, designed to give an accurate representation of the region of the orbital most distant from the nucleus. These are particularly useful for describing anionic systems as well as radial correlation.

The core regions of atoms are typically chemically unimportant, although they are very important energetically. Because inner electrons contribute a large amount to the total energy of the system, minimising the energy of the basis functions describing these optimises the core region, while the valence region, which is energetically smaller in magnitude, but chemically far more important than the core region is not described as well. In order to describe the outer region well, the basis set needs to be very large with most of the functions being used to describe the 1s electrons. The core region is relatively chemically inert, meaning that the majority of computational effort is spent describing an almost constant, as well as chemically unimportant region. The efficiency inherent in this is the motivation for basis set contraction.

The basis functions used to describe the inner electrons can be contracted into fewer functions by forming fixed linear combinations. This is done by fixing the values of the variational coefficients for each primitive basis function *i.e*. making them constant. Beginning with a basis set comprising, say, ten *s*-functions, the exponents can be optimised using a variational calculation on the atom of interest, and those which are found to chiefly describe the chemically inactive core region can be identified. Fixing the coefficients of these inner functions mean they no longer need to be determined using the variational principle. The core region is now described by a fixed combination of fewer basis functions. This decreases computational cost as fewer basis functions now need to be optimised using the variational principle, and as computational cost scales as at least the fourth power of the number of basis functions, savings can be significant.

Contracted basis sets are formed in one of two ways. In segmented contraction the entire set of primitive GTOs describing a core region is separated into groups of functions, which are then contracted, with each group of primitive functions forming one contracted function. In general contraction, each primitive is included in every contracted function, with different coefficients.

A pseudopotential, or effective core potential (ECP) presents a way of reducing computational cost by neglecting to treat the chemically unimportant core region of a large atom explicitly, instead replacing the core orbitals with an effective potential. This potential may include an implicit treatment of relativistic effects[233,283–289], as will be discussed further in Chapter 2.7: Relativistic Effects. A pseudopotential or ECP can be generated by first obtaining a good-quality all-electron wavefunction for the atom in question, and replacing the valance orbitals with nodeless pseudo-orbitals, which behave correctly in the valence region, but lack nodal structure in the core region. The core electrons can then be replaced by an appropriate potential, fit to parameters so that the pseudo-orbitals which are produced as a result of solving the many-electron Schrödinger equation (or Dirac equation or similar, see Chapter 2.7: Relativistic Effects) which match the valence orbitals from the all-electron calculation.

In general, larger basis sets result in improved accuracy in the results of calculations. The most realistic solution is found at the Hartree-Fock limit, as the basis set approaches completeness, *i.e.* as the basis set tends towards being infinitely large.

2.4. Introduction to Electronic Structure Calculations

The starting point for most quantum chemistry is to calculate the ground state energy of a molecular or periodic system. One must solve the Schrödinger equation which may be done exactly[290] for a one-electron atom. For many particle systems, this is somewhat more complicated. The time-independent Schrodinger equation is:

$$\hat{H}\Psi = E\Psi \qquad (Eq. 2.5)$$

where the wavefunction Ψ is a function of the spatial coordinates as well as the spin coordinate ω, for an n-particle system, and E is the energy of the state represented by Ψ. Atomic units, the system of units particularly useful for atomic calculations, where electron mass, electron charge, $\hbar$ and Coulomb's constant, $\kappa_e = 1/(4\pi\varepsilon_0)$ are defined as unity, are used. For molecular systems, the Hamiltonian, $\hat{H}$, contains five terms:

$$\hat{H} = -\frac{1}{2}\sum_{i}\nabla_i^2 - \sum_{\mathrm{A}}\frac{1}{2\mathrm{M_A}}\nabla_{\mathrm{A}}^2 - \sum_{\mathrm{A},i}\frac{\mathrm{Z_A}}{r_{\mathrm{A},i}} + \sum_{\mathrm{A}>B}\frac{\mathrm{Z_A Z_B}}{r_{\mathrm{A,B}}} + \sum_{i>j}\frac{1}{r_{i,j}} \qquad (Eq. 2.6)$$

Where the first term is the electronic kinetic energy term. The second term is the nuclear kinetic energy term, where M_A is the mass of each nucleus. The third term is the electron-nuclear attraction term, where Z_A is the charge on each nucleus and $r_{A,i}$ is the corresponding distance from nucleus A to electron i. The fourth term is the nuclear-nuclear repulsion term, where $r_{A,B}$ is the separation of nucleus A and nucleus B. The final term is the electron-electron repulsion term, with $r_{i,j}$ being the separation of electrons i and j.

Solving this equation for $4n$ variables is a hugely complicated task, and approximations must be made in order to obtain a solution. For cases where only electronic properties are of interest, the large mass and slow motion of an atomic nucleus compared to an electron allows the use of the Born-Oppenheimer approximation[291], which separates the molecular wavefunction into electronic and nuclear components:

$$\Psi_{total} = \Psi_{electronic} \times \Psi_{nuclear} \qquad (Eq. 2.7)$$

The time independent Schrödinger equation can then be solved for the electronic wavefunction with the nuclear coordinates assumed to be constant. To compute nuclear motion, as in a molecular geometry optimisation, the nuclear coordinates which minimise the energy of the system must be found.

Coulomb's law states that electrons repel one another with the repulsion energy = $\frac{1}{r_{ij}}$ where r_{ij} is the separation of electrons i and j. A simplification assumes that motion of any one electron is independent of the motion of all other electrons in the system. The actions of the other electrons can be accounted for in an average manner, known as the mean field approximation. Consequently, electron correlation, *i.e.* the energy which arises as a result of the interactions between electrons with other electrons in a quantum system, is completely neglected. Electron correlation is often a contribution of around 1% of the total energy of a system[224,231]. Although this is a small component of the total energy, it can be of great importance when relative energies are considered[228].

2.5. Hartree-Fock (HF) Theory

Hartree-Fock Theory

The Hartree product is the simplest way of describing a many electron wavefunction, built using the product of one electron wavefunctions. The Hartree product wavefunction for a system with two electrons is:

$$\Psi^{HP}(x_1, x_2) = \phi_1(x_1)\phi_2(x_2) \qquad (Eq. 2.8)$$

This corresponds to a system of non-interacting particles, where x_1 and x_2 are the spin and spatial coordinates of two electrons in spin-orbitals (the product of a spatial orbital and a spin function α or β) ϕ_1 and ϕ_2 respectively, which do not interact with one another, *i.e.* the probability of finding an electron with spin and spatial coordinates x_1 at a given point is not dependent on the location of electron with spin and spatial coordinates x_2. Aside from the fact that neglecting electron-electron interactions is not a suitable approximation for most systems, the Hartree product fails to obey the antisymmetry principle, which states that the wavefunction describing a given system of fermions should be antisymmetric under the exchange of any two of these fermions. A consequence of this is that if the spin and spatial coordinates of any two electrons in a system are exchanged with one another, the total wavefunction that describes them must change sign. The antisymmetry principle can be satisfied by taking a linear combination of Hartree products, *i.e.* by assuming that a single Slater determinant can be used to approximate an exact n-body wavefunction. The Slater determinant for an n electron wavefunction is:

$$\Psi(x_1, x_2, x_3, \ldots, x_n) = \frac{1}{\sqrt{n!}} \begin{vmatrix} \phi_1(x_1) & \phi_2(x_1) & \cdots & \phi_n(x_1) \\ \vdots & \vdots & \ddots & \vdots \\ \phi_1(x_n) & \phi_2(x_n) & \cdots & \phi_n(x_n) \end{vmatrix} \qquad (Eq. 2.9)$$

Where $\phi_n(x_n)$ are a set of one-electron wavefunctions (spin orbitals) with spatial coordinates x_n. The Slater determinant allows exchange, *i.e.* Fermi correlation, which exists between electrons of like spin, to be accounted for, but neglects correlation between electrons of unlike spin.

The starting point for a Hartree-Fock calculation requires an approximate set of one-electron wavefunctions. These are constructed as linear combinations of atomic orbitals using basis functions (see Chapter 2.3: Methodology: Basis Sets) to build a set of molecular orbitals. The Hartree-Fock wavefunction is a Slater determinant. The energy of this electronic wavefunction is given by:

$$E_e = \left\langle \Psi \middle| \widehat{H_e} \middle| \Psi \right\rangle \qquad (Eq. 2.10)$$

Where E_e is the energy of the wavefunction and $\widehat{H_e}$ is the electronic Hamiltonian. The variational principle states that our approximate wavefunction Ψ has an energy greater than or equal to the exact energy of a system, *i.e.*:

$$E_0 \leq \frac{\left\langle \Psi \middle| \hat{H} \middle| \Psi \right\rangle}{\langle \Psi | \Psi \rangle} \qquad (Eq. 2.11)$$

The problem is then finding the wavefunction which minimises the energy. There are infinitely many solutions to the Schrödinger equation, of which E_0 is the energy of the lowest. The Hartree-Fock energy, E_{HF}, is an upper bound to the true energy of the ground state, with the difference between the two being the neglected correlation energy. The energy of the ground state, E_0, cannot be obtained exactly with Hartree-Fock theory except in the one-electron case, but an improved approximate wavefunction can be obtained by variation of its parameters until the energy of the system is minimised. The molecular orbitals which minimize the electronic energy E_e can thus be found. These molecular orbitals can be written as a linear combination of a set of basis functions:

$$\varnothing_{\mathrm{MO}} = \sum_i c_i \varphi_i \qquad (Eq. 2.12)$$

Where $\varnothing_{\mathrm{MO}}$ is a molecular orbital, φ_i are the basis functions, and c_i are the expansion coefficients, which are the variational parameters.

The Fock operator is constructed as:

$$\hat{F}(i) = \hat{h}(i) + \sum_{j=1}^{n} \left[2J_j(i) - K_j(i) \right] \qquad (Eq. 2.13)$$

Where $\hat{h}(i)$ is the one-electron Hamiltonian for electron i, J_j and K_j are the terms accounting for the Coulomb repulsion between electrons and i and j, and the exchange term for electrons and i and j, respectively. The Fock operator is used to approximate the many electron Hamiltonian in the molecular Schrödinger equation to create the Hartree-Fock equations:

$$\hat{F}(i)\phi(i) = E\phi(i) \qquad (Eq.\ 2.14)$$

Where $\phi(i)$ are a set of spin-orbitals. These can be used to generate a potential. The energy of the wavefunction is minimised with respect to this potential, and a new set of molecular spin-orbitals, and in turn a new potential, is generated. This process is repeated until self-consistency is achieved, *i.e.* the energy of the molecular orbitals generated is the same as the energy of the input molecular orbitals to within a predefined tolerance.

2.6. Multiconfigurational (Post-HF) Methods

2.6.1. Introduction to Multiconfigurational Calculations

In many cases, the exact electronic wavefunction cannot be accurately described by a single Slater determinant and in these cases an improved approximation is achieved by a linear combination of Slater determinants. The Hartree-Fock method neglects correlated motion between electrons of unlike spin and so will always fail to reproduce the exact total energy of a system, and also fails to correctly model bond breaking processes. Post-Hartree-Fock methods represent ways of improving the HF energy by accounting for this correlation. First, the different types of correlation will be briefly introduced. The correlation accounted for by HF is known as Fermi correlation, or exchange, and acts to prevent two electrons of like spin occupying the same space at the same time. Coulomb correlation, completely neglected by the Hartree-Fock method, accounts for the electrostatic interactions between electrons. The energy difference between the exact energy of a system and the Hartree-Fock energy is known as the correlation energy:

$$E_{Correlation} = E_{Exact} - E_{HF} \qquad (Eq. 2.15)$$

It is a theoretical convenience to simplify modelling of the Coulomb correlation by separating it into two parts. Dynamic correlation is a short range effect, with a $\frac{1}{\boldsymbol{r}_{ij}}$

dependency, where r_{ij} is the separation of electrons i and j. Dynamic correlation, as the name suggests, is related to the motion of electrons. The other component, static correlation, acts over a greater range. Near-degeneracy effects occur when multiple states are lying close in energy to the ground state resulting in low-lying excited states, for example, as a consequence of the weak crystal fields experienced by the actinides, and it is in systems such as these that the single Slater determinant approximation of Hartree-Fock fails most significantly. These effects give rise to the static correlation, which is of greatest importance when the ground state of a molecule cannot be accurately represented by a single Slater determinant, and can be important when actinide complexes are considered[53,69,240,242,276]. Realistically, dynamic and static correlation are not so well defined, and it is more accurate to consider a spectrum with dynamic correlation at one end, and affecting all orbitals, and static correlation at the other end, affecting principally those orbitals close to the HOMO-LUMO gap.

Several post Hartree-Fock methods exist which attempt to include some or all of this correlation energy. For the purposes of this thesis, the focus will be on the Configuration Interaction[292] and the Complete/Restricted Active Space Self-Consistent Field (CASSCF/RASSCF)[273,293] methodologies. Other post HF methodologies have been used to model actinide containing systems, including coupled cluster (CC) methods[294] and Moller-Plessett (MP) perturbation theory[295], but these will not be discussed here.

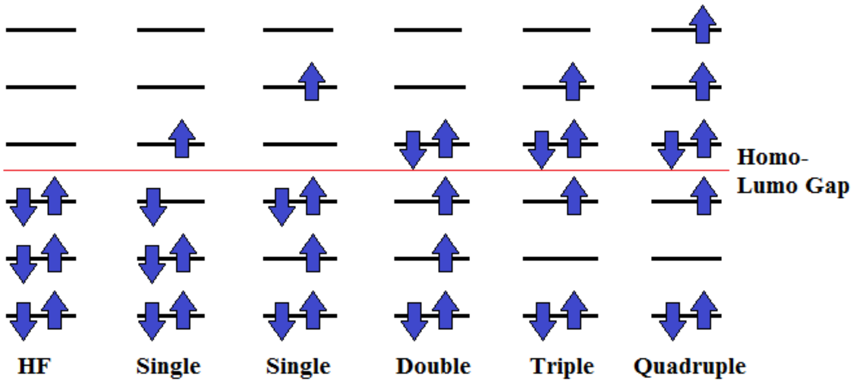

Figure 2.2: Excited Slater determinants and the Hartree-Fock reference determinant from which they are generated showing single, double, triple and quadruple excitations.

The Hartree-Fock method incorrectly assumes that for a given set of molecular orbitals (MOs), a single Slater determinant acts to describe the electronic wavefunction. Multiple additional determinants can be constructed by replacing the occupied molecular orbitals in the Hartree-Fock Slater determinant with unoccupied orbitals. These are referred to as singly, doubly, triply… etc. excited determinants depending on how many occupied MOs have been replaced with unoccupied MOs. The effects of electron correlation can be constructed based on a linear combination of the ground state (Hartree-Fock) determinant and that of all possible excited determinants:

$$|\Psi\rangle \; = \; c_0\left|\Psi_0\right\rangle + c_i^a \left|\Psi_i^a\right\rangle \; + \; c_{ij}^{ab}\left|\Psi_{ij}^{ab}\right\rangle + \; c_{ijk}^{abc}\left|\Psi_{ijk}^{abc}\right\rangle + \; \ldots \qquad (Eq. 2.16)$$

This is the full Configuration Interaction (full CI) wavefunction. The determinant in the first term is equal to the Hartree-Fock determinant. The determinant in the second term is obtained by considering all possible single excitations, the determinant in the third term by considering all possible double excitations and so on. The expansion coefficients c_n are variables that minimise the energy of the system and are found *via* diagonalisation of the CI Hamiltonian matrix:

$$\hat{H}^{\mathrm{CI}} = \begin{bmatrix} \langle\Psi_0|\hat{H}|\Psi_0\rangle & \langle\Psi_0|\hat{H}|\Psi_{\mathrm{S}}\rangle & \langle\Psi_0|\hat{H}|\Psi_{\mathrm{D}}\rangle & \langle\Psi_0|\hat{H}|\Psi_{\mathrm{T}}\rangle & \cdots \\ \langle\Psi_{\mathrm{S}}|\hat{H}|\Psi_0\rangle & \langle\Psi_{\mathrm{S}}|\hat{H}|\Psi_{\mathrm{S}}\rangle & \langle\Psi_{\mathrm{S}}|\hat{H}|\Psi_{\mathrm{D}}\rangle & \langle\Psi_{\mathrm{S}}|\hat{H}|\Psi_{\mathrm{T}}\rangle & \cdots \\ \langle\Psi_{\mathrm{D}}|\hat{H}|\Psi_0\rangle & \langle\Psi_{\mathrm{D}}|\hat{H}|\Psi_{\mathrm{S}}\rangle & \langle\Psi_{\mathrm{D}}|\hat{H}|\Psi_{\mathrm{D}}\rangle & \langle\Psi_{\mathrm{D}}|\hat{H}|\Psi_{\mathrm{T}}\rangle & \cdots \\ \langle\Psi_{\mathrm{T}}|\hat{H}|\Psi_0\rangle & \langle\Psi_{\mathrm{T}}|\hat{H}|\Psi_{\mathrm{S}}\rangle & \langle\Psi_{\mathrm{T}}|\hat{H}|\Psi_{\mathrm{D}}\rangle & \langle\Psi_{\mathrm{T}}|\hat{H}|\Psi_{\mathrm{T}}\rangle & \cdots \\ \vdots & \vdots & \vdots & \vdots & \ddots \end{bmatrix} \qquad (Eq. 2.17)$$

The matrix elements here consider all the possible matrix elements which exist between the determinants for, for example, single and double excitations:

$$\langle\Psi_{\mathrm{S}}|\hat{H}|\Psi_{\mathrm{D}}\rangle = \begin{bmatrix} \Psi_{\mathrm{S}1} & \Psi_{\mathrm{S}2} & \cdots & \Psi_{\mathrm{S}n} \end{bmatrix} \hat{H} \begin{bmatrix} \Psi_{\mathrm{D}1} \\ \Psi_{\mathrm{D}2} \\ \vdots \\ \Psi_{\mathrm{D}n} \end{bmatrix} \qquad (Eq. 2.18)$$

The CI Hamiltonian matrix can be evaluated using the Slater-Condon rules, which state that a CI matrix element is equal to zero unless the determinants differ by 0, 1 or 2 MOs, and Brillouin's theorem which causes the matrix elements which exist between the Hartree-Fock reference configuration and the singly excited configurations:

$$\langle\Psi_i|\hat{H}|\Psi_0\rangle = 0 \qquad (Eq. 2.19)$$

For a complete basis set (*i.e.* a theoretical, infinite basis set), the full CI approach results in the exact wavefunction. However, the size of the calculation scales factorially with the number of electrons, making full CI impossible for anything other than very small molecules.

2.6.2. The Complete/Restricted Active Space, Self-Consistent Field Methods

Truncated versions of configuration interaction are used, considering single excitations only, single and double excitations (CISD) only, single, double and triple excitations (CISDT) only, and so on. These too quickly become impractical for large systems.

The Complete/Restricted Active Space, Self-Consistent Field (CASSCF and RASSCF) approaches present a way of performing full CI on only the chemically important orbitals of a system, thus significantly reducing computational expense compared to CI. The CASSCF approach involves partitioning orbitals into active and inactive regions, where chemically important orbitals are identified and placed within the active space. The active space, according to Bjorn's Rules[274], is typically a number of the highest occupied and lowest unoccupied orbitals, and should include conjugated orbitals and any bonding and antibonding orbitals relating to a bond which is of interest. For each π bond, the ideal scenario is that two π orbitals be included. Otherwise, the most appropriate π orbitals should be selected by energy. For transition metals, all orbitals with d-character should be included. Metals in high oxidation states generally need a greater number of active orbitals. For lanthanides, the 4f shell should be active, as should 5d and 6s orbitals. Actinides should ideally have the 5f, 6d and 7s orbitals in the active space, but for highly charged systems, this can be reduced to 5f only. Highly covalent interactions, such as the U-O bonds in uranyl require a greater number of active orbitals. Uranyl needs an active space comprising 12 electrons in 12 orbitals[33].

Full CI is then performed on the active orbitals only. CASSCF allows larger systems to be examined than full CI, but quickly becomes impractical for large active spaces. However, the RASSCF approach allows further division of the orbitals[242,273,276,292,293,296]. In RASSCF, the active space is divided into three subspaces, RAS1, RAS2 and RAS3. The most important active space, RAS2, can then be treated using full CI. Excitations from RAS1 and into RAS3 can then be considered using truncated CI, typically CISD or CISDT. Identification of the active space is a complicated procedure. One method involves first performing a single point energy calculation with DFT or another method. Orbitals of interest can then be selected based on their character as suggested in Bjorn's Rules, and a CASSCF calculation can be performed. Orbitals must then be examined visually and occupation numbers must be monitored. The active space can be adjusted accordingly and the calculation rerun.

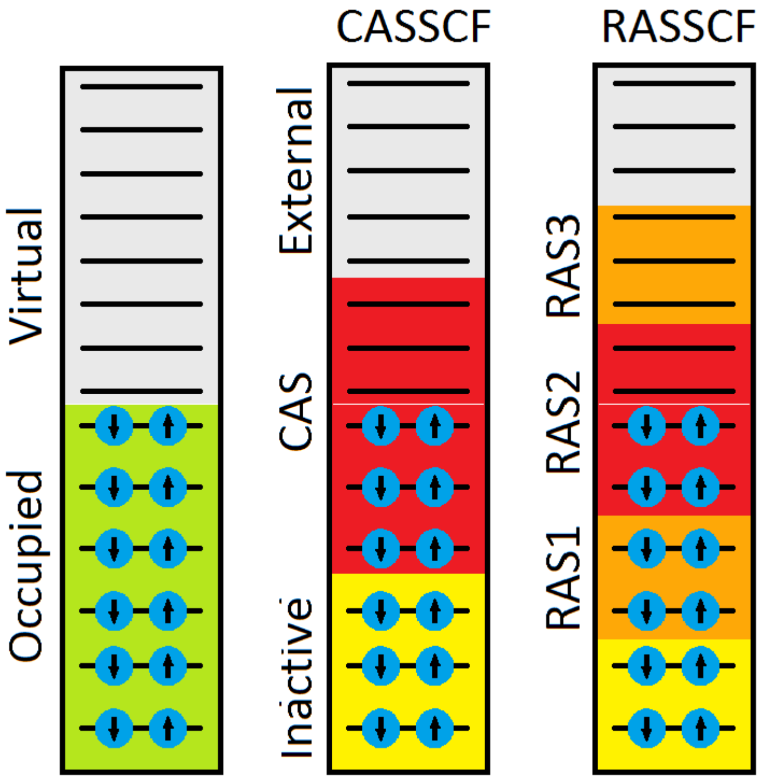

Figure 2.3: Partitioning of the orbital space into active, inactive and external regions, and partitioning of the CAS space into RAS1, RAS2 and RAS3 subspaces.

Another method involves a process known as RAS probing, where the active space is expanded systematically by adding orbitals to RAS1 and RAS3. The natural orbital occupations can then help inform the decision as to whether an orbital should be included. The natural orbitals have integer occupation numbers for monoconfigurational wavefunctions, and non-integer occupation numbers for multiconfigurational wavefunctions. In order to warrant inclusion in the active space, an 'occupied' orbital should typically have an orbital occupancy of less than 1.98, and an 'unoccupied' orbital should have an orbital occupancy of greater than 0.02, although this is just a rule of thumb. The most active orbitals, for example, those with occupations lower than 1.95 or higher than 0.05 should ideally be included in RAS 2 and thus treated with full CI. Orbitals should ideally be paired, with each pair containing one strongly occupied and one weakly occupied orbital.

By limiting calculations to active orbitals, CASSCF and RASSCF methods focus on recovering not the total correlation energy, but that part of it which is related to the effects of near degeneracy, *i.e*. the static correlation only. Dynamical correlation must be recovered perturbatively, and this can be achieved using, for example the CASPT2[297,298] and RASPT2[274,297] methods. Other methods for recovering dynamical correlation include the n-electron valence state perturbation theory (NEVPT2) method, a generalisation of MP2 to CAS scenarios, which will not be discussed here but can be read about in the referenced resources[299–303].

2.6.3. Many-Body Perturbation Theory and CASPT2

Mathematically, perturbation theory allows the approximation of solutions to complex problems from solutions to similar but simpler problems. The Hamiltonian of the perturbed system can be written as:

$$\widehat{H}_{total} = \widehat{H}_0 + \varepsilon \widehat{H}_{\mathrm{P}} \qquad (Eq. 2.20)$$

Where $\hat{\mathrm{H}}_0$ is the Hamiltonian for the unperturbed system, ε is a parameter accounting for the size of the perturbation and $\widehat{H}_{\mathrm{P}}$ is a small perturbation. The solution of the Schrödinger equation for this total Hamiltonian can be expanded as Taylor series in powers of the perturbation parameter ε:

$$\widehat{H}_{total}\Psi(x) = W\Psi(x) \qquad (Eq. 2.21)$$

$$W = W_0 + \varepsilon W_1 + \varepsilon^2 W_2 + \cdots \qquad (Eq. 2.22)$$

$$\Psi(x) = \Psi_0(x) + \varepsilon\Psi_1(x) + \varepsilon^2\Psi_2(x) + \cdots \qquad (Eq. 2.23)$$

Substituting $Eq. 2.22$ and $Eq. 2.23$ into $Eq. 2.21$, we get:

$$\widehat{(H_0} + \varepsilon \widehat{H}_{\mathrm{P}})(\Psi_0(x) + \varepsilon\Psi_1(x) + \varepsilon^2\Psi_2(x) + \cdots) \\ = (W_0 + \varepsilon W_1 + \varepsilon^2 W_2 + \cdots)(\Psi_0(x) + \varepsilon\Psi_1(x) + \varepsilon^2\Psi_2(x) + \cdots) \qquad (Eq. 2.24)$$

And gathering terms with the same power of ε results in:

$$\varepsilon_0\colon \widehat{H_0}\Psi_0(x) = W_0\Psi_0(x) \qquad (Eq. 2.25)$$

$$\varepsilon_1\colon \widehat{H_0}\Psi_1(x) + \widehat{H_{\mathrm{p}}}\Psi_0(x) = W_0\Psi_1(x) + W_1\Psi_0(x) \qquad (Eq. 2.26)$$

$$\varepsilon_2\colon \widehat{H_0}\Psi_2(x) + \widehat{H_{\mathrm{p}}}\Psi_1(x) = W_0\Psi_2(x) + W_1\Psi_1(x) + W_2\Psi_0(x) \qquad (Eq. 2.27)$$

$$\varepsilon_n\colon \widehat{H_0}\Psi_n(x) + \widehat{H_{\mathrm{p}}}\Psi_{n-1}(x) = \sum_{i=0}^{n} W_i\,\Psi_{n-i}(x) \qquad (Eq. 2.28)$$

Which are the perturbation equations for the zeroth, first, second and n^{th} order, respectively. Møller-Plesset perturbation theory is an *ab-initio*, post-HF method for the inclusion of the effects of electron correlation in quantum chemical calculations, which takes the sum over all the Fock operators for the system, and uses this as the unperturbed Hamiltonian. The CASPT2 method is a special case of MP2, the second order Møller-Plesset perturbation theory: an application of a second-order truncation of many-body perturbation theory. Once a good quality multiconfigurational wavefunction comprising the effects of static correlation has been obtained by CASSCF/RASSCF methods, the Hamiltonian for this CASSCF/RASSCF system (or a reference Hamiltonian with the same eigenfunctions) can be considered a reference Hamiltonian, with the improved CASPT2 wavefunction comprising the effects of dynamic correlation generated as a result of a small perturbation to this reference Hamiltonian, as discussed above. In CASPT2, the perturbation equation is truncated at the second order. The reference $\widehat{H}_0$, W_0 and $\Psi_0(x)$ are the CASSCF Hamiltonian, energy and wavefunction, respectively.

Post Hartree-Fock methods produce results which are an improvement upon Hartree-Fock energies because they include explicitly the electron correlation energy which is neglected by Hartree-Fock. This is an important consideration in systems with strong correlation, such as those with a partially filled f-shell. However, scaling is an important consideration. For Hartree-Fock calculations, every additional electron adds four variables to the system. Full CI scales factorially, and while CASSCF/RASSCF present a way to identify and perform Full CI on only the most chemically important orbitals, the computational expense involved in CASSCF/RASSCF calculations on systems containing f-elements, even when only a small active space is used, is such as to be impractical for everyday use, and for this reason, despite several shortfalls, much computational actinide chemistry is performed with Density Functional Theory (DFT).

2.7. Relativistic Effects

2.7.1. Effects of Relativity in Atoms

In atomic units, the radial velocity of the innermost electrons in an atomic system is approximately equal to the charge on the nucleus. For atoms with Z > 40, this radial velocity is a significant proportion of the speed of light, c, and relativistic effects become non-negligible.

Relativistic motion of the innermost electrons is partially responsible for the way that heavy elements behave, with a notable example being the yellow colouring of gold[234,235]: Non-relativistic calculations of the excitation energies from the 5d to 6s levels for gold predict transition bands at high energies, in the UV region, but relativistic motion of the inner electrons affects the energies of electron orbitals. When relativistic effects are included, transitions are seen at lower energies, in the middle of the visible region, accounting for the distinctive yellow colour of the metal. This demonstrates the importance of appropriately treating relativistic effects when dealing with heavy elements[232].

Two different components of relativistic effects can be defined: scalar relativistic effects or effects which are due to the spin-orbit coupling. Scalar effects are caused by the high velocities of inner electrons in heavy atoms. This leads to a relativistic mass increase,

$$m_e = \frac{m_o}{\sqrt{1 - \frac{v^2}{c^2}}} \qquad (Eq. 2.29)$$

Where m_o is the rest mass of the electron, v is its radial velocity and c is the speed of light. Where v is a significant percentage of c (true, in general, for elements heavier than Zirconium), this leads to a contraction of the inner orbitals, and an increased stabilisation of the s and p orbitals. The contraction of these orbitals increases the screening effect of the attractive force the nucleus enacts on the d and f electrons, causing them to become destabilised and extended.

Spin-orbit coupling effects arise due to the interaction between the magnetic field generated by an electron orbiting the atomic nucleus and the electron's spin. Russell-Saunders coupling is applicable when the spin-orbit coupling is weak, and has the effect of splitting orbitals into pairs according to the rule

$$j = l \pm \frac{1}{2} \qquad (Eq. 2.30)$$

Where j is the angular momentum quantum number and l is the orbital angular momentum quantum number. In a given system, for each value of l there are two orbitals, each with a differing j value.

2.7.2. Relativistic Hamiltonians

Relativistic effects can be accounted for in quantum chemical calculations by modifying the Hamiltonian to include scalar relativistic and/or spin-orbit coupling terms. This section will briefly discuss methods for inclusion of these terms, beginning with the Dirac equation $(Eq. 2.31)$ which attempts to account for relativistic effects for a single electron[304]. The time-independent Dirac equation is:

$$\left[c\boldsymbol{\alpha} \cdot \hat{P} + c^2\boldsymbol{\beta} + V\right]\Psi = E\Psi \qquad (Eq. 2.31)$$

With the Dirac Hamiltonian, where $\boldsymbol{\alpha}$ and $\boldsymbol{\beta}$ are both matrices:

$$\hat{h}_{\mathrm{D}} = c\boldsymbol{\alpha} \cdot \hat{P} + c^2\boldsymbol{\beta} + V \qquad (Eq. 2.32)$$

$$\boldsymbol{\alpha}_{x,y,z} = \begin{pmatrix} 0 & \boldsymbol{\sigma}_{x,y,z} \\ \boldsymbol{\sigma}_{x,y,z} & 0 \end{pmatrix}, \quad \boldsymbol{\beta} = \begin{pmatrix} \mathbf{I} & 0 \\ 0 & \mathbf{I} \end{pmatrix} \qquad (Eq. 2.33)$$

$\hat{P}$ is the momentum operator, c is the speed of light and V is a potential. $\boldsymbol{\sigma}_{x,y,z}$ are the three 2×2 Pauli spin matrices and $\mathbf{I}$ is a 2×2 unit matrix. This equation describes an electron-positron pair, with both spin states of each accounted for explicitly, hence the four component wavefunction:

$$\Psi(\boldsymbol{x}) = [\Psi_1(\boldsymbol{x}), \Psi_2(\boldsymbol{x}), \Psi_3(\boldsymbol{x}), \Psi_4(\boldsymbol{x})] \qquad (Eq. 2.34)$$

The Dirac equation is very computationally expensive compared to solving the non-relativistic Schrödinger equation and as it only describes a single electron-positron pair, it is not useful for molecular calculations.

For a molecular calculation, a generalisation of the Dirac equation to a many-particle system is needed. The Dirac-Coulomb-Breit (DCB) Hamiltonian is one such generalisation of the Dirac Hamiltonian to an N-particle system[305,306]. It accounts for both scalar and spin-orbit relativistic effects and despite being initially proposed in 1928, remains the most accurate way of including relativistic effects in quantum chemical calculations:

$$\hat{H}_{DCB} = \sum_{i} \hat{h}_i + \sum_{i<j} \hat{h}_{ij} \qquad (Eq. 2.35)$$

Where $\hat{h}_i$is the Dirac Hamiltonian and $\hat{h}_{ij}$ is the two-particle term:

$$\hat{h}_{ij} = \frac{1}{\boldsymbol{r}_{ij}} + \frac{1}{2\boldsymbol{r}_{ij}} \left[\boldsymbol{\alpha}_i \cdot \boldsymbol{\alpha}_j + \frac{(\boldsymbol{\alpha}_i \cdot \boldsymbol{r}_{ij})(\boldsymbol{\alpha}_j \cdot \boldsymbol{r}_{ij})}{\boldsymbol{r}_{ij}^2} \right] \qquad (Eq. 2.36)$$

Applying the Dirac-Coulomb-Breit Hamiltonian to a four-component wavefunction as in the Dirac equation is significantly more computationally expensive than solving the non-relativistic Schrodinger equation for the same system.

Decoupling the scalar relativistic effects from the relativistic effects due to the spin orbit coupling allows the latter to be neglected, if desired. The zeroth-order regular approximation (ZORA) is one such method[307–311]. ZORA is a zeroth-order perturbational expansion of the Dirac equation[312]:

$$\hat{\mathrm{H}}^{ZORA}_{scalar} + \hat{\mathrm{H}}^{ZORA}_{spin-orbit} = V + \boldsymbol{\sigma} \cdot \hat{P} \frac{c^2}{2c^2 - V} \boldsymbol{\sigma} \cdot \hat{P} \qquad (Eq. 2.37)$$

Where $\hat{P}$ is the momentum operator, *V* is a potential and **σ** is the spin-orbit matrix.

It is desirable to eliminate the positronic (negative energy) states present in the Dirac Hamiltonian. The Douglas-Kroll-Hess (DKH) Hamiltonian arises from a unitary transformation of the Dirac Hamiltonian[313–315], splitting it into two parts, with one part describing electrons and the other describing the positronic negative-energy states. Decoupling the negative and positive energy terms results in an infinite series of operators ($Eq. 2.38$), where $\hat{\varepsilon}_k$ are the expansion terms. The lower orders of this series can be used to account for relativistic effects in quantum calculations in a computationally efficient and accurate manner[316].

$$\hat{h}_{DKH\infty} = \sum_{k=0}^{\infty} \hat{\varepsilon}_k \qquad (Eq. 2.38)$$

Most quantum chemical calculations can be performed sufficiently with a second order expansion, so the expansion can be truncated at k=2, and the Hamiltonian is then known as DKH2[314,317].

2.7.3. Relativistic Pseudopotentials

As discussed in Chapter 2.3: Basis Sets, pseudopotentials present a way to reduce computational expense while treating relativistic effects implicitly[285,236]. Only the valence electrons are likely to be involved in chemical processes, so a heavier atom can be split into a core region, comprising the nucleus and the inner electrons which can then be treated implicitly with a relativistic pseudopotential (see Chapter 2.3: Basis Sets), and the valence electrons, which are treated explicitly.

To generate a relativistic pseudopotential, an all-electron wavefunction for the atom must be generated using a relativistic Hamiltonian[38,285,287,318]. As discussed previously, the valence orbitals are then replaced with one-electron pseudo-orbitals, which are fitted to the valence all-electron orbitals by parameterisation of the potential. Pseudopotentials designed for the treatment of f-block elements can treat the f electrons explicitly or model them as part of the core, which simplifies the calculations but reduces accuracy[284,287,318–322].

2.8. Density Functional Theory (DFT)

An alternative to performing calculations to obtain the electronic wavefunction is Density Functional Theory (DFT), which relies upon the fact that all information about a molecular system can be recovered from its electron density alone.

2.8.1. The Thomas-Fermi-Dirac Model: Orbital Free DFT

The Thomas-Fermi-Dirac model defines the energy of a system as a functional of its electron density, $E[\rho(\boldsymbol{r})]$, where E is a functional of the electron density, $\rho(\boldsymbol{r})$ *i.e.* a function of a function as the electron density is itself a function of position, $\boldsymbol{r}$. This functional can be split into three parts; the kinetic energy term $T[\rho(\boldsymbol{r})]$, the nucleus-electron attraction term $E_{Ne}[\rho(\boldsymbol{r})]$ and the electron-electron repulsion term. The nuclear-nuclear repulsion is held constant due to the Born-Oppenheimer approximation. The electron-electron repulsion is further divided as in the HF theory into a Coulomb and exchange term, $J[\rho(\boldsymbol{r})]$ and $K_D[\rho(\boldsymbol{r})]$[323], respectively.

$$E[\rho(\boldsymbol{r})] \ = T[\rho(\boldsymbol{r})] + \ E_{Ne}[\rho(\boldsymbol{r})] + \ J[\rho(\boldsymbol{r})] + \ K_D[\rho(\boldsymbol{r})] \qquad (Eq. 2.39)$$

In order to obtain approximations for the exchange and kinetic energy functional, a uniform gas of electrons is assumed. This model does not describe atomic systems well, and cannot predict chemical bonding.

2.8.2. The Hohenberg-Kohn Theorems

Hohenberg and Kohn introduced two theorems that formed the basis for modern density functional theory[324]. The first theorem proved that an electron density, depending on only three spatial coordinated, could be used to obtain the ground state energy of a system. For a fictitious system of particles in an external potential V_{EXT}, V_{EXT} and hence the total energy of the system E_{total} is a unique functional of the electron density, $\rho(\boldsymbol{r})$. The energy functional, $E[\rho(\boldsymbol{r})]$ can be written as:

$$E[\rho(\boldsymbol{r})] = \int \rho(\boldsymbol{r}) V_{EXT}(\boldsymbol{r}) d\boldsymbol{r} + F[\rho(\boldsymbol{r})] \qquad (Eq. 2.40)$$

Where $F[\rho(\boldsymbol{r})]$ is an unknown functional of the electron density.

The second theorem proved that the energy of a system was minimised with a ground state electron density and that the functional of the electron density which is used to obtain the ground state of a system gives the lowest energy of the system if and only if the electron density is the true ground state electron density. Performing calculations on the density rather than the wavefunction dramatically simplifies calculations, as instead of having to solve for 3*n* spatial coordinates, as in a wavefunction method, calculations are only required to solve for three. In addition, DFT models include approximations to the electron correlation, which if modelled correctly, can improve upon the Hartree-Fock results.

2.8.3. Kohn-Sham DFT

The Density Functional Theory that is so prevalent in the literature today is based on the Kohn-Sham equations. The independent particle model introduced by Kohn and Sham[324–327] allows an improved representation of the kinetic energy term *via* the introduction of orbitals. This kinetic energy term is split into two further terms; an exact component (the Hartree-Fock kinetic energy), and a term accounting for interactions between electrons (the exchange-correlation energy). The DFT energy is:

$$E_{DFT}[\rho] = T_{Exact}[\rho] + E_{Ne}[\rho] + J[\rho] + E_{ex}[\rho] \qquad (Eq. 2.41)$$

Where

$$E_{ex}[\rho] = (T[\rho] - T_{Exact}[\rho]) + K_D[\rho] \qquad (Eq. 2.42)$$

The only unknown term in $Eq. 2.41$ for which an approximation must be made is the exchange-correlation energy. Once this approximation is included, the ground state energy of the system can be found. Finding the ground state energy of the system involves solving the Kohn-Sham equations ($Eq. 2.43$), the Schrödinger-like equations for a reference system of non-interacting particles:

$$\left(-\frac{1}{2}\nabla^2 + V_{KS}(\boldsymbol{r})\right)\phi_i(\boldsymbol{r}) = \varepsilon_i\phi_i(\boldsymbol{r}) \qquad (Eq. 2.43)$$

Where V_{KS} $(Eq. 2.44)$ is the Kohn-Sham potential, the effective potential needed to generate the same electron density as found in a given system of interacting particles and ε_i is the energy corresponding to the orbital ϕ_i.

$$V_{KS}(\boldsymbol{r}) = V_{Ne}(\boldsymbol{r}) + \int \frac{\rho(\boldsymbol{r}')}{|\boldsymbol{r} - \boldsymbol{r}'|} d\boldsymbol{r}' + V_{xc}(\boldsymbol{r}) \qquad (Eq. 2.44)$$

$V_{xc}(\boldsymbol{r})$ is the exchange-correlation (*xc*) potential:

$$V_{xc}(\boldsymbol{r}) = \frac{\delta E_{xc}[\rho]}{\delta\rho(\boldsymbol{r})} = \varepsilon_{xc}[\rho(\boldsymbol{r})] + \int \rho(\boldsymbol{r}') \frac{\delta\varepsilon_{xc}[\boldsymbol{r}']}{\delta\rho(\boldsymbol{r})} d\boldsymbol{r}' \qquad (Eq. 2.45)$$

Where:

$$E_{xc}[\rho] = E_x[\rho] + E_c[\rho] = \int \rho(\boldsymbol{r})\varepsilon_x[\rho(\boldsymbol{r})]d\boldsymbol{r} + \int \rho(\boldsymbol{r})\varepsilon_c[\rho(\boldsymbol{r})]d\boldsymbol{r} \quad (Eq. 2.46)$$

ε_x and ε_c are the exchange and correlation energies per particle. The Kohn-Sham potential is dependent on the electron density, and as a result, on the molecular orbitals, which are initially unknown. Like HF theory, DFT relies on an initial set of approximate molecular orbitals and requires a self-consistent field procedure to solve the Kohn-Sham equations.

2.8.4. Pure Exchange-Correlation Functionals

As mentioned in section 2.5, the correlation energy is the difference between the exact energy and the energy calculated using Hartree-Fock theory. Classical electron-electron interactions are accounted for using the Coulomb interaction, which is repulsive for like-charged particles. The exchange energy accounts for additional repulsion arising from the Pauli Exclusion Principle, due to electrons being indistinguishable fermions with spin $s = \frac{1}{2}$. The probability of locating an electron close to another electron is lower than it would be if electrons were charge and spin free. This reduction in probability is known as the exchange-correlation hole and should be reproduced by the exchange-correlation functional.

The exact exchange-correlation functional is free of self-interaction error, a problem arising in all approximate functionals. The functional for the Coulomb energy is such that an electron interacts with itself, giving a non-zero electron-electron repulsion even in systems with only one electron.

In an ideal functional the self-interaction energy will be exactly cancelled by the exchange energy, although as the ideal functional does not exist and exchange must be approximated, error cancellation is not perfect. There is a variety of types of functionals in use, and they can be categorised by how they approximate the exchange-correlation energy (see Figure 2.4).

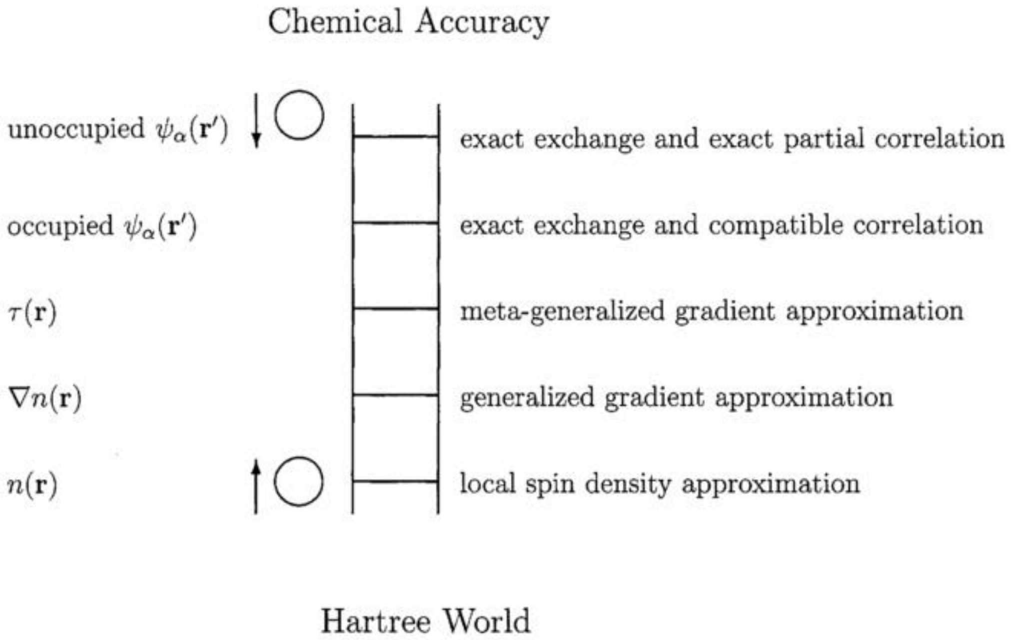

Figure 2.4: "Jacob's Ladder of Chemical Accuracy" representing different types of exchange-correlation functional. Reproduced from Perdew, J.P. and Schmidt, K. "Jacob's ladder of density functional approximations for the exchange-correlation energy", *AIP Conference Proceedings*, **2001** (Ref[328])

The simplest approximation from which an exchange-correlation functional can be constructed is the Local Density Approximation (LDA), which assumes that at a given point in space, the exchange-correlation energy is equal to the exchange-correlation energy for a uniform gas of electrons which is characterised by a single property, the electron density, ρ. The functional can be written as:

$$E_{xc}^{LDA}[\rho] = \int \rho(\boldsymbol{r})\, e_{xc}(\rho) d^3r \qquad (Eq. 2.47)$$

where $e_{xc}(\rho)$ is the exchange-correlation energy density. The LDA is dependent only on the value of the electron density at the point at which it is evaluated. It tends to cause overbinding in molecules as a result of overestimating correlation and underestimates the exchange energy by around 10%[329,330].

An improvement over the LDA, the Generalised Gradient Approximation (GGA) considers the fact that the electron density in an atom or molecule is not uniform. For this purpose, exchange-correlation (*xc*-)functionals constructed using the GGA include the first derivative of the electron density. This allows an improved treatment of regions where the electronic density may be changing rapidly. There are various functionals using the GGA approach in use, and they can be semi-empirical or non-empirical. BLYP[331,332] is an example of a semi-empirical GGA functional, which is dependent upon a parameter fitted to experimental data and a popular non-empirical GGA functional is PBE[333–335].

The next level of improvement is known as the meta-GGA approach. These functionals are dependent on the Laplacian of the electron density or on τ, the orbital kinetic energy density. TPSS[336] is a popular example of a meta-GGA functional.

2.8.4. Hybrid Exchange-Correlation Functionals

A hybrid functional includes an amount of the exact exchange obtained in Hartree-Fock theory. The popular B3LYP *xc*-functional[337] is an example of a semi-empirical hybrid functional containing exact exchange, LDA and GGA exchange (with the latter coming from the B88 functional[331,338]), plus LDA and GGA correlation (with the latter coming from the LYP functional). The B3LYP functional is defined in $Eq. 2.48$. The parameters a ≈ 0.2, b ≈ 0.7 and c ≈ 0.8 are fit to experimental data.

$$E_{xc}^{B3LYP} = (1-a)E_x^{LSDA} + aE_x^{exact} + b\Delta E_x^{B88} + (1+c)E_c^{LSDA} + cE_c^{LYP} \; (Eq. 2.48)$$

The PBE0[334] functional mixes exact exchange with exchange from the PBE functional, at an amount determined by perturbation theory, an example of a non-empirical hybrid functional.

The Random Phase Approximation (RPA) is the next level of improvement. Information about virtual orbitals is included alongside information about occupied orbitals. Inclusion of unoccupied orbitals improves the treatment of dispersion interactions, a known weakness for most DFT methods.

2.8.5. Time-Dependent Density Functional Theory

Time-Dependent Density Functional Theory (TDDFT) is the study of the electron density associated with molecular or solid-state systems in time-dependent potential fields. Most importantly, TDDFT allows vertical excitation energies and oscillator strengths to be calculated and UV-Vis spectra to be simulated.

The formalism of TDDFT begins with the Runge-Gross theorem which is fully described in several published resources[296,339,340], which states that given the starting conditions, the density of a system is related directly to the external time-evolving potential, for example, an electric field. The Kohn-Sham equations provide an approximation to the many-body, time-independent Schrodinger equation for a fictitious system of non-interacting particles, and the Runge-Gross theorem allows a generalisation of the Kohn-Sham equations to an approximation of the many-body time-dependent Schrodinger equation for a system of interacting particles. An external potential v_{KS} is defined to ensure that the density of the fictitious non-interacting system is the same as that of a given interacting system. Vertical excitation energies can then be calculated as dependent on the time-evolution of the potential.

2.8.6. Performing DFT Calculations

Single-point energy calculations are straightforward to understand: With the nuclear coordinates held fixed and an initial guess for the molecular orbitals coming from, for example, Extended Hückel Theory, the Kohn-Sham equations are solved iteratively to find the ground state energy of the system, *i.e*. the energy is minimised, as in Hartree-Fock theory.

Optimising a molecular geometry requires a stationary point on the potential energy surface to be found. At each step, the derivative of the energy with respect to nuclear position is calculated, and the nuclear coordinates adjusted according to the associated forces. The ground state energy is then minimised *via* the Kohn-Sham equations. This process is repeated until the energy gradients vanish to within a pre-defined tolerance. The gradient can be "followed" down its steepest path to aid convergence because the derivative of the energy with respect to position will be largest far from an energetic minimum, and will reduce as one approaches this minimum.

Vibrational frequency analysis involves calculation of analytical or numerical second derivatives. This process can only be performed where the energy gradient is tolerably close to zero and is vital for ensuring that a minimum (rather than a saddle point or transition state) in the potential energy surface has been found. These calculations also allow the vibrational spectrum to be simulated, allowing comparison with experimental IR spectroscopic data in some cases, and for thermochemical energy corrections to be calculated.

In a numerical calculation, the molecular coordinates are distorted slightly along each of these modes, and a single point energy calculation is performed to ensure the geometry is a true minimum. In an analytical calculation, the second derivatives are calculated directly to give the vibrational modes. For a structure that is at a minimum in the potential energy surface, there should be no imaginary frequencies.

2.8.7. Problems with DFT

Density functional theory has been successful in many areas, with many thousands of papers published and this number growing rapidly. However, there are problems that have proved difficult to resolve. Dispersion interactions (*e.g.* Van der Waals) are poorly described by most functionals, although there are methods which have had some success[341]. Self-interaction error is a major problem in DFT, present in all approximate exchange-correlation (*xc*-)functionals and can cause inaccuracies, particularly in systems with loosely bound electrons where the error may be larger than the binding energy, causing an electron to appear unbound[342,343]. In the absence of the ideal functional, DFT relies on error cancelation, and there is no systematic way by which the quality of results can be improved. Parameterising functionals using empirical data can improve results, but it is important to ensure that improvements apply to all systems, not just the data set that the functional has been fitted to. Regarding f-block elements, DFT struggles to describe the strong static electron correlation that arises in systems where the ground state is well-described only with multiple near-degenerate determinants, for example, as a result of a partially filled f-shell, but good results have been achieved, particularly with closed shell systems[40,43,44,58,77,94,97,221,241,244,254,344].

2.9. Analysis Methods

2.9.1. The Quantum Theory of Atoms in Molecules (QTAIM)

The Quantum Theory of Atoms in Molecules (QTAIM), introduced by Richard Bader[226,345,346], is a useful quantitative analysis tool relying on the topology of the electron density in a molecular system to analyse various molecular properties[347]. Molecules can be partitioned into atomic basins, consisting of the atomic nuclei and basins, which are bound by surfaces where when the scalar product of the gradient of the electron density with a vector normal to the surface is equal to zero, as seen in Figure 2.4. All gradient vector field lines in one basin converge to the atomic nucleus, defining the basin as region of space surrounding the nucleus.

Where the first derivatives of the electron density vanish are found four types of critical points.

$$\nabla\rho = \boldsymbol{i}\frac{d\rho}{dx} + \boldsymbol{j}\frac{d\rho}{dy} + \boldsymbol{k}\frac{d\rho}{dz} \rightarrow \begin{cases} \boldsymbol{0} \text{ (at critical points and } \infty) \\ \neq \boldsymbol{0} \text{ (in general, everywhere else)} \end{cases} \qquad (Eq. 2.49)$$

Calculating the second derivatives of the electron density allows one to discriminate between different types of critical point, *i.e.* local minima, local maxima and saddle points. $Eq. 2.50$ shows the Hessian matrix, formed from the nine second derivatives of $\rho(\boldsymbol{r})$ at a critical point located at $\boldsymbol{r_c}$:

$$\mathrm{A}(\boldsymbol{r_c}) = \begin{pmatrix} \frac{\delta^2\rho}{\delta x^2} & \frac{\delta^2\rho}{\delta x\delta y} & \frac{\delta^2\rho}{\delta x\delta z} \\ \frac{\delta^2\rho}{\delta y\delta x} & \frac{\delta^2\rho}{\delta y^2} & \frac{\delta^2\rho}{\delta y\delta z} \\ \frac{\delta^2\rho}{\delta z\delta x} & \frac{\delta^2\rho}{\delta z\delta y} & \frac{\delta^2\rho}{\delta z^2} \end{pmatrix}_{\boldsymbol{r}=\boldsymbol{r_c}} \qquad (Eq. 2.50)$$

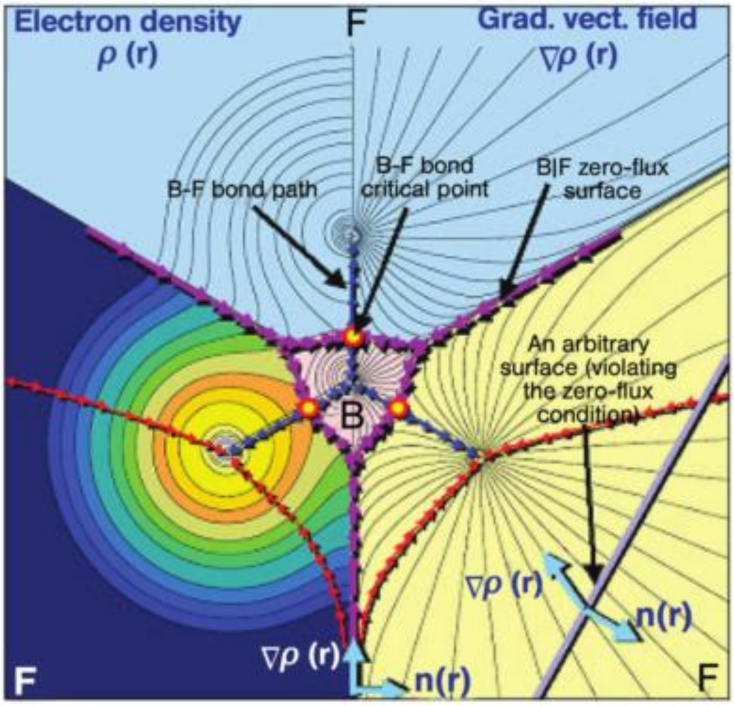

Figure 2.5: The gradient vector field (R) and electron density (L) in the plane of the BF_3 molecule showing bond paths (dark blue arrows), zero-flux surfaces (purple arrows) and bond critical points (yellow circles with red outlines). Reproduced from Matta and Boyd, "An Introduction to the Quantum Theory of Atoms in Molecules", Wiley, **2007** (Ref[347]).

The Hessian can be transformed into its diagonal form *via* a rotation of the coordinate system from $\boldsymbol{r}(x, y, z) \rightarrow \boldsymbol{r}(x', y', z')$ such that x', y' and z' are the principle curvature axis of the critical point at $\boldsymbol{r_c}$:

$$\boldsymbol{\Lambda} = \begin{pmatrix} \frac{\delta^2\rho}{\delta x'^2} & 0 & 0 \\ 0 & \frac{\delta^2\rho}{\delta y'^2} & 0 \\ 0 & 0 & \frac{\delta^2\rho}{\delta z'^2} \end{pmatrix}_{\boldsymbol{r'}=\boldsymbol{r_c}} = \begin{pmatrix} \lambda_1 & 0 & 0 \\ 0 & \lambda_2 & 0 \\ 0 & 0 & \lambda_3 \end{pmatrix} \qquad (Eq. 2.51)$$

λ_1, λ_2 and λ_3 are the curvatures of the electron density and characterise the type of critical point (CP). In a (3,-3) (nuclear) CP, λ_1, λ_2 and $\lambda_3$are all negative and the electron density is a local maximum. In a (3,-1) (bond) CP, two curvatures are negative, with ρ a maximum in the plane of these curvatures, but a minimum along a third, perpendicular plane (the bond path). In a (3,+1) (ring) CP, two curvatures are positive, with ρ a minimum in this plane, and a maximum in the third, perpendicular axis. In a (3,+3) (cage) CP, all three curvatures λ_1, λ_2 and $\lambda_3$are positive.

The aim here is simply to give a brief description of what QTAIM has been used for in the studies discussed in the results chapters of this thesis, which are concerned only with the integrated properties and the properties of bond critical points; other types of critical point (nuclear, ring, cage) are neglected here, but more information can be found in the referenced resources[226,347].

A bond path, as defined by QTAIM, is not a chemical bond[346], it is a line of locally maximum electron density connecting two bonded atoms. The bond critical point is the point at which the bond path crosses the zero-flux surface separating the atomic basins of the two bonded atoms. Measuring the electron density at this point reveals information about the nature of the bond. As a rule of thumb, covalent interactions are generally understood to have $\rho \geq 0.2$ a.u, and a strongly ionic interaction has a value of ρ which is significantly less than this.

From the electron density, other useful properties can be calculated at the BCP such as the Laplacian of the electron density,$\nabla^2\rho$, which alongside the electron density can help build a description of the nature of the bond. In regions where there is local depletion of charge compared to the average distribution, $\nabla^2\rho(\boldsymbol{r}) > 0$. In general, covalency has the property of a local concentration of charge, with the laplacian being negative accordingly.

The energy density, *H*, at the BCP, can also be used as a measure of covalency. For covalent interactions, the total energy density H is dominated by a local depletion in the potential energy, and is negative, with a greater magnitude indicating greater covalency. For predominantly ionic interactions, *H* is dominated by a local excess of kinetic energy and is positive. These topological properties can be used to characterise bonding interactions and are sensitive measures of covalency[27,60,345,347,348].

Additionally, this thesis makes extensive use of the integrated properties. The delocalisation index, $\delta(A, B)$ is a measure of the magnitude of the electron density shared between two atomic basins, A and B. It is obtained by integrating the exchange density over each of the two basins and when considered for bonded atoms, can be considered a direct measure of bond order[347].

The atomic population of atom A, $N(A)$ is a measure of the average number of electrons in the atomic basin of A. The localisation index of atom A, $\lambda(A)$, is a measure of the average number of electrons localised in atom A. In a molecule:

$$\sum N(A) = \sum \lambda(A) + \frac{1}{2}\sum_{A\neq B} \delta(A,B) \qquad (Eq. 2.52)$$

These properties have been used in the results chapters of this thesis to quantify the nature of interactions between atoms and to investigate the distribution of charge. The theory can be read about in more detail in several referenced resources[345–349].

2.9.2. The Electron Localisation Function

Another property of obtained from the electron density is the electron localisation function, which is described fully in several referenced resources[350–354]. The electron localisation function (ELF) is a scalar field, denoted by $n(\boldsymbol{r})$ which takes a value between 1 and 0. The value of $n(\boldsymbol{r})$ is a measure of the probability of finding an electron, given the presence of a second reference electron with the same spin:

$$n(\boldsymbol{r}) = \frac{1}{1 + \left(\frac{D_\sigma}{D_\sigma^0}\right)^2} \qquad (Eq. 2.53)$$

D_σ and D_σ^0 are the curvatures of the electron pair density for electrons of identical spins for the real system and for a homogeneous electron gas with the same density, respectively.

The topology of the ELF can be analysed in a similar way to that of the electron density, *via* analysis of critical points in the ELF isosurface. Four types of critical points (CPs) can be identified although the work in this thesis is only concerned with two of these. (3,-3) CPs correspond to local maxima in the $n(\boldsymbol{r})$ isosurface and (3,-1) CPs correspond to saddle points in the isosurface of $n(\boldsymbol{r})$. Intuitively, a strongly covalent interaction is characterised by the presence of a (3,-3) CP along a bond, and the value of $n(\mathbf{r})$ at a saddle point, a (3,-1) CP, defines a bifurcation point in $n(\boldsymbol{r})$. This bifurcation point represents a value for which an isosurface of $n(\boldsymbol{r})$splits into two (or more) separate surfaces. Bifurcation points in the ELF isosurface have previously been used as a measure of the delocalisation of electrons between atomic basins. The values of ELF at which these bifurcations occur have been proposed to act as indicators of covalent character[353,355–357].

2.9.3. Quantifying Weak Interactions with the Reduced Density Gradient

The reduced density gradient is defined as:

$$s(\boldsymbol{r}) = \frac{1}{2(3\pi^2)^{1/3}} \frac{|\nabla\rho(\boldsymbol{r})|}{\rho(\boldsymbol{r})^{4/3}} \qquad (Eq. 2.54)$$

While $\rho(\boldsymbol{r})$ can be large in covalent bonding regions, it is small but non-zero in regions of largely noncovalent interaction. The reduced density gradient (RDG), $s(\boldsymbol{r})$, takes very small values in regions of both predominately noncovalent and covalent interactions, tending towards zero at critical points in the electron density. Hence, when $s(\boldsymbol{r})$ is plotted against $\rho(\boldsymbol{r})$, spikes appear at low density which indicate interactions of largely noncovalent character[358], as seen in Figure 2.6.

Plotting the $s(\boldsymbol{r})$ isosurface at low-gradient values ($s(\boldsymbol{r}) \leq 0.5$ a.u.) indicates the spatial regions within a molecule where interactions occur that are predominantly noncovalent in origin. Colour-mapping the $s(\boldsymbol{r})$ isosurface with values of the signum function, $\text{sgn}(x)$, achieves this by taking the value of 1 when $x > 0$ and -1 when $x < 0$. Thus, the values of $\rho(\boldsymbol{r})\text{sgn}(\lambda_2)$ can be used to discriminate between attractive and repulsive interactions. λ_2 arises from the Hessian of $\rho(\boldsymbol{r})$, taking a positive value for repulsive interactions and a negative value for attractive interactions.

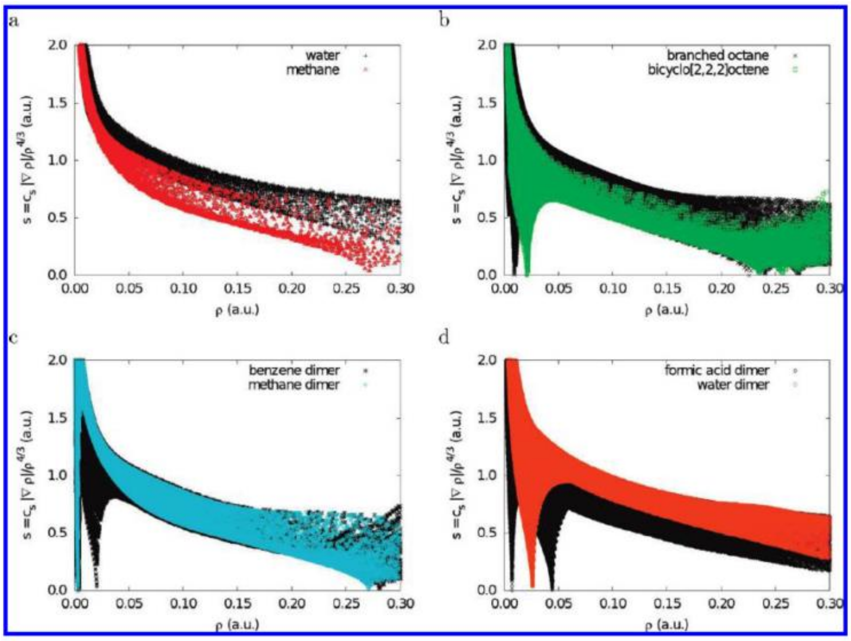

Figure 2.6: Plots of the electron density against the reduced density gradient for methane, water, branched octane, bicyclo[2.2.2]octene, and the dimers of methane, benzene, water, and formic acid. Reproduced from Johnson, E. R., Keinan, S., Mori-Sánchez, P., Contreras-García, J., Cohen, A. J., Yang, W., Revealing Noncovalent Interactions, J. Am. Chem. Soc., *132*, **2010,** 6499-6505 (Ref [358]).

2.9.4. Electron Density Difference Distributions

Electron density difference distributions are used in the results chapters of this thesis to visualise the redistribution of charge that occurs when complexes are formed. These plots are generated by performing a single point energy calculation for all fragments involved in a complex formation. These fragments must be held at their coordination geometry. The electron density of the fragments can then be subtracted from the electron density of the complex as a whole. What remains is a map showing accumulation and depletion of electronic charge upon complexation as a set of isosurfaces.

These plots allow a qualitative analysis of the source and destination of charge donation within complexes, which, aided by the more quantitative topological and integrated properties of the electron density, can create a useful picture of complex formation.

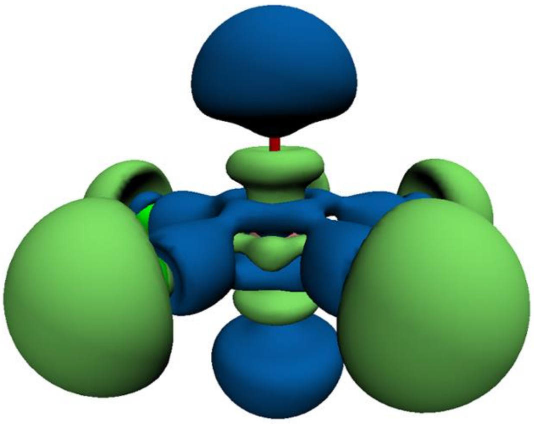

Figure 2.6: Example of an electron density difference distribution for a $[UO_2F^5]^{3-}$complex.

Figure 2.6 shows an example of one such electron density difference distribution, with regions of electron depletion, indicating the depletion of charge, coloured in green and electron accumulation coloured in blue.

2.10 Quantum Chemistry Software Packages

There are many commercially available quantum chemistry packages in use. This section will briefly summarise the codes used to perform calculations in the results chapters of this thesis.

TURBOMOLE: TURBOMOLE[359] is a multifunctional quantum chemistry software package initially developed in the group of Professor Reinhart Ahlrichs at the University of Karlsruhe. Turbomole is capable of performing *ab initio* electronic structure calculations using Hartree-Fock, density functional theory, time-dependent density functional theory, and Moller-Plesset perturbation theory, and coupled cluster calculations up to singles, doubles and triples. Additionally, vibrational frequencies and spectra can be produced and NMR shieldings can be calculated. TURBOMOLE can incorporate the effects of solvation through the COSMO solvation model

(COnductor-like Screening MOdel)[360]. COSMO approximates a solvent as a dielectric continuum with relative permittivity ε outside of a molecular cavity. This cavity is commonly defined as a series of spheres centred on atoms, with radii 20% larger than the atoms Van der Waal's radii. Setting the value of the relative permittivity, ε, allows different solvents to be approximated, for example, ε = 8.9 allows the simulation of solvation in dichloromethane. When the desired calculations have been performed, the results can be output to several formats for further analysis, most usefully for the purposes of this study to the .molden format which can subsequently be converted to .wfn format for analysis with various QTAIM codes. Website: http://www.turbomole.com

Molcas: Molcas is an *ab initio* quantum chemistry package whose primary function is to perform calculations using multiconfigurational methodologies[361,362], utilising the CASSCF/RASSCF and CASPT2/RASPT2 functionalities. Website: http://www.molcas.org

Multiwfn: Multiwfn[363] is a multifunctional wavefunction analyser. It can be used for topological analysis of the electron density and electron localisation function, among many other analyses. It has been used for the purposes of this thesis to obtain topological properties of the electron density, generate electron density difference distributions, obtain ELF data and reduced density gradient data. Website: https://multiwfn.codeplex.com

AIMAll: AIMAll[364] is a QTAIM software package developed by Todd A. Keith based on the Extreme and ProaimV programs from the AIMPAC package, developed and maintained by members of Richard F.W. Bader's research group. For the purposes of this thesis, AIMAll has been used in the calculation of topological and integrated properties of the electron density from wavefunction files. Website: http://aim.tkgristmill.com/index.html

VMD: Visual Molecular Dynamics[365] (VMD) has been used primarily for visualisation of cube files generated by Multiwfn. Website: http://www.ks.uiuc.edu/Research/vmd

Other packages mentioned in the Introduction and Literature Review Chapter 1 of this thesis include Gaussian[366], Priroda[245] and Amsterdam Density Functional (ADF)[367].

Chapter 3. Results: U-O_{yl} Stretching Vibrations as a Quantitative Measure of Equatorial Bond Covalency in Uranyl Complexes

3.1. Introduction

In this first results chapter, an analysis has been performed on the uranium-ligand and uranium-oxygen (with the oxygen associated with the $[O{=}U{=}O]^{2+}$ unit) bonding in a series of uranyl complexes (see Figure 3.1) with monodentate first-row ligands. Unambiguous characterisation of bonding in actinide species is, as explained in more detail in the Introduction and Literature Review (Chapter 1), of both fundamental and practical importance. From a fundamental perspective, a deeper understanding of bonding interactions can, amongst other things, aid in the assessment of the viability of novel synthetic targets, while from a practical perspective, variation in bonding character can be exploited in selective complexation, which is of particular current relevance to the nuclear power industry.

This chapter aims to characterise U-N bonding in a series of simple uranyl complexes and relate the character of the U-N bonding to changes to the U-O_{yl} unit which occur upon complexation. Selective separation processes rely upon the relative stability of actinide (An) complexes over their lanthanides (Ln) analogues. It is presumed that this stability is derived from an enhanced covalent interaction in the former due to the increased radial extent, and therefore chemical accessibility, of the An 5f over the Ln 4f orbitals. To date, however, although there is evidence for a correlation between enhanced covalency and enhanced stability, this has not been robustly established.

Although the electronic structure of uranyl, with its formally empty 5f shell, differs from that of the later actinides, it is expected that as covalent character decreases across the actinide series, uranyl is a good choice to begin to probe equatorial covalency as covalent character would be expected to be most pronounced here[48,49].

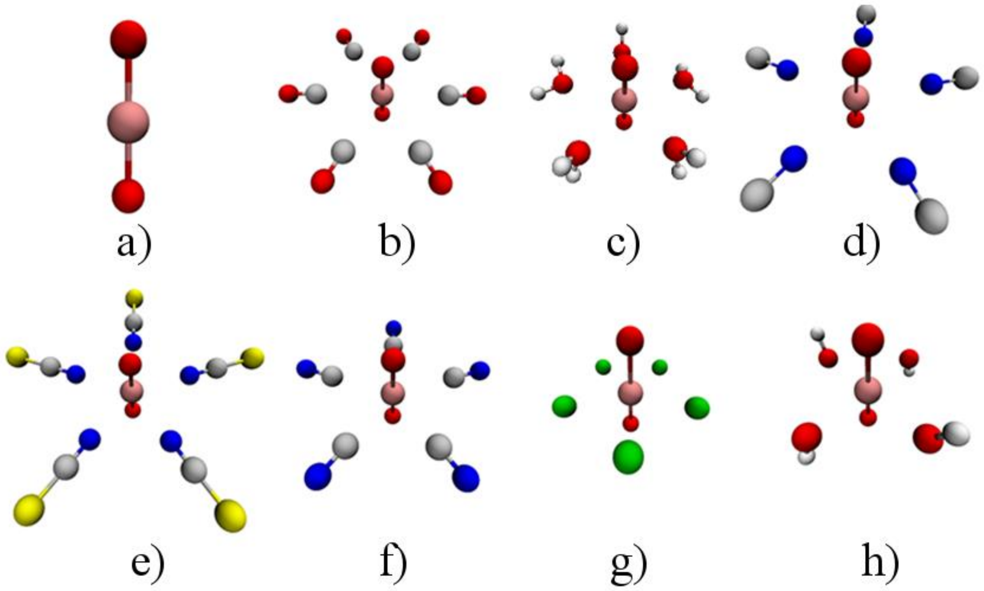

Figure 3.1: Optimised structures of complexes investigated in this study. a) $[UO_2]^{2+}$, b) $[UO_2(CO)_6]^{2+}$, c) $[UO_2(H_2O)_5]^{2+}$, d) $[UO_2(NC)_5]^{3-}$ e) $[UO_2(NCS)_5]^{3-}$, f) $[UO_2(CN)_5]^{3-}$, g) $[UO_2(F)_5]^{3-}$, h) $[UO_2(OH)_4]^{2-}$ all optimised using the PBE *xc*-functional.

The following ligands: H_2O, OH^-, CO, CN^-, NCS^- and F^-, all of which coordinate uranyl *via* a first row species, are considered. These ligands have been chosen as they are expected to bind uranium with a range of interaction strengths. Several of these complexes have been investigated in the literature and these appear in more detail in the Introduction and Literature Review (Chapter 1).

Important among the relevant literature is a previous theoretical study by Tsushima. Here, a weakening of the U-O interaction in similar complexes[368] was found, and this was attributed, *via* molecular orbital analyses, as being due to π or σ donation, where ligands compete with the uranyl oxygen ions for the U 5f, 6p or 6d orbitals, acting to weaken the covalent U-Oyl interaction. However this contradicts the findings of Ingram *et al.*, who attribute the weakening to a reduction in the U-O_{yl} ionic interaction[89]. This contradiction provides a motivation for the use of density-based, rather than orbital-based, analyses, particularly as DFT is known to produce potentially ambiguous orbital-based data.

In this chapter, the results of DFT simulations on these uranyl complexes are presented, combined with a series of analysis techniques based on the electron density, in order to quantify the relationship between covalency in the equatorial bonds and the variation in experimentally observable properties of the axial U-O_{yl} bond.

3.2. Computational Details

All calculations have been performed at the density functional theoretical (DFT) level using Version 6.4 of the TURBOMOLE quantum chemistry package[359]. For the geometry optimisations and vibrational frequency analysis, Ahlrichs basis sets of polarized triple-zeta quality[369] (def-TZVP for U and def2-TZVP for all other atoms) were used along with an associated relativistically contracted effective core potential replacing 60 core electrons on the uranium centre[285]. Subsequently, single-point calculations were performed on the optimised structures by utilising the segmented all-electron relativistically contracted (SARC) basis set[370] on the U centre, with scalar relativistic effects accounted for using the 2nd order Douglas-Kroll-Hess Hamiltonian[371,372]. The effects of spin-orbit coupling were not included in any calculations due to the closed shell nature of these systems.

This chapter will primarily focus on data obtained using two exchange-correlation (*xc*-) functionals. The PBE *xc*-functional[333] based on the generalised gradient approximation (GGA), and the popular hybrid-GGA *xc*-functional, B3LYP[373,374], both of which have previously successfully modelled molecular actinide complexes[375–377], with the B3LYP functional used to investigate the effect of the inclusion of exact exchange, as previous work has reported an improvement in uranyl reaction energies when hybrid functionals[344] are utilised. Starting points for these calculations were structures previously optimised using the non-empirical meta-GGA TPSS *xc*-functional[336], which has previously been used with success to model the electronic structure of hydrated uranyl[344], bulk actinide oxides[378], and has produced highly accurate hydration energies in aquo complexes of other ions[379]; and the related hybrid *xc*-functional, TPSSh[380]. The TPSS and TPSSh structures were the focus of a publication[381] wherein the PBE and B3LYP data were used principally to confirm the robustness of quantities calculated with TPSS and TPSSh. Here, TPSS and TPSSh data are used initially to determine coordination number and elsewhere referred to in the text when relevant. Additional TPSS/TPSSh data may be found in Appendix I.

In order to stabilise the anionic electronic structures present in many of these complexes, calculations were performed in the presence of a continuum aqueous solvent, defined using the COSMO model[360] (radii: H = 1.30 Å, C = 2.00 Å, N = 1.83 Å, O = 1.72 Å, F = 1.72 Å, S = 2.16 Å, U = 2.23 Å). Numerical frequency analysis (within the harmonic approximation) was used to confirm that each structure was at an energetic minima. All-electron densities were then used as the starting point for further analysis, employing the AIMAll[364] (Version 13.11.04) and Multiwfn[363] (Version 3.2) codes.

3.3. Results and Discussion

3.3.1. Binding Energies as a Function of Coordination Number

Initial investigations were performed using the TPSS and TPSSh *xc*-functionals to investigate the optimal coordination number for each complex. Drawing on experimental data, the limiting equatorial coordination number for the hydroxo complex has been shown to be four[81,382] whereas an equatorial coordination number of five[92,100,382–384] has been reported for both the aquo and fluoro complexes. The monocationic $[UO_2(CO)_5]^+$ complex has been reported in the gas phase[385]. Several theoretical studies[81,86,88,89,91,92,386–388] support the experimentally derived coordination numbers for the hydroxo and aquo complexes but there are less numerous data for the other species investigated here[91,92,389–391].

Considering this, an initial set of calculations was performed to investigate the relative stabilities of the fluoro, cyano, isocyano and carbonyl complexes of uranyl with the equatorial coordination number varying from four to six. The results of these calculations can be found in Table 3.1.

Binding energies have been calculated as the total energy difference between the complex and the sum of the optimised uranyl and individual ligand fragments.

$$E_\mathrm{b} = E_\mathrm{c} - (E_{\mathrm{UO_2}} + nE_\mathrm{L}) \qquad (Eq. 3.1)$$

In agreement with a previous study performed by Sonnenberg *et al.*[91], in aqueous solution, coordination of uranyl by five cyano/isocyano ligands is found to be energetically favourable. The D_{5h}-symmetry cyano complex is found to be more stable than the isocyano by 0.62 eV (0.61 eV) when using the TPSS (TPSSh) functional.

In contrast to this previous study, however, all carbonyl complexes are found to be stable in aqueous solution, albeit with binding energies much smaller than the isoelectronic (iso)cyano complexes and also significantly smaller than the binding energy of the aquo complex. Therefore, although coordination by six carbonyl ligands is found to be the energetically favourable complex, in practise these carbonyl ligands would be easily displaced by water. Coordination by six cyano ligands is found to be just 0.13 eV less stable at the TPSS level than coordination by five, with the inclusion of exact exchange leading to a 0.07 eV destabilisation of the higher coordination complex. Finally, in agreement with Vallet *et al.*[92], five-fold coordination is found to give a more stable fluoro complex than that with four or six coordinating ligands. The six coordinating fluoro complex is highly non-planar with pronounced distortion of the uranyl unit, indicating significant steric hindrance.

Ligand	Coordination number					
	4		5		6	
	TPSS	TPSSh	TPSS	TPSSh	TPSS	TPSSh
CO	*0.88*	*0.73*	0.83	0.70	1.21	1.00
CN-	5.72	5.54	*6.62*	*6.46*	6.49	6.26
NC-	5.63	5.47	*6.00*	*5.85*	5.21	5.00
F-	10.32	10.03	*10.63*	*10.32*	9.78	9.26

Table 3.1: DFT-calculated total binding energies of carbonyl, cyano, isocyano and fluoro complexes as a function of equatorial coordination number. All values are given in eV. Italicised entries indicate most stable complexes.

3.3.2. Structural and Vibrational Characterisation

In Table 3.2, key structural parameters of the energetically most stable complexes which will be considered in the remainder of this study are reported. All *xc*-functionals are found to be able to accurately reproduce experimentally determined structures, albeit with a small but consistent overestimate of axial $U-O_{yl}$ bond lengths in all but the aquo complex.

Considering structural characteristics, hybrid *xc*-functionals are found to give superior results compared to the pure functionals, with an approximately 40% reduction in the mean average deviation (MAD) of the axial $U-O_{yl}$ bond. When considering the longer and weaker equatorial bonds, all *xc*-functionals give excellent results, with MADs of less than 0.01 Å for all functionals excluding B3LYP. This demonstrates the suitability of this model chemistry for modelling these systems.

Ligand	CN	Symmetry	r_{UO} (Å)					r_{UL} (Å)				
			PBE	B3LYP	TPSS	TPSSh	Exp.	TPSS	PBE	TPSSh	B3LYP	Exp.
CO	6	D_{6h}	1.755	1.733	1.752	1.736	-	2.710	2.705	2.717	2.782	-
CN^-	5	D_{5h}	1.807	1.784	1.804	1.786	$1.773^{\dagger a}$	2.568	2.562	2.568	2.591	$2.567^{\dagger a}$
NC^-	5	D_{5h}	1.806	1.784	1.805	1.787	-	2.463	2.468	2.462	2.485	-
NCS^-	5	D_{5h} (C_s)	*1.815*	*1.788*	1.814	1.792	$1.762^{\dagger b}$	2.440	*2.445*	2.439	*2.467*	$2.446^{\dagger b}$
OH_2	5	C_2	1.779	1.759	1.777	1.761	1.78^{c}, 1.760^{d}	$2.427^{\dagger}$	$2.434^{\dagger}$	$2.424^{\dagger}$	$2.442^{\dagger}$	$2.41^{c,}$ 2.41^{d}
OH^-	4	D_{2d}	1.871	1.846	1.869	1.849	1.82^{c}, $1.82^{\dagger e}$	2.255	2.258	2.250	2.264	2.24^{c}, $2.26^{\dagger e}$
F^-	5	D_{5h}	1.865	1.838	1.866	1.844	1.80^{f}	2.258	2.267	2.255	2.274	2.26^{f}
MAD			0.042	0.022	0.041	0.025	-	0.006	0.009	0.005	0.021	-

Table 3.2: DFT-calculated structural parameters of energetically stable uranyl complexes considered in the first part of this study, along with comparisons to experimental data. [a] solid state XRD (ref [32]); [b] solid state XRD (ref [100]); [c] solution EXAFS (ref [81]); [d] solution EXAFS (ref [80]); [e] solid state XRD (ref [101]); [f] solution EXAFS (ref [92]). † Mean bond lengths.

Ligand	CN	ν_S (cm^{-1})				ν_{AS} (cm^{-1})			
		PBE	B3LYP	TPSS	TPSSh	PBE	B3LYP	TPSS	TPSSh
CO	6	902	958	908	947	965	1006	971	1005
CN$^-$	5	798	848	804	841	861	902	866	897
NC$^-$	5	797	848	799	838	861	902	862	895
NCS$^-$	5	774	844	839	850	847	891	845	883
OH$_2$	5	859	908	862	899	920	960	922	953
OH$^-$	4	720	760	724	753	756	786	759	786
F$^-$	5	720	768	723	756	753	795	753	784

Table 3.3: DFT-calculated U-O$_{yl}$ stretch vibrational frequencies of energetically stable uranyl complexes considered in this study.

In general, geometries obtained using the PBE and B3LYP exchange-correlation functionals are similar to those obtained using TPSS and TPSSh. Bond lengths obtained with PBE are closer to experimental values, where available, than bond lengths obtained using B3LYP. The [UO$_2$(NCS)$_5$]$^{3-}$ complex was reoptimised in C$_s$ symmetry with PBE and B3LYP. This was due to there being an imaginary vibrational frequency present when the D$_{5h}$ structures were reoptimised with these functionals. The [UO$_2$(NCS)$_5$]$^{3-}$ complexes were reoptimised without symmetry constraint for the same reason. Experimental U-O$_{yl}$ and U-L bond lengths tend to be slightly overestimated by both PBE and B3LYP, with PBE being the closer of the two.

It has been established previously that the frequencies of the uranyl U-O$_{yl}$ stretching vibrations are a sensitive probe of its coordination environment[56,85,101,392,393]. The frequencies of the symmetric (ν_S) and antisymmetric (ν_{AS}) uranyl stretching modes for these complexes are reported in Table 3.3. In every case, values calculated using hybrid functionals are higher than those obtained using pure functionals, as expected based on the shorter calculated U-O$_{yl}$ bond lengths discussed above. In order to establish a possible correlation between U-O$_{yl}$ vibrational frequencies and uranyl-ligand bond lengths, linear regression was performed. This regression revealed only moderate correlation between these two parameters, with R^2 values ranging from 0.72 to 0.79.

Next, binding energies were calculated in the same manner as those reported in Table 3.1 and are given in Table 3.4, in order of increasing binding energy per ligand. A strong relationship can be identified between total binding energies and the uranyl stretch frequencies, as can be seen in Figure 3.2. When considering correlation with the antisymmetric stretching mode, linear regression analysis produced R^2 values of

0.97-0.98 for the four functionals, whereas correlation with the symmetric stretching mode produced R^2 values of 0.90-0.98. Of these, the TPSSh functional gave the highest correlation in both cases.

Ligand	CN	PBE		B3LYP		TPSS		TPSSh	
		E_B	E_L	E_B	E_L	E_B	E_L	E_B	E_L
CO	6	1.51	0.25	0.40	0.07	1.21	0.20	1.00	0.17
OH_2	5	4.68	0.94	4.19	0.84	4.38	0.88	4.29	0.86
NC^-	5	6.55	1.31	5.81	1.16	6.00	1.20	5.85	1.17
NCS^-	5	6.65	1.33	5.79	1.16	6.13	1.23	5.90	1.18
CN^-	5	7.24	1.45	6.32	1.26	6.62	1.32	6.46	1.29
F^-	5	10.88	2.18	9.97	1.99	10.63	2.13	10.32	2.06
OH^-	4	10.15	2.54	10.25	2.56	10.44	2.61	10.18	2.55

Table 3.4: DFT-calculated total (E_B) and per ligand (E_L) binding energies of energetically stable uranyl complexes. $E_L = E_B/\mathrm{CN}$ gives the binding energy per ligand.

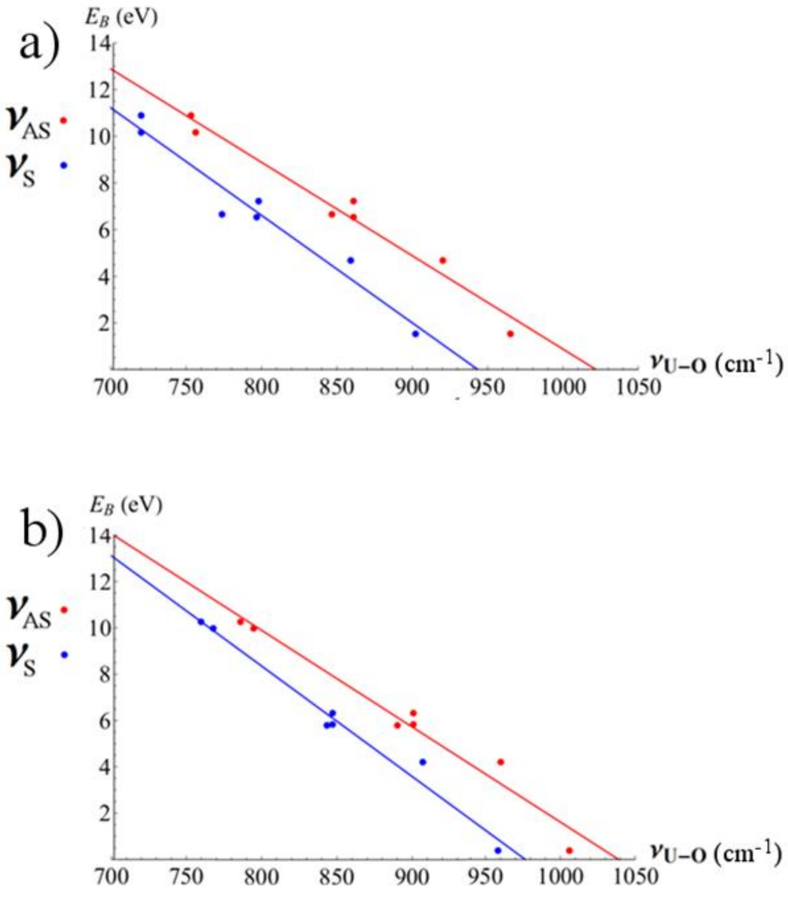

Figure 3.2: Linear fitting of calculated U-O_{yl} vibrational frequencies to binding energies: a) PBE data: $R^{2\,=}$ 0.97 and 0.95 for antisymmetric and symmetric stretch modes, respectively, b) B3LYP data: 0.97 and 0.90 for antisymmetric and symmetric stretch modes, respectively.

3.3.3. Density-Based Analyses of Electronic Structure

3.3.3.1. Electron Density Difference Distributions

There are many instances where the electronic structure of f-element complexes cannot be adequately described using monodeterminantal methods[33,237–240] and in these circumstances, orbital-based analyses may be ambiguous. It is therefore of great importance to develop an understanding of the strong correlations between binding energies and U-O$_{yl}$ stretching frequencies without relying upon analysis of the Kohn-Sham orbitals, *i.e*. we wish to understand the coordination of uranyl in terms of the electron density only. Electron density based methods of analysis are equally well-suited to monodeterminantal density-based and multireference wavefunction-based approaches, and therefore allow results from this study to be directly compared to investigations with multiconfigurational methodologies[27,239]. There are many published accounts of success with such density-based methods of analysis of f-element complexes in the literature[48,49,53,59,60,394], including some of the systems under consideration here[56].

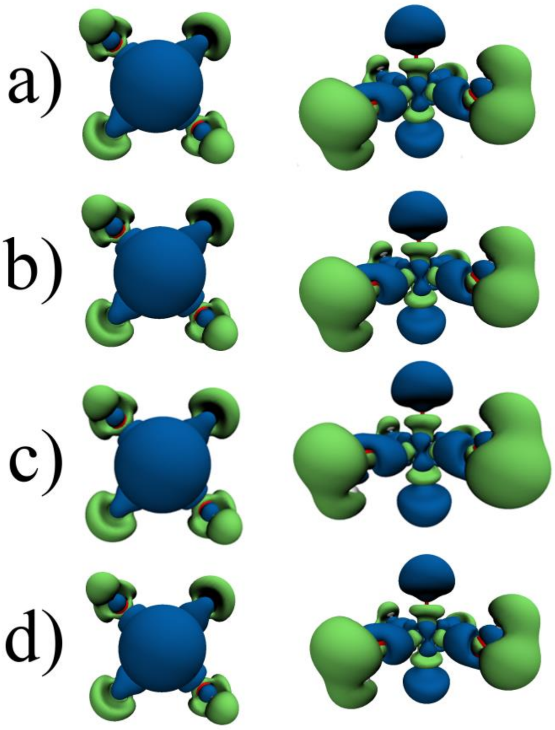

Figure 3.3: Electron density difference distributions showing accumulation of charge in blue and depletion of charge in green for the $[UO_2(OH)_4]^{2-}$ complex generated using: a) TPSS-derived electron density; b) TPSSh-derived electron density; c) PBE derived electron density; d) B3LYP-derived electron density. All drawn at an isosurface of 0.005 a.u.

Figure 3.3 shows the density difference distribution for the $[UO_2(OH)_4]^{2-}$ complex generated with all four *xc*-functionals, demonstrating that for this qualitative analysis, functional choice is relatively unimportant. Thus, for consistency with the remainder of this thesis, images for the purpose of qualitative analysis will be generated using data obtained using the PBE *xc*-functional only.

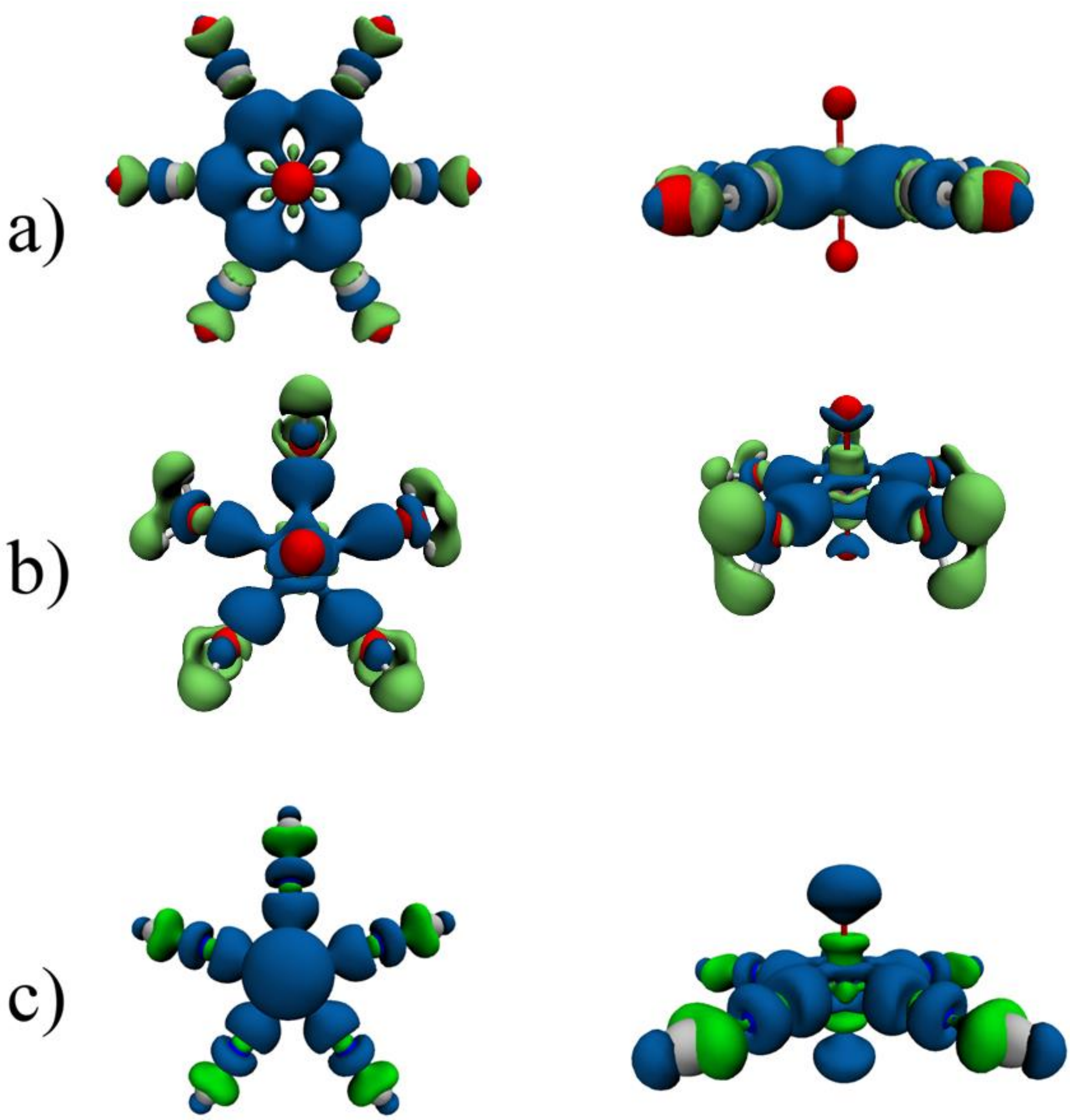

Figure 3.4: Electron density difference distributions showing accumulation of charge in blue and depletion of charge in green for a) $[UO_2(CO)_6]^{2+}$, b) $[UO_2(H_2O)_5]^{2+}$, c) $[UO_2(NC)_5]^{3-}$. Images generated from PBE-derived electron densities at an isosurface of 0.005 a.u.

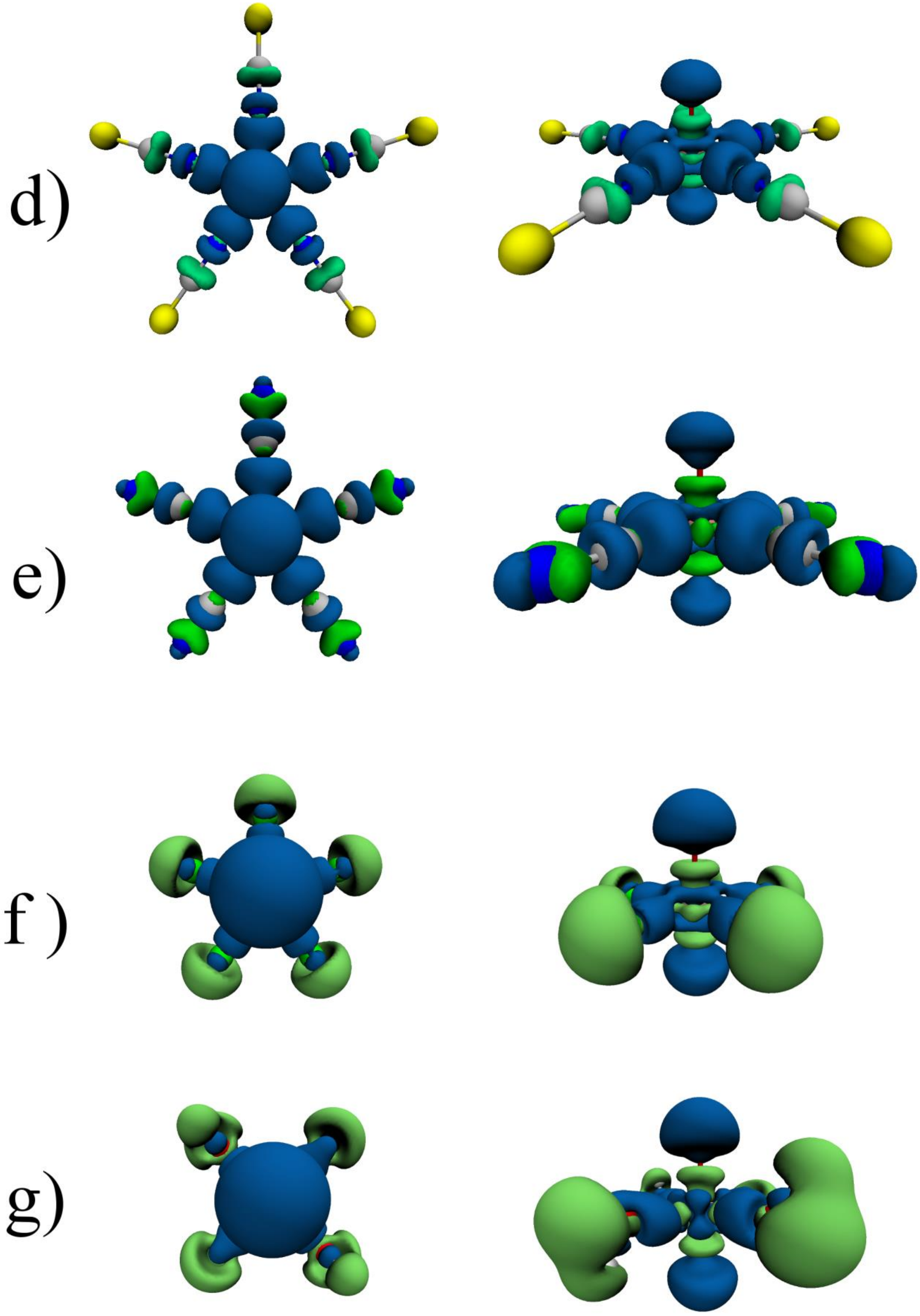

Figure 3.5. Electron density difference distributions showing accumulation of charge in blue and depletion of charge in green for d) $[UO_2(NCS)_5]^{3-}$, e) $[UO_2(CN)_5]^{3-}$, f) $[UO_2(F)_5]^{3-}$, g) $[UO_2(OH)_4]^{2-}$. Images generated from PBE-derived electron densities at an isosurface of 0.005 a.u.

Figures 3.4. and 3.5 show the electron density differences upon complexation for the complexes under investigation here, obtained for the structures optimised with the PBE *xc*-functional, ordered according to binding strength in the order of weak, intermediate and strong binding.

These plots reveal several distinct trends: firstly, considering the uranium-ligand bonding, as one moves from the weakly to the more strongly bound complexes, so the blue isosurfaces, which correspond to charge accumulation, become localised in the bonding region between the uranium centre and the equatorial ligand. For example, accumulation of charge (blue) in the equatorial bonding region of $[UO_2(CO)_6]^{2+}$ is diffuse, uncentred on any particular bond. Contrastingly, accumulation of charge in the equatorial bonding region of $[UO_2(OH)_4]^{2-}$ is concentrated into teardrop shaped regions focussed on the U-O_L bonds. This may be indicative of an interaction which is becoming more directed, with increased covalent character. Additionally, regions of charge depletion (green) localised on the ligands are observed to increase in magnitude as one traverses from the weakly bound CO complex to the strongly bound OH^- complex.

Secondly, a striking redistribution of charge within the uranyl unit is induced by the more strongly binding ligands. This redistribution corresponds to depletion of charge in the U-O_{yl} bonding region, represented by the green isosurfaces. This depletion is presumed to indicate a reduction in the covalent character of the U-O_{yl} bond. This is presumably due to the competing interactions in the equatorial plane and leads to the previously discussed weakening of the U-O_{yl} bond, as evidenced by the reduced vibrational frequencies. Along with this reduction in covalent U-O_{yl} bond character is a commensurate accumulation of charge on the oxygen centres, indicated by the blue isosurfaces, indicating enhanced ionic character in the U-O_{yl} bond. These isosurfaces are seen to increase in magnitude, from being non-existent for $[UO_2(CO)_6]^{2+}$ and barely present for the aquo complex, to fully enclosing the oxygen ions in the more strongly binding complexes, being particularly large in the fluoride and hydroxide complexes.

Finally, strong qualitative similarities are noted in the density difference plots of the fluoride and hydroxide complexes, which are also found to have very similar binding energies.

3.3.3.2 Analysis with the Quantum Theory of Atoms in Molecules

Subsequently, a more quantitative analysis method was used to further rationalise the density difference distributions, the Quantum Theory of Atoms in Molecules (QTAIM). QTAIM allows consideration of both topological and integrated properties of the electron density. QTAIM is described in detail in the Methodology (Chapter 2.9.1).

First, the topological characteristics are investigated, and these are summarised in Tables 3.5 and 3.6 for the PBE and B3LYP functionals, respectively. For the TPSS and TPSSh data, see Tables AI.1 and AI.2 in Appendix I.

Complex	U-O$_{yl}$			U-X/U-L		
	ρ_{BCP}	$\nabla^2\rho_{BCP}$	H	ρ_{BCP}	$\nabla^2\rho_{BCP}$	H
$[UO_2]^{2+}$	0.351	0.331	-0.364	-	-	-
$[UO_2(CO)_6]^{2+}$	0.324	0.321	-0.313	0.043	0.102	-0.003
$[UO_2(H_2O)_5]^{2+}$	0.306	0.321	-0.281	0.060	0.211	-0.005
$[UO_2(NC)_5]^{3-}$	0.284	0.326	-0.244	0.064	0.175	-0.008
$[UO_2(NCS)_5]^{3-}$	0.278	0.322	-0.234	0.064	0.197	-0.007
$[UO_2(CN)_5]^{3-}$	0.284	0.332	-0.243	0.062	0.111	-0.010
$[UO_2(F)_5]^{3-}$	0.246	0.335	-0.183	0.082	0.311	-0.014
$[UO_2(OH)_4]^{2-}$	0.242	0.343	-0.178	0.095	0.276	-0.022

Table 3.5: Topological parameters associated with all uranium bonds, obtained *via* QTAIM analysis of PBE-derived densities, in a.u. ρ_{BCP} is the magnitude of the electron density at the bond critical point (BCP), $\nabla^2\rho_{BCP}$ its Laplacian, and H the energy density at the BCP.

Complex	U-O$_{yl}$			U-X/U-L		
	ρ_{BCP}	$\nabla^2\rho_{BCP}$	H	ρ_{BCP}	$\nabla^2\rho_{BCP}$	H
$[UO_2]^{2+}$	0.366	0.271	-0.395	-	-	-
$[UO_2(CO)_6]^{2+}$	0.344	0.271	-0.354	0.036	0.091	-0.002
$[UO_2(H_2O)_5]^{2+}$	0.322	0.271	-0.313	0.058	0.211	-0.005
$[UO_2(NC)_5]^{3-}$	0.302	0.278	-0.277	0.061	0.174	-0.007
$[UO_2(NCS)_5]^{3-}$	0.299	0.275	-0.271	0.061	0.190	-0.006
$[UO_2(CN)_5]^{3-}$	0.301	0.285	-0.276	0.058	0.111	-0.009
$[UO_2(F)_5]^{3-}$	0.265	0.291	-0.214	0.080	0.313	-0.013
$[UO_2(OH)_4]^{2-}$	0.258	0.303	-0.205	0.093	0.283	-0.021

Table 3.6: Topological parameters associated with all uranium bonds, obtained *via* QTAIM analysis of B3LYP-derived densities in a.u. ρ_{BCP} is the magnitude of the electron density at the bond critical point (BCP), $\nabla^2\rho_{BCP}$ its Laplacian, and H the energy density at the BCP.

Looking first at the values of ρ_{BCP} (the magnitude of the electronic density at the bond critical point, BCP) of the U-O$_{\mathrm{yl}}$ bond, an almost monotonic decrease in ρ_{BCP} is found as the binding energy of the complex increases, a trend that is mirrored by H (the energy density at the BCP). This is observed with all four *xc*-functionals. Since equatorial binding has been shown in Figures 3.4 and 3.5 to lead to a lengthening and weakening of the axial U-O$_{\mathrm{yl}}$ bond, this is to be expected.

However, when linear regression is performed, the correlation between the U-O$_{\mathrm{yl}}$ ρ_{BCP} and complex binding energy, as shown in Figure 3.6, is striking - R^2 = 0.96 when the PBE functional is used and R^2 = 0.98 when the B3LYP functional is used. Additionally, R^2 values of 0.97 and 0.98 are found when the TPSS and TPSSh functionals, respectively, are employed.

Specifically, the QTAIM parameters reflect a reduction in covalent character in the U-O$_{\mathrm{yl}}$ bond upon complexation, which is commensurate with the trend seen in Figures 3.4 and 3.5, which show that strongly binding equatorial ligands deplete charge density in the axial U-O$_{\mathrm{yl}}$ bonding region to a greater extent than weakly binding ligands.

Similarities are present between the two hybrid functionals: Topological parameters of the U-O$_{\mathrm{yl}}$ bond calculated using the B3LYP *xc*-functional are broadly similar to those calculated using the TPSSh *xc*-functional. The same decrease in the value of ρ_{BCP} can be observed as binding energy increases, and the same decrease in H (See Tables 3.5 – 3.6). When the PBE *xc*-functional is used, the strength of the correlation between complex binding energy and U-O$_{\mathrm{yl}}$ ρ_{BCP} is slightly reduced compared to the other functionals, but still strong.

Considering the equatorial ligands themselves, correlation between ρ_{BCP} and binding energy per ligand is also strong (R^2 = 0.96 for the PBE functional and R^2 = 0.98 for the B3LYP functional, and R^2 = 0.97 for both the TPSS and TPSSh functionals), see Figure 3.6. This is somewhat surprising, bearing in mind the range of coordinating species, but demonstrates that variations in bond strength are well accounted for in terms of variation in covalent bonding character.

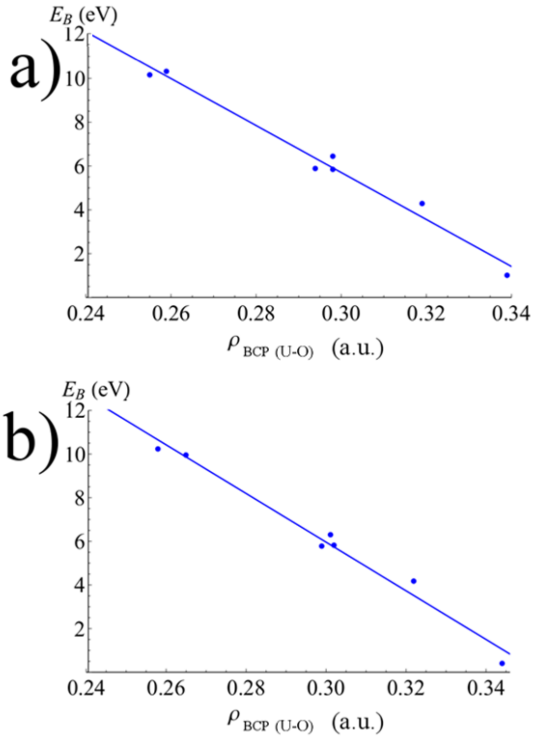

Figure 3.6: Linear fitting of calculated values of ρ_{BCP} for the U-O bonds to binding energies. a) PBE data: $R^2 = 0.96$, b) B3LYP data: $R^2 = 0.98$

Of more interest to the study in this chapter, however, is the potential correlation between QTAIM parameters associated with the equatorial bonding and the U-O$_{\mathrm{yl}}$ vibrational frequencies, as a strong relationship here would potentially present a way to assess equatorial covalent character *via* experimental measurements of the U-O$_{\mathrm{yl}}$ vibrational frequencies. These data are presented in Figure 3.7. Linear regression has been performed to quantify the strength of correlations. Here the values of ρ_{BCP} for each uranium-ligand bond have been summed. This is because the variation in vibrational frequencies is induced by the combined effect of the ligating species.

For the equatorial bonds, strong correlation is found between ρ_{BCP} and the frequencies of the stretching modes of the axial U-O$_{\mathrm{yl}}$ bonds, with the higher the sum of the electron densities at the equatorial BCPs, the lower the frequencies of the uranyl stretching modes. This data is presented in Figure 3.8. When the antisymmetric U-O$_{\mathrm{yl}}$ stretching mode is considered, linear regression reveals values of $R^2 = 0.90$ for the PBE *xc*-functional and $R^2 = 0.91$ for the B3LYP *xc*-functional. Additionally, values of $R^2 = 0.91$ for the TPSS *xc*-functional, $R^2 = 0.92$ for the TPSSh *xc*-functional were found. The correlation with the symmetric mode is slightly weaker, with R^2 = 0.84 for the PBE functional, R^2 = 0.89 for the B3LYP functional, R^2 = 0.87 for the TPSS functional, and R^2 = 0.89 for the TPSSh functional, but this is still indicative of a strong relationship. The strength of these correlations demonstrates that the U-O_{yl} stretching modes, which are readily identifiable *via* IR or Raman spectroscopies, can serve as a quantitative measure of equatorial bond covalency, as defined by the magnitude of the electron density at the QTAIM-derived BCP for the equatorial bonds.

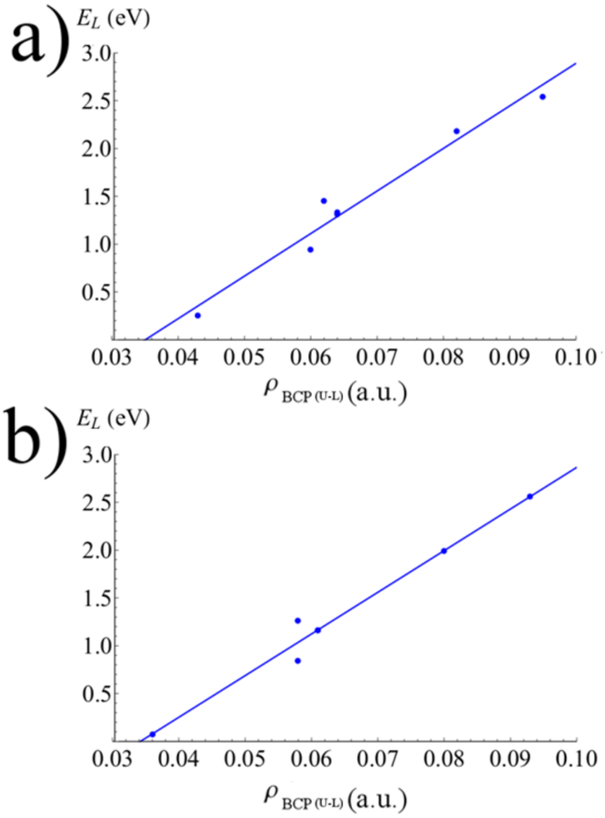

Figure 3.7: Linear fitting of calculated values of ρ_{BCP} for the U-L bonds to per ligand binding energies. a) PBE data: R^2 = 0.96, b) B3LYP data: R^2 = 0.98.

As might be expected, the relationship between the uranyl stretching frequencies and the values of ρ_{BCP} for the U-O_{yl} bonds is stronger still (See Figure 3.9). When the antisymmetric mode is considered, linear regression reveals values of R^2 = 1.00 using the PBE functional and R^2 = 1.00 using the B3LYP exchange correlation functional, as well as R^2 = 0.99 using the TPSS functional and R^2 = 1.00 using the TPSSh functional. For the symmetric mode, slightly weaker but still strong correlations of R^2 = 0.98 using the PBE functional and R^2 = 0.99 using the B3LYP exchange correlation functional are found, as well as R^2 = 0.95 using the TPSS functional and R^2 = 0.99 using the TPSSh functional.

These data show that there is a clear relationship between both U-O$_{yl}$ stretching frequencies and topological parameters of the U-O$_{yl}$ BCP, with very strong correlation for both antisymmetric and symmetric modes with ρ_{BCP}.

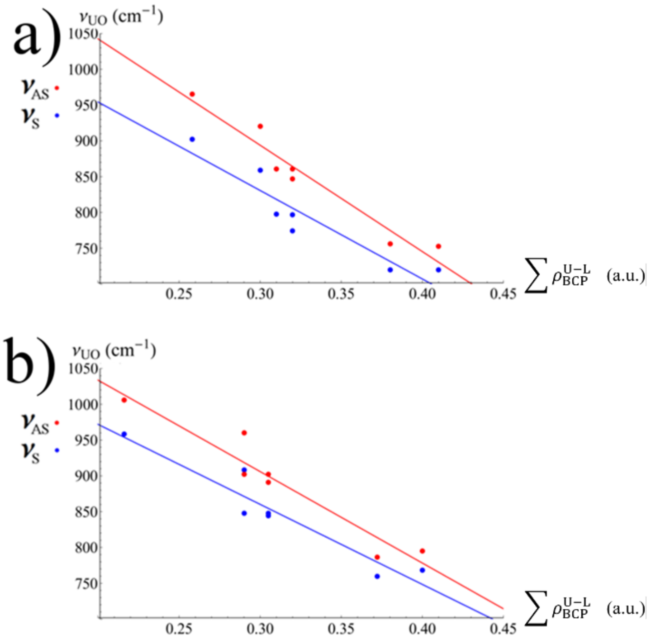

Figure 3.8: Linear fitting of calculated values of U-O$_{yl}$ vibrational frequencies to $\Sigma\rho_{BCP}$ for the U-L bonds: a) PBE data: $R^2 = 0.90$ (ν_{AS}), $R^2 = 0.84$ (ν_S), b) B3LYP data: $R^2 = 0.91$ (ν_{AS}), $R^2 = 0.89$ (ν_S).

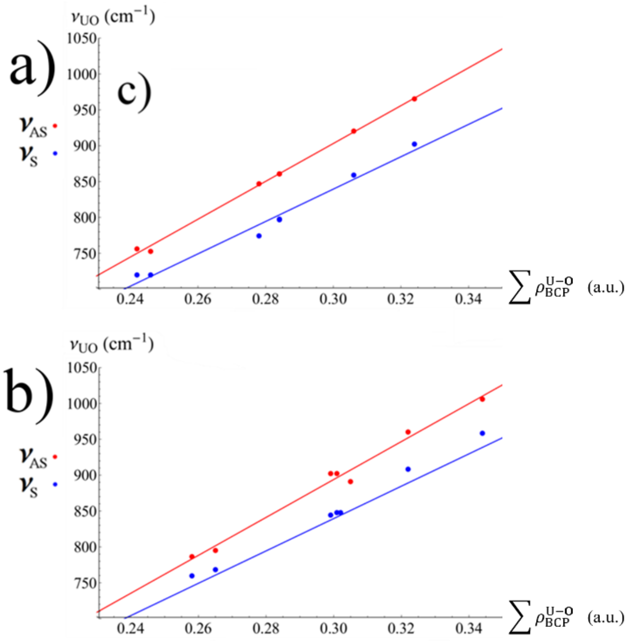

Figure 3.9: Linear fitting of calculated values of U-O$_{yl}$ vibrational frequencies to ρ_{BCP} for the U-O$_{yl}$ bonds: a) PBE data: $R^2 = 1.00$ (ν_{AS}), $R^2 = 0.98$ (ν_S), b) B3LYP data: $R^2 = 1.00$ (ν_{AS}), $R^2 = 0.99$ (ν_S).

Next, we turn to the integrated properties of the electron density with the purpose being to gain an improved understanding of the contribution of the uranium centre to equatorial bond covalency in these systems, and to quantify the redistribution of charge upon complexation.

For this purpose, several further QTAIM derived quantities are of use: $N(A)$, the electron population of atom A, which is obtained by integrating the electron density over the atomic basin Ω_A and from which atomic charges can be deduced; $\lambda(A)$, the localisation index, a measure of the number of electrons localised (*i.e.* not shared) on atom A; and $\delta(A, B)$, the delocalisation index, a measure of the number of electrons shared between atoms A and B. The (de)localisation index is obtained *via* integration of the exchange-correlation component of the electron pair-density. Using these integrated properties, two further quantities can be defined, specific to the uranyl unit: the uranyl electron population, $N(\mathrm{UO_2})$, and the uranyl localisation index, $\lambda(\mathrm{UO_2})$, defined as:

$$N(\mathrm{UO_2}) = N(\mathrm{U}) + \sum_{i=1,2} N(\mathrm{O}_i) \qquad (Eq. 3.2)$$

$$\lambda(\mathrm{UO_2}) = \lambda(\mathrm{U}) + \sum_{i=1,2} [\lambda \mathrm{O}_i + \delta(\mathrm{U}, \mathrm{O}_i)] + \delta(\mathrm{O}, \mathrm{O}) \qquad (Eq. 3.3)$$

For the isolated uranyl dication, $N(\mathrm{UO_2})$ and $\lambda(\mathrm{UO_2})$ are both equal to the total number of electrons in the system, 106. Deviations from 106 when uranyl is considered in a complex can inform as to the degree of charge redistribution within the uranyl unit as well as delocalisation between the uranyl unit and the ligands.

Tables 3.7 and 3.8 present the one-electron integrated QTAIM properties for complexes optimised using the PBE and B3LYP *xc*-functionals. Data for the TPSS and TPSSh *xc*-functionals is available in Appendix I. Ligand populations and charges are not reported, since trends will, by definition, mirror those of $q_{\mathrm{UO_2}}$. An overall increase in electron population of the uranyl unit is found upon stronger equatorial complexation. This leads to a reduction in the formal +2 charge to a value as low as + 0.88 upon complexation by hydroxide ligands.

There is clearly a significant transfer of charge: approximately 0.5 a.u. of electron density is donated to the uranium centre upon complexation, however the electron population of the uranium atom remains approximately constant irrespective of the nature of the coordinating equatorial ligand. There is, however, an increase of electronic charge on the O_{yl} atoms upon stronger equatorial complexation. This implies a charge transfer from the ligand to the uranyl oxygen, inducing an increased ionic interaction between the positively charged uranium centre and the (increasingly) negatively charged oxygen atoms.

Complex	$N(\mathrm{U})$ (q_{U})	$N(\mathrm{O})$ ($q_{\mathrm{O}_{yl}}$)	$N(\mathrm{UO_2})$ ($q_{\mathrm{UO_2}}$)
$[UO_2]^{2+}$	88.67(+3.33)	8.67(-0.67)	106(+2)
$[UO_2(CO)_6]^{2+}$	89.22 (+2.78)	8.73 (-0.73)	106.69 (+1.31)
$[UO_2(H_2O)_5]^{2+}$	89.02 (+2.98)	8.82 (-0.82)	106.66 (+1.34)
$[UO_2(NC)_5]^{3-}$	89.08 (+2.92)	8.90 (-0.90)	106.88 (+1.12)
$[UO_2(NCS)_5]^{3-}$	89.11 (+2.89)	8.92 (-0.92)	106.95 (+1.05)
$[UO_2(CN)_5]^{3-}$	89.24 (+2.76)	8.90 (-0.90)	107.04 (+0.96)
$[UO_2(F)_5]^{3-}$	88.98 (+3.02)	9.03 (-1.03)	107.04 (+0.96)
$[UO_2(OH)_4]^{2-}$	89.14 (+2.86)	9.04 (-1.04)	107.22 (+0.78)

Table 3.7: One-electron integrated QTAIM parameters of uranyl and complexing ligands, obtained *via* analysis of PBE-derived densities. *n* and *q* are electronic populations and overall charges, respectively.

Complex	$N(\mathrm{U})$ (q_{U})	$N(\mathrm{O})$ ($q_{\mathrm{O}_{yl}}$)	$N(\mathrm{UO_2})$ ($q_{\mathrm{UO_2}}$)
$[UO_2]^{2+}$	88.53 (+3.47)	8.73 (-0.73)	106 (+2)
$[UO_2(CO)_6]^{2+}$	89.01 (+2.99)	8.78 (-0.78)	106.57 (+1.43)
$[UO_2(H_2O)_5]^{2+}$	88.98 (+3.02)	8.79 (-0.79)	106.55 (+1.45)
$[UO_2(NC)_5]^{3-}$	88.87 (+3.13)	8.94 (-0.94)	106.74 (+1.26)
$[UO_2(NCS)_5]^{3-}$	88.88 (+3.12)	8.94 (-0.94)	106.77 (+1.22)
$[UO_2(CN)_5]^{3-}$	89.03 (+2.97)	8.94 (-0.94)	106.91 (+1.09)
$[UO_2(F)_5]^{3-}$	88.76 (+3.24)	9.05 (-1.05)	106.85 (+1.15)
$[UO_2(OH)_4]^{2-}$	88.91 (+3.09)	9.07 (-1.07)	107.05 (+0.95)

Table 3.8: One-electron integrated QTAIM parameters of uranyl and complexing ligands, obtained *via* analysis of B3LYP-derived densities.

Complex	$\lambda(\mathrm{U})$	$\lambda(\mathrm{O}_{yl})$	$\lambda(\mathrm{UO}_2)$	$\delta(\mathrm{U},\mathrm{O}_{yl})$	$\delta(\mathrm{O}_{yl1},\mathrm{O}_{yl2})$	$\delta(\mathrm{U},\mathrm{L})*$	$(n-\lambda)_{\mathrm{UO}_2}$
$[UO_2]^{2+}$	86.44	7.49	106.00	2.23	0.13	-	0.00
$[UO_2(CO)_6]^{2+}$	86.16	7.53	105.49	2.07	0.11	0.30	+1.20
$[UO_2(H_2O)_5]^{2+}$	86.06	7.68	105.51	1.99	0.11	0.37	+1.15
$[UO_2(NC)_5]^{3-}$	86.04	7.77	105.47	1.89	0.10	0.41	+1.41
$[UO_2(NCS)_5]^{3-}$	86.00	7.80	105.43	1.87	0.09	0.42	+1.52
$[UO_2(CN)_5]^{3-}$	86.11	7.76	105.52	1.89	0.10	0.42	+1.52
$[UO_2(F)_5]^{3-}$	85.92	7.98	105.44	1.73	0.08	0.53	+1.60
$[UO_2(OH)_4]^{2-}$	85.96	8.00	105.49	1.72	0.08	0.71	+1.73

Table 3.9: Two-electron integrated QTAIM parameters of uranyl and complexing ligands in a.u., obtained *via* analysis of PBE-derived densities. *delocalisation indices between uranium and coordinating species of the ligand, averaged over all ligands.

Complex	$\lambda(\mathrm{U})$	$\lambda(\mathrm{O}_{yl})$	$\lambda(\mathrm{UO}_2)$	$\delta(\mathrm{U},\mathrm{O}_{yl})$	$\delta(\mathrm{O}_{yl1},\mathrm{O}_{yl2})$	$\delta(\mathrm{U},\mathrm{L})*$	$(n-\lambda)_{\mathrm{UO}_2}$
$[UO_2]^{2+}$	86.36	7.59	106.00	2.17	0.11	-	0.00
$[UO_2(CO)_6]^{2+}$	86.14	7.62	105.60	2.06	0.11	0.25	+0.98
$[UO_2(H_2O)_5]^{2+}$	86.02	7.75	105.53	1.95	0.10	0.33	+1.02
$[UO_2(NC)_5]^{3-}$	86.01	7.84	105.50	1.86	0.09	0.34	+1.24
$[UO_2(NCS)_5]^{3-}$	85.98	7.85	105.47	1.85	0.09	0.37	+1.30
$[UO_2(CN)_5]^{3-}$	86.08	7.83	105.56	1.87	0.09	0.38	+1.35
$[UO_2(F)_5]^{3-}$	85.89	8.03	105.44	1.71	0.08	0.46	+1.41
$[UO_2(OH)_4]^{2-}$	85.92	8.06	105.48	1.69	0.07	0.64	+1.57

Table 3.10: Two-electron integrated QTAIM parameters of uranyl and complexing ligands, obtained *via* analysis of B3LYP-derived densities. *delocalisation indices between uranium and coordinating species of the ligand, averaged over all ligands.

While one-electron properties provide a reasonable overall description of charge transfer between the uranium centre and the ligand in these complexes, analysis of the two-electron properties, as given in Tables 3.9 and 3.10 for the PBE and B3LYP derived densities, respectively, is necessary to provide greater insight into the variation in bonding character upon complexation. As before, TPSS and TPSSh data can be found in Appendix I.

Focussing first on the localisation indices associated with individual atoms, a small decrease in $\lambda(\mathrm{U})$ is found, along with a more pronounced increase in $\lambda(\mathrm{O})$, similar to the trends found in atomic populations. This strengthens the previous assertion that equatorial complexation enhances the ionic character of the U-O_{yl} bond: the degree of electron localisation on the O_{yl} centres actually exceeds the degree of electron population increase.

When the integrated properties of the electron densities obtained using the PBE and B3LYP functionals are considered, $\lambda(\mathrm{U})$ values are seen to decrease from $[UO_2(CO)_6]^{2+}$ to $[UO_2(OH)_4]^{2-}$, while $\lambda(\mathrm{O})$ values are seen to increase. This suggests that, in general, as equatorial bonding becomes stronger, the amount of charge transferred from the uranium atom to the uranyl oxygen atoms increases. The same broad trends are seen with complexes optimised using the TPSS/TPSSh *xc*-functionals. The difference $(n-\lambda)_{\mathrm{UO_2}}$ increases from $[UO_2(CO)_6]^{2+}$ to $[UO_2(OH)_4]^{2-}$ when the B3LYP functional is employed, mirroring the increases seen with the TPSSh functional, although the B3LYP values differ in that for $[UO_2(H_2O)_5]^{2+}$, $(n-\lambda)_{\mathrm{UO_2}}$ is greater than for $[UO_2(CO)_6]^{2+}$, in contrast to the results obtained using the TPSSh functional. These trends are the same for the data obtained using the PBE functional.

A previous study of a series of complexes of formally tetravalent actinides[53] noted a strong correlation was present when comparing the quantity $Z_{\mathrm{An}} - \lambda_{\mathrm{An}}$ (where Z is the atomic number) with the formal oxidation state. This relationship is found to be present with these complexes: subtracting $\lambda(\mathrm{U})$ from the atomic number of uranium (Z = 92) results in a range of values between 5.88 and 6.12, which are in excellent agreement with the formal +VI oxidation state of uranium in these complexes.

Although the amount of charge transferred to the uranyl unit increases upon stronger equatorial complexation, the uranyl localisation index, $\lambda(\mathrm{UO_2})$, remains largely unchanged. Since $\lambda(\mathrm{UO_2})$ also accounts for all electron delocalisation *within* the uranyl unit, this implies that the excess charge transferred by more strongly binding equatorial ligands is, in fact, delocalised between the uranium centre and equatorial ligands, *i.e.* this charge contributes towards covalent interactions in the equatorial plane.

This requires a different origin for the increased electron population (and localisation) on the O_{yl} centres than that suggested by the one-electron data. The delocalisation index of the U-O_{yl} bond can be considered an alternative measure of bond covalency[347,348] to that provided by ρ_{BCP}. This is found to decrease upon stronger equatorial complexation. The origin of the excess charge on the O_{yl} centres can therefore be understood as a localisation of charge previously delocalised, prior to equatorial complexation, in the U-O_{yl} bond. This provides strong evidence that equatorial complexation enhances the ionic character of the U-O_{yl} bond: the elongation and weakening of the U-O_{yl} bond (as evidenced by the reduction in ν_{UO}) can be understood as originating from the fact that this increased ionic interaction comes at the expense of U-O_{yl} bond covalency. This interpretation is in keeping with the qualitative picture given by electron density differences, which clearly show a depletion of charge in the U-O_{yl} bonding region with a commensurate accumulation on the O_{yl} centres. The combined variation of $N(\mathrm{UO_2})$ and $(\mathrm{UO_2})$, shown in the final column of Tables 3.8 and 3.9, can be interpreted as further evidence for the increase in equatorial covalent character. As the electron population of the uranyl unit increases, the degree of electron localisation decreases, which means equatorial complexation induces a covalent contribution to the bond from the uranium centre itself.

As with the U-O_{yl} ρ_{BCP} data, very strong correlation is found between $\delta(\mathrm{U,O_{yl}})$ with and the U-O_{yl} stretch frequencies (see Figure 3.10). For the antisymmetric mode, R^2 = 1.0 when the PBE *xc*-functional is used, and R^2 = 0.99 when the B3LYP *xc*-functional is used. Additionally, R^2 = 1.0 when the TPSS *xc*-functional is used, and R^2 = 1.00 when the TPSSh *xc*-functional is used. For the symmetric mode, correlation is again found to be slightly weaker, but still strong, with R^2 = 0.99 when the PBE *xc*-functional is used, and R^2 = 0.99 when the B3LYP *xc*-functional is used. Values of R^2 = 0.94 and R^2 = 0.99 are found for the TPSS and TPSSh *xc*-functionals, respectively.

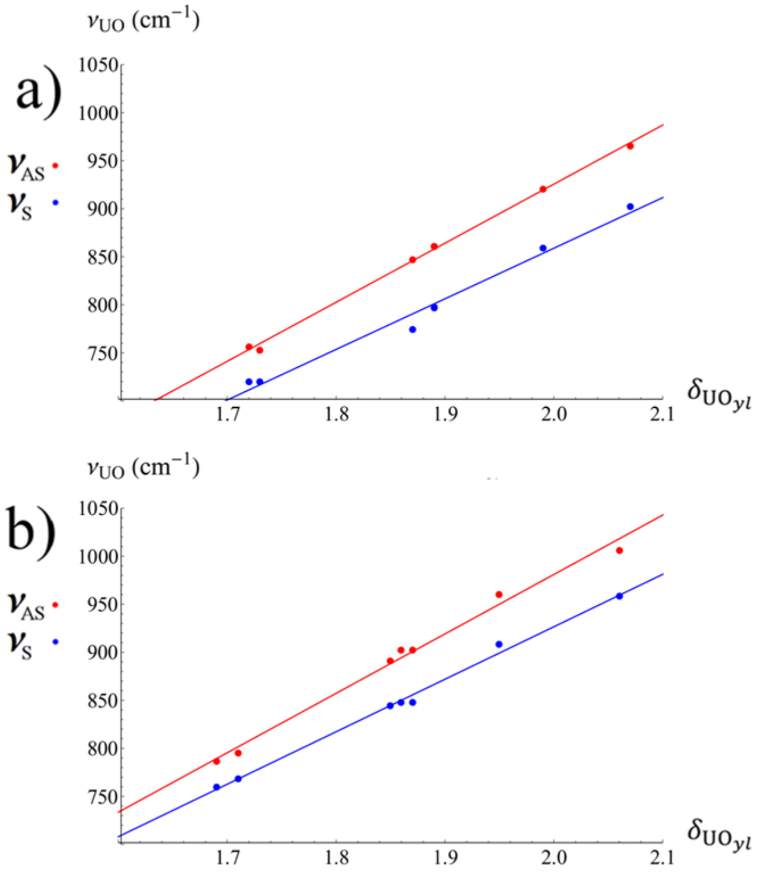

Figure 3.10: Linear fitting of calculated values of U-O vibrational frequencies to calculated values of $\delta(\mathrm{U},\mathrm{O}_{yl})$: a) PBE data: R^2 = 1.0 (ν_{AS}), 0.99 (ν_{AS}), b) B3LYP data: R^2 = 0.99 (ν_{AS}), 0.99 (ν_{AS}).

Turning to the more interesting (and perhaps more relevant) relationship between U-O$_{yl}$ vibrational frequencies and equatorial ligand covalency as measured by the delocalisation index, strong correlations are again found (see Figure 3.11). For the antisymmetric mode, R^2 = 0.91 when the TPSS *xc*-functional is used, R^2 = 0.94 when the TPSSh *xc*-functional is used, R^2 = 0.91 when the PBE *xc*-functional is used, and R^2 = 0.86 when the B3LYP *xc*-functional is used. For the symmetric mode, R^2 = 0.90 when the TPSS *xc*-functional is used, R^2 = 0.93 when the TPSSh *xc*-functional is used, R^2 = 0.83 when the PBE *xc*-functional is used, and R^2 = 0.83 when the B3LYP *xc*-functional is used. The strong correlations found using the delocalisation index further supports the assertion that U-O$_{yl}$ stretching modes serve as a quantitative measure of equatorial bond covalency.

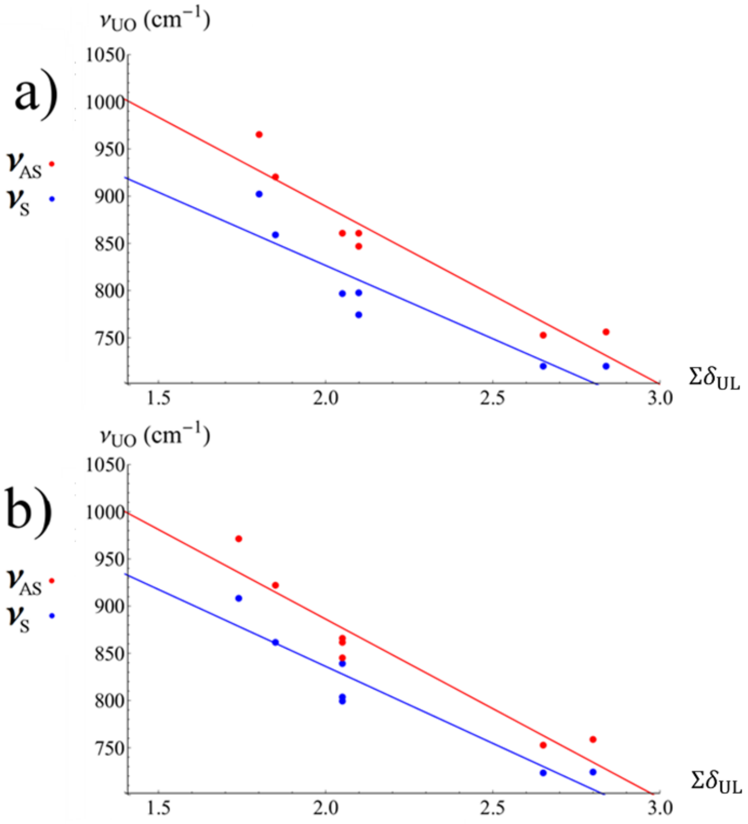

Figure 3.11: Linear fitting of calculated values of U-L vibrational frequencies to calculated values of $\sum\delta(\mathrm{U,L})$: a) PBE data: $R^2 = 0.91$ (ν_{AS}), 0.83 (ν_{AS}), b) B3LYP data: $R^2 = 0.86$ (ν_{AS}), 0.83 (ν_{AS}).

3.3.3.3. Analysis of the Electron Localisation Function (ELF)

Another density-based analysis tool, the electron localisation function[350,395], (ELF, denoted by $n(\boldsymbol{r})$) is now considered. $n(\boldsymbol{r})$ is a scalar field, and its topology can be analysed in a similar way as the electron density, $\rho(\boldsymbol{r})$[357]. Four types of stable critical points (CPs) exist in the $n(\boldsymbol{r})$ surface. As with those in $\rho(\boldsymbol{r})$, CPs denoted (3,-3) correspond to local maxima and those denoted (3,-1) correspond to saddle points in the $n(\boldsymbol{r})$ surface. An interaction with strongly covalent character is characterised by a local maxima in $n(\boldsymbol{r})$ (a (3,-3) CP) along the direction of a bond, unassociated with any nucleus, whereas the value of $n(\boldsymbol{r})$ at a (3,-1) CP defines a bifurcation point in $n(\boldsymbol{r})$. This bifurcation point represents a value for which an isosurface of $n(\boldsymbol{r})$ splits into two (or more) separate surfaces. Bifurcation points in the ELF isosurface have been proposed previously as a measure of electron delocalisation between atoms[353,356,357].

Complex	$n^c_{\mathrm{UO}_{yl}}$	n^c_{UL}
$[UO_2]^{2+}$	0.378	-
$[UO_2(CO)_6]^{2+}$	0.387	0.187
$[UO_2(H_2O)_5]^{2+}$	0.390	0.166
$[UO_2(NC)_5]^{3-}$	0.302	0.225
$[UO_2(NCS)_5]^{3-}$	0.387	0.199
$[UO_2(CN)_5]^{3-}$	0.380	0.300
$[UO_2(F)_5]^{3-}$	0.385	0.191
$[UO_2(OH)_4]^{2-}$	0.380	0.273

Table 3.11: Values of $n(\boldsymbol{r})$ at (3,-1) critical points of the electron localisation function $n(\boldsymbol{r})$ associated with axial and equatorial bonding to the uranium centre in all complexes studied, obtained *via* analysis of the PBE-derived densities.

Complex	$n^c_{\mathrm{UO}_{yl}}$	n^c_{UL}
$[UO_2]^{2+}$	0.385	-
$[UO_2(CO)_6]^{2+}$	0.390	0.151
$[UO_2(H_2O)_5]^{2+}$	0.394	0.154
$[UO_2(NC)_5]^{3-}$	0.390	0.205
$[UO_2(NCS)_5]^{3-}$	0.392	0.187
$[UO_2(CN)_5]^{3-}$	0.386	0.273
$[UO_2(F)_5]^{3-}$	0.392	0.179
$[UO_2(OH)_4]^{2-}$	0.386	0.253

Table 3.12: Values of $n(\boldsymbol{r})$ at (3,-1) critical points of the electron localisation function $n(\boldsymbol{r})$ associated with axial and equatorial bonding to the uranium centre in all complexes studied, obtained *via* analysis of the B3LYP-derived densities.

The topological analysis of $n(\boldsymbol{r})$ reveals no (3,-3) CPs associated with the U-O_{yl} bond in any complex considered in this chapter. However, all complexes exhibit (3,-1) CPs along the bond, the values of which are given in Tables 3.11 and 3.12 for the data obtained using the PBE and B3LYP *xc*-functionals, respectively. TPSS and TPSSh data can be found in Appendix I. The value of $n(\boldsymbol{r})$ at the (3,-1) CPs represent the point at which $n(\boldsymbol{r})$ bifurcates into a set of separate surfaces, which each encompass one of the three uranyl atoms. The variation in these bifurcation points is very small and the values themselves do not appear to correlate with any other properties reported in this chapter. Analysis of the equatorial bonds reveals a similar picture: values of $n(\mathbf{r})$ at the (3,-1) CPs do not correlate with either the reported structural, vibrational, topological or energetic properties. This is perhaps unsurprising considering the range of coordinating species.

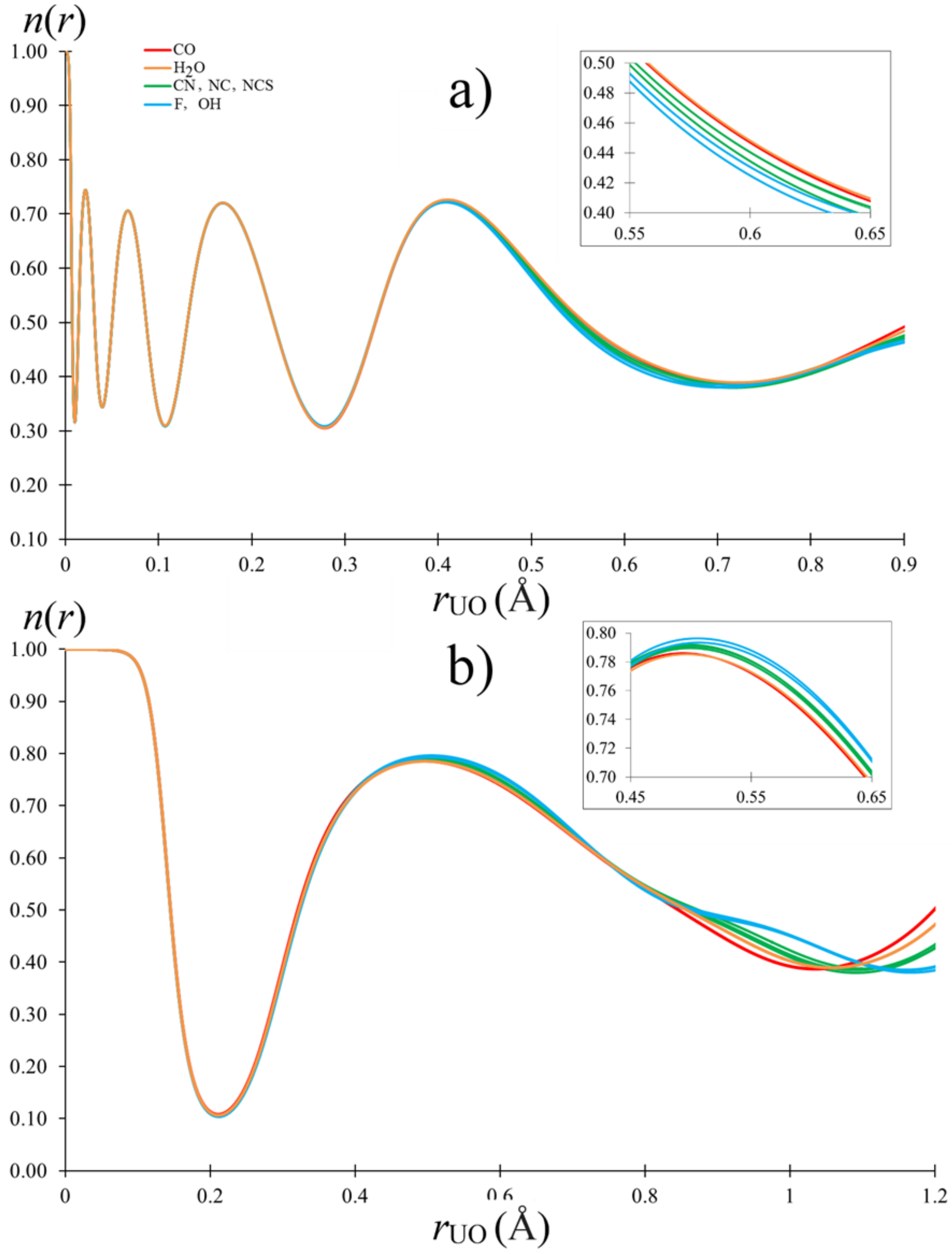

Figure 3.12: Behaviour of the electron localisation function, $n(\mathbf{r})$, along the U-O_{yl} bond. a) $n(\mathbf{r})$ between the uranium centre and (3,-1) CP; b) $n(\mathbf{r})$ between the oxygen centre and the (3,-1) CP. Data derived from the electron density of the complex optimised using the PBE *xc*-functional.

There appears to be some dependence of $n(\boldsymbol{r})$ along the U-O_{yl} bond on the strength of the equatorial coordination: approaching the (3,-1) CP from the uranyl centre (Figure 3.12(a)) there is a small reduction in $n(\boldsymbol{r})$, broadly commensurate with the strength of the equatorial coordination. Approaching from the O_{yl} centre (Figure 3.12(b)) and the opposite behaviour is revealed, *i.e.* an increase in $n(\boldsymbol{r})$ for complexes exhibiting strong equatorial binding. These observations may be indicative of variation in the U and O_{yl} contributions to the bond, however a quantitative relationship is not obviously apparent, particularly given the very small magnitude of the variation. Similar trends are observed with all four *xc*-functionals employed here.

Since strong correlations have already been demonstrated between QTAIM parameters and the physical properties of the complexes considered here, it would appear that, in these systems at least, analysis of $n(\boldsymbol{r})$ provides no great additional insight into the variation of the axial U-O bond induced by equatorial complexation.

3.3.3.4. Analysis of the Reduced Density Gradient

The final analysis performed on these complexes is of the reduced density gradient (RDG), defined as:

$$s(\boldsymbol{r}) = \frac{1}{2(3\pi^2)^{1/3}} \frac{|\nabla\rho(\boldsymbol{r})|}{\rho(\boldsymbol{r})^{4/3}} \qquad (Eq. 3.4)$$

The presence of weak interactions is indicated by low density ‘spikes’ in plots of the RDG, $s(\boldsymbol{r})$ against the density. These spikes arise due to the fact that while $\rho(\boldsymbol{r})$ can take large values in regions of covalent interactions, it takes small but non-zero values in regions of predominantly non-covalent character, as may be expected in the equatorial bonding regions of the complexes considered here. $s(\boldsymbol{r})$ takes very small values in regions of both covalent and non-covalent interactions, with $s(\boldsymbol{r}) \rightarrow 0$ at critical points in $\rho(\boldsymbol{r})$. As discussed in the Methodology (Chapter 2.9.3), plotting $s(\boldsymbol{r})$ against $\rho(\boldsymbol{r})\mathrm{sgn}(\lambda_2)$ rather than $\rho(\boldsymbol{r})$ allows discrimination between attractive and repulsive interactions.

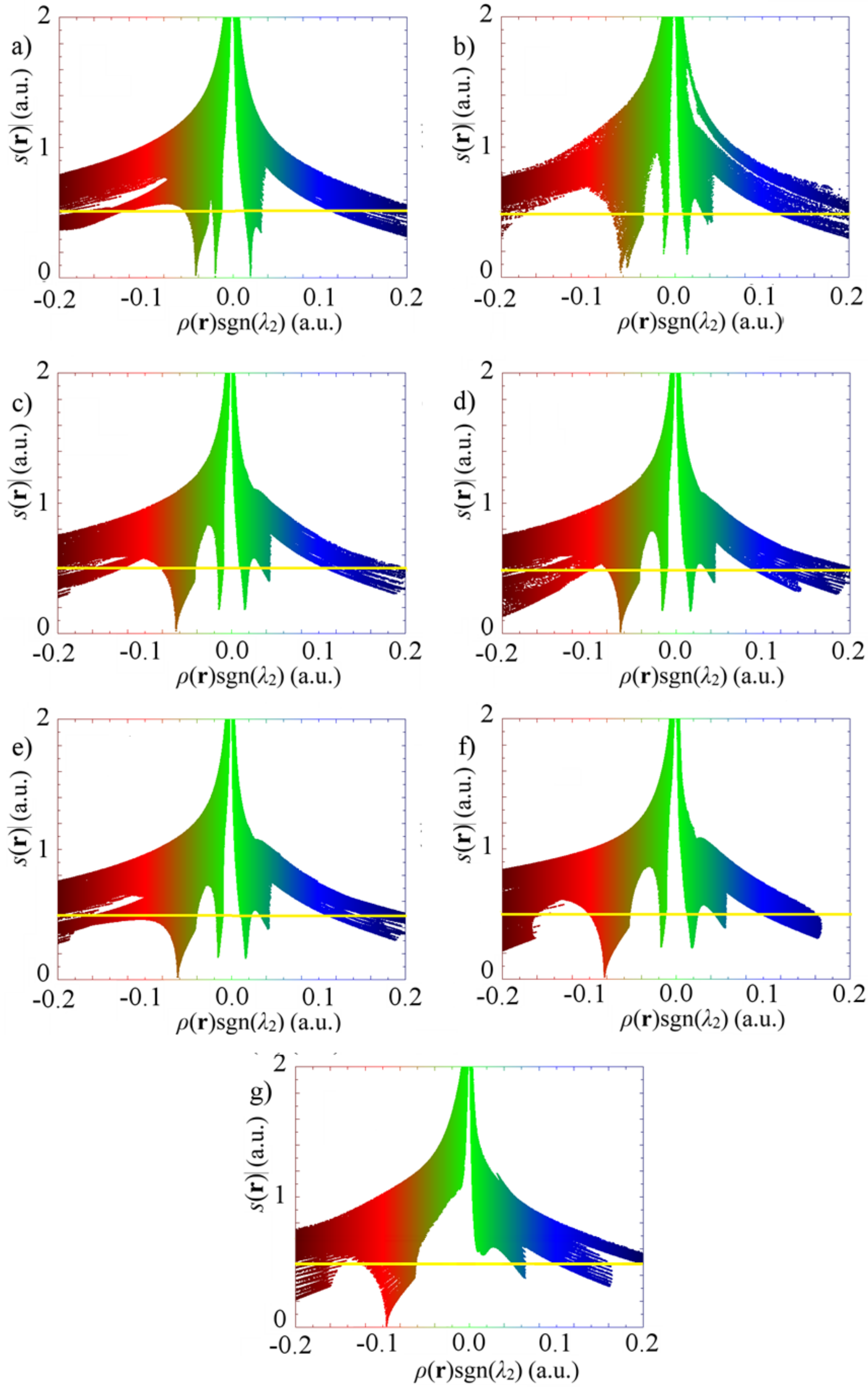

Figure 3.13: Analysis of the reduced density gradient (RDG) for a) $[UO_2(CO)_6]^{2+}$ b) $[UO_2(H_2O)_5]^{2+}$ c) $[UO_2(NC)_5]^{3-}$ d) $[UO_2(NCS)_5]^{3-}$ e) $[UO_2(CN)_5]^{3-}$ f) $[UO_2F_5]^{3-}$ and G) $[UO_2(OH)_4]^{2-}$. Colour mapping is identical in all plots. Horizontal yellow lines at 0.5 a.u. correspond to the isosurface value in Figure 3.14.

Plots of RDG against $\rho(\boldsymbol{r})\mathrm{sgn}(\lambda_2)$ are given in Figure 3.13. Understanding of these can be aided by spatial visualisation of the regions in which these interactions occur, achieved by plotting the $s(\boldsymbol{r})$ isosurface, as seen in Figure 3.14. The isosurfaces in Figure 3.14 have been colour mapped with values of $\rho(\boldsymbol{r})\mathrm{sgn}(\lambda_2)$, differentiating attractive interactions from repulsive interactions. For clarity, isosurfaces of the reduced density gradient associated with the atom centres have been manually deleted.

Three complexes have been selected for in-depth study: the weakly bound carbonyl complex; the isocyano complex; and the strongly bound fluoro complex. The $s(\mathbf{r})$ isosurface of the carbonyl complex (Figure 3.14(a)) reveals a region of spatially extended weak attraction surrounding the uranium centre corresponding to the two spikes in Figure 3.13(a) at negative values of $\rho(\boldsymbol{r})\mathrm{sgn}(\lambda_2)$. The spike at $\rho(\boldsymbol{r})\mathrm{sgn}(\lambda_2)$ $\approx$ -0.04 a.u. defines a set of annular attractive regions at the U-C bond centres. The spike occurring at positive $\rho(\boldsymbol{r})\mathrm{sgn}(\lambda_2)$ defines a weak repulsive annular area around each of these attractive regions.

Next, examining the $s(\boldsymbol{r})$ isosurface of the isocyano complex (Figure 3.14(e)), a stronger and more directed attractive interaction is revealed, occurring at the U-N bond centres. This is characterised by a broader spike at a more negative value of $\rho(\boldsymbol{r})\mathrm{sgn}(\lambda_2)$, $\approx$ -0.06 a.u. (Figure 3.13(e)). The spike at ~ -0.02 a.u. defines a set of weaker attractive regions between neighbouring cyanide ligands and, as before, the spike at ~ 0.02 a.u. defines a set of annular areas around each of the U-N bonding regions.

Finally, the fluoro complex continues the trend: the region defining the U-F bonding interactions is again broader and occurs at a more negative value of $\rho(\boldsymbol{r})\mathrm{sgn}(\lambda_2)$ $\approx$ -0.10 a.u., indicating an interaction with a greater degree of covalency, whereas the extent of inter-ligand attractive region continues to reduce (Figure 3.14(g)). The repulsive spike (Figure 3.13(g)) again defines a series of annular areas around the U-F bonding regions.

Additionally, it can be noted that the similarities apparent when considering the RDG isosurfaces of the cyano, isocyano and thiocyanate complexes reflect the similarities these complexes share in other properties. Similarly, the annular regions of the RDG isosurface centred on the U-O_L bond of the hydroxo complex are reminiscent of those centred on the U-F bond of the fluoro complex.

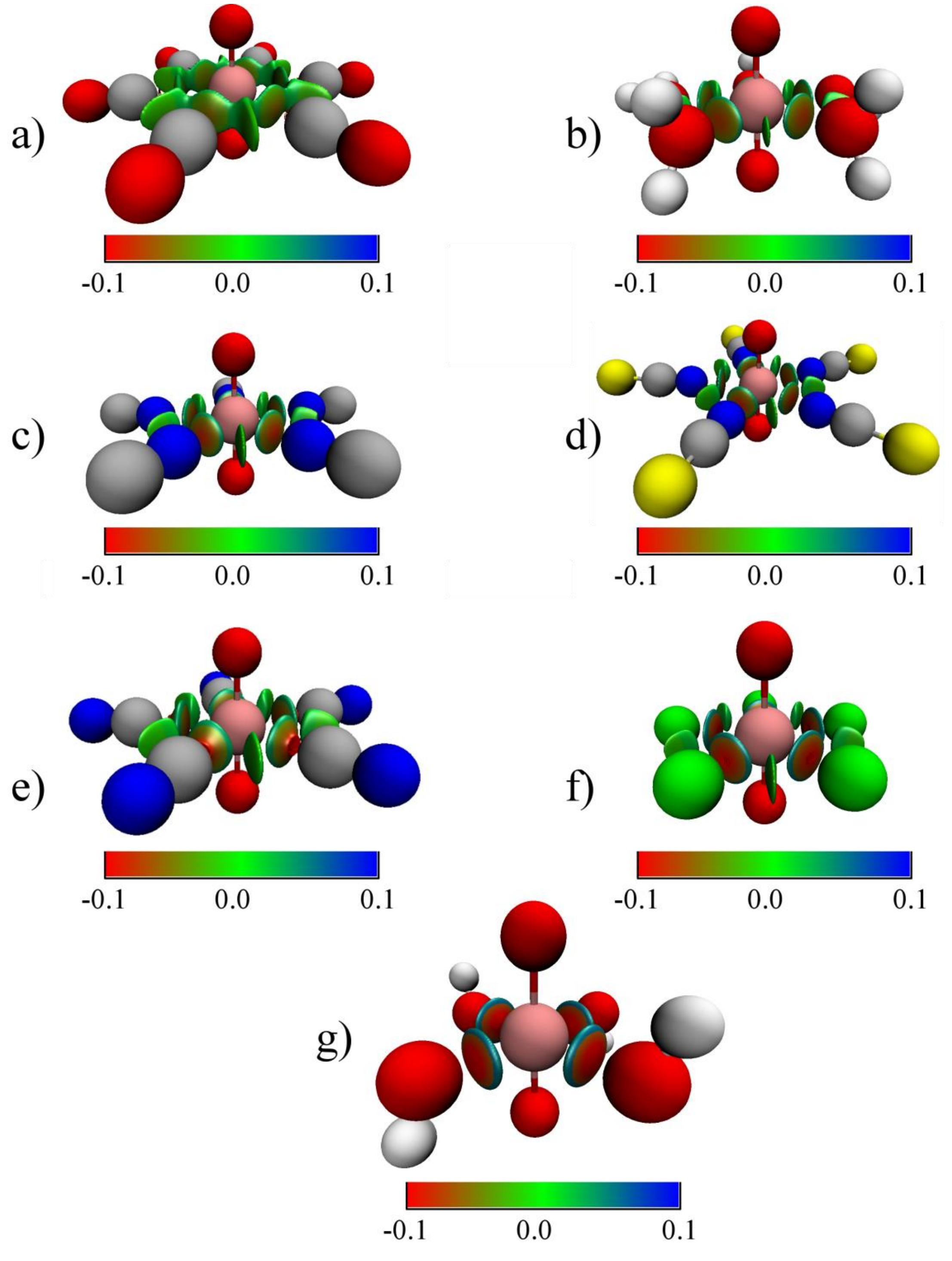

Figure 3.14: Isosurfaces of the RDG, rendered at 0.5 a.u., colour mapped with values of $\rho(\boldsymbol{r})\mathrm{sgn}(\lambda_2)$.

3.5. Summary and Conclusions

The effects of equatorial ligation on the U-O_{yl} bond of uranyl have been investigated using DFT. The U-O_{yl} stretch vibrational frequencies, which are known to be sensitive probes of the equatorial coordination environment, are demonstrated to have a strong correlation with the strength of equatorial bonding.

This relationship has been investigated using a series of density based analytical approaches, all of which are based on interrogation of the physically observable electron density. The qualitative effects of equatorial ligation were investigated using plots of electron density differences upon complexation. These demonstrated an intuitive description of the bonding process: as equatorial bond strength increased, so density was transferred from the U-O_{yl} bonding region, implying a reduction in the covalent character of the bond. The charge was transferred partly onto the *–yl* oxygens, but also into the equatorial bonding region, indicating an increase in equatorial covalency.

In order to quantify the variation deduced from density difference plots, the quantum theory of atoms in molecules (QTAIM) was employed. This approach allowed quantitative investigation of both the topological and integrated properties of the electron density, and strongly supported the qualitative description discussed above. Two key conclusions could be drawn from the QTAIM analysis: firstly, the redistribution of charge could not be fully understood by considering only one-electron integrated properties, *i.e.* the atomic electron populations. The localisation and delocalisation indices, both two-electron properties, were required in order to fully comprehend this. The indices revealed a reduction in U-O_{yl} electron sharing, along with an increase in electron localisation on the O_{yl} centres, upon stronger equatorial complexation. This demonstrated a transition from covalent to more ionic bonding character in the U-O_{yl} bond, as well a contribution from the uranium centre to equatorial bond covalency. Secondly, and more importantly, QTAIM analysis demonstrated, for the first time, a strong correlation between U-O_{yl} vibrational frequencies and equatorial bond covalency. This correlation allows for the experimental probing of this covalency *via* UV-vis and Raman spectroscopies. Topological and qualitative analysis of the fluoride complex supports a conclusion of equatorial covalency, which is in conflict with previous work[56]. However, this conclusion is supported by analysis of the electronic structure *via* one- and two-electron integrated properties.

Next, the electron localisation function (ELF) was used to probe the electron density. However, no correlation was found between properties of the ELF and bonding character/strength. Finally, attention was turned to analysis of the reduced density gradient (RDG), which has previously been used to investigate regions of weak interaction as might be found in the equatorial bonds of these complexes. This analysis demonstrated a concentration and increased directionality of the bonding interaction as equatorial binding increased, as revealed in isosurface plots of the RDG. These plots bear a qualitative similarity to those of electron density accumulation in the equatorial bonding region, and support the findings of our energetic and QTAIM analyses. This reaffirms the utility of the density difference plots as a simple visual depiction of bonding character which can be supported by quantitative analysis of the electron density.

In summary, it has been demonstrated in this chapter that a deep understanding of bonding can be obtained from combined analyses of the electron density. Furthermore, quantitative data from these analyses has been correlated with experimentally accessible measures. Strong correlation suggests that this approach will be of use when applied to more complex systems and could be used predictively in order to better understand environments in which experimental probes are impractical: in particular, potential application in developing a better understanding of actinide complexation in environments in which spent nuclear fuel is stored.

3.6. Publication Notes

Work from this chapter was published in:

Poppy Di Pietro and Andrew Kerridge, "U-O_{yl} stretching vibrations as a quantitative measure of equatorial bond covalency in uranyl complexes", *Inorganic Chemistry,* **2016** (Ref [381])**.**

4. Results: Density Based Measures of Bonding in Multidentate Complexes of Uranyl: Assessing Covalency in U-N Bonds.

4.1. Introduction

Chapter 3 focussed on characterising the bonding between a series of monodentate first row ligands and uranyl using various density based analysis methods. This chapter applies those same analytical methods to characterise the U-N and U-O bonding in two multidentate complexes: a complex of uranyl with two tridentate bis-triazinyl-pyridine (BTP) ligands, $[UO_2(BTP)_2]^{2+}$ and a complex of uranyl with the macrocyclic hexadentate expanded porphyrin ligand, hexaphyrin(1.0.1.0.0.0), commonly known as isoamethyrin (IA), UO_2-isoamethyrin (UO_2IA). In both of these experimentally realised[31,133] complexes, the uranyl unit is equatorially coordinated *via* six nitrogen donor atoms. Uranyl complexes with multidentate and macrocyclic ligands have many uses, from the Pacman complexes allowing access to unusual and novel chemistry[29], to crown ethers as potential extractants for uranyl[28].

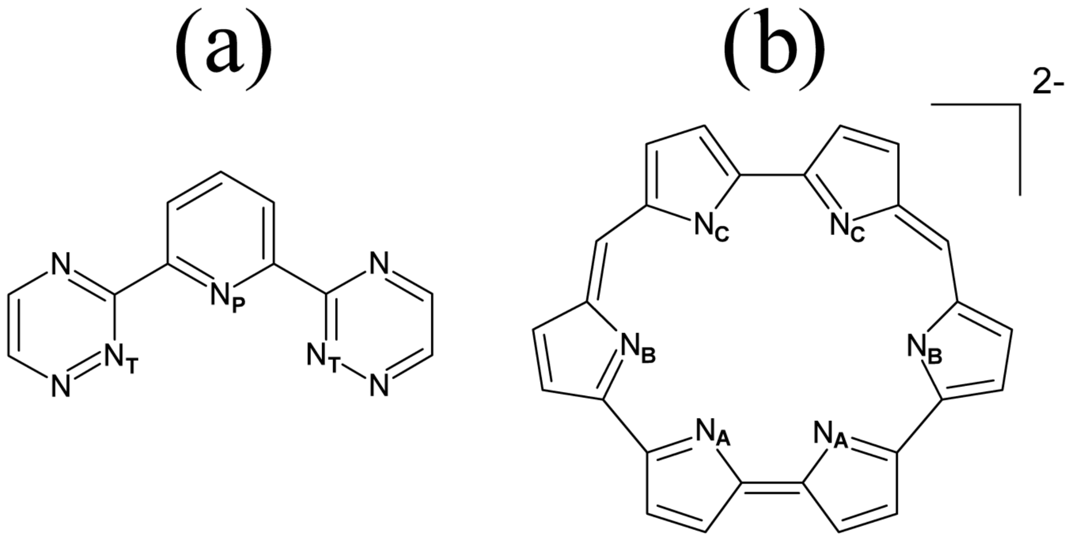

Figure 4.1: Molecular structure of (a) BTP and (b) the isoamethyrin dianion, the two ligands considered in this chapter. Symmetry-distinct coordinating nitrogens are labelled. Reproduced from Di Pietro and Kerridge, "Assessing covalency in equatorial U – N bonds : density based measures of bonding in BTP and isoamethyrin complexes of uranyl" *PCCP*, June 2016.

Schematics for the two ligands are shown in Figure 4.1. Isoamethyrin has previously been demonstrated to coordinate uranyl, neptunyl and plutonyl cations[35,133], suggesting its use as a potential colourimetric sensor for actinides in aqueous environments, while BTP has been demonstrated to coordinate uranyl as well as several minor actinides, for which it displays selectivity over the lanthanides. It was intended that, by examining in detail the electronic structure of uranyl as one moves from coordination by monodentate ligands[396] to coordination by multidentate and macrocyclic ligands, the effect the equatorial coordination environment has on the uranyl unit could be better understood. Additionally, the potential of isoamethyrin as an example system for investigating the coordination of uranium by nitrogen donor ligands was considered.

Although the electronic structure of uranyl, with its formally empty 5f-shell, will differ significantly from that of the later actinides, it is proposed in this chapter that if the U-N bonding in UO_2IA is of similar character to that in $[UO_2(BTP)_2]^{2+}$, then there is scope for future investigations of IA as a potential separation ligand for the trivalent minor actinides.

Here, the Quantum Theory of Atoms in Molecules (QTAIM)[348] is employed, with the aim being to focus solely on properties of the experimentally observable electron density, thus avoiding the ambiguity which can occur as a result of using orbital-based methods for characterising bonding in actinide complexes[49]. QTAIM analysis is described more completely in the Methodology section (Chapter 2.9.1), and in several published resources[347,348]. Here, it is sufficient to say that relevant properties of the bond critical point (BCP) are analysed and compared. Bond critical points are found when the bond path, the uniquely defined line of maximum density between two atoms has its minimum at the interatomic surface joining the two atomic basins[346]. The nature of the bond is then characterised by the values of the electron density, its Laplacian and the energy density at the BCP, with the general rule of thumb being that increasing values of ρ_{BCP} indicate increasing covalent character within a bond. Additionally, one- and two-electron properties are integrated over their respective basins, yielding information about the localisation and delocalisation of electrons.

QTAIM analysis is complemented with studies of the Electron Localisation Function (ELF)[397] and the reduced density gradient (RDG), both described in the Methodology section (Chapter 2.9.2 and 2.9.3, respectively). These results are compared to qualitative data from explicit electron density difference distributions resulting from complexation.

5.2. Computational Details

All molecular geometries were optimised at the density functional theoretical (DFT) level using version 6.4 of the TURBOMOLE quantum-chemical software package[359], employing the Ahlrichs basis sets[369] of polarised triple-zeta quality: def2-TZVP (H, C, N) and def-TZVP (U). For U, 60 core electrons were replaced with a Stuttgart-Dresden-Bonn relativistic effective core potential[285,318]. Analytical and numerical frequency analysis was performed in order to confirm the optimized structures as local energetic minima[i]. Subsequently, all-electron single point energy calculations were performed, replacing the def-TZVP basis set and RECP on the uranium centre with the corresponding segmented all-electron relativistically contracted (SARC) basis set[370] of polarised triple-zeta quality, and accounting for relativistic effects with the Douglas-Kroll-Hess Hamiltonian[371,372]. Initial optimisations were performed using the PBE functional[333] based on the generalised gradient approximation (GGA), and the effect of including exact exchange was investigated *via* subsequent reoptimisations using the popular hybrid-GGA functional, B3LYP[373,374]. Both of these functionals were used successfully in the previous chapter. The COSMO continuum solvation model[360] was used to incorporate solvation effects using a relative permittivity of 8.9 to simulate solvation in dichloromethane, in which the UO_2IA complexes of Sessler *et al*. were synthesised. The all-electron densities were employed in the QTAIM analysis, performed using the AIMAll code[364]. ELF and RDG analysis were performed using version 3.3.6 of the Multiwfn code[363], which was also employed in order to generate density difference data. RDG, ELF and density difference data were visualised using the VMD code[365].

---

[i] Frequency analysis was not performed on the UO_2IA' complex when using the B3LYP *xc*-functional due to significant computational expense.

5.3. Results and Discussion

5.3.1 Structural Characterisation

Figure 5.2 shows the gas phase molecular geometries of the three systems, optimised using the PBE functional. In good agreement with crystallographic data[31], $[UO_2BTP_2]^{2+}$ was found to be non-planar, optimising to a structure with two distinct U-N bond lengths and C_{2h} symmetry. In this case, non-planarity arises as a result of ligand-ligand repulsion[31].

The calculated structure for UO_2IA was found to deviate significantly from the structure derived from crystallographic data[133], optimising to a planar structure with C_{2v} symmetry, three distinct U-N bond lengths and the uranium ion sitting slightly off-centre. Reoptimising with the B3LYP functional revealed these same qualitative characteristics.

Omission of peripheral alkyl substituents is a relatively common simplification in theoretical chemistry, however in the case of UO_2IA, this omission results in significant deviations from the experimentally characterised complex, an alkyl substituted derivative of IA, which exhibits a non-planar geometry resulting in significant reduction in U-N bond-length when compared to the simplified optimised structure[150], with this difference being most pronounced for the longer U-N_B and U-N_C bonds (Figure 4.1).

The theoretical bond lengths obtained here for unsubstituted UO_2IA are, however, in excellent agreement with those obtained previously at the same level of theory[150]. In this previous study, the presence of alkyl substituents was found to be vital to inducing the non-planar structure observed experimentally. It is believed that this is due to the macrocyclic core being somewhat too large for the uranyl unit.

The stability gained by this formally Hückel aromatic system adopting a planar geometry is presumably smaller than that gained by the distortion of the ligand, which minimises steric effects among the alkyl groups and allows shorter, stronger U-N bonds to form. Reintroducing the alkyl groups, generating the complex hereby referred to as UO_2IA', and reoptimising without symmetry constraints resulted in a non-planar structure and improved agreement of U-N bond lengths with those found experimentally.

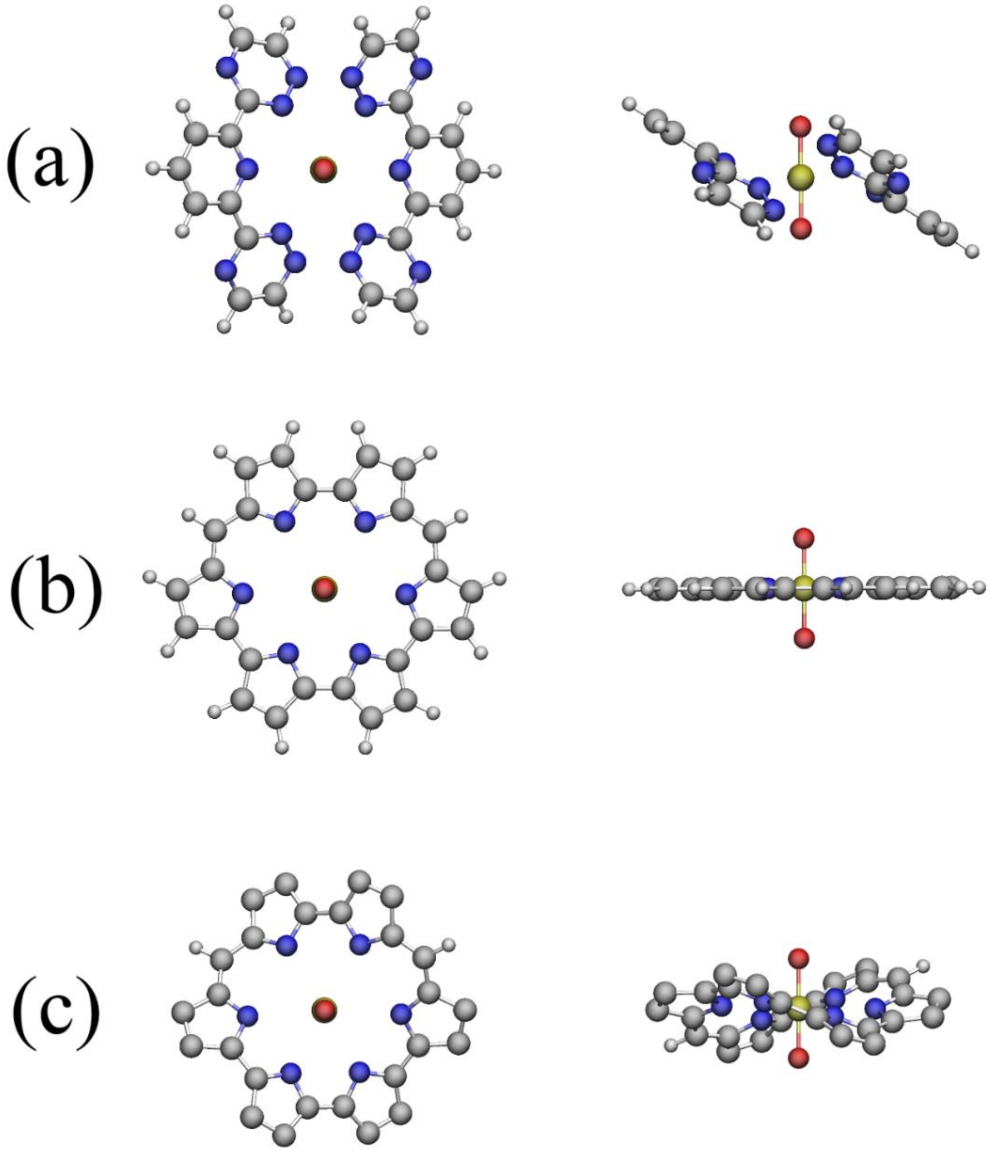

Figure 4.2: Top- and side-views of PBE-optimised gas-phase structures of (a) $[UO_2BTP_2]^{2+}$, (b) UO_2IA and (c) UO_2IA'. For clarity, substituents have been omitted from (c). U = yellow, O = red, N = blue, C = grey, H = white. Reproduced from Di Pietro and Kerridge, "Assessing covalency in equatorial U – N bonds: density based measures of bonding in BTP and isoamethyrin complexes of uranyl" *PCCP*, June 2016.

Table 4.1 contains U-O and U-N bond lengths for UO_2IA, UO_2IA' and $[UO_2BTP_2]^{2+}$. Calculated U-O bond lengths are in good agreement with experimental values.In the gas phase, these show an elongation of ~0.07 Å (~0.06 Å) compared to uncoordinated uranyl when the PBE (B3LYP) functional is employed. This elongation was also seen in the previous chapter, and in the literature relating to uranyl coordination[85,91,95,96], and indicates a weakening of the U-O bond. Its causes will be investigated in subsequent sections.

		PBE		B3LYP		Exp[a,b]	PBE/TZP[c]
		GP	DCM	GP	DCM		
$[UO_2(BTP)_2]^{2+}$	U-O	1.778	1.786	1.756	1.764	1.758	-
	U-N$_T$	2.634	2.612	2.657	2.635	2.565	-
	U-N$_P$	2.655	2.636	2.676	2.656	2.602	-
	$\overline{\text{U-N}}$	2.641	2.62	2.663	2.642	2.577	-
UO_2IA	U-O	1.777	1.787	1.758	1.767	-	1.79
	U-N$_A$	2.625	2.614	2.633	2.619	-	2.627
	U-N$_B$	2.915	2.908	2.91	2.903	-	2.906
	U-N$_C$	2.799	2.792	2.796	2.788	-	2.786
	$\overline{\text{U-N}}$	2.78	2.771	2.78	2.770	-	2.773
UO_2IA'	U-O	1.787	1.799	1.766	1.777	1.760	1.799
	U-N$_A$	2.586, 2.587	2.573, 2.573	2.602, 2.586	2.586	2.566	2.590
	U-N$_B$	2.772, 2.765	2.702, 2.693	2.790, 2.785	2.773, 2.766	2.677	2.773
	U-N$_C$	2.713, 2.705	2.755, 2.747	2.726, 2.724	2.716, 2.710	2.644	2.714
	$\overline{\text{U-N}}$	2.688	2.674	2.704	2.689	2.631	2.692

Table 4.1: Comparison of U-O and U-N bond lengths (in Å) with experimental values and previous work. [a] ref [31] (averaged values), [b] ref [190],[c] ref [150].

In the case of $[UO_2(BTP)_2]^{2+}$, there is a slight overestimation of U-N bond lengths, which are ~0.07 Å (~0.09 Å) longer than experimental values when employing the PBE (B3LYP) functional in the gas phase. Solvation improves this agreement with experiment, reducing the calculated difference by 20-40%, to ~0.04 Å (~0.07 Å) when using the PBE (B3LYP) functional. Overall though, there is good agreement with crystallographic data for this complex, demonstrating that the different model chemistries employed here are capable of adequately modelling the relevant uranyl-ligand interactions. However, as previously mentioned, the overestimation of U-N bonds lengths in UO_2IA are far more significant, with bonds of up to 0.24 Å (0.23 Å) longer than the crystallographic data found at the PBE (B3LYP) level of theory. Accounting for the effects of solvation reduces this overestimation slightly, to 0.23 Å (0.23 Å) at the PBE (B3LYP) level of theory, and also introduces a very slight degree of non-planarity in the IA complex, but in general, solvation made no substantial qualitative difference to any complex considered here. In both simplified and substituted isoamethyrin, the shortest U-N bonds occur when the pyrrole unit lacks any meso-carbon bridging. It appears that these meso-carbons give flexibility to the macrocycle, allowing the 2-2-bipyrrole subunit which incorporates the N_C-donors to approach closer than the groups which incorporate the N_B-donors: it is these which exhibit maximum deviation from the experimental value. Replacing the peripheral alkyl substituents to form UO_2IA′ causes a distortion of the ligand from planarity, allowing all U-N bonds to shorten. There are six distinct U-N bond lengths present in the optimised structure of this low symmetry distorted complex, although it remains the case that the shortest U-N bonds occur when the pyrrole unit lacks meso-carbon bridges. The U-N_A bonds are shortened by around 0.04 Å (0.03 Å) with the PBE (B3LYP) functional when compared to the UO_2IA complex, bringing them into good agreement with the experimental bond length of 2.566 Å. The most significant change is to the U-N_B bonds, which are reduced by up to 0.15 Å (0.11 Å) with the PBE (B3LYP) functional, bringing them into better agreement with the experimental values of 2.677 Å, although there remains an overestimation of up to ~0.10 Å (~0.13 Å). Inclusion of the peripheral alkyl groups improves the overall agreement with experiment, however, the overestimation of the U-O bond length is slightly increased, by ~0.01 Å (~0.02 Å) with the PBE (B3LYP) functional in the gas phase. It is the case for all complexes investigated here that geometries obtained using the PBE *xc*-

functional have slightly better agreement with experiment than those obtained with B3LYP.

4.3.2. Analysis with the Quantum Theory of Atoms in Molecules

The electronic structure of the complexes considered in this chapter has been investigated in detail using the Quantum Theory of Atoms in Molecules to probe the electron density. Tables 4.2 presents various properties of the electron density at the U-O bond critical points (BCPs), as well as delocalisation indices for both the PBE and the B3LYP *xc*-functional in the gas phase, and Table 4.3 presents the same properties for the solvated structures. Looking first at the U-O bonds, it can be seen that the large values of ρ and large negative values of the energy density, *H*, found at the U-O BCP in $[UO_2(BTP_2)]^{2+}$, UO_2IA and UO_2IA' complexes are indicative of a typical covalent interaction (although the fact that $\nabla^2\rho_{\mathbf{BCP}}$ is positive is atypical of a covalent bond within the QTAIM definition), as has been found previously[394,396].

Further support for this comes from the high degree of electron delocalisation between the U and O ions. The strong similarity of the topological properties considered here, in addition to the very similar bond lengths presented in Table 4.1, allow a prediction that the equatorial coordination environments of $[UO_2BTP_2]^{2+}$, UO_2IA and UO_2IA' may be comparable to one another.

Gas phase data		$[UO_2(BTP)_2]^{2+}$	UO_2IA	UO_2IA'
ρ_{BCP}	PBE	0.307	0.307	0.299
	B3LYP	0.325	0.323	0.317
$\nabla^2\rho_{BCP}$	PBE	0.314	0.314	0.315
	B3LYP	0.264	0.263	0.265
H_{BCP}	PBE	-0.283	-0.283	-0.270
	B3LYP	-0.318	-0.263	-0.303
δ(U,O)	PBE	1.992	2.011	1.971
	B3LYP	1.961	1.968	1.936*

Table 4.2: QTAIM–derived properties of the U-O bond of the three complexes considered in this study, derived from the gas phase electron densities obtained using both *xc*-functionals, PBE and B3LYP. ρ_{BCP} = electron density at BCP. $\nabla^2\rho_{BCP}$ = Laplacian of ρ_{BCP}. H_{BCP} = Energy density at BCP. δ(U,O) = delocalisation index between U and O centres. All reported quantities are in atomic units. * Average over both U-O bonds.

Solvated data		$[UO_2(BTP)_2]^{2+}$	UO_2IA	UO_2IA'
ρ_{BCP}	PBE	0.300	0.299	0.290
	B3LYP	0.318	0.316	0.308
$\nabla^2\rho_{\mathrm{BCP}}$	PBE	0.317	0.314	0.316
	B3LYP	0.268	0.264	0.267
H_{BCP}	PBE	-0.270	-0.270	-0.254
	B3LYP	-0.306	-0.302	-0.287
δ(U,O)	PBE	1.961	1.976	1.928*
	B3LYP	1.932	1.937	1.897*

Table 4.3: QTAIM–derived properties of the U-O bond of the three complexes considered in this study, derived from solvated electron densities obtained using both *xc*-functionals, PBE and B3LYP. All reported quantities are in atomic units. * Average over both U-O bonds.

Tables 4.4 and 4.5 present various topological properties of the U-N bond critical points, with Table 4.4 containing the gas phase data for both functionals, and Table 4.5 containing the solvated data. When the U-N bonds are considered, it is found that, as expected, values of ρ_{BCP} are significantly lower than for the U-O bonds in all complexes.

Gas phase data		$[UO_2(BTP)_2]^{2+}$		UO_2IA			UO_2IA'		
		U-N_T	U-N_P	U-N_A	U-N_B	U-N_C	U-N_A	U-N_B	U-N_C
ρ_{BCP}	PBE	0.048	0.045	0.049	0.026	0.034	0.052, 0.052	0.035, 0.036	0.039, 0.400
	B3LYP	0.045	0.043	0.048	0.026	0.033	0.050, 0.050	0.034, 0.034	0.038, 0.039
$\nabla^2\rho_{\mathrm{BCP}}$	PBE	0.117	0.113	0.117	0.065	0.081	0.128, 0.129	0.088, 0.089	0.099, 0.100
	B3LYP	0.116	0.111	0.118	0.068	0.085	0.127, 0.128	0.087, 0.088	0.099, 0.100
H_{BCP}	PBE	-0.005	-0.004	-0.005	-0.000	-0.002	-0.005, -0.005	-0.002, -0.002	-0.002, -0.003
	B3LYP	-0.004	-0.003	-0.004	-0.000	-0.002	-0.005, -0.005	-0.001, -0.001	-0.002, -0.002
δ(U,N)	PBE	0.305	0.290	0.348	0.221	0.264	0.354, 0.352	0.268, 0.272	0.283, 0.290
	B3LYP	0.272	0.262	0.313	0.198	0.241	0.318, 0.317	0.238, 0.240	0.256, 0.260

Table 4.4: QTAIM–derived properties of the U-N bond of the three complexes considered in this study derived from gas phase electron densities obtained using both functionals. ρ_{BCP} = electron density at BCP. $\nabla^2\rho_{\mathrm{BCP}}$ = Laplacian of ρ_{BCP}. H_{BCP} = Energy density at BCP. δ(U,N) = delocalisation index between U and N centres. All reported quantities are in atomic units (a.u.).

The small magnitude of ρ_{BCP} and the near-zero (but negative) energy densities, indicate that the U-N interactions are chiefly of ionic character, as might be expected, with an amount of electron sharing which is of similar character between complexes. Shorter U-N bonds are found to correspond to larger values of ρ_{BCP} and greater degrees of electron sharing. This is supportive of the intuitive view that shorter, stronger bonds exhibit a greater degree of covalency. When the U-N bonds of IA and IA′ are considered, differences in the QTAIM and structural parameters due to choice of *xc*-functional or inclusion of solvation effects are minor compared to the effects induced by inclusion of peripheral alkyl substituents

Solvated data		$[UO_2(BTP)_2]^{2+}$		UO_2IA			UO_2IA'		
		U-N$_T$	U-N$_P$	U-N$_A$	U-N$_B$	U-N$_C$	U-N$_A$	U-N$_B$	U-N$_C$
ρ_{BCP}	PBE	0.050	0.047	0.050	0.027	0.034	0.054, 0.054	0.041, 0.037	0.037, 0.042
	B3LYP	0.047	0.045	0.049	0.026	0.034	0.052, 0.052	0.035, 0.036	0.039, 0.040
$\nabla^2\rho_{\mathrm{BCP}}$	PBE	0.121	0.116	0.118	0.066	0.081	0.130, 0.131	0.100, 0.092	0.090, 0.100
	B3LYP	0.120	0.115	0.120	0.068	0.085	0.130, 0.130	0.089, 0.090	0.100, 0.101
H_{BCP}	PBE	-0.005	-0.004	-0.005	-0.001	-0.002	-0.006, -0.006	-0.003, -0.002	-0.002, -0.003
	B3LYP	-0.005	-0.004	-0.005	-0.000	-0.002	-0.006, -0.006	-0.002, -0.002	-0.003, -0.003
δ(U,N)	PBE	0.318	0.303	0.367	0.233	0.276	0.375, 0.371	0.286, 0.290	0.296, 0.304
	B3LYP	0.284	0.273	0.330	0.207	0.251	0.337, 0.335	0.253, 0.257	0.267, 0.273

Table 4.5: QTAIM–derived properties of the U-N bond of the three complexes considered in this study derived from complexes optimised with both functionals with the inclusion of solvation effects. All reported quantities are in atomic units.

Choice of functional appears to have consistent, small, but non-negligible effects on the QTAIM parameters. When B3LYP is used, there is an appreciable increase in ρ_{BCP} in the U-O bond of all complexes, and a small reduction in delocalisation. There is a small reduction in all properties measured at the U-N BCPs with B3LYP compared to PBE. The implication here is that B3LYP, comprising a proportion of exact Hartree-Fock exchange, leads to increased electron localisation as has been seen previously[61]. The effect of solvation on the topological parameters amounts to a slight reduction in the amount of electron sharing in the U-O interaction compared to the gas phase, with a commensurate minor increase in electron sharing in the U-N bonds.

The U-O bond is seen to lengthen upon complexation in all cases. This implies that whilst the U-N interaction is weak, with a small covalent component, there is a non-negligible effect on the U-O interaction. This effect can be further investigated by considering QTAIM parameters of the isolated uranyl unit and comparing them to those of the uranyl unit after complexation. This data is presented in Tables 4.6, 4.7, 4.8 and 4.9 for the PBE structures optimised in the gas phase, the B3LYP structures optimised in the gas phase, the PBE structures optimised with DCM, and the B3LYP structures optimised with DCM, respectively. The two additional parameters defined in Chapter 3 are used to aid analysis of the changes that occur upon complexation:

$$N(\mathrm{UO_2}) = N(\mathrm{U}) + \sum_{i=1,2} N(\mathrm{O}_i) \qquad (Eq.4.1)$$

$$\lambda(\mathrm{UO_2}) = \lambda(\mathrm{U}) + \sum_{i=1,2} [\lambda \mathrm{O}_i + \delta(\mathrm{U},\mathrm{O}_i)] + \delta(\mathrm{O},\mathrm{O}) \qquad (Eq.4.2)$$

Where $N(\mathrm{UO_2})$ gives the uranyl electronic population (from which the charge $q(\mathrm{UO_2})$ can be derived) and $\lambda(\mathrm{UO_2})$ the number of electrons localised on the uranyl unit. In the case of isolated $\mathrm{UO_2^{2+}}$, $N(\mathrm{UO_2}) = \lambda(\mathrm{UO_2}) = 106$.

	$[\mathrm{UO_2(BTP)_2}]^{2+}$			$\mathrm{UO_2IA}$			$\mathrm{UO_2IA'}$		
	$\mathrm{UO_2^{2+}}$	Complex	Δ	$\mathrm{UO_2^{2+}}$	Complex	Δ	$\mathrm{UO_2^{2+}}$	Complex	Δ
$N(\mathrm{U})$	88.92	89.21	0.28	88.92	89.16	0.23	88.94	89.17	0.24
$N(\mathrm{O})$	8.54	8.81	0.27	8.54	8.83	0.29	8.53	8.85	0.31
$N(\mathrm{UO_2})$	106	106.82	0.82	106	106.81	0.81	106	106.86	0.86
$\lambda(\mathrm{U})$	86.61	86.14	-0.47	86.61	86.18	-0.43	86.62	86.14	-0.48
$\lambda(\mathrm{O})$	7.31	7.62	0.31	7.31	7.67	0.36	7.31*	7.69*	0.38
$\lambda(\mathrm{UO_2})$	106	105.47	-0.53	106	105.64	-0.36	106	105.56	-0.44
$\delta(\mathrm{U,O})$	2.32	1.99	-0.33	2.32	2.01	-0.31	2.32*	1.97*	-0.35

Table 4.6: QTAIM–derived properties of isolated and complexed uranyl. Isolated uranyl simulated at the complexed geometry. Δ gives the difference between isolated and complexed values. *Values averaged over both O centres. Properties derived from PBE/def(2)-TZVP densities. All quantities are in atomic units.

	$[UO_2(BTP)_2]^{2+}$			UO_2IA			UO_2IA'		
	UO_2^{2+}	Complex	Δ	UO_2^{2+}	Complex	Δ	UO_2^{2+}	Complex	Δ
$N(U)$	88.79	88.99	0.20	88.79	88.95	0.16	88.62	88.96	0.34
$N(O)$	8.61	8.85	0.25	8.61	8.87	0.27	8.69	8.89	0.20
$N(UO_2)$	106	106.70	0.70	106	106.69	0.69	106	106.74	0.74
$\lambda(U)$	86.52	86.09	-0.42	86.52	86.13	-0.39	86.44	86.09	-0.35
$\lambda(O)$	7.41	7.70	0.29	7.41	7.74	0.33	7.54*	7.76*	0.22
$\lambda(UO_2)$	106	105.51	-0.49	106	105.65	-0.35	106	105.59	-0.41
$\delta(U,O)$	2.27	1.96	-0.31	2.27	1.97	-0.30	2.18*	1.94*	-0.24

Table 4.7: QTAIM–derived properties of isolated and complexed uranyl. Isolated uranyl simulated at the complexed geometry. Δ gives the difference between isolated and complexed values. *Values averaged over both O centres. Properties derived from B3LYP/def(2)-TZVP/SARC-TZVP gas phase densities. All quantities are in atomic units.

	$[UO_2(BTP)_2]^{2+}$			UO_2IA			UO_2IA'		
	UO_2^{2+}	Complex	Δ	UO_2^{2+}	Complex	Δ	UO_2^{2+}	Complex	Δ
$N(U)$	88.76	89.21	0.45	88.75	89.16	0.41	88.77	89.18	0.41
$N(O)$	8.62	8.83	0.21	8.62	8.86	0.23	8.62	8.89	0.27
$N(UO_2)$	106	106.88	0.88	106	106.88	0.88	106	106.95	0.95
$\lambda(U)$	86.53	86.12	-0.41	86.52	86.16	-0.36	86.54	86.12	-0.42
$\lambda(O)$	7.44	7.66	0.23	7.44	7.71	0.27	7.43*	7.75*	0.31
$\lambda(UO_2)$	106	105.46	-0.54	106	105.65	-0.35	106	105.56	-0.44
$\delta(U,O)$	2.23	1.96	-0.27	2.23	1.98	-0.25	2.23*	1.93*	-0.30

Table 4.8: QTAIM–derived properties of isolated and complexed uranyl. Isolated uranyl simulated at the complexed geometry. Δ gives the difference between isolated and complexed values. *Values averaged over both O centres. Properties derived from PBE/def(2)-TZVP/SARC-TZVP solvated densities. All quantities are in atomic units.

	$[UO_2(BTP)_2]^{2+}$			UO_2IA			UO_2IA'		
	UO_2^{2+}	Complex	Δ	UO_2^{2+}	Complex	Δ	UO_2^{2+}	Complex	Δ
$N(U)$	88.62	88.99	0.37	88.62	88.95	0.33	88.63	88.96	0.33
$N(O)$	8.69	8.88	0.19	8.69	8.90	0.21	8.69	8.92	0.24
$N(UO_2)$	106	106.74	0.74	106	106.75	0.75	106	106.81	0.81
$\lambda(U)$	86.44	86.08	-0.36	86.44	86.11	-0.33	86.45	86.08	-0.38
$\lambda(O)$	7.54	7.73	0.19	7.54	7.78	0.24	7.54*	7.81*	0.27
$\lambda(UO_2)$	106	105.50	-0.50	106	105.65	-0.35	106	105.59	-0.41
$\delta(U,O)$	2.18	1.93	-0.25	2.18	1.94	-0.24	2.18*	1.90*	-0.28

Table 4.9: QTAIM–derived properties of isolated and complexed uranyl. Isolated uranyl simulated at the complexed geometry. Δ gives the difference between isolated and complexed values. *Values averaged over both O centres. Properties derived from B3LYP/def(2)-TZVP/SARC-TZVP solvated densities. All quantities are in atomic units.

The data in Tables 4.6 - 4.9 give further insight into the effect of equatorial complexation on U-O bonding, which can be summarised as in increase in the ionic interaction commensurate with a decrease in the covalent interaction. Looking first at the calculated differences in properties upon complexation, it can be seen that the three complexes exhibit strong qualitative similarities. The lengthening of the U-O bond upon complexation can be explained by three factors. Firstly, approximately 0.8 – 0.9 a.u of electronic charge for the PBE data and approximately 0.7-0.8 a.u for the B3LYP data, with these values being slightly greater when the effects of solvation are included, is donated onto the uranyl unit in each complex. This donated charge is split into approximately equal amounts (0.2 - 0.3 a.u.) which populate the uranium and each of the oxygen ions. This additional electronic charge on all ions reduces the electrostatic attraction between them, since the interaction is between a negative oxygen ion and a positive uranium. Secondly, the electronic localisation on each ion in the uranyl unit can be considered, to a first approximation, to dictate the degree of ionic interaction. In all complexes, electron localisation is observed to increase on each oxygen centre, while decreasing on the uranium centre, implying a more ionic U-O interaction upon complexation. Finally, a corresponding reduction in δ(U,O) upon complexation indicates a reduction in the covalent interaction. Combined, these factors explain the lengthening, and hence weakening, of the U-O interaction in the complexes.

Analysis of the quantities $N(UO_2)$ and $\lambda(UO_2)$ gives further insight into the U-N interactions upon complexation.. Whilst $N(UO_2)$ increases by approximately 0.8–0.9 a.u. upon complexation, $\lambda(UO_2)$ reduces to a value below that of the isolated dication. This reduction is more pronounced in the BTP complex (0.53 a.u. compared to 0.36 a.u. in UO_2IA and 0.44 a.u in UO_2IA′). This is consistent with the studies of uranyl coordination by nitrogen donors presented in Chapter 3. Since $\lambda(UO_2)$ takes into account U-O delocalisation, any differences between $N(UO_2)$ and $\lambda(UO_2)$ must therefore be due to electron sharing between the uranyl unit and the ligand, *i.e.* covalency in the U-N bonds. When considering the data derived from the electron density optimised using the PBE *xc*-functional in the gas phase, this difference is 1.35 a.u., 1.17 a.u. and 1.30 a.u. for the BTP, IA and IA′ complexes, respectively, suggesting a degree of electron sharing in the U-N bonds consistent with that indicated by the U-N topological QTAIM parameters ρ_{BCP} and H. Since the increase in electron localisation on the oxygen ions, λ(O), is approximately equal in magnitude but opposite in sign to the decrease in electron sharing in the U-O bond, δ(U,O) (+0.33 *vs* -0.33, +0.36 *vs* -0.31 and +0.38 *vs* -0.35 a.u. in the BTP, IA, and IA′ complexes, respectively), it can be concluded that the increase in λ(O) is almost exclusively due to donation from the U-O bond. The reduction in electron localisation on the uranium centre, λ(U), is therefore almost entirely due to electron sharing in the U-N bond. Put simply, the ~0.8-0.9 a.u. of charge donated upon complexation is almost entirely donated into the U-N bonds, and also induces a donation of ~ 0.4 - 0.5 a.u. of charge from the uranyl unit itself into the U-N bonds. This cannot be interpreted as 'traditional' back-bonding due to the formal $5f^0 6d^0$ occupation of U(VI), although there is still unambiguous evidence here of a significant contribution from the uranium atom to the equatorial U-N bonds.

4.3.3. Electron Localisation Function

The variation in U-N bond lengths combined with the previously discussed QTAIM parameters provides evidence of weak but non-negligible covalent interactions in the U-N bonds. These interactions are now investigated using the electron localisation function, $n(\boldsymbol{r})$. The Electron Localisation Function (ELF) is described in the Methodology Chapter 2.9.2. Analysis has been performed as in Chapter 3. Table 4.10 gives the values of $n(\boldsymbol{r})$ at the (3, -1) CPs for the U-N bonds of all complexes considered in this study and Figure 4.3 shows $n(\boldsymbol{r})$ evaluated at isosurfaces above and below these critical values, illustrating the bifurcation; the value at which one localisation domain splits into two or three.

Figure 4.3 shows that for $n(\mathbf{r})$ below the lowest value of n_C, the ELF surface consists of a single localisation domain. Above the highest value of n_C, bifurcation occurs, resulting in three ($[UO_2(BTP)_2]^{2+}$) or two (UO_2IA/UO_2IA') localisation domains, corresponding to the uranyl unit and the ligand(s). This indicates that in both complexes the U-N bonding region exhibits the lowest degree of electron sharing, as expected in the otherwise covalently bonded complexes. In the case of the isoamethyrin complex, bifurcation occurs at a very low value, due to the long, weak, U-N_B bond. Table 4.10 shows that the critical value associated with the U-N_T bond is marginally higher than that of the U-N$_P$ bond, suggesting higher electron delocalisation and therefore covalency.

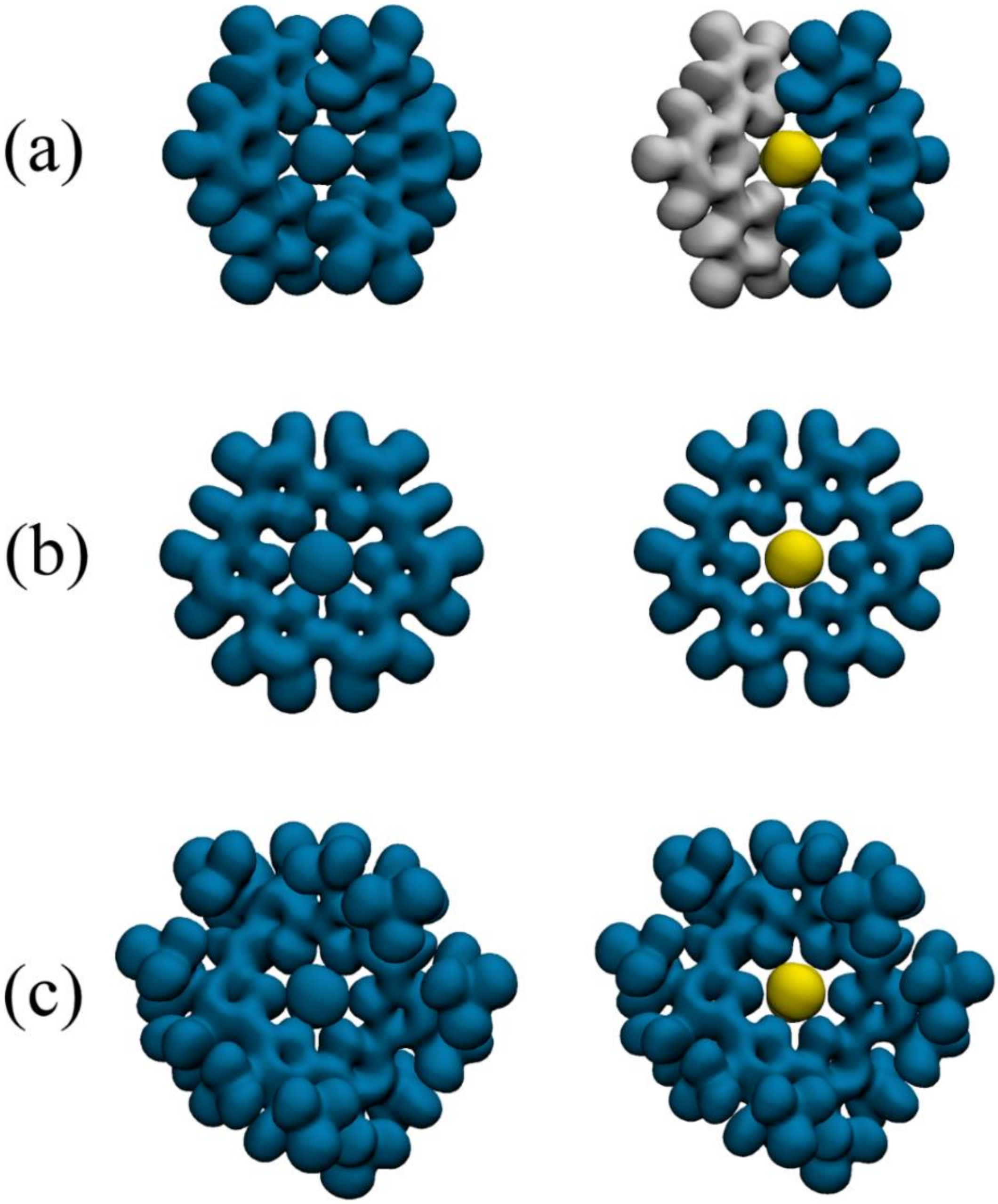

Figure 4.3: ELF isosurfaces of (a) ($[UO_2(BTP)_2]^{2+}$), visualised at $n(\mathbf{r}) = 0.17$ (left) and 0.24 (right), (b) UO_2IA, visualised at $n(\mathbf{r}) = 0.10$ (left) and 0.24 (right), (c) UO_2IA', visualised at $n(\mathbf{r}) = 0.14$ (left) and 0.24 (right). Distinct localisation domains are indicated by colour. Visualisations are of structures optimised using the PBE *xc*-functional in the gas phase. Reproduced from Di Pietro and Kerridge,, "Assessing covalency in equatorial U – N bonds: density based measures of bonding in BTP and isoamethyrin complexes of uranyl" *PCCP*, June 2016.

		$[UO_2(BTP)_2]^{2+}$		UO_2IA			UO_2IA'		
		U-N$_T$	U-N$_P$	U-N$_A$	U-N$_B$	U-N$_C$	U-N$_A$	U-N$_B$	U-N$_C$
Gas Phase	PBE	0.197	0.183	0.204	0.112	0.150	0.210, 0.209	0.149, 0.151	0.166, 0.170
	B3LYP	0.175	0.164	0.189	0.103	0.139	0.193, 0.193	0.134, 0.135	0.152, 0.154
DCM	PBE	0.208	0.193	0.214	0.117	0.157	0.219, 0.219	0.161, 0.158	0.179, 0.174
	B3LYP	0.185	0.174	0.200	0.109	0.146	0.205, 0.205	0.146, 0.143	0.163, 0.160

Table 4.10: Critical values of the ELF, n_C, calculated in the U-N bonding regions. Properties derived from PBE/def(2)-TZVP/SARC-TZVP and B3LYP/def(2)-TZVP/SARC-TZVP gas phase and solvated densities.

This is commensurate with the structural and QTAIM data, which show the U-N$_T$ bonds to be slightly shorter, with larger values of both ρ_{BCP} and δ(U,N), when compared to the U-N$_P$ bonds. The same behaviour is observed in UO_2IA and UO_2IA', although it is more pronounced for these complexes due to the larger differences between different U-N bonds. Here, the critical values associated with the U-N bonds are ordered as follows: U-N$_B$ < U-N$_C$ < U-N$_A$, in complete agreement with the structural and topological analyses, which show the U-N$_A$ (U-N$_B$) bonds to be shortest (longest) and most (least) covalent.

.

4.3.4. Analysis of the Reduced Density Gradient

Analysis of regions of weak interaction using the reduced density gradient has been performed for these three complexes. The theory underpinning this is explained more thoroughly in the Methodology (Chapter 2). The U-N interactions of the complexes considered here are largely ionic interactions with some covalent character, so it is expected that they will be indicated by the presence of such spikes. These plots can be complemented by visualisations of the $s(\boldsymbol{r})$ isosurface, revealing the spatial regions in which these interactions are taking place. Mapping $s(\boldsymbol{r})$ isosurfaces with values of $\rho(\boldsymbol{r})\mathrm{sgn}(\lambda_2)$ allows discrimination between attractive and repulsive interactions: sgn(x) is the signum function, returning -1 if $x < 0$ and 1 if $x > 0$, and λ_2 is the second largest eigenvalue of the Hessian of $\rho(\boldsymbol{r})$: λ_2 is typically negative (positive) for attractive (repulsive) interactions[345]. Scatter plots of $s(\boldsymbol{r})$ against $\rho(\boldsymbol{r})\mathrm{sgn}(\lambda_2)$ are given in Figure 4.4 for all complexes: the data are evaluated over the entire molecule and overlaid with higher fidelity data generated by focussing on the U-N bonding regions.

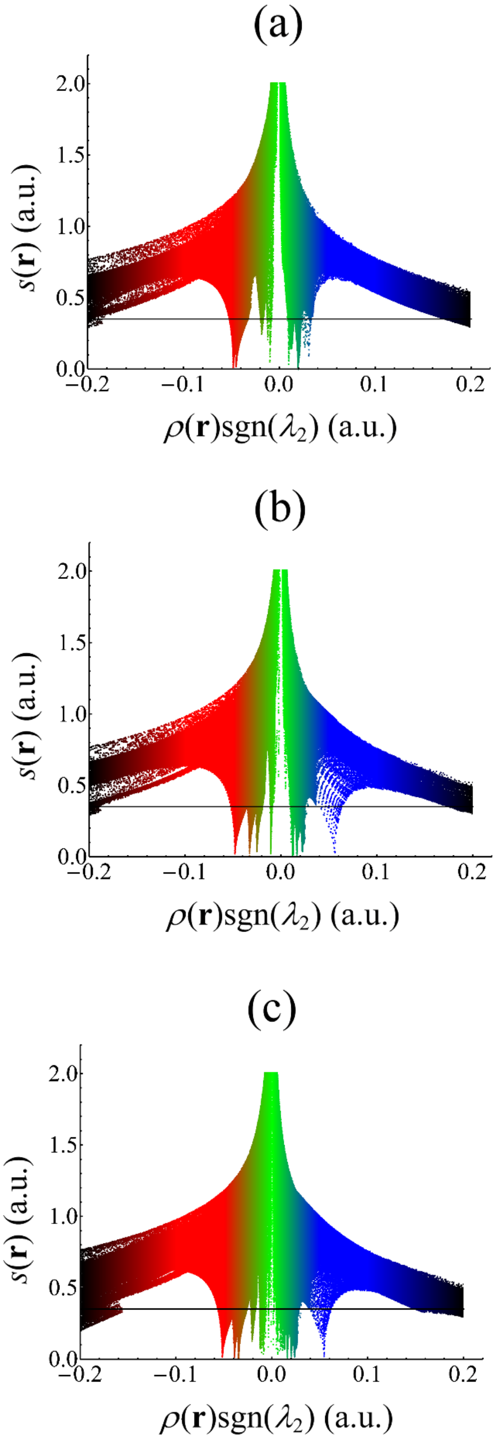

Figure 4.4: Scatter plots of $s(\mathbf{r})$ against $\rho(\boldsymbol{r})\mathrm{sgn}(\lambda_2)$in (a) $[UO_2(BTP)_2]^{2+}$, (b) UO_2IA and (c) UO_2IA′. Reproduced from Di Pietro and Kerridge, "Assessing covalency in equatorial U – N bonds: density based measures of bonding in BTP and isoamethyrin complexes of uranyl" *PCCP*, June 2016.

For all complexes, there are several points at which $s(\boldsymbol{r})$ falls to zero. Formally, these correspond to critical points in the electron density, which can be verified by comparing those occurring at negative values of $\rho(\boldsymbol{r})\mathrm{sgn}(\lambda_2)$ to the values of $\rho(\boldsymbol{r})$ at the U-N BCPs given in Table 4.3. $s(\boldsymbol{r})$ also falls to zero at $\rho(\boldsymbol{r})\mathrm{sgn}(\lambda_2)$ ~ -0.01 (a.u) and at small positive values indicating other weak interactions. The spatial regions associated with the interactions have been visualised by plotting isosurfaces of $s(\mathbf{r})$, colour-mapped with $\rho(\boldsymbol{r})\mathrm{sgn}(\lambda_2)$.

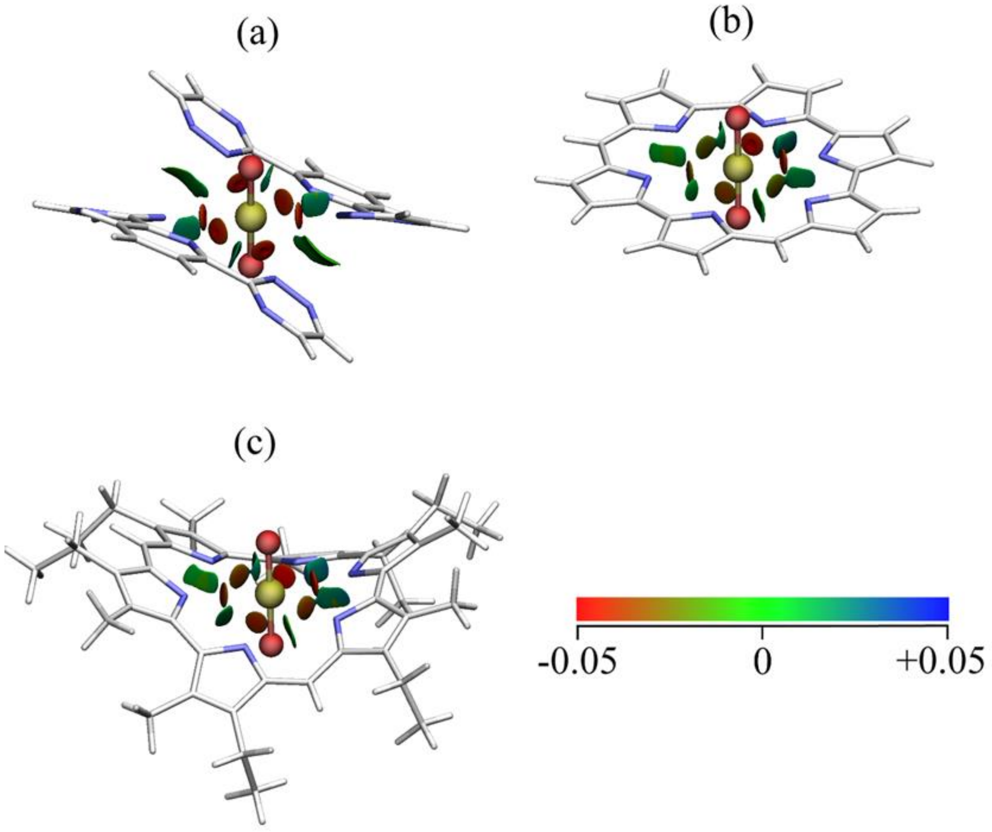

Figure 4.5: Isosurfaces of the reduced density gradient, $s(\boldsymbol{r})$, mapped with values of $\rho(\boldsymbol{r})\mathrm{sgn}(\lambda_2)$ for (a) $[UO_2(BTP)_2]^{2+}$, (b) UO_2IA and (c) UO_2IA'. Red regions indicate attractive interactions with weakly covalent character. Isosurfaces are rendered at $s(\boldsymbol{r}) = 0.35$ a.u., corresponding to the horizontal lines in Figure 4.4. Reproduced from Di Pietro and Kerridge, "Assessing covalency in equatorial U – N bonds: density based measures of bonding in BTP and isoamethyrin complexes of uranyl" *PCCP,* June 2016.

These isosurfaces can be seen in Figure 4.5. As would be expected, the red regions, associated with the zeroes of $s(\boldsymbol{r})$ and negative values of $\rho(\boldsymbol{r})\mathrm{sgn}(\lambda_2)$, correspond to attractive U-N interactions. There are striking similarities in the size and shape of these regions between the three systems, supporting the assertion that U-N bonding is very similar in these complexes. Regions of weak interaction, coloured green, can be seen between ligand nitrogens: in $[UO_2(BTP)_2]^{2+}$ this is an interligand interaction, whereas in UO_2IA and UO_2IA′ this is an interaction between nitrogens on either side of the bridging carbon. These regions may be indicative of steric repulsion or, alternatively, of weak attraction. All repulsive interactions are N-N interactions, and can be interpreted as weak steric repulsion.

4.3.5. Electron Density Difference Distributions

Density difference distributions generated for the complexes optimised using the PBE *xc*-functional in the gas phase can be seen in Figure 4.6. Again, the $[UO_2(BTP)_2]^{2+}$, UO_2IA and UO_2IA′ complexes exhibit similar characteristics, and these strongly support the other data presented so far regarding U-N bonding and the effect on the uranyl U-O bond as well as the conclusions of Chapter 3. There is a clear accumulation of electron density in the U-N bonding region and, in keeping with previous measures, this is more pronounced in $[UO_2(BTP)_2]^{2+}$ than UO_2IA, presumably due to the (typically) shorter U-N bonds in the former. UO_2IA′ has somewhat more pronounced accumulation in the U-N bonding region than UO_2IA, consistent with both the shorter U-N bonds and our QTAIM analysis which indicates greater covalency. The size of the isosurfaces in the U-N bonding region of both UO_2IA and UO_2IA′ (although easier to observe in the former) follows the order previously identified in i) the value of $\rho(\mathbf{r})$ at the U-N BCP, ii) the magnitude of δ(U,N), iii) the ordering of the critical values of $n(\mathbf{r})$ for the U-N bonds and iv) the magnitude of $\rho(\mathbf{r})\operatorname{sgn}(\lambda_2)$ in the regions of weak interaction found *via* analysis of the reduced density gradient. This charge density is contributed partly from the C-N bonds on the ligands and partly from the uranyl unit itself. The isosurfaces show characteristics of both σ- and π-donation, in keeping with the ability of uranyl to act as both a σ- and π-acceptor. The density difference plots also clearly show the charge transfer from the U-O bonding region onto the uranyl oxygens, visualising the process discussed at length during analysis of QTAIM properties, and observed in Chapter 3. This serves to further justify the conclusions drawn in this previous work that ligand complexation results in reduced covalent character in the U-O bond, leading to the bond lengthening found in the present calculations, as well as throughout the literature.

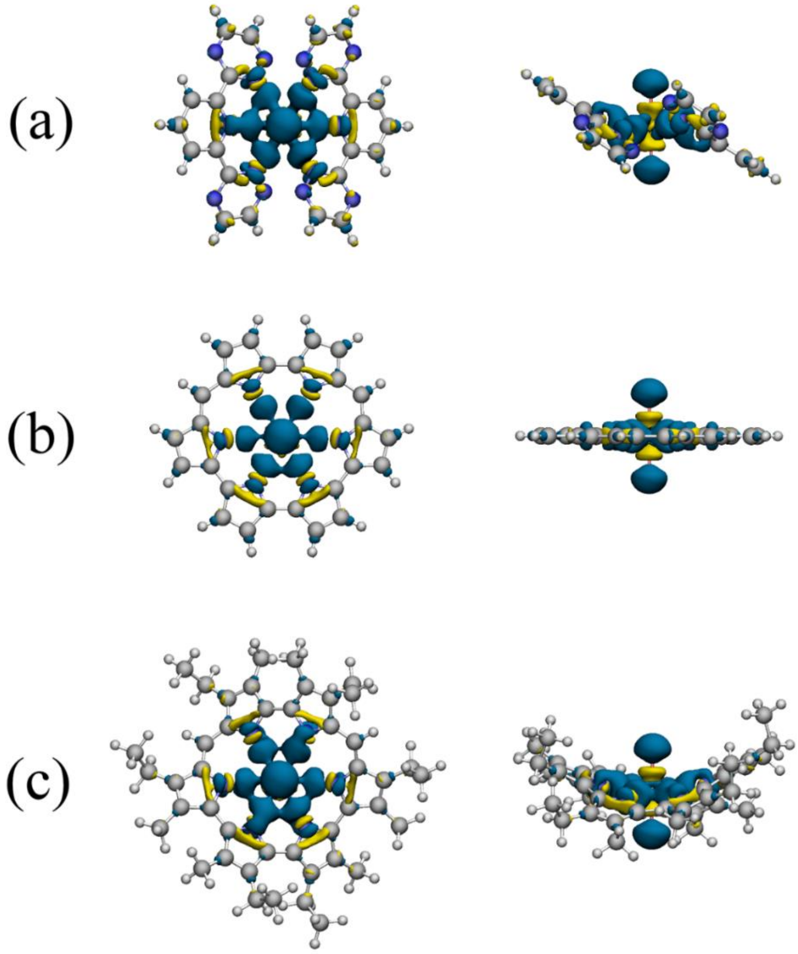

Figure 4.6: Electron density differences in (a) $[UO_2(BTP)_2]^{2+}$, (b) UO_2IA and (c) UO_2IA′ upon complexation. Blue regions indicate charge accumulation and yellow areas charge depletion. All densities visualised using an isosurface of $\rho = 0.005$ a.u. Reproduced from Di Pietro and Kerridge, "Assessing covalency in equatorial U – N bonds: density based measures of bonding in BTP and isoamethyrin complexes of uranyl" *PCCP,* June 2016.

4.4. Summary and Conclusions

A series of density functional theory calculations has been performed on complexes of uranyl with three multidentate nitrogen-donor ligands. The effects of the choice of exchange-correlation functional and solvation on a range of properties have been investigated, finding that, in agreement with a previous theoretical study[150], the gas phase structure of UO_2IA is planar, with a very slight degree of non-planarity introduced by solvation. This contradicts the experimentally synthesized alkyl substituted complex and it can be concluded that, since the dianionic IA ligand is formally Hückel aromatic, the energetic stability afforded by a planar geometry in the simplified complex is sufficient to outweigh the penalty associated with the unusually long U-N bonds found in the unsubstituted complex. However, when the substituents are included, the steric effects associated with alkyl substitution are more substantial than the stability gained by planarity, causing the ligand to distort and form shorter, stronger U-N bonds which are in improved agreement with crystallographic data.

Four different electron density based analytical methods have been utilised to characterise the bonding in these complexes. These analyses focus on the nature of U-N bonding in these complexes and the consequent effects on the highly covalent U-O bond of uranyl. These measures involve the use of the Quantum Theory of Atoms in Molecules to investigate topological and integrated properties of the electron density, and the Electron Localisation Function. Regions of weak covalent interaction have also been examined through analysis of the reduced density gradient, and these studies have been complemented with visualisation of the electron density difference induced *via* complexation of the uranyl unit by the IA, IA′ and BTP ligands. Complete agreement was found between all these four analyses, all of which demonstrated clear, unambiguous evidence for weak, but non-negligible, covalent character in the U-N bonding region of all three complexes. As might be expected, the covalent character of the bonds was found to increase as the U-N bond length shortened. Use of the B3LYP exchange-correlation functional leads to slightly increased electron localisation when compared to results obtained using the PBE functional. The B3LYP functional incorporates a degree of exact exchange, and it is known that this results in localisation of the electron density in the valence shell of transition metals and f-elements[27]. This is sometimes used to reduce the well-known self-interaction error present in approximate exchange-correlation functionals. This spurious self-interaction leads to an overestimate of electron delocalisation, especially in strongly correlated systems. Nevertheless, the results derived from the structures optimised with B3LYP still exhibit significant sharing of electrons. The effect of removing peripheral alkyl substituents from isoamethyrin, a common simplification in computational chemistry, has been analysed in detail and found to have a pronounced effect on both geometry and QTAIM parameters. There are small and consistent effects induced by the inclusion of solvent effects in all complexes; a shortening of U-

N bond lengths by around ~0.01 Å with a corresponding increase in electron sharing. Similarly, when solvent effects are considered, a small lengthening of U-O bonds is observed, and correspondingly, a small reduction in electron sharing.

The changes undergone by the uranyl unit upon complexation are particularly striking, as seen in the electron density difference distributions and, more quantitatively, with the integrated properties of the electron density. Upon complexation, there is a redistribution of charge among the oxygen and uranium centres of the uranyl dication. This redistribution takes the form of a noticeable reduction in sharing of electrons between the uranium and oxygen basins, with charge instead localising on the oxygen centres. Consequently, an increase in the ionic character of the U-O bond is observed, corresponding to a reduction in covalency. Since the covalent interaction is the stronger of the two, this reduction explains the increased U-O bond lengths upon complexation, compared to uncoordinated uranyl at the same level of theory.

It has been demonstrated through analysis of the integrated properties of the electron density that charge is donated from the uranyl unit itself into the U-N bonding region. Since the U(VI) centre is formally $5f^0 6d^0$, this cannot be explained as being due to traditional back-bonding, but instead is a contribution that is localised on the uranium centre in the isolated uranyl dication. Based on the behaviour of uranyl complexes in the previous chapter, this uranium donation appears to be a general feature of equatorial bonding in uranyl complexes[396].

Ultimately, it can be concluded that the results presented here support the possibility that, from an electronic perspective at least, multidentate expanded porphyrin ligands may provide interesting model systems for investigating An-N bonding characteristics and potentially, selectivity in nitrogen donor ligands. The following chapter will explore these possibilities further.

4.5. Publication Notes

Work included in this chapter was published in:

Poppy Di Pietro and Andrew Kerridge, “Assessing covalency in equatorial U-N bonds: density based measures of bonding in BTP and isoamethyrin complexes of uranyl”, *Physical Chemistry Chemical Physics*, June 2016.

5. Results: The Ligand Size Dependence of Equatorial Covalency and Stability, and Corresponding Effects on U-O Character, in a Series of Uranyl Hexaphyrins

5.1 Introduction

As discussed in earlier chapters, investigations of actinide coordination are challenging from both experimental and theoretical perspectives. Radioactivity and toxicity, amongst several other factors, hamper experimental study, while strong electron correlation, weak crystal fields and significant relativistic effects mean that the modelling of these complexes is not trivial[37–42]. However, developing our understanding of the bonding interactions of actinide elements is desirable from both a fundamental and practical perspective. The coordination chemistry of the actinides is a widely researched topic, with coordination by mono- and multi-dentate, as well as macrocyclic, ligands of great fundamental interest[12,21–33]. From a practical perspective, developing an improved characterisation of bonding in actinide complexes may be useful to the development of selective separation ligands in the nuclear industry.

The potential of relatively soft N-donor ligands as selective separation ligands for An(III) over Ln(III) have been investigated with varying degrees of success[12]. Ligands from the BTP, BTBP and BTPhen families have exhibited promising selectivity[13–15] for actinides over lanthanides, although with the source of this selectivity not fully understood, this selectivity can be destroyed, or greatly enhanced, with small modifications to the ligand[10,16,18–20], albeit not yet in a predictable way.

The expanded porphyrins are large, flexible, synthetic ligands capable of coordinating actinyl (di)cations in the equatorial plane[35,133,187,188,398] *via* pyrrolic nitrogen centres. The presence of meso-carbon centres between pyrrole units allows for modification to the size and shape of the ligand, and there are many possible substitution sites, allowing the possibility of ligands being 'tuned' to fit a specific cation[139,142,398,399].

Additionally, expanded porphyrins follow the CHON principle, a desirable criteria of an industrially useful separation ligand, specifically that it consist only of carbon, hydrogen, nitrogen and oxygen, which can be fully combusted after use to form environmentally safe products.

Several uranyl complexes with expanded porphyrin ligands have been experimentally realised. The hexaphyrins are expanded porphyrin macrocycles comprised of six pyrrolic subunits separated by varying numbers of meso-carbon atoms. Sessler *et al*. reported the synthesis of a uranyl complex of the hexaphyrin ligand isoamethyrin(1.0.1.0.0.0)[133], where the numbers in parentheses denote the number and position of meso-carbons (see Figure 5.1), and suggested its possible use as a colorimetric actinide sensor[133,134]. The Sessler group has also reported neptunyl and plutonyl complexes with isoamethyrin[133,190] as well as several other expanded porphyrins and similar expanded porphyrin-like macrocycles[35], and uranyl complexes of the hexaphyrin ligands cyclo[6]pyrrole (comprising no meso-carbons) and amethyrin(1.0.0.1.0.0)[187,188]. Uranyl complexes of the rubyrin(1.1.0.1.1.0), rubyrin(1.1.1.1.0.0) and hexaphyrin(1.1.1.1.1.1) ligands have not been reported, however the ligands themselves have been synthesized either as free-base macrocycles or complexes of, for example, transition metals[141,146,147,149,152,157,162,191,193,195,398–401]. To date, many different expanded porphyrin ligands have been synthesised[129,139–141,165,167,197,398,402]. Due to the existence of many possible substitution sites, the basic hexapyrrolic structure of the ligands may be modified with peripheral or meso-substituents[141,152,184,193,205,403], or for example, replacement of a pyrrolic subunit with a different kind of ring, *e.g.* a furan or pyridine subunit[154]. Actinide and actinyl complexes of several other expanded porphyrin-type ligands have been reported and investigated both experimentally and theoretically[172,211,216–218,220,249,250].

Although the equatorial bonding characteristics of uranyl, with its formally empty 5f-shell, and the trivalent minor actinides with their partially filled f-shells are expected to differ, it is intended in this instance simply to investigate the potential for expanded porphyrin ligands to coordinate a uranyl dication and to quantify the nature of the U-N bonds in such complexes. Additionally, as demonstrated in Chapter 3, the presence of the distinctive and experimentally accessible U-O_{yl} stretching modes[85,87,95] may act as probes of equatorial covalency[381].

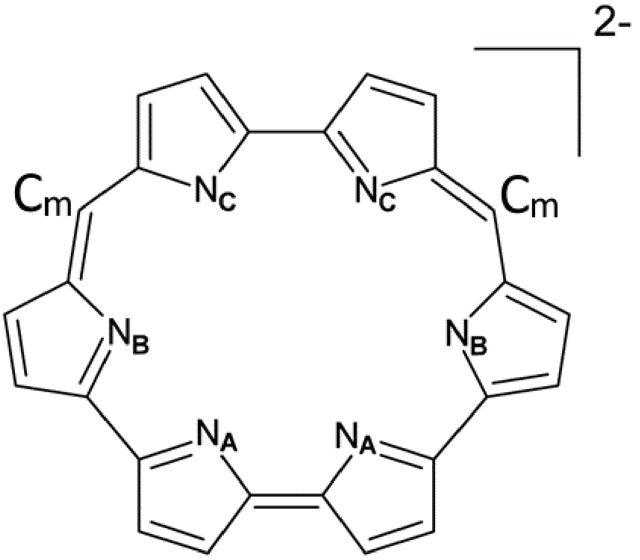

Figure 5.1: Molecular structure of isoamethyrin dianion omitting peripheral groups for clarity. Symmetry-distinct coordinating nitrogens are labelled N_A, N_B and N_C. Meso-carbon atoms are labelled C_m. Reproduced from Di Pietro and Kerridge, “Ligand size dependence of U-N and U-O bond character in a series of uranyl hexaphyrin complexes: quantum chemical simulation and density based analysis” *PCCP*, March 2017.

The study on the equatorial coordination behaviour of uranyl with a range of monodentate first row ligands[381] reported in Chapter 3 determined a strong correlation between covalent character in equatorial bonding and the vibrational frequencies of the U-O_{yl} stretching modes. Subsequently, Chapter 4 compared two complexes of uranyl with multidentate ligands[404]: a complex with the hexadentate macrocyclic expanded porphyrin ligand isoamethyrin and a complex with two tridentate bis-triazinyl-pyridine (BTP) ligands which have been shown to act selectively for An(III) over Ln(III) in industrial separation processes, concluding that the U-N bonding in these two complexes was strongly similar: largely ionic equatorial bonds with a comparable degree of covalency and a commensurate weakening of the U-O covalent interaction suggesting a redistribution of charge in the uranyl unit, with the very similar equatorial bonding in the two complexes suggesting that expanded porphyrin ligands may be interesting candidates for future investigations of actinide selectivity[404].

In this chapter, quantum chemical calculations at the density functional (DFT) level of theory are combined with several of the density-based analysis techniques used in Chapters 3 and 4 to show that complexes of uranyl with hexaphyrin ligands provide an interesting set of systems for investigating covalency in the U-N interaction. The size of the ligand core is controlled *via* the number of meso-carbon atoms, and the effect of ligand size on the degree of covalent character in equatorial U-N bonds has been investigated, and the extent of the charge redistribution in the uranyl unit that occurs upon complexation quantified. Density-based analyses have previously been successfully applied to f-element complexes[27,48,49,53,54,56,60,394].

Quantum chemical calculations have been used to investigate eight complexes in total, of which three have previously been synthetically realised: UO_2-cyclo[6]pyrrole, which contains no meso-carbon atoms, as well as UO_2-isoamethyrin(1.0.1.0.0.0) and UO_2-amethyrin(1.0.0.1.0.0) which each contain two meso-carbon atoms. Additionally, four hypothetical complexes with synthetically realised ligands are studied: UO_2-rubyrin(1.1.1.1.0.0), UO_2-rubyrin(1.1.1.0.1.0), UO_2-rubyrin(1.1.0.1.1.0), which each contain four meso-carbon atoms, and UO_2-hexaphyrin(1.1.1.1.1.1) which contains six, one bridging each of its pyrrolic subunits. Finally, one system for which both the complex and the ligand are hypothetical, UO_2-hexaphyrin(1.1.0.0.0.0), has been investigated. These ligands were selected so that the effect of increasing the size of the hexaphyrin core *via* meso-substitution could be directly investigated.

All complexes have been optimised at the density functional level of theory and, as a representative sample, four complexes were selected for detailed density analysis. For simplicity, the eight complexes will be referred to throughout using the labelling defined in Table 1.

	Simplified Complex	Substituted Complex
Cyclo[6]pyrrole	C_0	C_0'
Hexaphyrin(1.1.0.0.0.0)	C_2a	C_2a'
Isoamethyrin(1.0.1.0.0.0)	C_2b	C_2b'
Amethyrin(1.0.0.1.0.0)	C_2c	C_2c'
Rubyrin(1.1.1.1.0.0)	C_4a	C_4a'
Rubyrin(1.1.1.0.1.0)	C_4b	C_4b'
Rubyrin(1.1.0.1.1.0)	C_4c	C_4c'
Hexaphyrin(1.1.1.1.1.1)	C_6	C_6'

Table 5.2: Complex naming convention used in this chapter. The subscript refers to the number of meso-carbon atoms.

The quantum theory of atoms in molecules[347,348] (QTAIM) has been used to assess covalent character in U-N and U-O bonds. QTAIM is introduced more thoroughly in the Methodology chapter. Here it is sufficient to say that QTAIM relies upon the partitioning of a molecule into atomic basins bound by surfaces satisfied by the condition $\nabla\rho(\boldsymbol{r})\cdot\mathbf{n}(\boldsymbol{r}) = 0$ where $\mathbf{n}(\boldsymbol{r})$ is the unit vector normal to the basin surface. Points at which the gradient in the electron density vanishes, $\nabla\rho(\boldsymbol{r}) = 0$, define the critical points in $\rho(\boldsymbol{r})$. Of particular interest in this study are "bond critical points" (BCPs), which are found where the line of maximum density defining a bond path between bonded atoms is at its minimum[346]. Values of topological indicators at the BCP characterise the bonding interaction. In general, where the BCP has $\rho > 0.20$ a.u. and $\nabla^2\rho < 0$, a bond can be described as covalent. Broadly speaking, the higher the value of ρ, the higher the covalent character of the bond. The energy density, H, can also be used as a measure of covalency[347,348]. For a covalent bond, its value is expected to be negative, with the degree of covalency indicated by the magnitude. In addition, integrated properties such as atomic populations, as well as localisation and delocalisation indices can be obtained by integrating over atomic basins. These give insight into both electron sharing and charge donation.

QTAIM studies are complemented by considering regions of weak interaction[358] using the reduced density gradient (RDG) (see Methodology, Chapter 2.9.3.) and electron density difference distributions upon complexation. These analytical tools are used to qualitatively analyse the changes that occur upon complex formation and develop a comprehensive description of the nature of U-N and U-O bonding in these complexes.

5.2. Computational Details

As in the previous chapter, Density Functional Theory (DFT) calculations have been performed using version 6.4 of the TURBOMOLE quantum chemistry software package[359]. Ahlrichs def2-TZVP basis sets of triple-zeta quality have been used for the C, H, O and N atoms[369] and the Ahlrichs def-TZVP basis set of triple-zeta quality, incorporating a relativistic ECP comprising 60 core electrons[285] has been used for the U atoms. Due to the closed shell nature of these systems, the effects of spin-orbit coupling were not included in the calculations. All complexes summarised in Figures 2 and 3 were optimised using the PBE exchange-correlation *xc*-functional[333] which employs the generalised gradient approximation (GGA). Subsequent reoptimisation of a representative sample of complexes was also performed using the B3LYP hybrid-GGA *xc*-functional[373,374] to approximate the exchange correlation energy. This was done in order to investigate the effects of incorporating exact exchange on properties of the electron density. Both PBE and B3LYP have previously be shown to be suitable for the accurate modelling of actinide-containing systems[27,39,241,381,404,405]. Initial optimisations were carried out in the gas phase. Subsequently, the COSMO continuum solvation model[360], using a relative permittivity of $\varepsilon_r = 8.9$ was used to simulate solvation in DCM, for which there is experimental precedent[133]. Vibrational analysis was performed to ensure that all structures represented energetic minima[‡].

All of the hexaphyrin macrocycles reported experimentally feature methyl substituents on the periphery of their pyrrole units (see Figure 3). These are generally assumed to have little effect on the geometry and electronic structure of the molecule and in order to minimise computational expense, such substituents are often omitted when performing DFT simulations. However it has been shown that for UO_2-isoamethyrin(1.0.1.0.0.0), this simplification leads to severely overestimated (by ~0.1 Å) U-N bond lengths[150]. Thus, as in Chapter 4, where UO_2-isoamethyrin(1.0.1.0.0.0) was compared with $[UO_2(BTP)_2]^{2+}$, optimisations have been performed with and without these substituents so that their effects on geometry could be assessed. U-N and U-O bond lengths have been compared to experimental data where available. For electron density analysis, single point energy calculations were performed at the optimised geometries using the SARC all-electron uranium basis set[370] and the second-order Douglas-Kroll-Hess (DKH2) Hamiltonian to account for scalar relativistic effects[313,314]. QTAIM analysis was performed using the Multiwfn[363] and AIMAll[364] codes in order to calculate topological and integrated properties of the electron density. RDG and density difference data were visualised using the VMD code[365].

[‡] Due to computational expense, vibrational frequency analysis was not performed on the C_2b' complex when optimised with the B3LYP functional. Similarly, large peripherally substituted complexes, with the exception of C_2b' which was selected for further study, were optimised using only the PBE functional.

5.3. Results and Discussion

5.3.1. Structural and Energetic Characterisation

Geometries of the complexes optimised using the PBE *xc*-functional in the gas phase are shown in Figures 5.2 and 5.3. It is apparent (see Table 5.2) that, in most cases, the inclusion of peripheral alkyl groups has a relatively small effect on the average U-N bond length, with differences of only a few hundredths of an Angstrom, and results in no significant structural variation. The exception is with the C_2x complexes, in which simplified and substituted forms have differences in average bond lengths of approximately 0.1 Å, nearly an order of magnitude higher than for the C_0, C_4 and C_6 complexes.

	Simplified Complexes	Substituted Complexes	Difference
	$\overline{r_{\mathrm{U-N}}}$	$\overline{r_{\mathrm{U-N}}}$	$\Delta\overline{r_{\mathrm{U-N}}}$
C_0	2.532/*2.527*	2.554/*2.543*	0.022/*0.016*
C_2a	2.804/*2.799*	2.673/*2.659*	0.131/*0.140*
C_2b	2.780/*2.771*	2.688/*2.674*	0.112/*0.097*
C_2c	2.776/*2.770*	2.689/*2.674*	0.087/*0.096*
C_4a	2.717/*2.706*	2.689/*2.680*	0.028/*0.026*
C_4b	2.701/*2.687*	2.684/*2.673*	0.017/*0.014*
C_4c	2.703/*2.692*	2.689/*2.678*	0.014/*0.014*
C_6	2.700/*2.697*	2.696/*2.688*	0.004/*0.009*

Table 5.2: Average U-N bond lengths in Angstrom for complexes optimised with the PBE exchange correlation functional in the gas phase/*DCM*, with and without peripheral substituents**.**

All C_2x complexes exhibit significant structural variation when peripheral substituents are included, with a degree of non-planarity introduced that acts to shorten the U-N bonds. Based on these results, C_0, C_4x and C_6 complexes will all be considered in their simplified form for the remainder of this chapter, and substituents will only be considered in the case of the C_2x complexes, with the substituted system referred to as C_2x'. Table 5.3 U-N bond lengths for the complexes C_0, C_2x', C_4x and C_6 and U-O bond lengths can be found in Table 5.4.

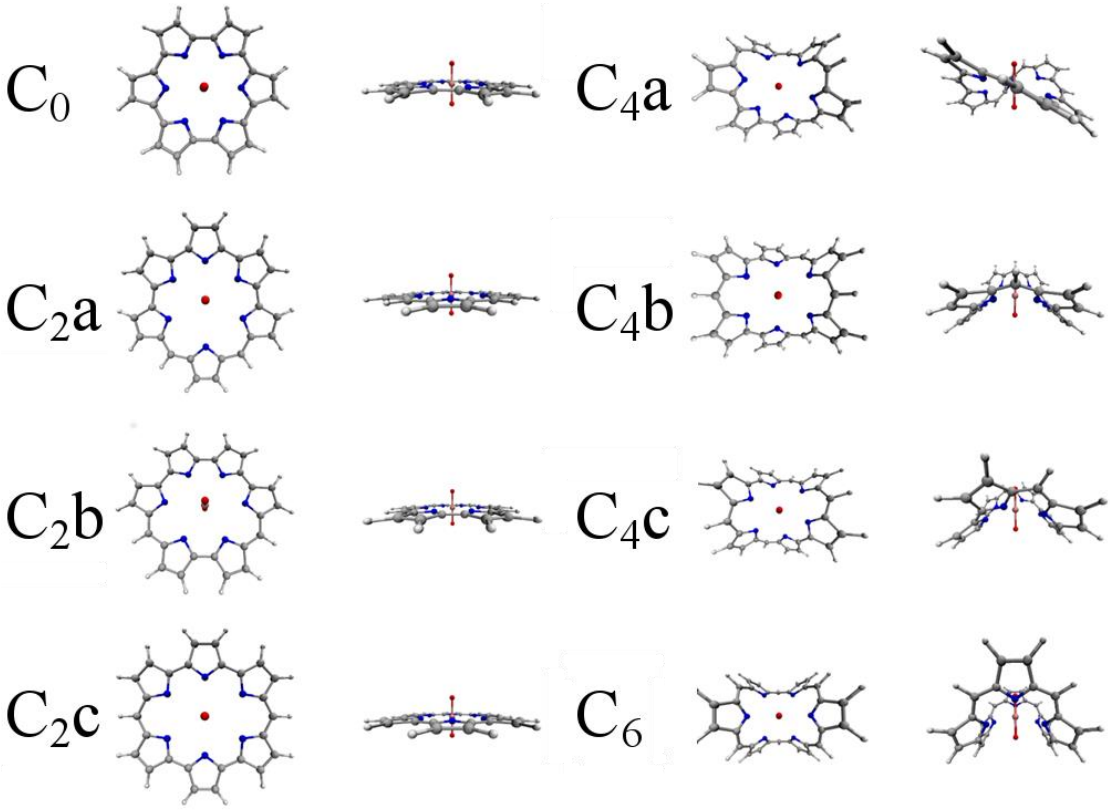

Figure 5.2: Optimised structures of the eight uranyl hexaphyrins considered in this study, optimised in the gas phase using the PBE exchange-correlation functional, without peripheral alkyl substituents. Reproduced from Di Pietro and Kerridge, "Ligand size dependence of U-N and U-O bond character in a series of uranyl hexaphyrin complexes: quantum chemical simulation and density based analysis" *PCCP*, March 2017.

An examination of U-N and U-O bond lengths reveals that complex C_0 has the shortest average U-N bond lengths of all eight complexes, 2.532 Å (2.527 Å), when optimised in the gas phase (DCM). C_0 features four longer and two slightly shorter (by ~0.01 Å) U-N bonds. This complex also has the longest calculated U-O bond length, 1.799 Å (1.812 Å), when optimised in the gas phase (DCM), thereby exhibiting the strongest perturbation of the uranyl unit due to equatorial complexation. A very slight degree of non-planarity is introduced upon solvation (and upon addition of peripheral substituents), although this causes no significant changes to bond lengths. When compared to experimental values, the U-N bond lengths of C_0 are reproduced to within 0.01 Å (0.01 Å) in the gas phase (DCM), an excellent level of agreement, while the U-O bonds are reproduced to within 0.02 Å (0.03 Å) in the gas phase (DCM), a good level of agreement[187]. It is worth mentioning that the crystal structure of C_0 exhibits nearly perfect planarity, in agreement with the calculated gas phase structure.

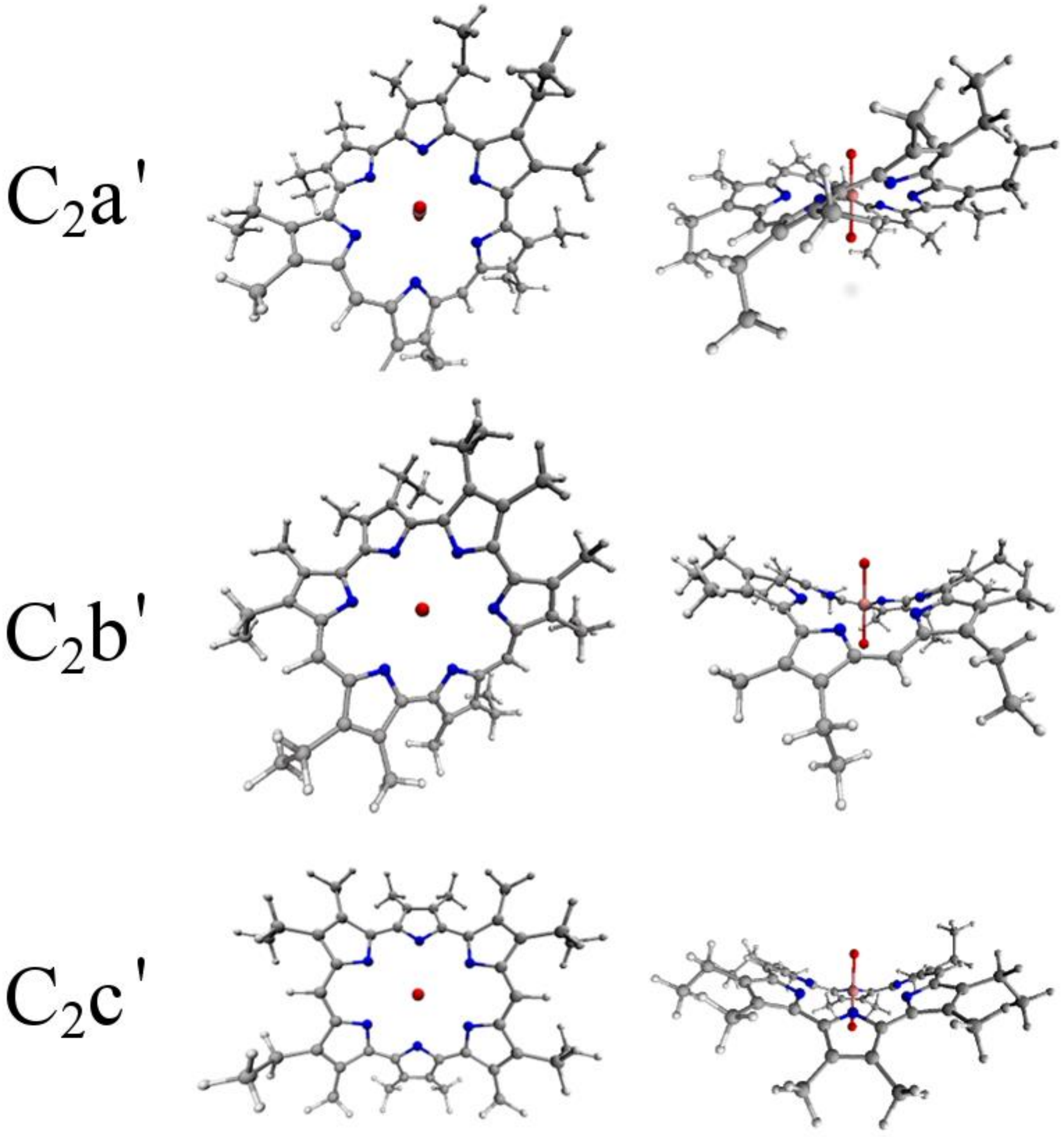

Figure 5.3: Optimised peripherally substituted C_2 structures, optimised in the gas phase using the PBE exchange-correlation functional. Reproduced from Di Pietro and Kerridge, “Ligand size dependence of U-N and U-O bond character in a series of uranyl hexaphyrin complexes: quantum chemical simulation and density based analysis” *PCCP*, March 2017.

	$r_{\text{U-N}}$	$r_{\text{U-N}}$	$r_{\text{U-N}}$	$r_{\text{U-N}}$	$r_{\text{U-N}}$	$r_{\text{U-N}}$	$\overline{r_{\text{U-N}}}$	range of $r_{\text{U-N}}$
$\mathrm{C_0}$	2.534/ *2.530*	2.528/ *2.522*	-	-	-	-	2.532/ *2.527*	2.528-2.534 / *2.522-2.530*
$\mathrm{C_2a'}$	2.835/ *2.812*	2.709/ *2.696*	2.709/ *2.694*	2.604/ *2.591*	2.593/ *2.581*	2.591/ *2.579*	2.673/ *2.659*	2.591-2.835 / *2.591-2.812*
$\mathrm{C_2b'}$	2.586/ *2.573*	2.587/ *2.573*	2.772/ *2.702*	2.765/ *2.693*	2.713/ *2.755*	2.705/ *2.747*	2.688/ *2.674*	2.586-2.772 / *2.573-2.755*
$\mathrm{C_2c'}$	2.751/ *2.736*	2.749/ *2.733*	2.749/ *2.733*	2.749/ *2.732*	2.569/ *2.557*	2.569/ *2.557*	2.689/ *2.674*	2.569-2.751 / *2.557-2.736*
$\mathrm{C_4a}$	2.827/ *2.811*	2.763/ *2.754*	2.593/ *2.578*	2.533/ *2.527*	-	-	2.717/ *2.706*	2.533 - 2.827 / *2.527-2.811*
$\mathrm{C_4b}$	2.720/ *2.700*	2.692/ *2.682*	2.690/ *2.678*	-	-		2.701/ *2.687*	2.690-2.720 / *2.678-2.700*
$\mathrm{C_4c}$	2.785/ *2.769*	2.663/ *2.654*	-	-	-	-	2.703/ *2.692*	
$\mathrm{C_6}$	2.820/ *2.818*	2.640/ *2.637*	-	-	-	-	2.700/ *2.697*	

Table 5.3: Distinct U-N bond lengths in Angstrom for complexes optimised using the PBE exchange-correlation functional in the gas phase/*DCM*. Experimental data obtained from refs: a) [187], b) [133].

Complex	r_{U-O} (Gas phase/*DCM*)
C_0	1.799/*1.812*
C_2a'	1.789/*1.802*
C_2b'	1.787/*1.799*
C_2c'	1.787/*1.800*
C_4a	1.784/*1.793*
C_4b	1.783/*1.792*, 1.785/*1.793*
C_4c	1.784/*1.792*
C_6	1.784/*1.791*, 1.789/*1.796*
UO_2^{2+}	1.711/*1.721*

Table 5.4: U-O bond lengths in Angstrom for complexes optimised using the PBE exchange-correlation functional in the gas phase/*DCM*.

Moving on to the complexes containing two meso-carbons, the simplified complexes C_2a, C_2b and C_2c share several characteristics. All are perfectly or very nearly planar, with average U-N bond lengths of 2.776-2.804 Å (2.770-2.799 Å) when optimised in the gas phase (DCM) and U-O bonds of 1.777-1.778 Å (1.786-1.793 Å) when optimised in the gas phase (DCM). The calculated U-N and U-O bond lengths for both C_2b and C_2b' are in good agreement with the previous theoretical values reported by Shamov and Schreckenbach[150], and, for C_2b', structural parameters are in good agreement with experimental data[133]. Shamov and Schreckenbach's work illustrated the importance of including these substituents when modelling uranyl isoamethyrin, and here it is found that substituents have a similar distorting effect on both C_2a' and the hypothetical C_2c', where a presumably sterically-induced twisting of the ligand results in average U-N bond lengths of 2.673-2.689 Å (2.659-2.674 Å) when optimised in the gas phase (DCM), ~0.1 Å shorter than their simplified analogs. Commensurately, U-O bonds in the C_2x' complexes are slightly longer than their simplified analogs, 1.787-1.789 Å (1.799-1.802 Å) when optimised in the gas phase (DCM). These differences demonstrate that careful consideration of the effects of both substituents and solvation models are essential when modelling hexaphyrin complexes. It may be interesting to investigate the rigidity of these structures using perhaps MD simulations, although this has not been performed as part of this study.

Non-planarity in C_4a, C_4b and C_4c is pronounced. Average U-N bond lengths are typically a few hundredths of an Angstrom longer than for the C_2x' complexes, 2.701-2.707 Å (2.692-2.706 Å) when optimised in the gas phase (DCM). U-O bonds are commensurately slightly shorter than those in the C_2x' complexes, 1.783-1.785 Å (1.792-1.793 Å) when optimised in the gas phase (DCM).

C_6, the largest complex, is also highly non-planar, allowing equatorial U-N bonds of comparable length to the C_2x' and C_4x complexes to be formed. Interestingly, in this complex the ligand is folded almost completely in half (reminiscent of a Pacman-style ligand[29,34,217,219]), although here the uranyl unit is coordinated at the ligands centre. This folding has the effect of bringing some ligand atoms significantly closer to the –yl oxygen ions than in any of the other complexes. Average U-N bonds are 2.700 Å (2.697 Å) when optimised in the gas phase (DCM). U-O bond lengths are 1.789 Å (1.796 Å) and 1.784 Å (1.791 Å), with an 0.005 Å elongation of one bond due to the aforementioned $C\text{-}O_{yl}$ interaction.

Reoptimisations of C_0, C_2b', C_4a, and C_6 were performed using the hybrid B3LYP functional but led to no significant structural changes. U-N bond lengths were calculated to be in the region of 0.005 Å longer and U-O bond lengths were found to be shorter by approximately the same amount. Irrespective of the functional employed, continuum solvation acts to give a slight shortening of the U-N bonds and a corresponding lengthening of U-O bonds.

5.3.2. Binding and Deformation Energies

Complex stability was investigated by calculating molecular binding energies as well as ligand deformation energies. Molecular binding energies (ΔE) were calculated as defined in $Eq. 5.1$ by subtracting the energies of the optimised uranyl dication and ligand dianion fragments from that of the complex:

$$\Delta E = E_{\mathrm{C}} - \left(E_{\mathrm{UO_2^{2+}}} + E_{\mathrm{L^{2-}}}\right) \qquad (Eq. 5.1)$$

The highly flexible nature of the macrocyclic ligands considered here is such that it is informative to evaluate the degree by which the fragments deform from their optimal geometries upon complexation. Ligand deformation energies (E_{DL}) were calculated by subtracting the energy of each ligand in its coordination geometry from that of the optimised free ligand:

$$E_{\mathrm{DL}} = E_{\mathrm{L}^{2-}}^{\mathrm{Opt}} - E_{\mathrm{L}^{2-}}^{\mathrm{Coord}} \qquad (Eq. 5.2)$$

And similarly for the uranyl dication:

$$E_{\mathrm{DU}} = E_{\mathrm{UO}_2^{2+}}^{\mathrm{Opt}} - E_{\mathrm{UO}_2^{2+}}^{\mathrm{Coord}} \qquad (Eq. 5.3)$$

The deformation energies may be considered independently or subtracted from the calculated binding energy to obtain a deformation adjusted binding energy (E_{DA}).

$$\Delta E_{\mathrm{DA}} = \Delta E - (E_{\mathrm{DL}} + E_{\mathrm{DU}}) \qquad (Eq. 5.4)$$

In this way, complex stabilities can be considered in a manner that allows for the effects of the destabilisation of the uranyl and hexaphyrin fragments to be taken into account.

Molecular binding energies and deformation adjusted binding energies calculated from PBE gas phase optimisations are listed in Table 5.5. The overall trend is for binding energies to fall as the ligands become larger, decreasing by ~1.5 eV from C_0 to the C_2x' complexes, then by another ~1.5 eV from the C_2x' to the C_4x complexes, where the effect appears to plateau. There is a decrease of only ~0.2 eV from the C_4x complexes to the C_6 complex. Notably, the complexes predicted to be most stable here, C_0 and C_2x', are those that have been synthetically realised, while the less stable C_4x and C_6 complexes have proven, so far, to be experimentally inaccessible.

It is interesting to note that the deformation energy of the ligand increases as the core size is increased. This increase is ~1 eV per pair of meso carbon up to the C_4x complexes, which appear to represent a maximum. Beyond this, increased flexibility in the ligand presumably reduces the deformation energy penalty. The deformation energy of the uranyl unit decreases slightly as the ligand core size increases: it is comparable, and in fact dominant, to that of the ligand in C_0, whereas it is of comparable magnitude in all other complexes studied. Combined, the result is a net increase in deformation energy from C_0 to C_6. Whilst the deformation energy doesn't fully account for the relative stability of the smaller ligands, it does strongly correlate ($R^2 = 0.98$) as shown in Figure 5.4.

	ΔE (eV)	ΔE_{DA} (eV)	E_{DL} (eV)	E_{DU} (eV)
C_0	-29.74	-30.37	0.25	0.38
C2a′	-28.17	-29.52	1.05	0.30
C2b′	-27.96	-29.26	1.02	0.29
C2c′	-28.05	-29.30	0.96	0.29
C4a	-26.26	-28.51	1.98	0.27
C4b	-26.03	-28.39	2.09	0.27
C4c	-26.17	-28.46	2.03	0.27
C6	-26.07	-28.16	1.80	0.28

Table 5.5: Molecular binding energies (ΔE) and deformation adjusted binding energies (ΔE_{DA}), with deformation energies of the UO_2^{2+} unit (E_{DL}) and the ligands (E_{DU}). Data was obtained using the PBE *xc*-functional, and due to the simple COSMO solvation model being a rather poor approximation for solvated uncoordinated UO_2^{2+}, are given in the gas phase only.

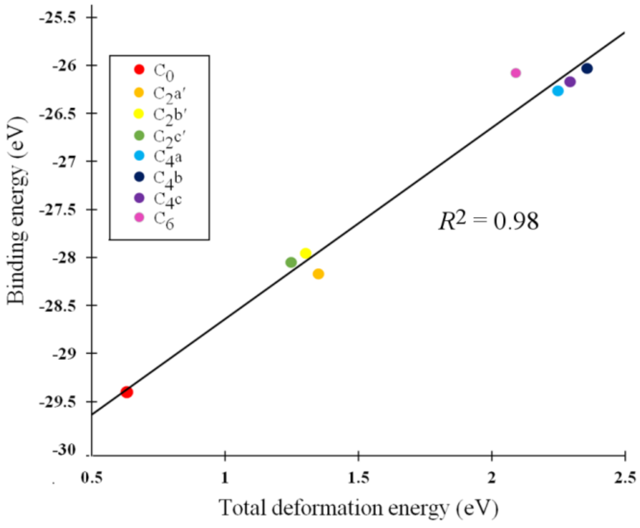

Figure 5.4: Molecular binding energy plotted against total deformation energy for all eight complexes. Energies are taken from the structures optimised in the gas phase. Reproduced from Di Pietro and Kerridge, "Ligand size dependence of U-N and U-O bond character in a series of uranyl hexaphyrin complexes: quantum chemical simulation and density based analysis" *PCCP*, March 2017.

When the deformation energy is subtracted from the binding energy to obtain a deformation adjusted binding energy, the relationship between binding energy and ligand size persists and there is a loss of stability for each pair of meso-carbons added, reaching a plateau at the C_4x and C_6 complexes.

5.3.3. U-O Stretching Frequencies

Frequencies of the U-O stretching modes calculated using the PBE functional in the gas phase and in the presence of a DCM continuum solvent are presented in Table 5.6. In previous studies, a degree of U-O bond weakening upon equatorial uranyl complexation has been both spectroscopically observed and theoretically calculated[56,85,87,95,96,103,381], with the magnitude of this weakening corresponding to a redshift in the distinctive uranyl stretching modes. The study in Chapter 3 demonstrated strong correlations between binding energy and the frequency of the uranyl stretching modes in a series of monodentate complexes in which uranyl is coordinated by a first row species[381].

	$\nu_{U\text{-}Os}$ cm^{-1}	$\nu_{U\text{-}Oas}$ cm^{-1}
C_0	817.74/*788.41*	897.56/*856.30*
C_2a'	830.41/*800.15*	916.13/*873.18*
C_2b'	834.35/*803.25*	921.88/*878.08*
C_2c'	834.07/*802.73*	921.75/*878.54*
C_4a	836.81/*810.84*	923.95/*887.87*
C_4b	836.02/*813.31*	923.72/*888.99*
C_4c	837.01/*813.26*	923.53/*889.73*
C_6	823.98/*809.39*	909.92/*886.52*

Table 5.6: Uranyl stretching frequencies from structures calculated using the PBE functional in the gas phase/*DCM*.

Figure 5.5 shows both the symmetric and asymmetric stretching frequencies of uranyl in C_0, C_2a', C_2b', C_2c', C_4a, C_4b, C_4c and C_6 plotted against the deformation adjusted binding energy. It is immediately clear that such a linear relationship is not present here, with only very weak correlation ($R^2 \leq 0.3$ in all cases).

Plotting these frequencies against the uranyl deformation energy however, as seen in Figure 5.6, results in weak correlation (R^2 = 0.68 and 0.71 for the symmetric and asymmetric modes, respectively) with the C_6 complex being an obvious outlier. When the C_6 complex is omitted from the linear regression analysis, correlation becomes very strong (R^2 = 0.99 and 0.94 for the symmetric and asymmetric modes, respectively). Returning to the relationship between the symmetric/asymmetric stretching frequencies of uranyl and the binding energy/deformation adjusted binding energy, omitting the C_6 complex results in moderate correlation, with R^2 values of between 0.53 and 0.83 and correlation being slightly stronger when considering the adjusted binding energy. Possible reasons for the anomalous behaviour exhibited by the C_6 complex will be further explored in later sections.

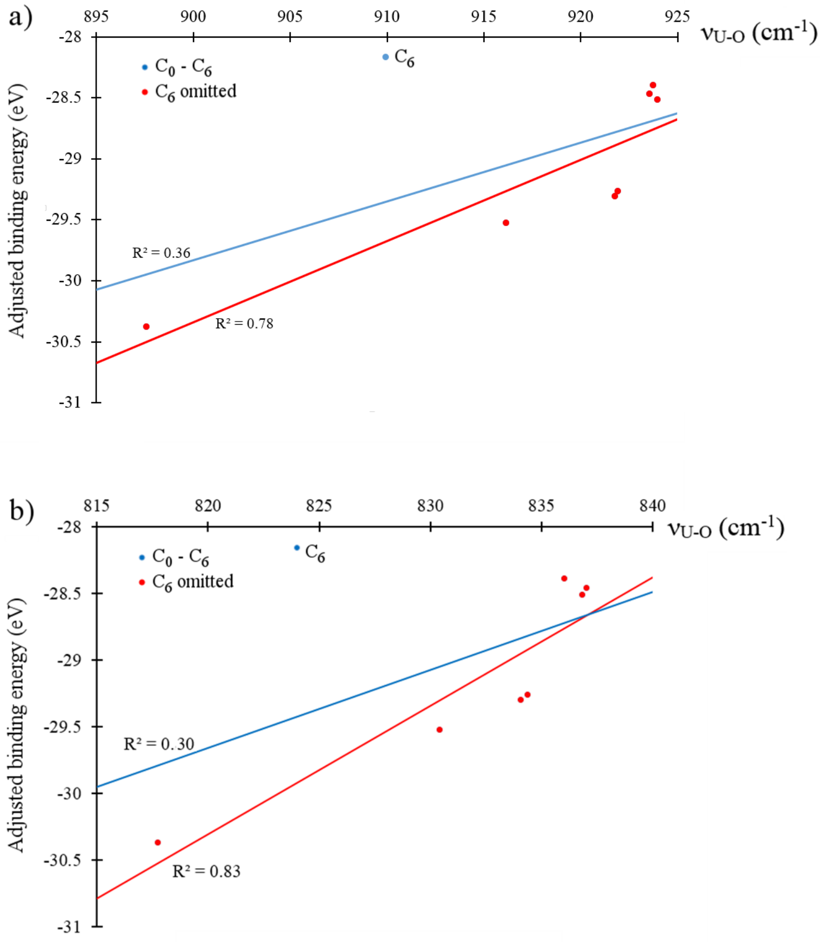

Figure 5.5: Linear fitting of the relationship between deformation adjusted binding energies and a) antisymmetric and b) symmetric stretching modes of uranyl; Fits are given for the entire data sets (blue) and omitting the outlying C_6 results (red). Generated from data obtained using the PBE *xc*-functional in the gas phase. Reproduced from Di Pietro and Kerridge, "Ligand size dependence of U-N and U-O bond character in a series of uranyl hexaphyrin complexes: quantum chemical simulation and density based analysis" *PCCP*, March 2017.

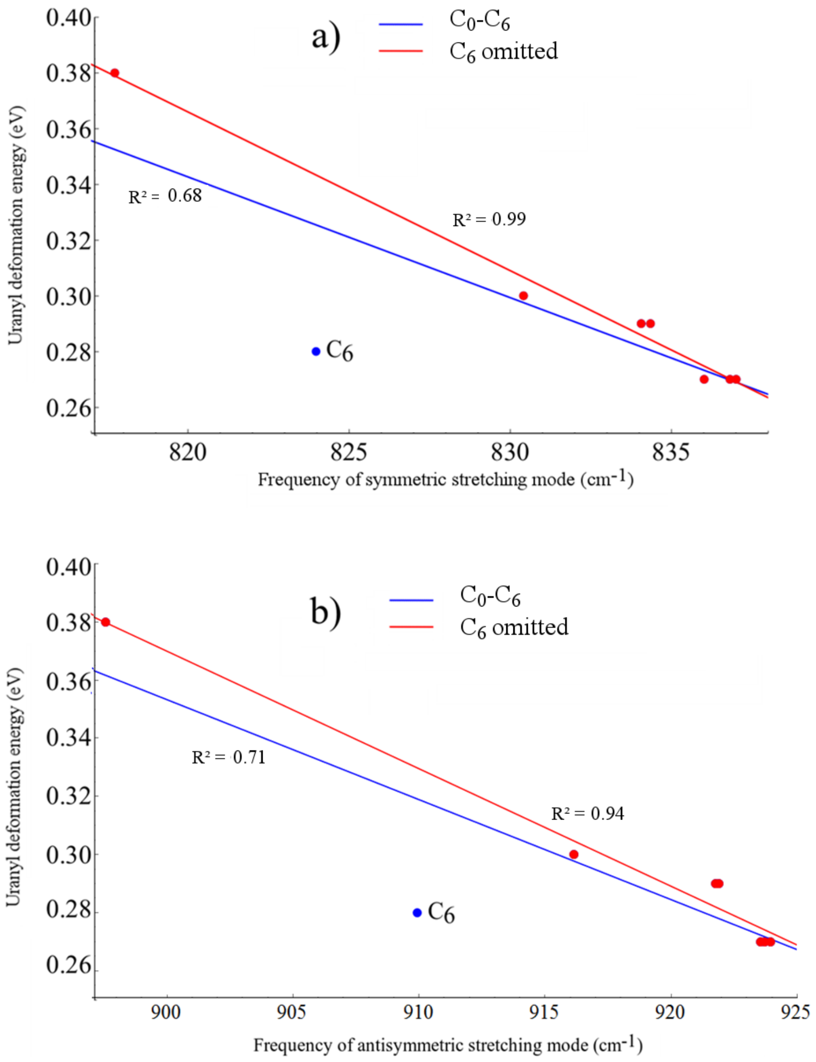

Figure 5.6: Linear fitting of the relationship between uranyl deformation energies and the frequencies of a) the symmetric, and b) the antisymmetric stretching modes of uranyl. Fit lines are given for the entire data set (blue) and omitting the outlying C_6 result (red). Generated from data obtained using the PBE functional in the gas phase. Reproduced from Di Pietro and Kerridge, “Ligand size dependence of U-N and U-O bond character in a series of uranyl hexaphyrin complexes: quantum chemical simulation and density based analysis” *PCCP*, March 2017.

For the following density based analysis, a representative set of complexes have been selected. This set comprises C_0, C_2b' (which is the experimentally best characterised C_2x' complex), C_4a (the most stable of the three hypothetical C_4x complexes) and C_6. All are simplified complexes except for C_2b' since, as discussed above, substitution was found to only impact significantly on C_2x geometries. The characterisation will focus on PBE-optimised gas phase complexes, with data from B3LYP-optimised and solvated simulations given in Appendix II and discussed where relevant.

5.3.4. Topological Analysis of the Electron Density

Topological properties of the U-N and U-O bonds are now considered. The values of the electron density, ρ, its laplacian, $\nabla^2\rho$, and the energy density, H, were investigated at the U-N and U-O bond critical point (BCP). Also included in this section is the delocalisation index δ(A,B), defined as the number of electrons delocalised between two atomic basins A and B. Table 5.7 contains average and total values of topological descriptors at the U-N BCPs. It is immediately apparent from the data in Table 5.7 that, as expected, none of the U-N bonds investigated here exhibit pronounced covalency, rather each U-N bond has a small degree of covalent character which can be quantified by the values of these topological properties at the BCP. Average and total properties are given in Table 5.7 since it is the effect of the ligand as a whole on the uranyl unit which is of greatest interest, however there is a strong relationship between individual U-N bond lengths in C_0, C_2b', C_4a and C_6 and ρ_{BCP} values, (see Figure 5.7) where the shorter the bond, the larger the covalent component of the interaction.

	C_0	C_2b'	C_4a	C_6
$\sum \boldsymbol{\rho}_{\mathbf{U-N}}$	0.350	0.255	0.244	0.248
$\overline{\boldsymbol{\nabla}^2\boldsymbol{\rho}_{\mathbf{U-N}}}$	0.149	0.106	0.101	0.103
$\sum \boldsymbol{H}_{\mathbf{U-N}}$	-0.042	-0.019	-0.019	-0.018
$\sum \boldsymbol{\delta}(\mathbf{U},\mathbf{N})$	2.143	1.819	1.761	1.766

Table 5.7: Topological parameters obtained at the bond critical points of the U-N bonds and delocalisation indices between the U-N atomic basins, given as total or average values measured in atomic units (a.u). Data is from structures calculated using the PBE functional in the gas phase.

When average values are considered (see Table 5.8), it can be seen that equatorial covalency decreases and U-N bond length increases in the order $C_0 > C_2b' > C_6 > C_4a$, with C_0 having by far the most U-N covalency (and shortest U-N bonds) and the other three complexes being broadly similar in their U-N character. It is worth emphasising that the U-N bonding character of C_2b′, C_4a and C_6 is very similar in comparison to the differences between these complexes and C_0.

	$\overline{\rho_{\mathrm{U-N}}}$	$\overline{r_{\mathrm{U-N}}}$
C_0	0.058	2.532
C_2b'	0.042	2.668
C_4a	0.041	2.717
C_6	0.041	2.700

Table 5.8: Average values of ρ_{BCP} and bond lengths for the U-N bonds in C_0, C_2b', C_4a, and C_6, given in Angstrom and a.u., respectively. Data is from structures calculated using the PBE functional in the gas phase.

When the relationship between the frequencies of the uranyl stretching modes and the sum of ρ_{BCP} (see Table 5.6) for the U-N bonds is investigated, linear regression reveals only weak correlations with $R^2 = 0.74$ and 0.61 for the antisymmetric and symmetric modes, respectively. The values of the energy density, H, at the BCPs of all U-N bonds, support conclusions drawn from the electron density, ρ, of weak covalent character**.** H takes negative, albeit very small, values in all complexes, with C_0 having the largest magnitude, indicating the greatest degree of covalent character.

The delocalisation index (see Table 5.7), summed over all U-N bonds, may be considered a direct measure of electron sharing between the uranyl unit and the ligand. Supporting the assertion based on analysis of ρ_{BCP} that the U-N bonds in C_0 have significantly more covalent character than any of the other complexes, C_0 exhibits the greatest degree of electron delocalisation in its U-N bonds, with C_2b', C_4a and C_6 all exhibiting comparable values character, similar to that of the $[UO_2(BTP)_2]^{2+}$ complex we considered previously[404].

In Table 5.9, various topological parameters of the U-O bonds are given. Strong inverse correlation ($R^2 = 0.97$) is found between average values of ρ_{BCP} for the U-N bonds and values of ρ_{BCP} for the U-O bonds (see Figure 5.8). This can be explained in terms of the effect on the uranyl unit due to the bonding in the equatorial plane, which acts to destabilise it, as we have previously reported[381,404], resulting in U-O covalency being weakest when equatorial covalency is strongest.

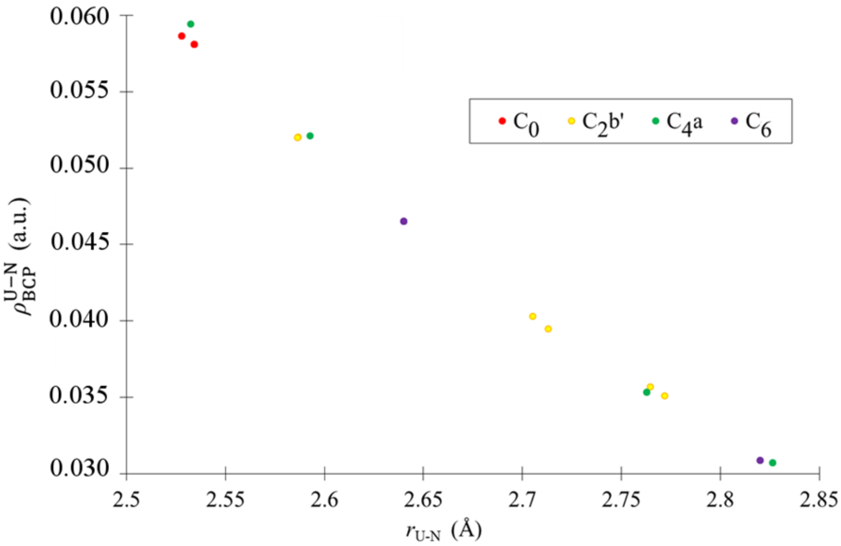

Figure 5.7: Values of U-N ρ_{BCP} plotted against individual U-N bond lengths for C_0, C_2b', C_4a and C_6, for complexes optimised using the PBE *xc*-functional in the gas phase. Reproduced from Di Pietro and Kerridge, "Ligand size dependence of U-N and U-O bond character in a series of uranyl hexaphyrin complexes: quantum chemical simulation and density based analysis" *PCCP*, March 2017.

	C_0	C_2b'	C_4a	C_6			
	U-O	U-O	U-O	U-O_1	U-O_2	O_1-C_m	O_2-N
$\rho_{\text{A-B}}$	0.290	0.299	0.301	0.301	0.299	0.009	-
$\nabla^2\rho_{\text{A-B}}$	0.320	0.315	0.314	0.323	0.307	0.037	-
$H_{\text{A-B}}$	-0.253	-0.270	-0.274	-0.272	-0.269	0.002	-
$\delta(\text{A,B})$	1.915	1.971	1.977	1.958	1.961	0.033	0.091

Table 5.9: Topological parameters obtained at the bond critical points of the U-O bond, and the U-O delocalisation index, measured in atomic units (a.u). Data is from structures calculated using the PBE *xc*-functional in the gas phase.

Two things are of note when these data are considered. Firstly, C_0 is again set apart from the other complexes, with significantly greater equatorial covalency and a commensurately smaller degree of covalency in the U-O interaction. Secondly, C_6 again appears to differ from the other complexes in that its two U-O bonds have noticeably different values of ρ_{BCP}. This is explained by the fact that C_6 has a characteristic unique amongst the complexes investigated here: QTAIM analysis reveals bond paths between two ligand meso-carbons and one of the uranyl oxygens, which is enclosed by the ligand in a manner reminiscent of a Pacman-style complex[222]. Topological properties associated with this interaction are given in Table 8, showing that they are weak non-covalent interactions with ρ_{BCP} an order of magnitude lower than in the U-O bonds. When only the value of ρ_{BCP} for the unenclosed U-O bond in C_6 is used, the frequencies of the uranyl stretching modes and values of ρ_{BCP} for the U-O bonds are found to have an improved linear relationship with R^2 = 0.88 and 0.79 for the antisymmetric and symmetric modes, respectively. When the value of ρ_{BCP} for the enclosed U-O bond of C_6 is used, linear correlations decrease to R^2 = 0.70 and 0.58 for the antisymmetric and symmetric modes, respectively. Thus the uranyl stretching modes in the C_6 complex are significantly perturbed by these additional interactions.

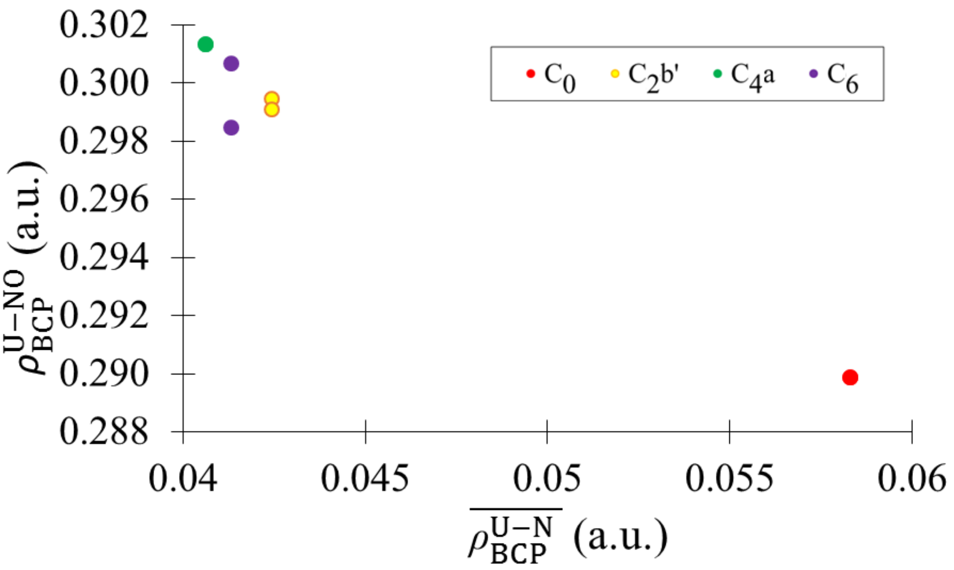

Figure 5.8: Average values of ρ_{BCP} for the U-N bonds plotted against values of ρ_{BCP} for the U-O bonds. Reproduced from Di Pietro and Kerridge, “Ligand size dependence of U-N and U-O bond character in a series of uranyl hexaphyrin complexes: quantum chemical simulation and density based analysis” *PCCP*, March 2017.

The effect of solvation is to slightly increase topological parameters in all U-N bonds, with a commensurate small decrease in the values of the topological parameters in the U-O bonds (see Tables AII.4-AII.7). As in previous work[381,404], choice of functional appears to have consistent, small, but non-negligible effects on the QTAIM parameters (see Tables AII.6 and AII.7). For all complexes, use of the hybrid B3LYP *xc*-functional results in a small but appreciable increase in ρ_{BCP} for the U-O bond, and a small reduction in delocalisation. At the U-N BCPs, optimisation with B3LYP results in a small reduction in all properties measured compared to those obtained using PBE, implying that inclusion of a proportion of exact exchange results in increased electron localisation[27,61,381,404].

5.3.5. Analysis of the Reduced Density Gradient

As in previous chapters, visualising the $s(\boldsymbol{r})$ isosurface therefore allows the spatial regions in which equatorial U-N bonding takes place to be examined qualitatively. examine which these weakly covalent interactions are taking place. These isosurfaces, which are presented in Figure 5.9, are colour-mapped with values of $\rho(\boldsymbol{r})\mathrm{sgn}(\lambda_2)$, where $\mathrm{sgn}(x)$ is the signum function, returning a value of 1 where x is positive, and -1 where x is negative. λ_2 is the second largest eigenvalue of the Hessian of $\rho(\boldsymbol{r})$ and is typically negative for attractive interactions and positive for repulsive interactions[345]. This allows us to discriminate between attractive and repulsive interactions.

The isosurfaces, plotted at a value of $s(\boldsymbol{r}) = 0.35$, show regions of weak attraction in each of the U-N bonding regions, with the colouring corresponding to the strength of the interaction, as can be best seen for C_2b'. In all complexes, green regions may be interpreted as either weak steric repulsion or weak attraction between adjacent nitrogen atoms, although a distinction is difficult to make. As the ligands become larger and the complexes more non-planar, we find additional regions of weak interaction, between uranyl oxygen ions and nearby pyrrole units in C_4a, and between the enclosed oxygen ion and interacting meso-carbons in C_6. These latter interactions correspond to the bond paths identified between the uranium and meso-carbon centres in the QTAIM analysis and, as discussed above, are strong enough to noticeably perturb other molecular properties. Additionally, in C_6, regions of weak interaction between two pyrrolic nitrogen centres and the uranium ion are seen to extend towards the unenclosed oxygen ion, suggesting the possible presence of further ligand-oxygen interactions, although these are not identified by bond paths in the QTAIM analysis.

Scatter plots of $s(\boldsymbol{r})$ against $\rho(\boldsymbol{r})\mathrm{sgn}(\lambda_2)$, indicating the presence of largely noncovalent interactions *via* spikes which occur at low densities are given in Figure 5.10. In all complexes, $s(\boldsymbol{r})$ falls to zero at several points, corresponding to critical points in the electron density. $s(\boldsymbol{r})$ also falls to zero at some small positive values of $\rho(\boldsymbol{r})\mathrm{sgn}(\lambda_2)$, indicating the presence of weak repulsive interactions.

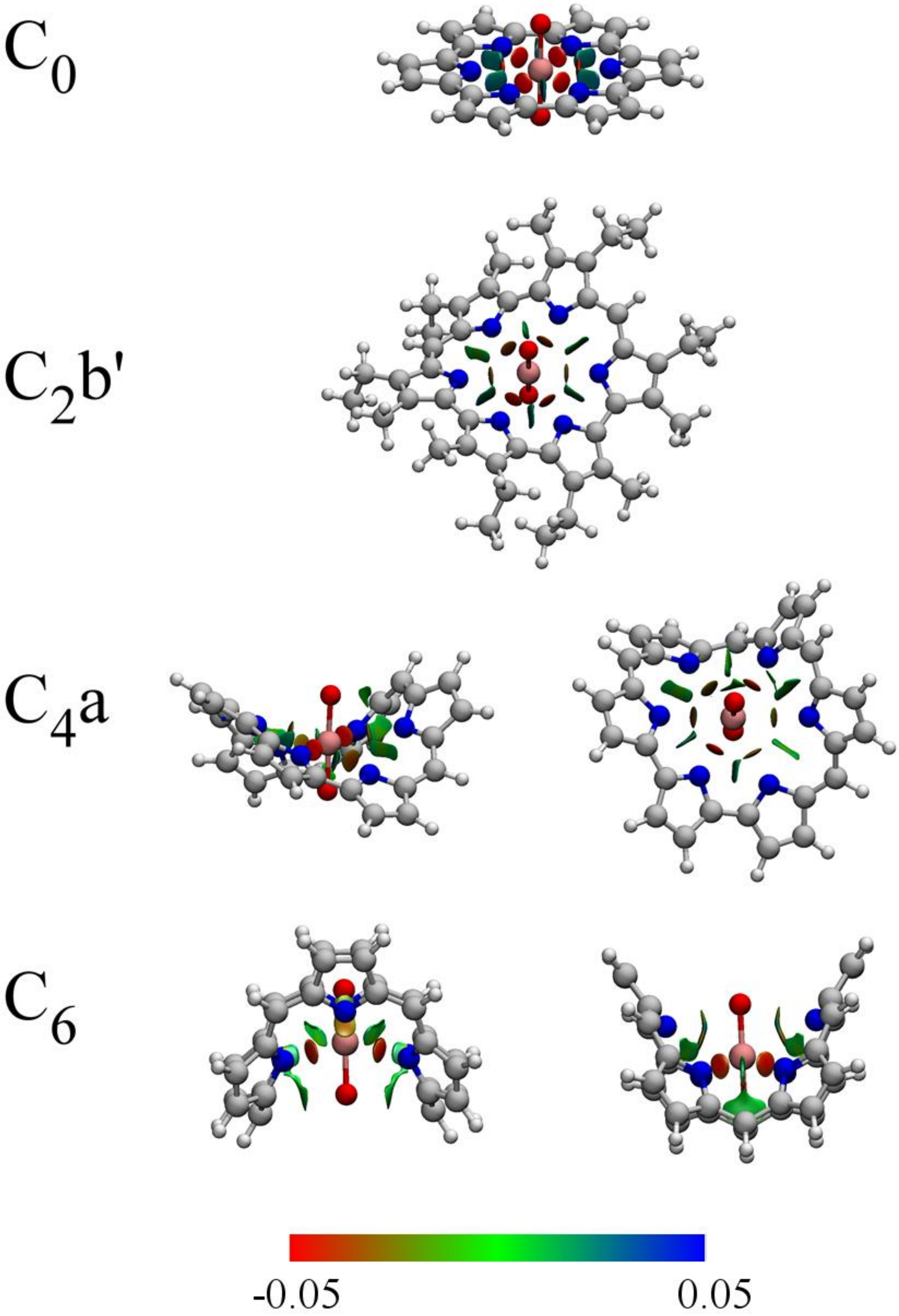

Figure 5.9: Isosurfaces of the reduced density gradient, $s(r)$, mapped with values of $\rho(r)\mathrm{sgn}(\lambda_2)$. Red regions indicate attractive interactions with weakly covalent character. Green areas indicate regions of weak interaction which may be attractive or repulsive. Isosurfaces are rendered at $s(r) = 0.35$ a.u. Reproduced from Di Pietro and Kerridge, “Ligand size dependence of U-N and U-O bond character in a series of uranyl hexaphyrin complexes: quantum chemical simulation and density based analysis” *PCCP*, March 2017.

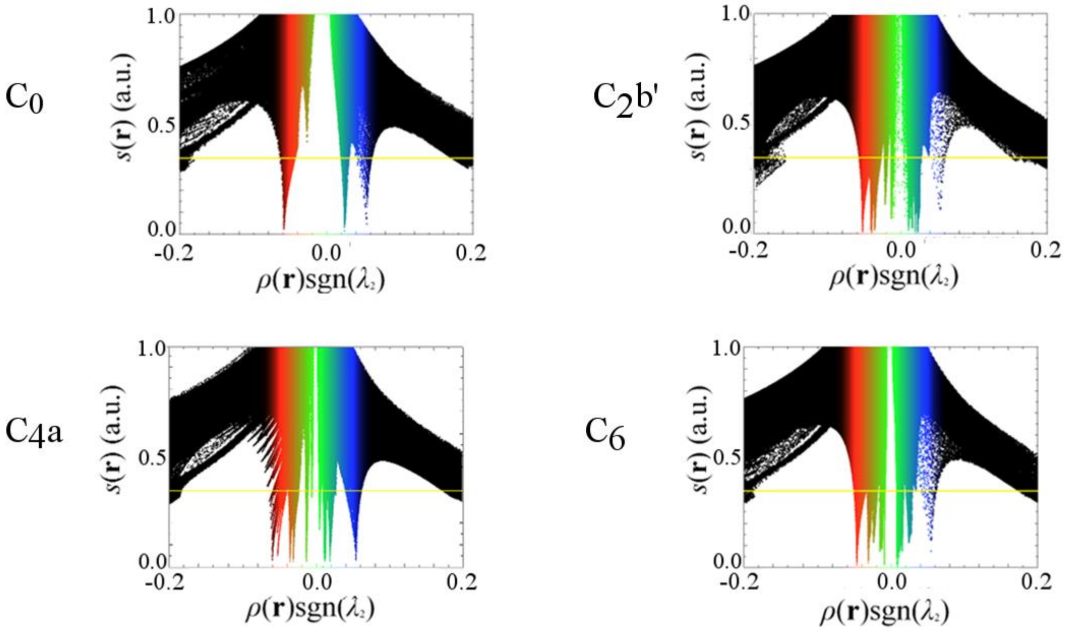

Figure 5.10: Scatter plots of the reduced density gradient against $\rho(r)\mathrm{sgn}(\lambda_2)$ coloured with values of $\rho(r)\mathrm{sgn}(\lambda_2)$ from the isosurfaces in Figure 5.9. Horizontal lines indicate isosurface value of $s(r) = 0.35$ a.u. from Figure 5.9. Reproduced from Di Pietro and Kerridge, "Ligand size dependence of U-N and U-O bond character in a series of uranyl hexaphyrin complexes: quantum chemical simulation and density based analysis" *PCCP*, March 2017.

5.3.6. Integrated Properties of the Electron Density

Using the atomic populations, localisation and delocalisation indices associated with the uranyl unit, the accumulation and depletion of charges which occur upon complexation can be further probed. The population and localisation of the uranyl unit, as defined in Chapters 3 and 4, are used:

$$N(\mathrm{UO_2}) = N(\mathrm{U}) + \sum_{i=1,2} N(\mathrm{O}_i) \qquad (Eq.5.1)$$

$$\lambda(\mathrm{UO_2}) = \lambda(\mathrm{U}) + \sum_{i=1,2} [\lambda\mathrm{O}_i + \delta(\mathrm{U},\mathrm{O}_i)] + \delta(\mathrm{O},\mathrm{O}) \qquad (Eq.5.2)$$

Where $N(\mathrm{UO_2})$ gives the electronic population of the uranyl unit as a whole, and $\lambda(\mathrm{UO_2})$ the number of electrons localised on the uranyl unit. In the case of free $\mathrm{UO_2}^{2+}$, $N(\mathrm{UO_2}) = \lambda(\mathrm{UO_2}) = 106$ but, when complexed, deviations from this value allow insight into the nature of the interaction between the uranyl unit and the ligand. Table 5.10

gives the atomic populations, localisation and delocalisation data for the uranyl units in each complex, as well as those of isolated uranyl.

	UO_2^{2+}	C_0	C_2b'	C_4a	C_6
N(U)	88.84	89.19	89.17	89.17	89.17
N(O)	8.58	8.86	8.84, 8.85	8.84	8.84
λ(U)	86.52	86.05	86.13	86.15	86.16
λ(O)	7.35	7.71	7.69	7.66	7.63, 7.61
δ(U,O)	2.32	1.92	1.97	1.98	1.96
$\delta(O_1,O_2)$	0.13	0.10	0.10	0.10	0.10
$N(UO_2)$	106.00	106.90	106.86	106.84	106.85
$\lambda(UO_2)$	106.00	105.40	105.56	105.52	105.41
$N(UO_2) - \lambda(UO_2)$	0.00	1.50	1.30	1.32	1.44

Table 5.10: Integrated properties associated with the uranyl ions of each complex. Data is from structures calculated using the PBE *xc*-functional in the gas phase.

These data allow the effect of equatorial complexation by each of the ligands on the uranyl unit to be quantified. This effect is broadly similar for each of the four complexes, differing only in magnitude. For all complexes $N(UO_2)$ is found to be greater than 106 and, as found in the comparison of C_2b, C_2b' and $[UO_2(BTP)_2]^{2+}$ [404] in Chapter 4, approximately 0.8 – 0.9 a.u of electronic charge is donated into the uranyl unit. This additional charge is distributed between the uranium ion and each of the oxygen ions and therefore acts to increase the electrostatic repulsion between the ions.

It might be expected that the localisation index, *i.e.* the amount of electronic charge density localised on an ion, may be used to estimate the strength of an ionic interaction. In all four complexes, greater electron localisation is present on the oxygen centre compared to free uranyl, alongside a decrease in localisation on the uranium centre, demonstrating that complexation results in increased ionic interaction.

Additionally, for all complexes, a reduction in the delocalisation index of the U-O bond, δ(U,O), which can be considered an alternative measure of bond covalency, is apparent upon complexation, indicating a reduction in the covalent interaction. This provides evidence that the ionic character of the U-O_{yl} bond is enhanced by equatorial complexation, and the elongation and weakening of the U-O_{yl} bond can thus be understood to originate from the fact that this increased ionic interaction comes at the expense of U-O_{yl} bond covalent interaction. The lengthening and weakening of the U-O bond compared to free uranyl seen in all four complexes investigated here can therefore be attributed to these factors. As might be expected, the effects are most pronounced for C_0, with $N(UO_2)$ being 0.9 a.u. greater and $\lambda(UO_2)$ 0.6 a.u. less than in free uranyl. These values, combined, suggest he greatest amount of electron delocalisation between the uranyl and the ligand, commensurate with the topological data which demonstrates that C_0 has the largest U-N covalent bond character.

In terms of charge donation onto the uranyl unit, C_2b' and C_4a are similar to one another. C_6 exhibits similar donation to these complexes, but less of this charge is actually localised on the uranyl unit, with C_6 having a $\lambda(UO_2)$ value more comparable to that of C_0, suggesting greater uranyl-ligand delocalisation than can be accounted for by considering the values of $\delta(U,N)$. C_6 also has the smallest amount of electronic charge localised on the oxygen centres and the largest amount localised on the uranium centre. This can be explained in terms of the additional interactions between the uranyl oxygen centres and the ligand in this complex. Table 5.9 shows that, in total, an additional ~0.07 a.u. of charge is delocalised in the interactions between the enclosed oxygen centre with the nearby meso-carbons, which partially accounts for the difference between C_6 and C_2b′/C_4a. Based on the RDG isosurface of C_6, further examination of the integrated properties reveals that 0.09 a.u. of charge is delocalised between the unenclosed oxygen ion and each of the two nearby nitrogen atoms, contributing to the lower than expected $\lambda(UO_2)$ value found in C_6 and suggesting that, while ligand-uranyl interactions in planar complexes may be fairly straightforward, in larger, less planar complexes, there are potentially many other interactions which need to be considered in order to explain the charge redistribution in the uranyl unit. This O-N electron sharing also exists in the other complexes considered, but its magnitude is typically only ~50% of that found in C_6.

Solvation, irrespective of which functional is used (see Tables AII.9 and AII.11), results in slightly higher values of $N(UO_2)$ for all four complexes, while $\lambda(UO_2)$ remains largely unchanged. Reoptimisation with B3LYP (see Tables AII.10 and AII.11) results in greater localisation compared to the PBE data, as reported in the topological properties. Also apparent are lower values of $N(UO_2)$ (by ~0.1 a.u.) and higher values of $\lambda(UO_2)$ (by ~0.01 a.u.)

5.3.7. Electron Density Difference Distributions

Finally, electron density difference distributions are used to qualitatively examine the changes undergone by the system upon complexation. The density difference distributions in Figure 10 are generated by subtracting the electron density of uranyl and ligand fragments held at the coordination geometry from the electron density of the complex. This leaves a map of the changes that occur when a complex is formed, with regions of electron density accumulation coloured blue and depletion coloured in green. Regions of depletion on the ligands are evidence of electron donation from the ligand, and the teardrop shaped regions of accumulation in each U-N bonding region may be interpreted as evidence of covalent interactions. It is possible, particularly in C_0 and C_2b', to see that the size of these regions of accumulation varies between the different U-N bonds. The regions of accumulation in C_0 are large and well-focused on the bonds whereas C_2b', exhibits smaller regions for the longest, least covalent bonds and larger regions for the shorter, more covalent interactions. The study[381] in Chapter 3 has shown that for more ionic uranyl-ligand interactions, these regions of charge accumulation are more diffuse.

The striking changes undergone by the uranyl unit lend qualitative support to the assertion that there is a significant redistribution of charge in the uranyl unit upon complexation, based on the calculated increased U-O bond lengths, redshifted frequencies of the uranyl stretching modes, uranyl deformation energies and decreased U-O delocalisation, all compared to free UO_2^{2+}. The charge accumulation on the oxygen ions and depletion in the U-O interaction region upon complexation potentially signifies the involvement of density formally associated with the uranium centre with bonding in the U-N region. The depletion in the U-O bond regions is also consistent with a reduction in the covalent character of these bonds, while accumulation on the uranyl oxygen ions and uranium ion suggests that the U-O interaction is, in accord with our other analyses, becoming more ionic upon complexation. In addition to this, charge accumulation around the uranium centre appears to have some f-like character (see Figure 5.12). The size of the regions of accumulation and depletion on the uranyl unit appear to be related to the interactions in the U-N region, *i.e*. as the amount of electron sharing in the U-N bonds is increased, the effects on the uranyl unit become more pronounced.

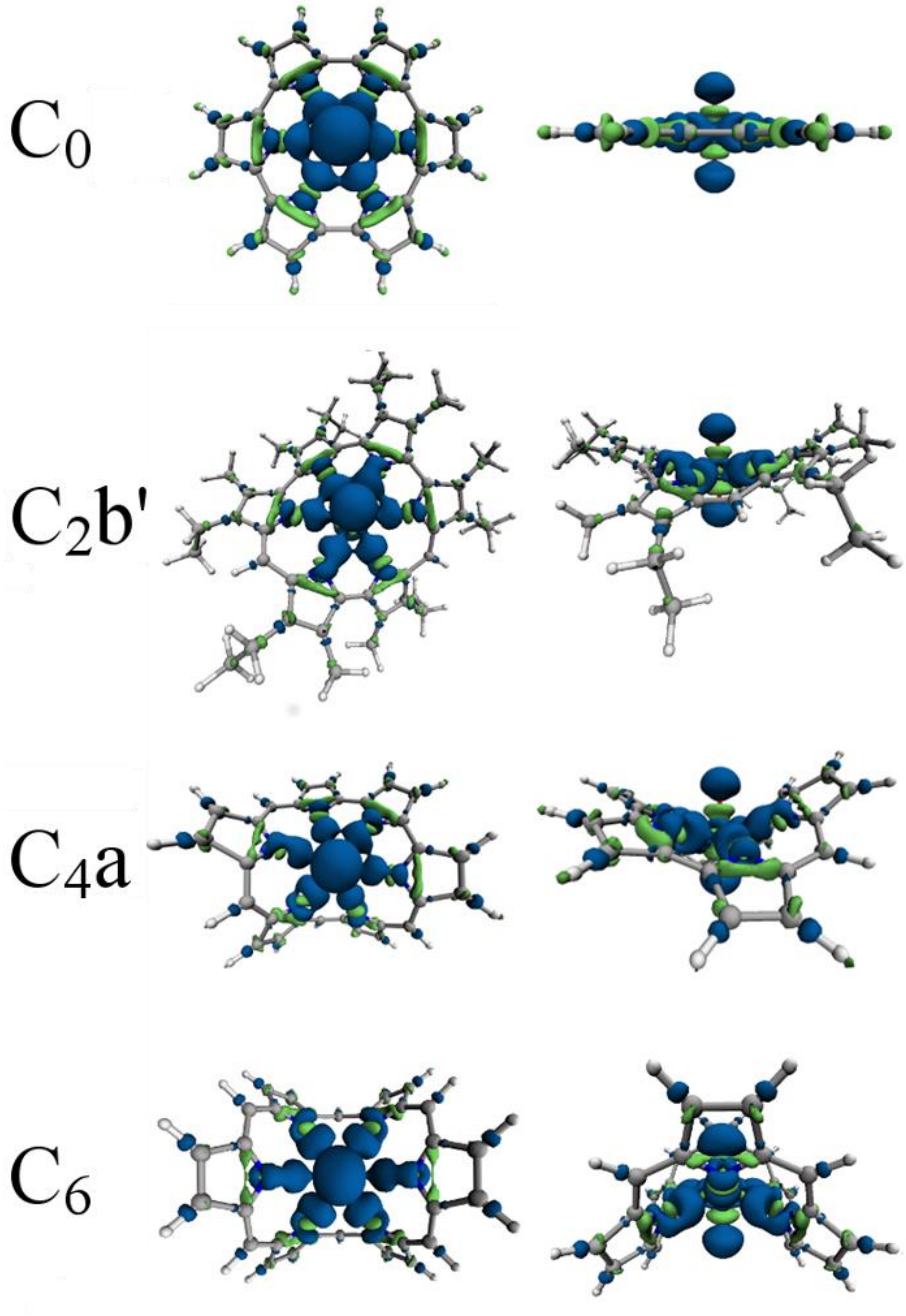

Figure 5.11: Electron density differences upon complexation viewed from above, and in the plane of, the ligand. Blue regions indicate charge accumulation and green areas charge depletion. All densities visualised using an isosurface of $\rho = 0.005$ a.u. Reproduced from Di Pietro and Kerridge, “Ligand size dependence of U-N and U-O bond character in a series of uranyl hexaphyrin complexes: quantum chemical simulation and density based analysis” *PCCP*, March 2017.

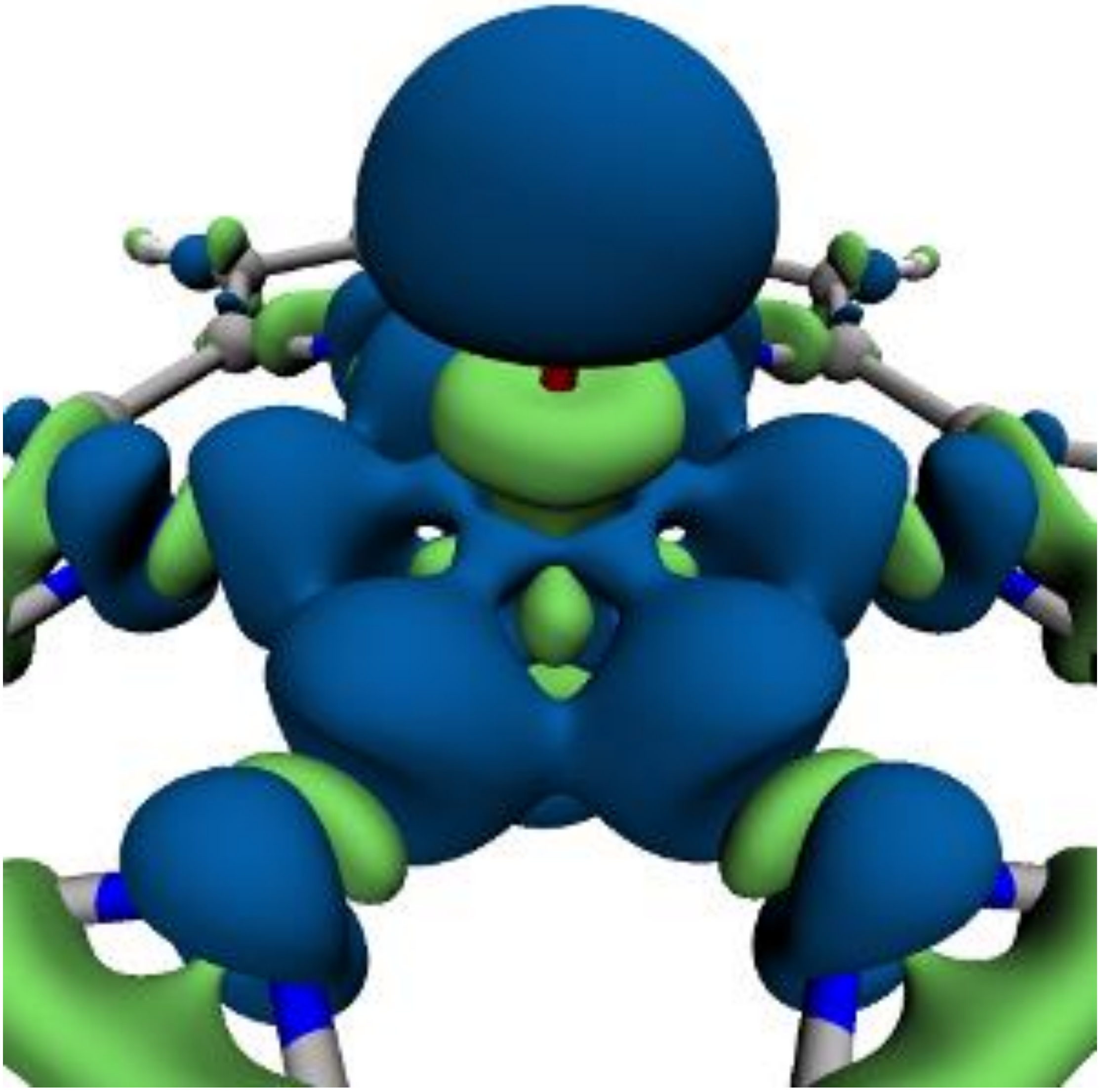

Figure 5.12: Close up view of the U-N bonding region in a density difference distribution from C_0, showing teardrop-shaped regions of accumulation (blue) and depletion (green) around the uranium atom. Reproduced from Di Pietro and Kerridge, "Ligand size dependence of U-N and U-O bond character in a series of uranyl hexaphyrin complexes: quantum chemical simulation and density based analysis" *PCCP*, March 2017.

5.4. Summary and Conclusions

We have investigated by means of quantum chemical calculations and a range of density based analyses the U-N and U-O interactions of several uranyl hexaphyrin complexes. It has been determined through a comparison of the geometries of simplified and peripherally substituted complexes that it is of great importance when dealing with systems such as these to ensure that the effects of common simplifications such as the removal of alkyl groups are indeed minimal. This is especially important when dealing with hypothetical complexes. It was found that in most, but not all, cases that removal of the alkyl groups had little geometrical impact.

Initially a relationship was established between complex stability and ligand size, as well as a weak relationship between stability and uranyl stretching mode frequencies, when a set of eight complexes were considered. This relationship was significantly weaker than that found by in Chapter 4, but could be strengthened by omitting the anomalous data associated with the C_6 complex. Subsequently, justification for considering the C_6 complex as being qualitatively different from the others was found in the density based analysis.

A representative set of four complexes was selected for further analysis. We found a relationship between complex stability and the degree of covalent character as defined by the total value of ρ_{BCP} in the U-N bonds in these complexes. The magnitude of the energy density, H, is also higher for these U-N BCPs than in any other complex. Additionally, there is unambiguous evidence of electron sharing in all U-N bonds, and this is at a maximum for C_0. This complex has short, strong U-N bonds and, commensurately, we see the largest effects on the uranyl unit here: complex C_0 has the most significant reduction in U-O bond covalency when compared to free uranyl, the most significant U-O bond lengthening, and pays the greatest energy penalty in terms deformation of the uranyl unit. Despite this, it is the most stable complex of any we have investigated here, which may, in part, be due to covalent stabilisation from the relatively large amount of electron sharing in the U-N bonds.

Electron delocalisation and covalent character as defined by values of ρ_{BCP} and H in the U-N bonds is reduced for C_2b′, C_4a, and C_6, although not drastically so, and these all have bond lengths which are comparable due to the flexibility of the ligands, which contort to better fit the uranyl dication in the cavity. There is an energy penalty for this, however and there is a decrease in stability in the order C_0 > C_2b′ > C_4a > C_6, a trend which appears to be replicated experimentally: the C_0 and C_2b′ complexes are known synthetically, while C_4a and C_6 are not. This energy penalty can be seen using both the molecular binding energies and the ligand deformation energies which decrease and increase, respectively, with increasing ligand size.

There is also a limit as to how much this ligand distortion can act to increase the covalent character of the U-N bonds; a notable plateau is found in terms of both stability and U-N covalent bond character for C_4a and C_6. When the frequencies of the uranyl stretching modes are considered, The C_6 data is anomalous, falling somewhere between that of the C_2b′ and C_4a complexes. With all complexes but C_6, as in the previous study of complexes involving coordination by 1st row species[381] in Chapter 3, there is a degree of equatorial planarity. The interactions between the nitrogen ligands and the uranium ion are more or less perpendicular to the U-O_{yl} axis and, as such, the ligands only interact directly with the U atom and this in turn affects the U-O interaction. However in the C_6 complex we see additional interactions between the uranyl oxygen ion enclosed by the ligand and two of the ligand meso-carbons, confirmed by QTAIM analysis and RDG isosurface plots, which also indicate the presence of weak interactions between two pyrrolic nitrogens with the other oxygen ion. These interactions, although weak, act to perturb the frequencies of the uranyl stretching modes as well as the topological and integrated properties of the uranyl unit.

We see dramatic and consistent changes to the uranyl unit upon complexation which are related to the covalent character of interactions in the U-N bonding region as well as the stability of the complex. This is evident in U-O bond lengths, the frequencies of the distinctive uranyl stretching modes (with the exception of C_6, as discussed above), values of QTAIM descriptors and integrated charges, and can be visualised *via* electron density difference distributions. These add qualitative support to our assertions that electron density is redistributed in the uranyl unit upon equatorial complexation, with the magnitude of this redistribution related to the magnitude of the equatorial covalent interaction. Density difference distributions also clearly show charge accumulation in the U-N bonding regions, providing qualitative evidence of electron sharing in these interactions.

Analysis of the reduced density gradient allowed visualisation of the regions of weakly covalent interaction in all complexes, with weak attractive regions corresponding to each U-N bond found in all cases and, in the C_6 complex, additional interactions between the uranyl oxygen ions and the ligand identified.

Ultimately, it can be concluded that hexaphyrin ligands coordinate uranyl in a broadly similar way to one another, with the uranium atom coordinated *via* largely ionic interactions with small but measurable amounts of covalent character, to six pyrrolic nitrogen atoms. However, the size of the ligand core has pronounced effects on complex stability. U-N covalent character is found to correlate strongly with bond length, however ligand flexibility and its effects (shortened and thus more covalent U-N bonds, but a loss of stability) mean that no clear relationship can be identified between equatorial covalency and stability in these complexes. However, the interesting changes to the electronic structure of the uranyl unit upon complexation suggest that expanded porphyrins are useful systems for investigating the effects of complexation on the uranyl bond.

The complicating factor of additional interactions caused by the proximity of the ligand in C_6 suggest that investigation of complexes which have well-defined planarity may be preferable The fact that the most stable complex, C_0, is obtained using the ligand with the smallest core suggests that a fruitful avenue of future research may be into pentapyrrolic complexes of uranyl, of which there are several experimentally realised examples including uranyl pentaphyrin[21] and uranyl superphthalocyanine[406].

5.6. Publication Notes

Work from this chapter was published in:

Poppy Di Pietro and Andrew Kerridge, “Ligand size dependence of U-N and U-O bond character in a series of uranyl hexaphyrin complexes: quantum chemical simulation and density based analysis”, *PCCP*, 2017 (Ref [407]).

6. Results: AnO_2^{2+}(An = U, Np, Pu) Complexes with Hexaphyrin Ligands Investigated Using DFT

6.1. Introduction

Sessler *et al*. have reported the NpO_2^+ and PuO_2^+ complexes of the expanded porphyrin ligand isoamethyrin(1.0.1.0.0.0)[35,190] and of the related ligand amethyrin(1.0.0.1.0.0)[35]. Formation of the abovementioned complexes was confirmed *via* dramatic changes to the UV-vis spectra and associated ^1H NMR spectra, although, except for the case of Np(V)O_2-isoamethyrin(1.0.1.0.0.0), crystallographic data could not be obtained meaning the bond lengths of these are not known. It is interesting to consider that the Pu(V)O_2-isoamethyrin(1.0.1.0.0.0) and Pu(V)O_2-isoamethyrin(1.0.1.0.0.0) complexes, unlike the U(VI)O_2-isoamethyrin(1.0.1.0.0.0) complex, could be formed without heating. This is because the complexes were formed from NpO_2^{2+} and PuO_2^{2+}, both readily reduced to NpO_2^+ and PuO_2^+, *i.e*. Np(V) and Pu(V), aiding the oxidation of the macrocycle. Uranium, however prefers the (VI) oxidation state, so the macrocycle must undergo air-based oxidation: a process which requires ~24 hours or the addition of heat. This led the Sessler group to suggest that, due to the dramatic spectroscopic changes undergone by the macrocycle upon complex formation, the possible use of isoamethyrin(1.0.1.0.0.0) as an actinide-specific sensor[35,133]. The formation of actinyl complexes with pentaphyrin and several other expanded porphyrin type molecules[21,35,36,129,134,154,217] have also been reported suggesting that these macrocyclic systems are interesting targets for investigating the An-N interaction. In addition, there are many expanded porphyrins for which actinide/actinyl complexes are not known and these can be read about in more detail in Chapter 1 and several referenced resources[129,132,139,141,142,146,147,149,166,203,398,401,403].

In the previous chapter, uranyl complexes with eight different hexaphyrin ligands were optimised with a representative sample of four complexes investigated in detail. Evidence for equatorial covalency was found in all U-N bonds, with the magnitude of this covalency dependent on the size and shape of the ligand. In this chapter, three of the four UO_2^{2+} expanded porphyrin complexes examined in detail in the previous chapter, UO_2-cyclo[6]pyrrole, UO_2-isoamethyrin(1.0.1.0.0.0)′ and UO_2-rubyrin(1.1.1.1.0.0) are compared to NpO_2^{2+} and PuO_2^{2+} analogs. Complexes with the hexaphyrin(1.1.1.1.1.1) ligand examined in Chapter 5 are omitted here due to the complications in interpreting changes to the U-O interaction caused by additional ligand-oxygen interactions in the uranyl complex.

In this study, NpO_2^{2+} and PuO_2^{2+} are investigated rather than NpO_2^{+} and PuO_2^{+} which represent Np/Pu(V) and are more commonly found experimentally[35,38,75,76,79,408,409]. This allows direct comparison with the uranyl U(VI) complexes, for which there is crystallographic data in the case of the cyclo[6]pyrrole and isoamethyrin complexes[133,187].

As in previous chapters, geometry optimisations have been performed at the Density Functional level of theory, utilising the spin unrestricted approach. Density based analysis has been performed to qualitatively and quantitatively investigate the An-N and An-O bonding. Topological analysis using QTAIM[348] has been used to investigate and compare covalent character in the An-N and An-O bonds, and integrated properties of the electron density have been used to probe the changes that occur upon complexation. These changes have been visualised using density difference distributions upon complexation. Subsequently, single-point energy calculations using the spin-constrained approach[410] were performed at the optimised geometries of all open shell complexes to investigate to what extent this would remedy what was found to be significant spin contamination in some complexes. This approach has been successfully used for open-shell actinide complexes in the past[61].

6.2. Computational Details

As in previous chapters of this thesis, Density Functional Theory (DFT) calculations have been performed using version 6.4 of the TURBOMOLE quantum chemistry software package[359]. Ahlrichs def2 basis sets of triple-zeta quality have been applied to the C, H, O and N atoms[369] and the Ahlrichs def basis set of triple-zeta quality including a relativistic ECP comprising 60 core electrons[285] has been applied to the U, Np and Pu atoms. The exchange-correlation energy was approximated using the PBE *xc*-functional[333] based on the generalised gradient approximation (GGA). Initial optimisations were carried out in the gas phase.

Subsequently, the COSMO continuum solvation model[360] with a relative permittivity of 8.9 was used to simulate solvation in DCM, for which there is experimental precedent[133] for actinyl hexaphyrin complexes, but as structural differences were minimal, data obtained using the COSMO model are not discussed in the text. Justification for this lies in the data presented in Chapters 4 & 5, where minimal differences in topological and integrated properties of the electron density were found in these complexes when a solvent is used.

Vibrational analysis was performed to ensure structures were energetic minima. Optimisations were subsequently performed using the B3LYP hybrid GGA functional[373,374] to investigate the effects of the inclusion of exact exchange.

For further analyses of the electron density, single point energy calculations were performed on the optimised geometries using the SARC all electron basis set[370] and the Douglas-Kroll-Hess (DKH) Hamiltonian to account for scalar relativistic effects[313,314]. This was necessary due to AIMAll requiring a .wfx rather than a .wfn file in order to calculate integrated properties of the electron density where an ECP is used, which at the time, could not be generated from TURBOMOLE data output files.

QTAIM analysis was then performed using the Multiwfn[363] and AIMAll[364] codes to calculate various topological and integrated properties of the electron density. Electron density difference distributions were visualised using the VMD code[365]. Although open shell $\mathrm{NpO_2^{2+}}$ and $\mathrm{PuO_2^{2+}}$experience effects due to the spin orbit coupling, this was omitted for the purposes of this study. It has been previously demonstrated that inclusion of spin orbit coupling effects has very little impact on molecular geometries[240] and therefore can be predicted to have little effect on bonding character.

Subsequently, single-point energy calculations were performed at the optimised geometries using spin-constrained DFT[410] to investigate the effects on the electronic structure of treating what was found to be significant spin contamination. Ideally, complexes would have been reoptimised with spin constraint, however due to time constraint and computational expense, this was not possible. The purpose of spin constrained calculations in this chapter therefore is intended as a preliminary study to investigate whether spin contamination can be improved by this method, and whether significant effects on topological and integrated properties of the electron density are induced by constraining the spin. A spin constraint parameter of $\tau = 0.75$ was used in all cases, as this value has previously been shown to give good results with similar systems[61]. These calculations were performed at a later time, when new functionality allowed density based analyses to be performed on densities incorporating ECPs, so the ECP was left in place and AIMALL calculations were performed using a .wfx file.

6.3. Results and Discussion

6.3.1. Isolated AnO_2^{2+}; An = U, Np, Pu

6.3.1.1. Structural and Vibrational Characterisation

It is useful to begin with an analysis of the optimised, uncoordinated actinyls. Table 6.1 contains An-O bond lengths for dicationic uranyl, neptunyl and plutonyl optimised with both the PBE and B3LYP *xc*-functionals in the gas phase, without spin constraint. Understanding the differences between the uncoordinated actinyls will provide a useful reference point for the differences between their complexes with the various ligands in this section. It can be seen that the An-O bond lengths decrease from U to Np and Pu, with a greater difference between the U-O bonds and the Np-O bonds than Np-O and Pu-O bonds. This is consistent with the reduction observed in ionic radius from U > Np > Pu[37,295,411]. Additionally, there is a functional dependence: An-O bonds are all ~0.01 Å longer with the PBE functional than when the B3LYP functional is employed.

		UO_2^{2+}	NpO_2^{2+}	PuO_2^{2+}
PBE	$r_{\text{An-O}}$	1.711	1.709	1.697
B3LYP	$r_{\text{An-O}}$	1.696	1.691	1.677

Table 6.1: An-O bond lengths in Angstrom (Å) for uncoordinated dicationic actinyls, obtained using both *xc*-functionals.

Table 6.2 contains the frequencies of the actinyl stretching modes for the three actinyls calculated using both functionals in the gas phase. It can be seen that as one moves from U to Pu, the frequencies become shifted towards lower frequencies. As with the bond lengths, differences are more pronounced between UO_2^{2+} and NpO_2^{2+} than NpO_2^{2+} and PuO_2^{2+}. Use of the B3LYP *xc*-functional results in a shift towards higher frequencies compared to the results obtained using the PBE *xc*-functional. In coordination complexes, the actinyl stretching frequencies are known to act as sensitive probes of the coordination environment[56,85,101,368,381,392,393].

xc-functional		UO_2^{2+}	NpO_2^{2+}	PuO_2^{2+}
PBE	ν_S	994.04	962.2	938.06
	ν_{AS}	1090.75	1074.16	1059.36
B3LYP	ν_S	1046.14	1020.35	999.98
	ν_{AS}	1139.43	1129.35	1118.94

Table 6.2: Symmetric (ν_S) and antisymmetric (ν_{AS}) frequencies of the stretching modes of the optimised uncoordinated actinyls in cm^{-1}.

6.3.1.2. QTAIM - Topological and Integrated Properties

Tables 6.3 and 6.4 show selected topological properties of the An-O bonds in the optimised, uncoordinated actinyls obtained using the PBE and B3LYP *xc*-functionals, respectively. It can be seen that covalent character in the U-O bond as defined by QTAIM increases as one moves from U to Pu when only the spin constraint free data are considered. This is commensurate with the reduced U-O bond lengths seen from U to Pu in Table 6.1. However, when the results of the single-point energy calculations utilising the spin constraint parameters are considered, a slight drop in An-O covalency as defined by $\rho_{\mathrm{An-O}}$ and $H_{\mathrm{An\text{-}O}}$ is observed for Np and Pu compared to the unconstrained calculations, making the Np-O bond slightly less covalent than the U-O bond. The Pu-O bond is still found to have greater covalent character than the Np-O bond. This is true for both *xc*-functionals. Values of the laplacian are increased for both neptunyl and plutonyl compared to the unconstrained values. Variations in the delocalisation index are quite small, but are more significant when the B3LYP *xc*-functional is employed.

PBE		UO_2^{2+}	NpO_2^{2+}	PuO_2^{2+}
$\rho_{\mathrm{An-O}}$	Unconstrained	0.365	0.366	0.372
	Constrained	-	0.358	0.362
$\nabla^2\rho_{\mathrm{An-O}}$	Unconstrained	0.330	0.334	0.332
	Constrained	-	0.419	0.441
$H_{\mathrm{An\text{-}O}}$	Unconstrained	-0.389	-0.387	-0.396
	Constrained	-	-0.360	-0.363
δ(An-O)	Unconstrained	2.322	2.349	2.371
	Constrained	-	2.349	2.378

Table 6.3: QTAIM parameters for the An-O bond in the uncoordinated actinyls in atomic units (a.u.) utilising the spin unconstrained and spin constrained approaches with the PBE *xc*-functional.

B3LYP		UO_2^{2+}	NpO_2^{2+}	PuO_2^{2+}
ρ_{An-O}	Unconstrained	0.381	0.385	0.394
	Constrained	-	0.374	0.383
$\nabla^2\rho_{An-O}$	Unconstrained	0.273	0.260	0.247
	Constrained	-	0.409	0.368
H_{An-O}	Unconstrained	-0.425	-0.429	-0.443
	Constrained	-	-0.392	-0.405
δ(An-O)	Unconstrained	2.272	2.306	2.336
	Constrained	-	2.352	2.344

Table 6.4: QTAIM parameters for the An-O bond in the uncoordinated actinyls in atomic units (a.u.) utilising the spin unconstrained and spin constrained approaches with the B3LYP *xc*-functional.

As seen in previous chapters of this thesis, the values of the topological parameters have a functional dependence. Use of the B3LYP functional results in a small increase in the covalent character of the An-O bonds, commensurate with the small decrease in B3LYP-optimised bond lengths compared to those obtained using the PBE *xc*-functional.

Next, integrated properties are considered. Two properties defined in previous chapters as the atomic population of the uranyl unit as a whole and the uranyl localisation as a whole are extended to Np and Pu:

$$N(\mathrm{AnO_2}) = N(\mathrm{An}) + \sum_i N(\mathrm{O}_i) \qquad [Eq.6.1]$$

$$\lambda(\mathrm{AnO_2}) = \sum_{i=\mathrm{An,O}} \left[\lambda(i) + \frac{1}{2}\sum_{j=\mathrm{U,O}\neq i} \delta(i,j)\right] \qquad [Eq.6.2]$$

Where in the optimised, uncoordinated actinyl dications, $N(\mathrm{AnO_2})$ = $\lambda(\mathrm{AnO_2})$ = 106, 107 and 108 for An = U, Np and Pu, respectively.

	xc-functional	UO_2^{2+}	NpO_2^{2+}		PuO_2^{2+}	
			Unconstrained	Constrained	Unconstrained	Constrained
N(O)	PBE	8.58	8.49	8.49	8.43	8.43
	B3LYP	8.65	8.56	8.51	8.49	8.49
N(An)	PBE	88.84	90.02	90.01	91.15	91.14
	B3LYP	88.71	89.88	89.99	91.02	91.01
N(AnO_2)	PBE	106.00	107.00	107.00	108.00	108.00
	B3LYP	106.00	107.00	107.00	108.00	108.00

Table 6.5: Atomic populations in a.u. for the uncoordinated actinyls An = U, Np, Pu for both *xc*-functionals with and without spin constraint for the neptunyl and plutonyl.

Tables 6.5 and 6.6 show that for both *xc*-functionals investigated, as one crosses from U to Pu, there is a reduction in both atomic population and localised charge on the oxygen ions, which combined with increased An-O electron delocalisation culminates in a reduced ionic and increased covalent interaction from $\mathrm{UO_2^{2+}}$ to $\mathrm{NpO_2^{2+}}$ to $\mathrm{PuO_2^{2+}}$ as has been reported before[52,412]. Differences between the spin unconstrained and spin constrained approaches are minimal.

	xc-functional	$\mathrm{UO_2^{2+}}$	$\mathrm{NpO_2^{2+}}$		$\mathrm{PuO_2^{2+}}$	
			Unconstrained	Constrained	Unconstrained	Constrained
$\lambda(\mathrm{O})$	PBE	7.35	7.23	7.23	7.14	7.13
	B3LYP	7.45	7.33	7.24	7.23	7.23
$\lambda(\mathrm{An})$	PBE	86.52	87.67	87.66	88.78	88.77
	B3LYP	86.44	87.58	87.64	88.68	88.67
$\delta(\mathrm{An\text{-}O})$	PBE	2.32	2.35	2.35	2.37	2.38
	B3LYP	2.27	2.31	2.35	2.34	2.34
$\delta(\mathrm{O_1\text{-}O_2})$	PBE	0.13	0.17	0.17	0.21	0.21
	B3LYP	0.11	0.15	0.17	0.18	0.18
$\lambda(\mathrm{AnO_2})$	PBE	106.00	107.00	107.00	108.00	108.00
	B3LYP	106.00	107.00	107.00	108.00	108.00

Table 6.6: Localisation and delocalisation indices in a.u. for the uncoordinated actinyls An = U, Np, Pu.

6.3.2. Spin Contamination Analysis for Unconstrained Systems

All complexes investigated in this chapter are neutral, with formally dianionic ligands and dicationic actinyls. Assuming no open shells on the ligand, there should be one unpaired f-electron present in all neptunyl complexes. The spin multiplicity $S(S+1)$ gives rise to an expectation value of the S^2 operator, $\langle S^2 \rangle$, of 0.75. Similarly, the plutonyl complexes should each have two unpaired f-electrons, giving rise to an expectation value of the S^2 operator, $\langle S^2 \rangle$, of 2.0. Spin contamination, which can be understood as a mixing of electronic spin states, is known to be a problem when performing DFT calculations on open-shell systems[410,413,414], so it is necessary to examine the neptunyl and plutonyl complexes for signs of spin contamination. This data is presented in Table 6.7, showing that spin contamination is a serious problem for these systems, and this is most severe for the plutonyl systems. In the cyclo[6]pyrrole systems, $\langle S^2 \rangle$ is approximately twice what it should be for the neptunyl complexes although the atomic spin population analysis of the neptunyl atom deviates from the formal spin by approximately 10-15%, not an unreasonable amount considering that formal spin assumes completely localised electron density.

		xc-functional	$\langle S^2 \rangle$	$N_s(A)$	$\Delta N_s(A)$
0.0.0.0.0.0	Np	PBE	1.54	1.10	0.10 (10%)
		B3LYP	1.83	0.87	-0.13 (13%)
	Pu	PBE	2.99	0.01	-1.99 (99%)
		B3LYP	2.99	0.01	-1.99 (99%)
1.0.1.0.0.0'	Np	PBE	0.76	1.14	0.14 (14%)
		B3LYP	0.76	1.11	0.11 (11%)
	Pu	PBE	2.09	2.34	0.34 (17%)
		B3LYP	2.03	2.23	0.23 (12%)
1.1.1.1.0.0	Np	PBE	0.88	1.29	0.29 (29%)
		B3LYP	1.76	1.10	0.10 (10%)
	Pu	PBE	2.43	2.68	0.68 (34%)
		B3LYP	3.05	3.22	1.22 (61%)

Table 6.7: The expectation value $\langle S^2 \rangle$, atomic spin population of atom A ($N_s(A)$), the difference between the atomic spin population and formal spin ($\Delta N_s(A)$) and this difference expressed as a percentage of the formal spin.

The plutonium atoms in the plutonyl cyclo[6]pyrrole complexes, with $\langle S^2 \rangle \approx 3$, have values of N_s(Pu) which indicate an equal alpha and beta population, at odds with the MO occupation which indicates that the complex has two additional alpha electrons than beta electrons. It appears in this case that these although the two unpaired electrons are present in the complex, they are not located on the plutonium centre. The expectation value $\langle S^2 \rangle$ again suggests significant spin population must be present in the ligand.

The isoamethyrin(1.0.1.0.0.0)′ complexes are approximately as they should be. Spin population is higher in the plutonyl isoamethyrin(1.0.1.0.0.0)′ complexes, as would be expected, and is slightly reduced by use of the B3LYP *xc*-functional.

The rubyrin complexes are again problematic. Considering the neptunyl complexes, The expectation value $\langle S^2 \rangle$ when the PBE functional is used is much too high. Employing the B3LYP *xc*-functional appears to make the situation worse. The atomic spin population analysis demonstrates a deviation from the formal spin of ~30% when the PBE *xc*-functional is used, reducing to 10% when the B3LYP *xc*-functional is employed. Considering the plutonyl rubyrin complex, it is clear that when the PBE *xc*-functional is used that there is significant spin contamination manifesting as a high $\langle S^2 \rangle$ and an atomic spin population for the plutonium atom which deviates from the formal spin by ~ 30 %. When the B3LYP functional is employed, the data is indicative of a change in oxidation state of the plutonium atom rather than spin contamination, with the atomic spin population deviating from the formal spin by 61% if the formal spin is 2, but only 7.33% if the formal spin is 3. This conclusion is supported by examination of the integrated properties and the visualisation of the spin density in this complex, which will be explored later in the chapter.

There is considerable evidence for the model chemistries employed here being insufficient for modelling open shell actinides. It is interesting to note that complexes with the isoamethyrin(1.0.1.0.0.0)′ ligand are the best behaved computationally in addition to isoamethyrin(1.0.1.0.0.0)′ being the only ligand investigated here which has been experimentally observed to form complexes with Np(V) and Pu(V).

The remainder of this chapter will be informed by the results presented in this section. The next section contains a full analysis of the actinyl isoamethyrin complexes, as the spin contamination in these systems is judged to be not so significant as to render the data meaningless.

Subsequently, preliminary investigations are begun focussing on attempting to resolve the spin contamination problems in the other complexes using spin-constrained DFT.

6.3.3. AnO_2-isoamethyrin(1.0.1.0.0.0)′; An = U, Np, Pu

6.3.3.1. Structural and Energetic Data

Isoamethyrin is the only expanded porphyrin ligand here investigated for which there has been an experimentally characterised uranyl, neptunyl and plutonyl complex. These are also the only complexes investigated here for which significant spin contamination was not an issue. Thus the data contained in this section was obtained using the spin-unconstrained approach, with the topological and integrated properties obtained using the spin-constrained approach at the geometry optimised with the spin unconstrained approach included for comparison.

Due to aforementioned difficulties in reproducing the experimental structure when a simplified ligand is used (Chapter 4, Chapter 5), peripheral alkyl substituents are included for each complex here, and for the sake of consistency with Chapters 4 and 5, complexes will be referred to as AnO_2-isoamethyrin(1.0.1.0.0.0)′, where the prime indicates the presence of peripheral alkyl groups. The only geometrical differences between different complexes are slight variations in bond length, with no significant structural differences to be found. Because of this, Figure 6.1 shows only the optimised geometry for NpO_2-isoamethyrin(1.0.1.0.0.0)′ optimised using the PBE *xc*-functional in the gas phase (for the uranyl complex, see Chapter 5).

Table 6.8 shows average and individual An-N and An-O bond lengths for uranyl, neptunyl and plutonyl complexes with isoamethyrin for complexes optimised using the PBE and B3LYP *xc*-functionals in the gas phase. Crystallographic data is available for the uranyl(VI) isoamethyrin complex[133,190], revealing an average U-N bond length of 2.66 Å and a U-O bond length of 1.760 Å. Both *xc*-functionals employed here replicate the average U-N bond length to within a few hundredths of an angstrom, likewise the U-O bond. Crystallographic data for the neptunyl(V) complex[190] reveals two distinct U-O bond lengths of 1.762 and 1.826 Å, and Np-N bond lengths of 2.649 to 2.880 Å, with the existence of a short contact, typical of hydrogen bonding, seen between the oxygen ion involved in the longer Np-O bond and a solvent molecule. An average Np-N bond length of 2.772 Å, somewhat greater than the average experimental U-N bond length in the uranyl(VI) complex of 2.66 Å, although the different charge state of the neptunyl complex means a comparison to calculated values cannot be made.

	U		Np		Pu	
	PBE	B3LYP	PBE	B3LYP	PBE	B3LYP
$\overline{r_{\mathrm{An-N}}}$	2.688	2.705	2.687	2.698	2.699	2.716
$r_{\mathrm{An-O}}$	1.787	1.766	1.779	1.746	1.764	1.734
$\Delta r_{\mathrm{An-N2}}$	0.076	0.070	0.070	0.055	0.067	0.057

Table 6.8: Average An-N and An-O bond lengths and $\Delta r_{\mathrm{An-O}}$, the difference between the coordinated and uncoordinated An-O bond length, all in Å for AnO_2-isoamethyrin(1.0.1.0.0.0)′ (An = U, Np, Pu) calculated using the PBE and B3LYP *xc*-functionals.

It is apparent that as one moves from U to Np, An-N bonds are very similar in length, with at most, a difference of a few thousandths of an Angstrom on average, while Np-O bonds are shorter than U-O bonds by ~0.2 Å at most. These changes occur with both functionals. Pu-N bonds are longer than Np-N and U-N bonds by a few hundredths to a few thousandths of an Angstrom on average, depending on which model chemistry is used, and Pu-O bonds are shorter than Np-O bonds by a few hundredths of an Angstrom, again independent of *xc*-functional or solvation state. All An-O bonds are longer than their uncoordinated counterparts.

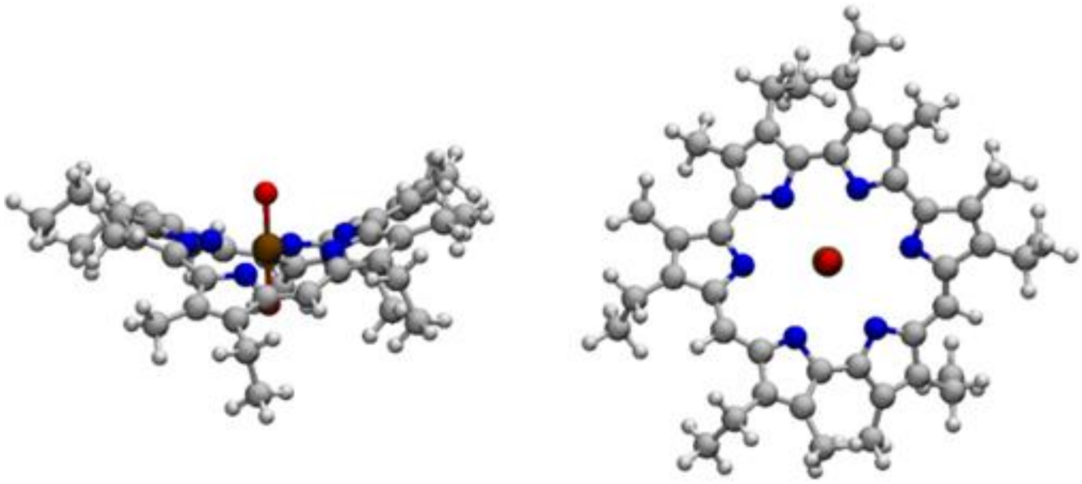

Figure 6.1: Optimised structure for NpO_2-isoamethyrin(1.0.1.0.0.0)′ generated from data obtained using the PBE *xc*-functional in the gas phase.

Considering the binding energies given in Table 6.9, the uranyl complex is found to be more stable than the neptunyl complex by ~ 0.4 – 0.5 eV, dependent on *xc*-functional. The neptunyl complex is slightly more stable than the plutonyl complex, by only 0.02 eV when the PBE *xc*-functional is used, and 0.1 eV when the B3LYP *xc*-functional is employed. The deformation adjusted binding energy shows decreasing stability in the order U > Np > Pu. The deformation energies are given in Table 6.10.

The distortion of the ligand upon complexation appears to be more or less independent of the actinide centre, and ligand deformation energy is calculated to be almost constant from U to Pu, with at most a few hundredths of an eV difference, and an overall small decrease from U to Pu. The actinyl deformation energy, which decreases by up to 0.1 eV from the neptunyl complex to the plutonyl complex, consistent with the lengthening of An-N bonds from Np to Pu, possibly suggesting that the plutonyl unit is less affected by complexation with the isoamethyrin(1.0.1.0.0.0)′ ligand than the neptunyl unit. Again, the uranyl deformation energy is in all cases higher than the neptunyl deformation energy.

When the total binding energy is considered, the uranyl complex is more stable than the neptunyl complex by ~ 0.4 – 0.5 eV, dependent on *xc*-functional. The neptunyl complex is slightly more stable than the plutonyl complex, by only 0.02 eV when the PBE *xc*-functional is used, and 0.1 eV when the B3LYP *xc*-functional is employed. The deformation adjusted binding energy shows decreasing stability in the order U > Np > Pu.

	xc-functional	U	Np	Pu
ΔE_B	PBE	-27.96	-27.52	-27.50
	B3LYP	-27.78	-27.27	-27.17
ΔE_{DA}	PBE	-29.26	-28.76	-28.54
	B3LYP	-29.02	-28.44	-28.16

Table 6.9: Binding energies and deformation-adjusted binding energies in eV for An_2-isoamethyrin(1.0.1.0.0.0)′.

	xc-functional	U	Np	Pu
E_{DU}	PBE	0.29	0.23	0.11
	B3LYP	0.28	0.16	0.05
E_{DL}	PBE	1.02	1.01	0.93
	B3LYP	0.96	1.01	0.94

Table 6.10: Deformation energies for the actinyl unit and ligand in eV for An_2-isoamethyrin(1.0.1.0.0.0)′.

6.3.3.2. Vibrational Data

Table 6.11 contains the frequencies of the actinyl stretching modes for uranyl, neptunyl and plutonyl isoamethyrin(1.0.1.0.0.0)′. As mentioned in Chapters 4 and 5, the peripherally substituted isoamethyrin complexes have many more atoms than the simplified complexes studied and as such, calculations, particularly calculations where the hybrid B3LYP *xc*-functional is employed, are very computationally expensive. In this case, it was decided that numerical force calculations on the peripherally substituted complexes optimised with the B3LYP *xc*-functional could be omitted, meaning that here it is only the vibrational frequencies of the structures optimised with the PBE *xc*-functional which are reported.

As one moves from uranyl to the neptunyl complex, the frequency of the symmetric stretching mode decreases by ~15 cm^{-1} in the case of structures optimised in the gas phase. The asymmetric stretching mode is found to be ~5 cm^{-1} greater in the neptunyl complex than the uranyl complex. The frequencies for the uranyl complex are shifted ~160-170 cm^{-1} compared to uncoordinated uranyl, with the asymmetric mode being more significantly shifted. The shifts of the neptunyl stretching modes are somewhat smaller, ~140-155 cm^{-1} with the asymmetric mode again being the most significantly affected. Both plutonyl stretching modes are shifted by ~145 cm^{-1}.

		U		Np		Pu	
		ν	Δ	ν	Δ	ν	Δ
PBE	ν_S	834.35	-159.69	820.61	-141.59	793.20	-144.86
	ν_{AS}	921.88	-168.87	923.42	-150.74	915.29	-144.07

Table 6.11: Frequencies of the actinyl stretching modes in the optimised AnO$_2$-isoamethryin(1.0.1.0.0.0)′ complexes in cm^{-1} and, Δ, their shifts respective to the uncoordinated actinyls in Table 6.2.

In general, a lowering of frequency is calculated moving from uranyl to plutonyl. The asymmetric mode for the neptunyl complex is slightly higher than the same mode for the uranyl complex, indicating the gap between the frequencies is increased for neptunyl. Shifts relative to uncoordinated actinyls suggest that the uranyl unit is the most significantly affected.

6.3.3.3. QTAIM - Topological and Integrated Properties

Tables 6.12 and 6.13 show topological QTAIM parameters for An-N bonds in isoamethyrin complexes optimised with the PBE and B3LYP *xc*-functionals, respectively. In Tables 6.22 and 6.23, ρ, H and $\delta(\mathrm{An}-\mathrm{N})$ are summed over, as it makes sense to consider the effect of the ligands as a whole. Summing over the $\nabla^2\,\rho_{\mathrm{An-N}}$ however, is unphysical so an average value has been used. Tables 6.14 and 6.15 show topological parameters of the An-O bonds for the same complexes. Total and average properties at the An-N BCP reflect a decrease in equatorial covalency as the central ion is changed across the series from U to Pu with both *xc*-functionals. Delocalisation indeces show, with both *xc*-functionals, a small increase from U to Np, while the value for the Pu complex is lower than both U and Np. The effects on $\sum\rho_{\mathrm{An-N}}$ of using the spin constraint are seen as small increases for both the neptunyl and plutonyl complexes, with larger differences being induced by changing the *xc*-functional. The effect of the spin constraint on the laplacian was a reduction, bringing the average value of the An-N laplacian for both the Np and Pu systems to below that of the U system. The energy density, conversely, was the most significantly affected topological parameter and was seen to increase from the unconstrained value by slightly more than 50% for the Np complex, regardless of *xc*-functional, and to almost double for the Pu complex, again, regardless of *xc*-functional. Differences induced in the total An-N delocalisation index by use of the spin constraint are small: of the order of 0.01 a.u. for the PBE *xc*-functional and slightly larger than this for the B3LYP functional. As with the electron density, larger differences (~ an order of magnitude greater) are induced by changing the *xc*-functional.

PBE		U	Np	Pu
$\sum \rho_{\mathrm{An-N}}$	Constrained	0.255	0.244	0.231
	Unconstrained	-	0.247	0.235
$\overline{\nabla^2 \rho_{\mathrm{An-N}}}$	Constrained	0.106	0.112	0.107
	Unconstrained	-	0.104	0.099
$\sum H_{\mathrm{An-N}}$	Constrained	-0.019	-0.016	-0.012
	Unconstrained	-	-0.025	-0.022
$\sum \delta(\mathrm{An-N})$	Constrained	1.819	1.832	1.787
	Unconstrained	-	1.837	1.716

Table 6.12: QTAIM parameters for the An-N bond in the AnO$_2$-isoamethyrin(1.0.1.0.0.0)′ complexes, given as average or total values, in a.u. obtained using the PBE *xc*-functional, with and without spin constraint.

B3LYP		U	Np	Pu
$\sum \rho_{\mathrm{An-N}}$	Constrained	0.244	0.240	0.229
	Unconstrained	-	0.243	0.232
$\overline{\nabla^2 \rho_{\mathrm{An-N}}}$	Constrained	0.105	0.106	0.107
	Unconstrained	-	0.098	0.099
$\sum H_{\mathrm{An-N}}$	Constrained	-0.017	-0.015	-0.012
	Unconstrained	-	-0.025	-0.022
$\sum \delta(\mathrm{An-N})$	Constrained	1.629	1.653	1.586
	Unconstrained	-	1.662	1.607

Table 6.13: QTAIM parameters for the An-N bond in the AnO$_2$-isoamethyrin(1.0.1.0.0.0)′ complexes, given as average or total values, in a.u., obtained using the B3LYP *xc*-functional with and without spin constraint.

.

The An-O bonds, have values of ρ at the BCP which increase from U to Pu, consistent with their decreasing bond length. Use of the spin constraint, independent of *xc*-functional, reduces the value of $\rho_{\mathrm{An-O}}$ for the Np and Pu complexes by ~ 0.01 a.u. As with the An-N bonds, this difference is smaller than that induced by changing the *xc*-functional.

	xc-functional	U	Np	Pu
$\rho_{\mathrm{An-O}}$	Constrained	0.299	0.304	0.310
	Unconstrained	-	0.297	0.302
$\nabla^2\rho_{\mathrm{An-O}}$	Constrained	0.315	0.340	0.327
	Unconstrained	-	0.416	0.421
$H_{\mathrm{An-O}}$	Constrained	-0.270	-0.273	-0.281
	Unconstrained	-	-0.247	-0.252

Table 6.14: QTAIM parameters for the An-O bond in the AnO_2-isoamethyrin(1.0.1.0.0.0)′, (An = U, Np, Pu) complexes measured in a.u. obtained using the PBE *xc*-functional.

	xc-functional	U	Np	Pu
$\rho_{\mathrm{An-O}}$	Constrained	0.317	0.330	0.338
	Unconstrained	-	0.321	0.327
$\nabla^2\rho_{\mathrm{An-O}}$	Constrained	0.265	0.243	0.251
	Unconstrained	-	0.343	0.362
$H_{\mathrm{An-O}}$	Constrained	-0.303	-0.323	-0.332
	Unconstrained	-	-0.293	-0.298

Table 6.15: QTAIM parameters for the An-O bond in the AnO_2-isoamethyrin(1.0.1.0.0.0)′, (An = U, Np, Pu) complexes measured in a.u. obtained using the B3LYP *xc*-functional.

Use of the spin constraint increases the value of the laplacian of the electron density at the An-O BCP of the Np and Pu complexes such that it increases in the order U < Np < Pu, rather than the U < Pu < Np (Np < Pu < U) ordering seen when the unconstrained approach is used with the PBE (B3LYP) *xc*-functional. The values for the energy density for the An-O bonds are reduced by use of the spin constraint, with this being most pronounced when the B3LYP *xc*-functional is used. All An-O bonds have QTAIM parameters indicative of a reduction in covalency in the An-O bonds compared to the uncoordinated actinyls (Tables 6.3 and 6.4), commensurate with the lengthening of these bonds upon complexation.

Tables 6.16, 6.17, 6.18 and 6.19 contain integrated properties of the electron density for the AnO$_2$-isoamethyrin(1.0.1.0.0.0)′ complexes. All quantities are shown alongside their deviation from the quantities calculated for the uncoordinated, optimised actinyls in Tables 6.5 and 6.6. Looking first at Table 6.16 which contains the atomic populations for the actinyl units obtained using the PBE *xc*-functionals, in all cases the total atomic population is larger than 106,107 and 108 for the uranyl, neptunyl and plutonyl units, respectively. Approximately 0.9 a.u. of charge is donated into the actinyl unit, divided approximately equally between the three ions. There is no obvious trend in the amount of charge donated into the actinyl unit from U to Pu, but the amount of this charge which populates the oxygen ions (*i.e.* the difference between the atomic population of the oxygen ions in the free and complexed actinyls) is at a minimum for the uranyl complex regardless of which *xc*-functional is used. The changes in atomic population induced by inclusion of spin constraint are minimal, with larger differences being induced by changing *xc*-functional, although the effect of utilising the spin constraint is most pronounced when the B3LYP *xc*-functional is used.

PBE		U		Np		Pu	
		complex	Δ	complex	Δ	complex	Δ
N(O)	Unconstrained	8.86	0.28	8.77	0.28	8.72	0.30
	Constrained	-	-	8.78	0.28	8.73	0.30
N(An)	Unconstrained	89.19	0.35	90.34	0.32	91.47	0.32
	Constrained	-	-	90.34	0.33	91.48	0.34
N(AnO$_2$)	Unconstrained	106.91	0.91	107.88	0.88	108.91	0.91
	Constrained	-	-	107.89	0.89	108.93	0.93

Table 6.16: Atomic populations obtained using the PBE *xc*-functional using both the spin-unconstrained and the spin-constrained approaches for the AnO$_2$-isoamethyrin(1.0.1.0.0.0) complexes, alongside differences from values for uncoordinated actinyls given in Table 6.5.

B3LYP		U		Np		Pu	
		complex	Δ	complex	Δ	complex	Δ
N(O)	Unconstrained	8.89	0.24	8.83	0.27	8.75	0.26
	Constrained	-	-	8.83	0.33	8.76	0.26
N(An)	Unconstrained	88.96	0.25	90.11	0.23	91.24	0.22
	Constrained	-	-	90.12	0.13	91.25	0.24
N(AnO$_2$)	Unconstrained	106.74	0.74	107.77	0.77	108.74	0.74
	Constrained	-	-	107.78	0.78	108.76	0.76

Table 6.17: Atomic populations obtained using the B3LYP *xc*-functional using both the spin-unconstrained and the spin-constrained approaches for the AnO$_2$-isoamethyrin(1.0.1.0.0.0) complexes, alongside differences from values for uncoordinated actinyls given in Table 6.5.

The total amount of charge donated into the actinyl unit is reduced by ~0.1-0.2 a.u. when the B3LYP functional is employed, reflected in a reduction in the additional charge populating each of the ions.

Considering the localisation and delocalisation indices in Tables 6.18 and 6.19 it is apparent that the localisation index of the actinyl oxygens increases upon complexation in all complexes, independent of *xc*-functional. The increase relative to the localisation index of the uncoordinated actinyl is larger in the plutonyl complex than the neptunyl complex, and larger in the neptunyl complex than the uranyl complex.

PBE		U		Np		Pu	
	xc-functional	complex	Δ	complex	Δ	complex	Δ
λ(O)	Unconstrained	7.69	0.34	7.58	0.34	7.51	0.37
	Constrained	-	-	7.59	0.35	7.51	0.37
λ(An)	Unconstrained	86.13	-0.39	87.23	-0.44	88.33	-0.45
	Constrained	-	-	87.23	-0.44	88.32	-0.45
δ(An-O)	Unconstrained	1.97	-0.35	2.02	-0.33	2.05	-0.32
	Constrained	-	-	2.02	-0.33	2.06	-0.32
δ(O$_1$-O$_2$)	Unconstrained	0.10	-0.03	0.13	-0.04	0.15	-0.05
	Constrained	-	-	0.13	-0.04	0.15	-0.05
λ(AnO$_2$)	Unconstrained	105.56	-0.44	106.55	-0.45	107.60	-0.40
	Constrained	-	-	106.57	-0.43	107.61	-0.39

Table 6.18: Localisation and delocalisation indices in a.u. for AnO$_2$-isoamethyrin(1.0.1.0.0.0)′; An = U, Np, Pu; for complexes optimised using the PBE *xc*-functionals alongside differences from values for uncoordinated actinyls given in Table 6.6, obtained using both the spin unconstrained and spin constrained approaches.

B3LYP		U		Np		Pu	
	xc-functional	complex	Δ	complex	Δ	complex	Δ
λ(O)	Unconstrained	7.76	0.31	7.66	0.33	7.56	0.32
	Constrained	-	-	7.67	0.42	7.56	0.33
λ(An)	Unconstrained	86.09	-0.35	87.18	-0.40	88.31	-0.38
	Constrained	-	-	87.17	-0.47	88.29	-0.38
δ(An-O)	Unconstrained	1.94	-0.33	1.99	-0.32	2.03	-0.31
	Constrained	-	-	1.99	-0.36	2.04	-0.31
δ(O$_1$-O$_2$)	Unconstrained	0.1	-0.01	0.12	-0.03	0.15	-0.03
	Constrained	-	-	0.12	-0.05	0.15	-0.03
λ(AnO$_2$)	Unconstrained	105.59	-0.41	106.6	-0.40	107.62	-0.38
	Constrained	-	-	106.61	-0.39	107.63	-0.37

Table 6.19: Localisation and delocalisation indices in a.u. for AnO$_2$-isoamethyrin(1.0.1.0.0.0)′; An = U, Np, Pu; for complexes optimised using the B3LYP *xc*-functionals alongside differences from values for uncoordinated actinyls given in Table 6.6, obtained using both the spin unconstrained and spin constrained approaches.

There is a reduction in the amount of charge delocalised in the An-O bonds upon complexation. For all complexes, the total actinyl localisation is less than 106, 107 or 108 for the uranyl, neptunyl and plutonyl complex, respectively, suggesting significant delocalisation between the actinyl unit and the ligand.

As with the atomic populations, changes induced by use of the spin constraint are smaller than those induced by changing *xc*-functional, although similarly, use of the spin constraint has the greatest effect when the B3LYP *xc*-functional is used.

6.3.3.4. Electron Density Difference Distributions

Figure 6.2 shows electron density difference distributions for uranyl, neptunyl and plutonyl isoamethyrin complexes optimised with the PBE *xc*-functional in the gas phase without spin constraint.

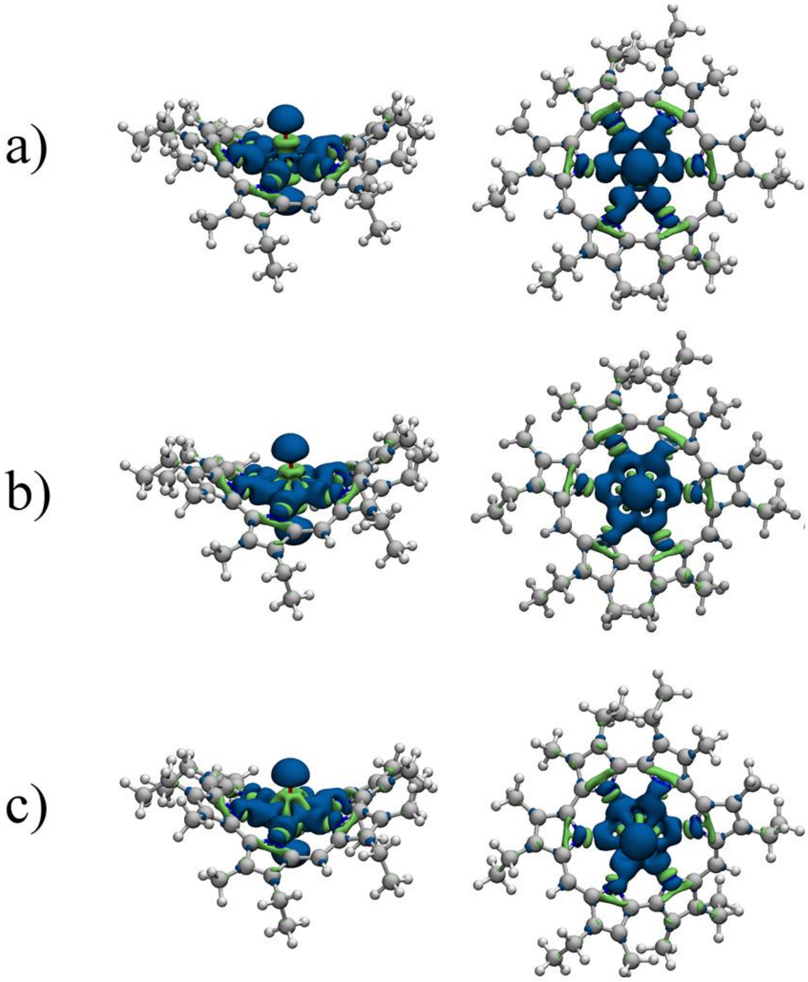

Figure 6.2: Electron density difference distributions for a) UO$_2$-isoamethyrin(1.0.1.0.0.0); b) NpO$_2$-isoamethyrin(1.0.1.0.0.0); c) PuO$_2$-isoamethyrin(1.0.1.0.0.0); generated from data obtained using the PBE *xc*-functional in the gas phase without spin constraint, isosurface value = 0.005 a.u.

There are regions of accumulation and depletion with f-like character around the actinide centre in the Np and Pu complexes. This can be explained as being due to changes to the f-occupation upon complexation occurring as a result of a reduction in symmetry. Regions of accumulation in the An-N bonding region appear to become more diffuse as one moves from U to Pu, commensurate with the QTAIM data showing reduced covalency in these interactions. Regions of accumulation around the actinyl oxygen ions appear to be fairly consistent in magnitude, as supported by the localisation indices and atomic populations of the O ions in Table 6.16-6.17. Depletion on the ligands can be interpreted as donation into the An-N bonding region, while depletion in the An-N bonding region supports the assertion from the integrated property section that these interactions become less covalent upon complexation. In the neptunyl and plutonyl complexes these regions of depletion appear to be significantly perturbed by the change in f-occupation between the uncoordinated and complexed actinyl.

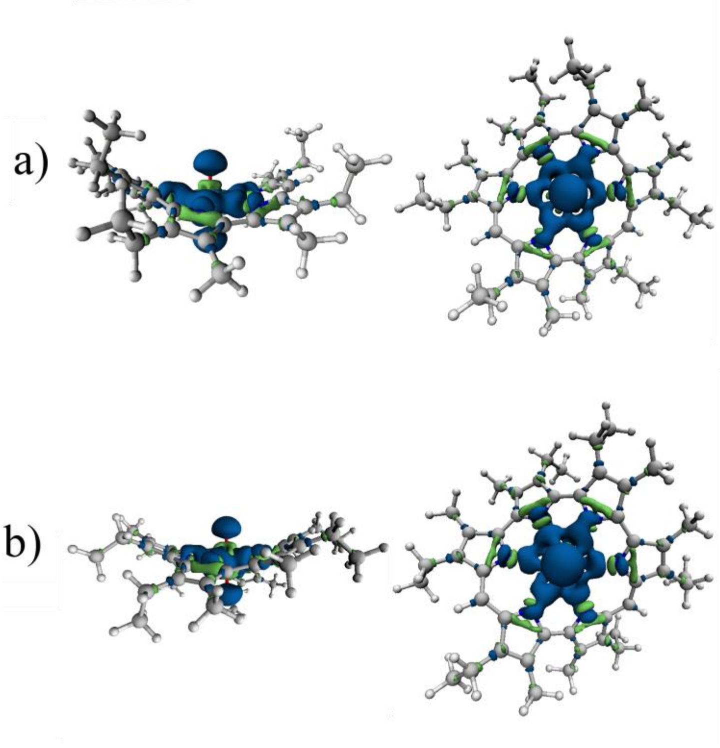

Figure 6.3: Electron density difference distributions for a) NpO_2-isoamethyrin(1.0.1.0.0.0); b) PuO_2-isoamethyrin(1.0.1.0.0.0); generated from data obtained using the PBE *xc*-functional in the gas phase with spin constraint, isosurface value = 0.005 a.u

Inclusion of the spin constraint parameter had minimal effects on the electron density at the BCP and the integrated properties of the electron density, so it is reasonable to expect that effects on the electron density difference distributions will also be minimal. Figure 6.3 demonstrates this to be the case.

6.3.3.5. Spin Density and Spin Population Analysis for AnO_2-isoamethyrin(1.0.1.0.0.0)′, An = Np and Pu

Figure 6.4 shows spin densities for the neptunyl and plutonyl isoamethyrin complexes, with and without spin constraint. Figure 6.4 a) and c) show the spin densities for the unconstrained systems, with positive spin density in purple around the actinide ion, consistent with the presence of one and two unpaired electrons for the neptunyl and plutonyl system, respectively. There is also a small amount of negative spin density associated with the oxygen ions in these complexes, most pronounced in the plutonyl complex, suggesting a small amount of spin delocalisation here. However, given the similarities between the integrated properties for the oxygen ions whether spin constraint was used or not, this can be assumed to be unimportant. Figure 6.4 b) and d) show the spin densities for the neptunyl and plutonyl systems, respectively, when the spin constraint is used, showing that spin associated with the oxygen ions has been reduced with the use of the constraint.

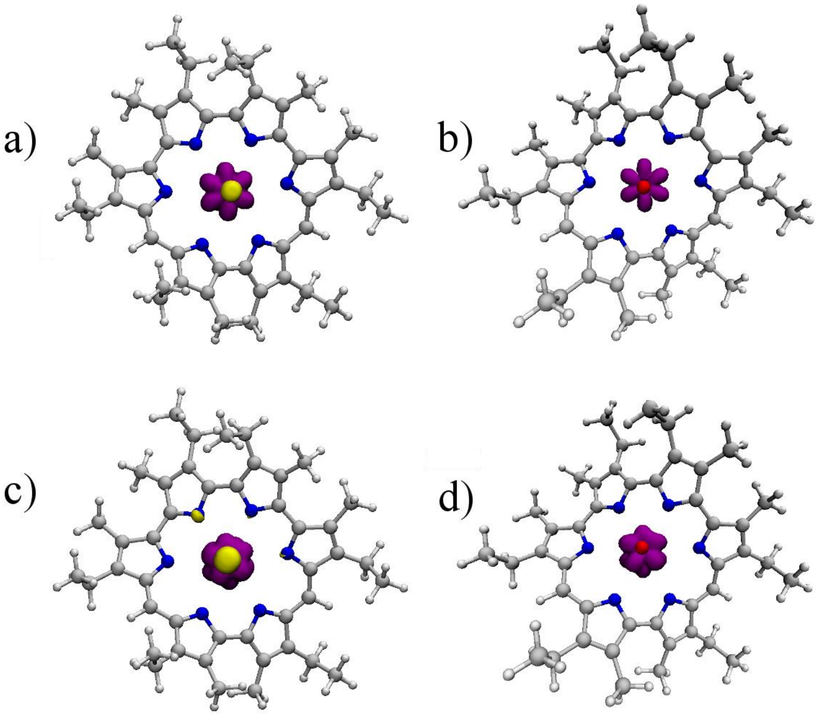

Figure 6.4: Spin densities for a) NpO_2-isoamethyrin(1.0.1.0.0.0) without spin constraint; b) NpO_2-isoamethyrin(1.0.1.0.0.0) with spin constraint; c) PuO_2-isoamethyrin(1.0.1.0.0.0) without spin constraint; d) PuO_2-isoamethyrin(1.0.1.0.0.0) with spin constraint; all generated from data obtained using the PBE *xc*-functional in the gas phase, isosurface value = 0.005 a.u. Positive spin density = purple, negative spin density = yellow.

Table 6.20 shows spin analysis for the neptunyl and plutonyl isoamethyrin complexes. It can be seen that use of the spin constrained approach brings the spin population of the actinide ion very close to the value of the formal spin, although as stated previously, the effect this has on the topological and integrated properties are small.

		xc-functional	$\langle S^2 \rangle$	$N_s(A)$	$\Delta N_s(A)$
Unconstrained	Np	PBE	0.76	1.14	0.14 (14%)
		B3LYP	0.76	1.11	0.11 (11%)
	Pu	PBE	2.09	2.34	0.34 (17%)
		B3LYP	2.03	2.23	0.23 (12%)
Constrained	Np	PBE	0.75	0.98	-0.02 (2%)
		B3LYP	0.75	0.98	-0.02 (2%)
	Pu	PBE	2.00	1.96	-0.04 (2%)
		B3LYP	2.00	1.97	-0.03 (1.5%)

Table 6.20: The expectation value $\langle S^2 \rangle$, atomic spin population of atom A ($N_s(A)$), the difference between the atomic spin population and formal spin ($\Delta N_s(A)$) and this difference expressed as a percentage of the formal spin.

6.3.3.6. AnO$_2$-isoamethyrin(1.0.1.0.0.0)′ Conclusions

As one moves from the uranyl complex with isoamethyrin to neptunyl and plutonyl complexes, it is first apparent that there is a slight increase in An-N bond lengths, perhaps as a result of the reduced ionic radius of Pu(VI) compared to Np(VI) and Np(VI) compared to U(VI), and the fact that this ligand, unlike cyclo[6]pyrrole, appears not to contract significantly as a result of this.

Evidence for this lies in the ligand deformation energy which is more or less constant across all complexes, and the slight lengthening of An-N bonds from U to Pu due to the smaller ionic radius U > Pu. Vibrational analysis points to the uranyl stretching frequencies being most significantly shifted.

Considering the total binding energies, the uranyl complex is calculated to be the most stable with both *xc*-functionals, followed by the neptunyl complex, and the plutonyl complex is least stable. The actinyl deformation energy is most significant for the uranyl complex, decreasing in the order U > Np > Pu.

Analysis of topological parameters of the electron density indicate less equatorial covalency as the actinide series is crossed. This is in contrast to the An-N delocalisation data which suggests slightly higher Np-N delocalisation than U-N delocalisation. QTAIM parameters for the An-O bond indicate a reduction in covalency upon complexation in all cases, supported by the integrated properties of the electron density which show a similar process happening in all actinyls: charge being donated into the actinyl unit and localised on the three ions, increasing the electrostatic component of the An-O interaction while depletion on the An-O bond indicates a reduction in the covalent component of the interaction. The integrated properties indicate that these effects are most significant in the uranyl complex, which sees the largest increase in oxygen localisation as well as the largest decrease in An-O delocalisation, commensurate with the uranyl deformation energy and uranyl stretching frequencies. The total actinyl localisation being lower than the total actinyl population supports the assertion of significant An-N delocalisation. These data are given qualitative support by the electron density difference distributions.

Use of the spin constraint has small effects on the topological properties of the Np-N, Np-O, Pu-N and Pu-O bonds, with the energy density being the most significantly effected. Effects on the integrated properties of the electron density were minimal, as were effects on the qualitative electron density difference distributions. Use of the spin constraint brought the spin population of each actinide centre very close to the formal spin state. In general, effects of including the spin constraint appear to be quite small, but a full reoptimisation would be necessary to state this with certainty.

6.3.4. Density-based Analysis of AnO_2-cyclo[6]pyrrole; An = U, Np, Pu: the Spin Unrestricted Approach *vs.* the Spin Constrained Approach.

6.3.4.1. Structural Data

Figure 6.5 shows the optimised geometry for the NpO_2-cyclo[6]pyrrole complex optimised using the PBE *xc*-functional in the gas phase. No major structural differences were found between the uranyl, neptunyl and plutonyl complexes, so the neptunyl complex only is shown (for the uranyl complexes, see Figures 5.2 and 5.3, Chapter 5). Table 6.21 shows averaged An-N and An-O bond lengths in cyclo[6]pyrrole complexes optimised using the PBE and B3LYP *xc*-functionals in the gas phase. In Chapter 5, the uranyl cyclo[6]pyrrole complex was compared to crystallographic data[187], with which excellent agreement was found. In general, there appears to be a small decrease in average An-N bond lengths as one moves from U to Np. Moving from the Np to the Pu complex using the PBE *xc*-functional in the gas phase, the average Pu-N bond length is found to be 0.003 Å longer than the average Np-N bond length. It ought to be stressed that greater differences in An-N bond length are induced by choice of functional than by changing the actinide species, and that all optimised complexes are very similar in terms of their An-N bonds. Calculated An-O bond lengths, on the other hand, decrease by up to ~0.1 of an Angstrom moving from U to Np, however moving from the Np to the Pu species optimised with the PBE *xc*-functional in the gas phase, where the Pu-O bond is in fact 0.001 Å longer than the Np-O bond. Lengthening of the An-O bond relative to the uncoordinated actinyls is most pronounced in the uranyl complexes, suggesting that the uranyl unit may be most affected by complexation.

	U		Np		Pu	
	PBE	B3LYP	PBE	B3LYP	PBE	B3LYP
$\overline{r_{\mathrm{An-N}}}$	2.532	2.536	2.523	2.532	2.526	2.529
$r_{\mathrm{An-O}}$	1.799	1.781	1.772	1.758	1.773	1.745
$\Delta r_{\mathrm{An-O}}$	0.088	0.085	0.063	0.067	0.076	0.068

Table 6.21: Average An-N and An-O bond lengths and $\Delta r_{\mathrm{An-O}}$, the difference between the coordinated and uncoordinated An-O bond length, all in Å for complexes with the cyclo[6]pyrrole ligand, optimised with the PBE and B3LYP functionals in the gas phase

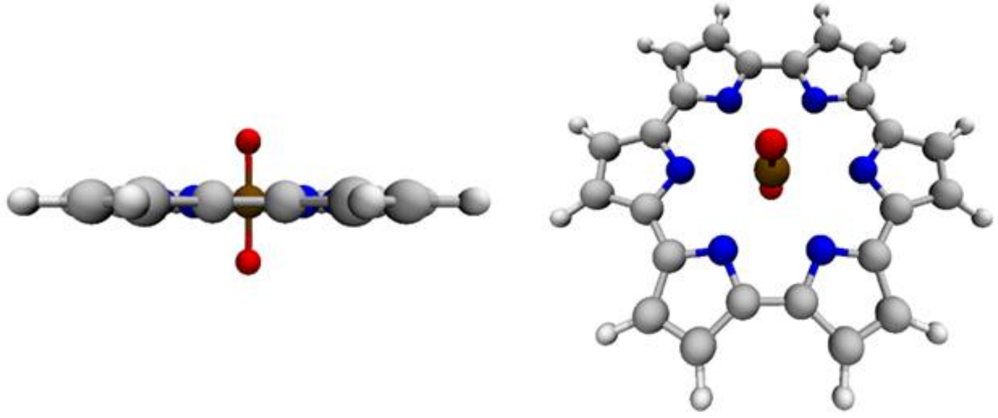

Figure 6.5: Optimised NpO_2-cyclo[6]pyrrole complex, generated from data obtained using the PBE *xc*-functional in the gas phase.

6.3.4.2. QTAIM - Topological and Integrated Properties

Tables 6.22 and 6.23 shows topological QTAIM parameters for An-N bonds in cyclo[6]pyrrole complexes optimised with the PBE and B3LYP *xc*-correlation functionals in the gas phase. Tables 6.24 and 6.25 shows topological parameters of the An-O bonds for the same complexes.

First, covalency in the An-N bonds will be discussed for the calculations omitting spin constraint. As the central ion is changed from U to Np, it is noticed that all indicators point to the An-N bonds being very similar in terms of covalent character. There is some dependence on which *xc*-functional is used: for complexes optimised using the PBE *xc*-functional without spin constraint, the sum of ρ_{BCP} and H_{BCP} point to the An-N bond character of the uranyl and neptunyl complexes being almost identical, while use of the B3LYP *xc*-functional appears to induce differences in ρ_{BCP} and H_{BCP} of ~0.01 a.u. between the uranyl and neptunyl complexes, although it is apparent that the character of these bonds is very alike irrespective of which *xc*-functional is used. With both *xc*-functionals, without spin constraint, the average value of $\nabla^2 \rho_{\mathrm{An-N}}$ is approximately a thousandth of an a.u higher in the neptunyl complex than the uranyl complex, a difference of the order of 1%. There is a slightly larger increase in the value of $\nabla^2 \rho_{\mathrm{An-N}}$ between the neptunyl and plutonyl complexes. There is a notable increase in An-N delocalisation in the neptunyl complex compared to the uranyl complex, which is most significant when the PBE *xc*-functional is used. This may be an effect of the self-interaction error which is more pronounced with PBE than with a hybrid *xc*-functional such as B3LYP where the presence of exact exchange partially cancels the spurious self-interaction[343,373]. Use of the B3LYP *xc*-functional results in slightly lower values of ρ_{BCP} and H_{BCP} in the NpO_2 complexes compared with UO_2, which is at odds with the delocalisation data. Moving from Np to Pu, ρ_{BCP} and H_{BCP} indicate a reduction in An-N covalency for the plutonyl complex compared to the uranyl and neptunyl complexes, while δ(Pu,N) is very slightly (an increase of less than 1%) larger than δ(U,N).

Spin constraint were subsequently applied and a single point energy calculation was run at the geometry previously optimised without spin constraint. When the PBE *xc*-functional was used, $\sum \rho_{\mathrm{An-N}}$ was found to increase slightly compared to the unconstrained systems, with the effect being most significant for the neptunyl complex. When the PBE *xc*-functional was used, $\sum \rho_{\mathrm{An-N}}$ was found to increase more significantly compared to the unconstrained system for the neptunyl complex, whereas a slight decrease is calculated for the plutonyl complex. The average value of the laplacian of the electron density at the An-N BCP is slightly reduced by constraining the spin, such that for both the neptunyl and plutonyl complexes with both *xc*-functionals, $\overline{\nabla^2 \rho_{\mathrm{An-N}}}$ is lower than the corresponding value in the uranyl complex. As with the isoamethyrin complexes, the magnitude of the energy density increases when spin constraint are used. When the delocalisation indices are considered, the neptunyl complex is the most significantly affected when the spin constraint is used, increasing by ~ 0.3 a.u. when the PBE *xc*-functional is employed and ~ 0.4 a.u. when the B3LYP xc-functional is employed. In the plutonyl complex with both *xc*-functionals, there are small decreases in the values of the delocalisation indices when the spin is constrained, but these changes are an order of magnitude smaller than those induced by the spin constraint in the neptunyl system. Overall, it appears that the inclusion of spin constraint seems to have a greater effect on topological parameters of the neptunyl complex than the plutonyl complex. This will be investigated further when the integrated properties and spin densities are analysed, although it is likely that full reoptimisations are needed in this case in order to fully rationalise these data.

	xc-functional	U	Np	Pu
$\sum \rho_{\mathrm{An-N}}$	Constrained	0.350	0.350	0.330
	Unconstrained	-	0.358	0.333
$\overline{\nabla^2 \rho_{\mathrm{An-N}}}$	Constrained	0.149	0.150	0.159
	Unconstrained	-	0.138	0.147
$\sum H_{\mathrm{An-N}}$	Constrained	-0.042	-0.039	-0.030
	Unconstrained	-	-0.058	-0.047
$\sum \delta(\mathrm{An-N})$	Constrained	2.143	2.343	2.184
	Unconstrained	-	2.647	2.179

Table 6.22: QTAIM parameters for the An-N bond in the cyclo[6]pyrrole complexes, given as average or total values, in a.u. obtained using the PBE *xc*-functional, with and without spin constraint.

	xc-functional	U	Np	Pu
$\sum \rho_{\mathrm{An-N}}$	Constrained	0.344	0.337	0.334
	Unconstrained	-	0.350	0.330
$\overline{\nabla^2 \rho_{\mathrm{An-N}}}$	Constrained	0.152	0.154	0.161
	Unconstrained	-	0.136	0.149
$\sum H_{\mathrm{An-N}}$	Constrained	-0.040	-0.036	-0.030
	Unconstrained	-	-0.056	-0.047
$\sum \delta(\mathrm{An-N})$	Constrained	1.970	1.985	1.973
	Unconstrained	-	2.342	1.962

Table 6.23: QTAIM parameters for the An-N bond in the cyclo[6]pyrrole complexes, given as average or total values, in a.u. obtained using the B3LYP *xc*-functional, with and without spin constraint.

When the An-O bonds are considered (Tables 6.24 and 6.25) without spin constraint, it is noticed that there is an increase in covalency as defined by QTAIM moving across the series from U to Pu. This is in keeping with previous studies[412].

Differences between the values in Tables 6.24 and 6.25 and those of the uncomplexed actinyls indicate that reduction of covalent character in the An-O bond occurs upon complexation. When the unconstrained neptunyl and plutonyl systems are compared to the uranyl system, it appears that uranyl is the most affected by complexation with this ligand. This can perhaps be attributed to the larger ionic radius of uranium(VI) compared to neptunium/plutonium(VI). The An-N QTAIM parameters for the unconstrained systems suggest that the uranyl and neptunyl complex are very similar to one another while the plutonyl complex demonstrates less An-N covalency, in contrast with structural data which suggests that the largest differences are to be found between the uranyl complex and the neptunyl/plutonyl complexes.

When the spin constraint is applied, a reduction in the value of $\rho_{\mathrm{An-O}}$ is found with both xc-functionals for both the neptunyl and plutonyl complexes. This reduction is slight and maintains the trends from the unconstrained calculations: Np > Pu > U (Pu > Np > U) when the PBE (B3LYP) *xc*-functional is employed. The laplacian is increased by the application of spin constraint, such that it increases in the order U > Np > Pu regardless of *xc*-functional. The energy density is reduced when spin constraint are applied, by approximately the same amount as for the isoamethyrin systems. Topological parameters, as expected, still indicate a reduction in covalent character upon complexation. Overall, the topological properties of the An-O bonds seem less significantly affected than those of the An-N bonds in the cyclo[6]pyrrole complexes.

PBE		U	Np	Pu
$\rho_{\mathrm{An-O}}$	Constrained	0.290	0.306	0.303
	Unconstrained	-	0.301	0.295
$\nabla^2\rho_{\mathrm{An-O}}$	Constrained	0.320	0.319	0.349
	Unconstrained	-	0.427	0.430
$H_{\mathrm{An-O}}$	Constrained	-0.253	-0.278	-0.268
	Unconstrained	-	-0.254	-0.240

Table 6.24: QTAIM parameters for the An-O bond in the cyclo[6]pyrrole complexes measured in a.u., obtained using the PBE *xc*-functional, with and without spin constraint.

B3LYP		U	Np	Pu
$\rho_{\mathrm{An-O}}$	Constrained	0.304	0.318	0.327
	Unconstrained	-	0.312	0.318
$\nabla^2\rho_{\mathrm{An-O}}$	Constrained	0.274	0.271	0.276
	Unconstrained	-	0.367	0.369
$H_{\mathrm{An-O}}$	Constrained	-0.281	-0.301	-0.313
	Unconstrained	-	-0.275	-0.280

Table 6.25: QTAIM parameters for the An-O bond in the cyclo[6]pyrrole complexes measured in a.u., obtained using the B3LYP *xc*-functional, with and without spin constraint.

Next, integrated properties of the electron density are examined. Tables 6.26 and 6.27 contain atomic populations for complexes optimised using the PBE and B3LYP *xc*-functionals, respectively. Tables 6.28 and 6.29 contain localisation and delocalisation data for the actinyl units in cyclo[6]pyrrole complexes optimised using PBE and B3LYP *xc*-functionals, respectively.

Looking first at the atomic populations obtained using the PBE *xc*-functional with both the spin-unconstrained and spin-constrained approach in Table 6.26, it can be seen for the complexes optimised using the PBE *xc*-functional in the gas phase without spin constraint, that upon complexation, a total of approximately 0.85-0.95 a.u. of charge is donated into the actinyl unit. This is reduced to 0.80-0.85 when the data obtained using the B3LYP *xc*-functional is considered (Table 6.27). When the spin constraint are applied, the amount of charge donated into the neptunyl unit drops to 0.78 (0.71) a.u. when the PBE (B3LYP) *xc*-functional is employed, while there is a slight increase in the amount of charge donated into the plutonyl unit, 0.97 (0.84) a.u. with the PBE (B3LYP) *xc*-functional. As with the topological properties, it is the neptunyl complexes which are most significantly affected by the spin constraint.

		U		Np		Pu	
PBE		Complex	Δ	Complex	Δ	Complex	Δ
N(O)	Unconstrained	8.86	0.28	8.78	0.29	8.73	0.30
	Constrained	-	-	8.74	0.25	8.74	0.31
N(An)	Unconstrained	89.19	0.35	90.31	0.30	91.49	0.34
	Constrained	-	-	90.29	0.27	91.49	0.35
N(AnO_2)	Unconstrained	106.90	0.90	107.87	0.87	108.95	0.95
	Constrained	-	-	107.78	0.78	108.97	0.97

Table 6.26: Atomic populations obtained using the PBE *xc*-functional with both the spin-constrained and spin unconstrained approach for AnO_2-cyclo[6]pyrrole

		U		Np		Pu	
B3LYP		Complex	Δ	Complex	Δ	Complex	Δ
N(O)	Unconstrained	8.91	0.26	8.85	0.29	8.78	0.29
	Constrained	-	-	8.81	0.30	8.78	0.29
N(An)	Unconstrained	88.98	0.27	90.14	0.26	91.28	0.26
	Constrained	-	-	90.10	0.11	91.27	0.26
N(AnO_2)	Unconstrained	106.81	0.81	107.83	0.83	108.83	0.83
	Constrained	-	-	107.71	0.71	108.84	0.84

Table 6.27: Atomic populations obtained using the B3LYP *xc*-functional with both the spin-constrained and spin unconstrained approach for AnO_2-cyclo[6]pyrrole

Moving on to the actinyl localisation indices in Table 6.28 and 6.29, it is apparent that for all complexes, with both *xc*-functionals, and irrespective of spin constraint, there is an increase in localisation on the oxygen centres which is approximately equal in magnitude to the reduction of charge delocalised in all An-O bonds. The actinide centres themselves become more positively charged, and the total localisation, compared to the uncoordinated actinyls, decreases upon complexation by 0.5-0.9 a.u. when the spin is not constrained, suggesting in all cases, substantial delocalisation between the actinyl unit and the ligand. Differences in the Pu systems induced by the application of spin constraint are minimal, however spin constraint significantly reduces the localisation on the Np centre compared to that of the unconstrained system.

$\lambda(NpO_2)$ for this system when the spin constraint is applied is ~ 0.45 (0.70) a.u. lower than for the unconstrained system when the PBE (B3LYP) *xc*-functional is employed, with λ(An), the value of which can be used to infer an oxidation state, suggesting a number of electrons localised on the neptunium centre closer perhaps to Np(VII) than Np(VI). This is particularly pronounced where the B3LYP *xc*-functional is employed. This will be further investigated when the spin densities and spin populations are analysed.

		U		Np		Pu	
PBE		Complex	Δ	Complex	Δ	Complex	Δ
λ(O)	Unconstrained	7.71	0.36	7.58	0.35	7.51	0.37
	Constrained	-	-	7.53	0.30	7.52	0.39
λ(An)	Unconstrained	86.05	-0.47	86.87	-0.80	88.22	-0.56
	Constrained	-	-	86.45	-1.22	88.23	-0.53
δ(An-O)	Unconstrained	1.92	-0.4	1.99	-0.36	2.02	-0.35
	Constrained	-	-	2.02	-0.33	2.01	-0.37
$\delta(O_1-O_2)$	Unconstrained	0.1	-0.03	0.13	-0.04	0.15	-0.06
	Constrained	-	-	0.14	-0.03	0.15	-0.06
$\lambda(AnO_2)$	Unconstrained	105.4	-0.60	106.15	-0.85	107.43	-0.57
	Constrained	-	-	105.69	-1.31	107.46	-0.54

Table 6.28: Localisation and delocalisation indices in a.u. obtained using the PBE *xc*-functional with both the spin constrained and spin unconstrained approach for AnO_2-cyclo[6]pyrrole

		U		Np		Pu	
B3LYP		Complex	Δ	Complex	Δ	Complex	Δ
λ(O)	Unconstrained	7.80	0.35	7.70	0.37	7.59	0.36
	Constrained	-	-	7.63	0.39	7.60	0.37
λ(An)	Unconstrained	86.01	-0.43	87.08	-0.50	88.19	-0.49
	Constrained	-	-	86.48	-1.16	88.19	-0.47
δ(An-O)	Unconstrained	1.87	-0.40	1.94	-0.37	1.98	-0.36
	Constrained	-	-	1.97	-0.38	1.98	-0.37
$\delta(O_1-O_2)$	Unconstrained	0.09	-0.02	0.11	-0.04	0.14	-0.04
	Constrained	-	-	0.13	-0.04	0.14	-0.04
$\lambda(AnO_2)$	Unconstrained	105.44	-0.56	106.47	-0.53	107.48	-0.52
	Constrained	-	-	105.81	-1.19	107.49	-0.51

Table 6.29: Localisation and delocalisation indices in a.u. obtained using the PBE *xc*-functional with both the spin constrained and spin unconstrained approach for AnO_2-cyclo[6]pyrrole

When the unconstrained data is considered, $N(AnO_2)$ in particular is seen to increase by ~1 moving from U to Pu, consistent with the increase in the number of electrons formally present in the actinyl. This is not the case for $\lambda(NpO_2)$ where the constrained data is considered. The localisation index of the neptunyl ion when optimised with the PBE *xc*-functional is somewhat anomalously low even when the constrained data is considered, although this is commensurate with the relatively large Np-N delocalisation index seen in this complex. As reported elsewhere, use of the B3LYP functional results in decreased delocalisation and increased localisation, consistent with previous findings[27,61,381,404].

6.3.4.3. Electron Density Difference Distributions

Visualisation of the electron density differences upon complexation allow qualitative examination of the changes upon complexation seen in the topological and integrated properties. First, the density difference distributions obtained from the unconstrained calculations are analysed. Figure 6.6 shows these plots for uranyl, neptunyl and plutonyl cyclo[6]pyrrole optimised with the PBE *xc*-functional in the gas phase, without spin constraint.

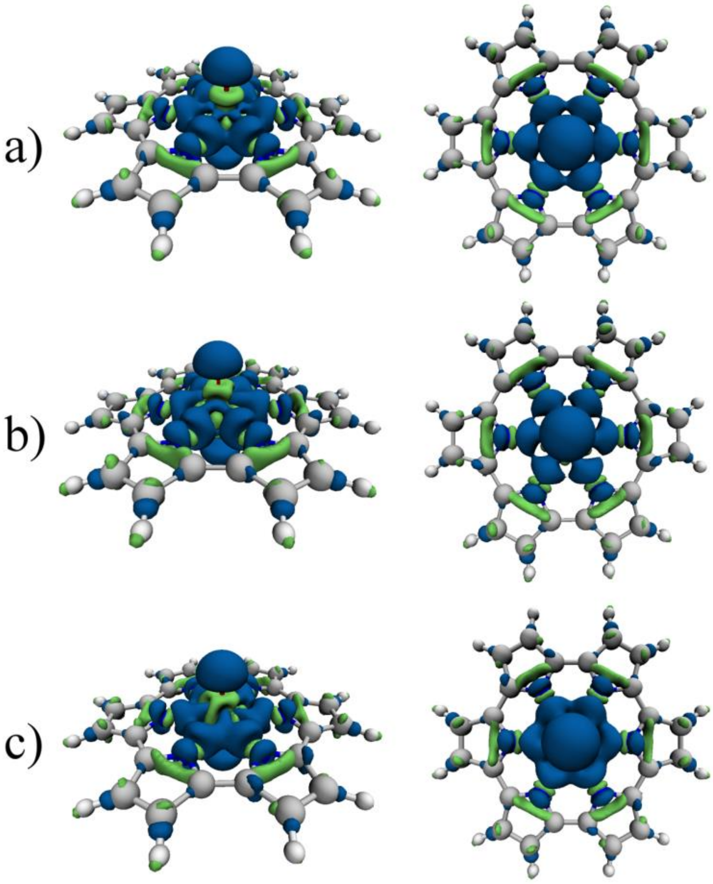

Figure 6.6: Electron density difference distributions for a) UO_2-cyclo[6]pyrrole; b) NpO_2-cyclo[6]pyrrole; c) PuO_2-cyclo[6]pyrrole; generated from data obtained using the PBE *xc*-functional in the gas phase without spin constraint, isosurface value = 0.005 a.u.

There are several strong qualitative similarities, beginning with regions of depletion of charge (green) on the An-O bonds and accumulation (blue) on the -yl oxygen ions. It can be seen that the magnitude of the accumulation on the –yl oxygen ions appears more or less identical between complexes, commensurate with the data in Tables 6.26-6.27 showing that the increase in negative charge on the –yl oxygen centres is approximately 0.3 a.u. regardless of actinyl. A significant difference is apparent between the uranyl complex and the neptunium/plutonium complexes, where there is accumulation/depletion of f-like character in the region of the actinide centre, appearing to perturb the cylindrical region of depletion on the An-O bonds. This is because the 5f orbitals, formally empty in the uranyl complex, are occupied by one and two electrons in the neptunyl and plutonyl complexes, respectively. The regions of accumulation and depletion that we see particularly around the neptunium and plutonium atom, where they are seen to, are due to changes to this f-occupation upon complexation. These can be better illustrated by viewing the distribution at a greater isosurface value in order to eliminate much of the isosurface, as in Figure 6.7

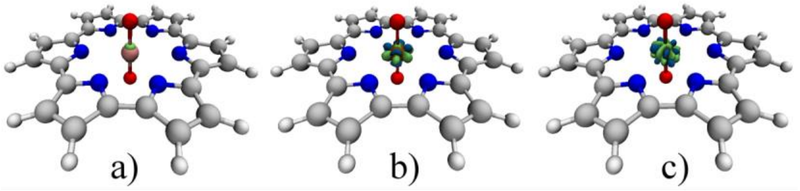

Figure 6.7: Electron density difference distributions showing change (or lack thereof) in f-occupation for a) UO_2-cyclo[6]pyrrole; b) NpO_2-cyclo[6]pyrrole; c) PuO_2-cyclo[6]pyrrole; generated from data obtained using the PBE *xc*-functional in the gas phase, without spin constraint isosurface value = 0.05 a.u.

Accumulation is also seen in the An-N bonding region, with the magnitude of this teardrop-shaped accumulation seen to be virtually identical as one moves from U to Np. The accumulation in the Pu-N bonding region appears to be somewhat more diffuse, and less focussed on individual Pu-N bonds than in the uranyl and neptunyl complexes. This is commensurate with the QTAIM data showing a reduction in Pu-N covalent character compared to U/Np-N bonds.

Considering the electron density difference distributions generated from the spin constrained SPEs shown in Figure 6.8, as with the isoamethyrin complexes the data are similar enough for the distributions to not appear qualitatively different. The magnitude of donation from the ligand perhaps appears slightly larger in the neptunyl complex when the spin constraint is applied, commensurate with the slightly increased indicators of equatorial covalency in this complex compared to the data obtained from the calculations without spin constraint. Additionally, the ligand in the neptunyl complex appears to have somewhat larger regions of accumulation itself, suggestive of redistribution of charge within the ligand, perhaps reduction of the ligand commensurate with the apparent oxidation of the Np ion.

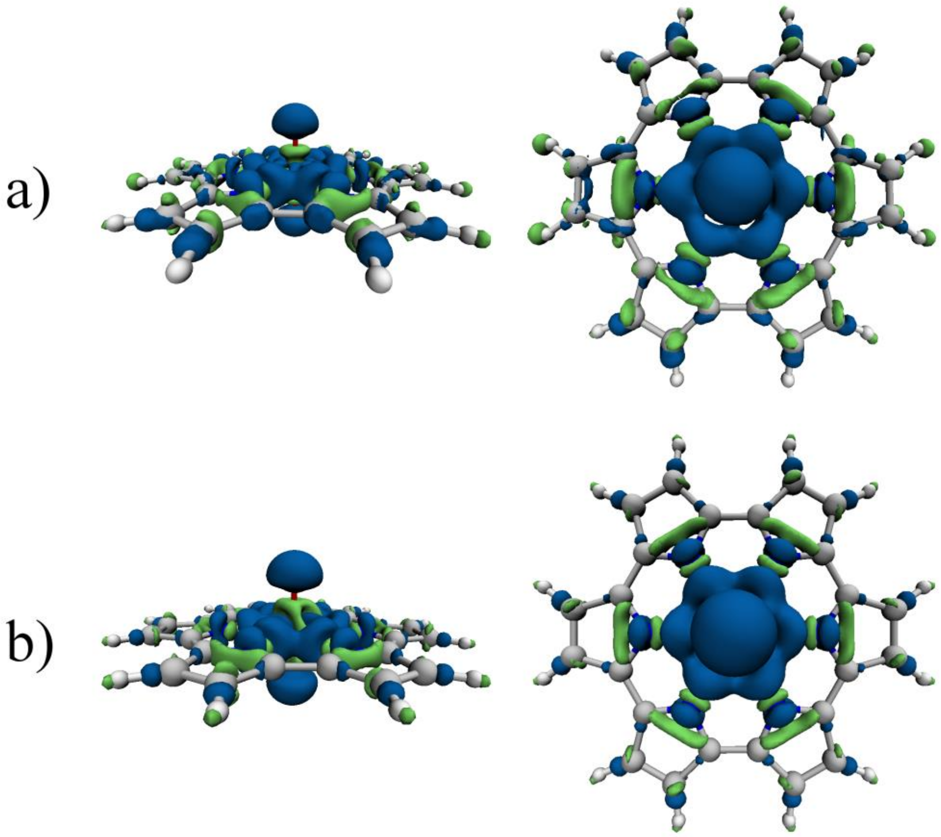

Figure 6.8: Electron density difference distributions for a) NpO_2-cyclo[6]pyrrole; b) PuO_2-cyclo[6]pyrrole; generated from data obtained using the PBE *xc*-functional in the gas phase with spin constraint, isosurface value = 0.005 a.u.

6.3.4.4. Spin Density and Spin Population Analysis for AnO_2-cyclo[6]pyrrole, An = Np and Pu

Figure 6.9 shows the spin densities for the unconstrained and constrained neptunyl and plutonyl cyclo[6]pyrrole complexes optimised with the PBE *xc*-functional. It is immediately clear that spin contamination is a bigger problem for these systems than for the isoamethyrin systems. This appears to be improved, but not completely resolved, by applying spin constraint.

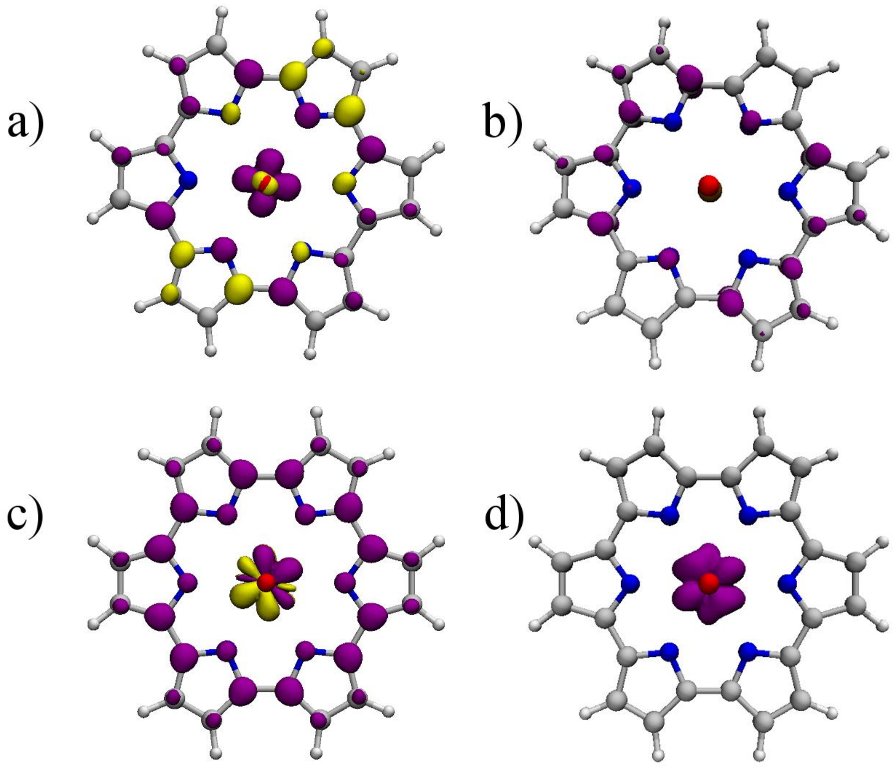

Figure 6.9: Spin densities for a) NpO_2-cyclo[6]pyrrole without spin constraint; b) NpO_2-cyclo[6]pyrrole with spin constraint; c) PuO_2-cyclo[6]pyrrole without spin constraint; d) PuO_2-cyclo[6]pyrrole with spin constraint; all generated from data obtained using the PBE *xc*-functional in the gas phase, isosurface value = 0.005 a.u. Positive spin density = purple, negative spin density = yellow.

Figure 6.9 a) shows the spin density for the unconstrained neptunyl complex. Spin density centred on the neptunium ion consistent with a single unpaired electron is present, however regions of both positive and negative spin density on the ligand are present, perhaps suggesting that two unpaired electrons of opposite spin may be localised here. Application of spin constraint reduces this to a single unpaired electron present on the ligand, which, consistent with the unusually low localisation index for the Np ion in Table 6.28, may support the idea of a spontaneous oxidation of the Np centre with corresponding reduction of the ligand. Considering the plutonyl complex, Figure 6.9 c) suggests regions of opposite spin on the plutonium centre, with further positive spin density localised on the ligand. Application of spin constraint appears to completely resolve this, with Figure 6.9 d) showing spin density consistent of two like-spin unpaired electrons localised on the plutonium centre. This is supported by the expectation value $\langle S^2 \rangle$ and spin populations for the actinide ions in Table 6.30.

		xc-functional	$\langle S^2 \rangle$	$N_s(A)$	$\Delta N_s(A)$
Unconstrained	Np	PBE	1.54	1.10	0.10 (10%)
		B3LYP	1.83	0.87	-0.13 (13%)
	Pu	PBE	2.99	0.01	-1.99 (99%)
		B3LYP	2.99	0.01	-1.99 (99%)
Constrained	Np	PBE	0.75	0.00	1.00 (100%)
		B3LYP	0.75	0.00	1.00 (100%)
	Pu	PBE	2.00	1.95	0.05 (2.5%)
		B3LYP	2.00	1.96	0.04 (2%)

Table 6.30: The expectation value $\langle S^2 \rangle$, atomic spin population of atom A ($N_s(A)$), the difference between the atomic spin population and formal spin ($\Delta N_s(A)$) and this difference expressed as a percentage of the formal spin for cyclo[6]pyrrole complexes.

What Table 6.30 shows is that application of spin constraint is beneficial for the plutonyl cyclo[6]pyrrole complexes: Values of $\langle S^2 \rangle$ become consistent with there being two unpaired electrons in the system, and the spin population analysis reveals these to be located on the plutonium centre. The neptunyl complexes are more problematic. Application of the spin constraint brings the expectation value $\langle S^2 \rangle$ to a value consistent with a single unpaired electron, however this electron is localised on the ring, with the spin population of the neptunium atom along with its localisation index consistent with the neptunium centre being oxidised to Np(VII).

6.3.4.5. AnO$_2$-cyclo[6]pyrrole Conclusions.

When uranyl, neptunyl and plutonyl complexes with cyclo[6]pyrrole are optimised without spin constraint, there is a small reduction in An-N bond lengths as the series is crossed from U to Pu, which, since there is no commensurate increase in An-N covalency, may be attributed to the decrease in ionic radius as the actinide series is crossed. The slight shortening of Np-N and Pu-N bonds compared to U-N bonds arises from an increased distortion of the ligand with the uranyl unit being the most significantly affected of all the actinyls by complexation.

This can be further demonstrated using topological parameters: When the unconstrained systems are considered, all An-O bonds are seen to decrease in covalency upon complexation, but the uranyl unit is the most significantly affected. When the character of the An-N interaction is considered, covalency as defined by

ρ_{BCP} and H_{BCP} indicate that the uranyl and neptunyl complexes are very similar in character. Considering these same values for the spin constrained systems, there are minimal differences in ρ_{BCP} the plutonyl complex, regardless of which *xc*-functional is used, while ρ_{BCP} for the constrained neptunyl complex suggests greater covalent character compared to the unconstrained system. $\delta(\mathrm{An,N})$ for the unconstrained neptunyl complex is somewhat anomalously high, which was initially thought to be an effect of the self-interaction error, but the fact that the application of spin constraint makes this value higher still makes it likely that is related to the apparent oxidation of the neptunium ion to Np(VII) and corresponding reduction of the ring. ρ_{BCP} and H_{BCP} for the Pu-N interactions point to reduced covalent character compared to the U-N and Np-N interactions, while $\delta(\mathrm{Pu,N})$ is very slightly (an increase of less than 1%) larger than $\delta(\mathrm{U,N})$.

Electron density difference distributions reflect the topological data, with strong similarities between the uranyl and neptunyl complexes, and somewhat more diffuse regions of equatorial charge accumulation in the plutonyl complex. Also apparent in the neptunyl and plutonyl complexes are perturbations around the actinide centre consistent with there being a change in f-occupation between the uncoordinated dication and the complex. Regenerating these distributions for the spin constrained data suggests a larger redistribution of charge within the ligand in the neptunium complex than in the unconstrained system. The integrated properties indicate that all actinyls undergo a significant redistribution of charge upon complexation, however no trends were found regarding the magnitude of this redistribution. Application of spin constraint result in minimal differences to the integrated properties of the plutonyl complexes, but the neptunyl complexes are significantly affected. Integrated properties and spin data point to the oxidation of neptunium in the neptunyl complexes to Np(VII). What can be taken from the spin analysis is that single-point energy calculations certainly resolve spin contamination in that, formally, the expectation values $\langle S^2 \rangle$ are what they ought to be: 0.75, reflecting a single unpaired electron, in the neptunyl complexes and 2.0, reflecting two unpaired electrons in the plutonyl complexes. However, the localisation of these unpaired electrons is still not correct in the case of the neptunyl complexes. Reoptimisation of the complexes with the spin constraint may be helpful here.

6.3.5. Density-based Analysis of AnO_2-rubyrin(1.1.1.1.0.0); An = U, Np, Pu: the Spin Unrestricted Approach *vs.* the Spin Constrained Approach.

6.3.5.1. Structural Data

The final systems examined in this chapter are complexes of uranyl, neptunyl and plutonyl with rubyrin(1.1.1.1.0.0). As in previous sections, there are no major structural changed induces by changing the central ion, so Figure 6.10 shows the optimised geometries for only the NpO_2-rubyrin(1.1.1.1.0.0) complex (the uranyl complex can be seen in Chapter 5), optimised using the PBE *xc*-functional. Table 6.31 shows average and individual An-N and An-O bond lengths for uranyl, neptunyl and plutonyl complexes with rubyrin(1.1.1.1.0.0) for complexes optimised using the PBE and B3LYP *xc*-functionals.

	U		Np		Pu	
	PBE	B3LYP	PBE	B3LYP	PBE	B3LYP
$\overline{r_{\mathrm{An-N}}}$	2.717	2.742	2.736	2.747	2.779	2.912
$r_{\mathrm{An-O}}$	1.784	1.762	1.778	1.751	1.768	1.771
$\Delta r_{\mathrm{An-N2}}$	0.073	0.066	0.069	0.060	0.071	0.094

Table 6.31: An-N and An-O bond lengths for complexes with the rubyrin(1.1.1.1.0.0) ligand optimised with the PBE and B3LYP functionals in the gas phase.

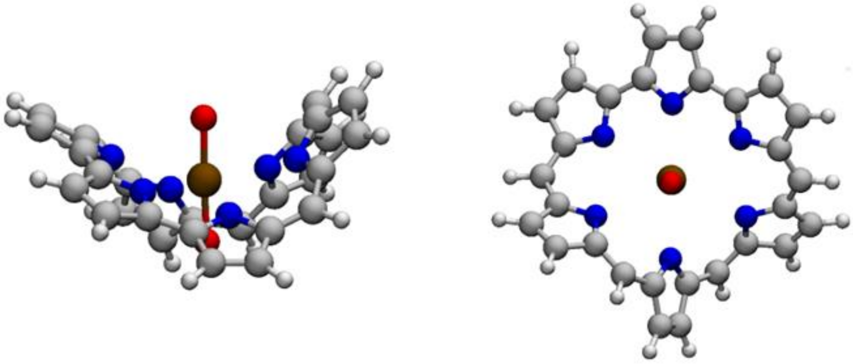

Figure 6.10: Optimised NpO_2-rubyrin(1.1.1.1.0.0) complexes, generated from data obtained using the PBE *xc*-functional in the gas phase.

There is, in general, a slight lengthening in An-N bonds as one moves from U to Pu, occurring with both *xc*-functionals. The An-O bonds decrease in length from U to Pu for complexes optimised using the PBE *xc*-functional. For complexes optimised using the B3LYP *xc*-functional, in the gas phase, the Np-O bond is slightly shorter (~0.02 Å) than the U-O bond, and the Pu-O bond, unusually, is longer than both the U-O and

Np-O bond. Compared to the An-O bond lengths in the uncoordinated actinyls, the U-O and Np-O bonds are increased by ~ 0.070-0.075 Å upon complexation when the PBE *xc*-functional is used, and ~ 0.060-0.065 Å when the B3LYP *xc*-functional is used. In the plutonyl complex, use of the PBE *xc*-functional results in a Pu-O bond which is ~ 0.070 Å longer than in the uncoordinated dication, employing the B3LYP *xc*-functional results in a more significant lengthening, of ~0.09 Å. This is almost certainly an effect induced by the significant spin contamination present in this system, and will be explored further in subsequent sections.

6.3.5.2. QTAIM - Topological and Integrated Properties

QTAIM parameters for An-N bonds in U, Np and Pu complexes with the rubyrin(1.1.1.1.0.0) ligand are given Table 6.32 and 6.33. Recalling the data from Table 6.7, the neptunyl and plutonyl complexes with rubyrin were found to be significantly affected by spin contamination, manifesting in the PuO_2-rubyrin(1.1.1.1.0.0) complex when optimised with the B3LYP *xc*-functional as a spin population index for the plutonium ion which is suggestive of spontaneous reduction of Pu(VI) to Pu(V). Looking first at the data obtained from the unconstrained calculations, it is apparent that regardless of *xc*-functional choice, there is a reduction in the electron density at the An-N BCP as the actinide ion is changed from U to Pu. The average value of the laplacian decreases slightly as one traverses U > Pu with both *xc*-functionals. There is a marked decrease in the total value of the energy density from U to Pu. When the PBE *xc*-functional is used, the sum of H_{BCP} for the plutonyl complex is a third of its value for the uranyl complex. When the B3LYP *xc*-functional is used this decrease is even more extreme and the total value for the energy density at the Pu-N BCPs is < 0.001 a.u. Although the data for individual bonds are not given here, it should be mentioned that this is the result of several individual bonds having small positive values of H_{BCP} (indicating an interaction without significant electron sharing[347]). When the spin constraint is applied, small increases in the values of $\sum \rho_{\mathrm{An-N}}$ are found when the PBE *xc*-functional is utilised. Use of the B3LYP xc-functional results in a drop in $\sum \rho_{\mathrm{An-N}}$ for the neptunyl complex and a significant increase in $\sum \rho_{\mathrm{An-N}}$ for the plutonyl complex. Average values for the laplacian of the electron density in the An-N bonds are found to be slightly lower for both complexes when the PBE *xc*-functional is used, as well as for the neptunyl complex where the B3LYP *xc*-functional is used, but this value is increased for the PuO_2-

rubyrin(1.1.1.1.0.0) complex optimised using the B3LYP *xc*-functional. $\sum H_{\mathrm{An-N}}$ increases compared to the unconstrained values for the complexes optimised using the PBE xc-functional, as seen in the previous sections. It is slightly lower compared to the unconstrained value when the neptunyl complex optimised with the B3LYP functional is considered, but the largest change is the increase in $\sum H_{\mathrm{An-N}}$ for the plutonyl complex optimised with the B3LYP *xc*-functional.

The An-N delocalisation index decreases from U to Pu for both *xc*-functionals, when spin constraint is omitted, however these effects are more dramatic for the plutonyl complex optimised using the B3LYP *xc*-functional, supporting the idea that there is little equatorial electron sharing in this complex when considered with the B3LYP *xc*-functional. Overall, there is a more notable decrease in covalency in the order U > Np > Pu than for either the cyclo[6]pyrrole or isoamethyrin(1.0.1.0.0.0) complexes and this is most pronounced between the Np and Pu complexes, and particularly when the B3LYP *xc*-functional is employed. When the spin constraint is applied, small increases (~ 0.1 a.u.) are seen compared to the unconstrained systems for the neptunyl and plutonyl complexes optimised using the PBE *xc*-functional, as well as for the neptunyl complex optimised with the B3LYP *xc*-functional. The increase in the value of the delocalisation index compared to the value obtained from the unconstrained calculations is again more significant for the PuO_2-rubyrin(1.1.1.1.0.0) complex optimised using the B3LYP *xc*-functional than for the neptunyl complex.

PBE		U	Np	Pu
$\sum \rho_{\mathrm{An-N}}$	Unconstrained	0.244	0.222	0.194
	Constrained	-	0.226	0.199
$\overline{\nabla^2 \rho_{\mathrm{An-N}}}$	Unconstrained	0.101	0.102	0.096
	Constrained	-	0.095	0.088
$\sum H_{\mathrm{An-N}}$	Unconstrained	-0.019	-0.013	-0.006
	Constrained	-	-0.021	-0.015
$\sum \delta(\mathrm{An-N})$	Unconstrained	1.761	1.672	1.493
	Constrained	-	1.716	1.596

Table 6.32: QTAIM parameters for the An-N bond in the AnO_2-rubyrin(1.1.1.1.0.0), (An = U, Np, Pu) complexes, given as average or total values, in a.u., obtained using the PBE *xc*-functional, with and without spin constraint.

B3LYP	*xc*-functional	U	Np	Pu
$\sum \rho_{\mathrm{An-N}}$	Unconstrained	0.230	0.222	0.138
	Constrained	-	0.152	0.226
$\overline{\nabla^2 \rho_{\mathrm{An-N}}}$	Unconstrained	0.098	0.097	0.078
	Constrained	-	0.068	0.090
$\sum H_{\mathrm{An-N}}$	Unconstrained	-0.016	-0.014	0.000
	Constrained	-	-0.006	-0.023
$\sum \delta(\mathrm{An-N})$	Unconstrained	1.558	1.573	0.950
	Constrained	-	1.584	1.243

Table 6.33: QTAIM parameters for the An-N bond in the AnO$_2$-rubyrin(1.1.1.1.0.0), (An = U, Np, Pu) complexes, given as average or total values, in a.u., obtained using the B3LYP *xc*-functional, with and without spin constraint.

PBE		U	Np	Pu
$\rho_{\mathrm{An-O}}$	Unconstrained	0.301	0.305	0.307
	Constrained	-	0.297	0.299
$\nabla^2 \rho_{\mathrm{An-O}}$	Unconstrained	0.314	0.325	0.316
	Constrained	-	0.413	0.416
$H_{\mathrm{An-O}}$	Unconstrained	-0.274	-0.275	-0.276
	Constrained	-	-0.249	-0.248

Table 6.34: QTAIM parameters for the An-O bond in the AnO$_2$-rubyrin(1.1.1.1.0.0), (An = U, Np, Pu) complexes, given as average or total values, in a.u., obtained using the PBE *xc*-functional, with and without spin constraint.

B3LYP		U	Np	Pu
$\rho_{\mathrm{An-O}}$	Unconstrained	0.320	0.325	0.305
	Constrained	-	0.317	0.300
$\nabla^2 \rho_{\mathrm{An-O}}$	Unconstrained	0.264	0.245	0.229
	Constrained	-	0.345	0.366
$H_{\mathrm{An-O}}$	Unconstrained	-0.309	-0.315	-0.277
	Constrained	-	-0.285	-0.250

Table 6.35: QTAIM parameters for the An-O bond in the AnO$_2$-rubyrin(1.1.1.1.0.0), (An = U, Np, Pu) complexes, given as average or total values, in a.u., obtained using the B3LYP *xc*-functional, with and without spin constraint.

Topological parameters for the An-O bonds calculated with both *xc*-functionals are given in Tables 6.34 and 6.35 for the PBE and B3LYP *xc*-functionals, respectively. Overall, considering first the data obtained from the unconstrained calculations, QTAIM parameters for the An-O bonds seem to support a slight increase in covalency as one traverses U to Pu, with the exception again of the plutonyl complex optimised using the B3LYP *xc*-functional. This Pu-O interaction appears to have less covalency than the U-O interaction optimised using the same model chemistry, and this is consistent with the more significant Pu-O bond lengthening upon complexation when the B3LYP *xc*-functional is employed. This is however, at odds with the conclusion from Chapter 3 that the magnitude of U-O covalency (and the magnitude of the redshift of the U-O stretching modes) can act as an indicator of equatorial covalency. Chapter 5 concluded that with multidentate ligands, the picture is much less straightforward than the simple relationship found to exist with monodentate ligands in Chapter 3 and additional interactions between the ligand and uranyl unit must be considered, however it appears that changing the actinide centre complicates the situation further. Applying the spin constraint results in values of $\rho_{\mathrm{An-O}}$ and $H_{\mathrm{An-O}}$ indicative of slightly lower covalency, although values of $\nabla^2\rho_{\mathrm{An-O}}$, in keeping with those of the isoamethyrin and cyclo[6]pyrrole complexes, are higher than in their unconstrained analogs.

Next, integrated properties are discussed. Tables 6.36 and 6.37 contain atomic populations for complexes optimised with PBE and B3LYP in the gas phase, respectively. Tables 6.38 and 6.39 contain localisation and delocalisation data for complexes optimised with PBE and B3LYP in the gas phase, respectively. All quantities are shown alongside their deviation from those of the uncoordinated optimised actinyls.

Looking first at the atomic populations in Table 6.36 and 6.37, it is first apparent that for both *xc*-functionals, the increase of the population of the actinyl unit as a whole is more significant in the plutonyl complexes than the neptunyl complexes, and more significant in the neptunyl complexes than the uranyl complexes, likewise the charge on the oxygen ions. $N(\mathrm{PuO_2})$ is greater than 109, indicating that a whole unit of charge has been donated into the plutonyl unit, consistent with the idea that the Pu ion has been reduced to Pu(V). This is the case with both *xc*-functionals, but is most pronounced for the complex optimised with the B3LYP *xc*-functional. Application of spin constraint resolves this. Differences induced by spin constraint are minimal (~ 0.01) for the neptunyl complex optimised with the PBE *xc*-functional, slightly more significant for the plutonyl complex optimised with the PBE *xc*-functional. For the plutonyl complex optimised using the B3LYP *xc*-functional however, changes induced by the application of spin constraint are an order of magnitude higher (~ 0.1), and the population data is no longer consistent with the spontaneous reduction of Pu(VI) to Pu(V).

		U		Np		Pu	
PBE	*xc*-functional	complex	Δ	complex	Δ	complex	Δ
N(O)	Unconstrained	8.84	0.26	8.78	0.29	8.75	0.33
	Constrained	-	-	8.77	0.28	8.74	0.31
N(An)	Unconstrained	89.17	0.33	90.35	0.33	91.52	0.37
	Constrained	-	-	90.34	0.33	91.50	0.36
N(AnO_2)	Unconstrained	106.84	0.84	107.90	0.90	109.03	1.03
	Constrained	-	-	107.89	0.89	108.98	0.98

Table 6.36: Atomic populations in a.u. for AnO2-rubyrin(1.1.1.1.0.0); An = U, Np, Pu; obtained using the PBE *xc*-functional with both the spin-unconstrained and spin-constrained approach, alongside Δ, the differences from values for uncoordinated actinyls given in Table 6.5.

		U		Np		Pu	
B3LYP	*xc*-functional	complex	Δ	complex	Δ	complex	Δ
N(O)	Unconstrained	8.88	0.23	8.82	0.26	8.90	0.41
	Constrained	-	-	8.82	0.32	8.76	0.27
N(An)	Unconstrained	88.95	0.24	90.12	0.23	91.51	0.49
	Constrained	-	-	90.12	0.13	91.32	0.31
N(AnO_2)	Unconstrained	106.72	0.72	107.76	0.76	109.31	1.31
	Constrained	-	-	107.76	0.76	108.85	0.85

Table 6.37: Atomic populations in a.u. for AnO2-rubyrin(1.1.1.1.0.0); An = U, Np, Pu; obtained using the B3LYP *xc*-functional with both the spin-unconstrained and spin-constrained approach, alongside Δ, the differences from values for uncoordinated actinyls given in Table 6.5.

Moving on to the localisation and delocalisation data in Table 6.38 and 6.39, and again considering first the unconstrained data, it is apparent that consistent with the structural and topological data, there is significant functional dependence concerning the plutonyl complex, which was not seen in previous chapters, or previous sections of this chapter. Looking first at the data obtained using the PBE *xc*-functional, it can be seen that the localisation on the oxygen ions increases upon complexation, with the magnitude of the change increasing from U to Pu.

The localisation on the actinide centres decreases upon complexation, as does the charge delocalised in the An-O interaction, indicating, as in previous sections, this interaction becoming more ionic in nature. The overall actinyl localisation index deviates most from that of the uncomplexed actinyls for the uranyl complex and least for the plutonyl complex, suggesting the maximum An-N delocalisation can be found for the uranyl complex. This is consistent with the data in Table 6.32 showing that for the PBE *xc*-functional in the gas phase, the uranyl complex has the greatest total An-N delocalisation.

However, when the B3LYP *xc*-functional is employed without spin constraint, the behaviour of the plutonyl unit, like with the atomic population data in Table 6.37, is consistent with a change in oxidation state of the plutonium atom. The increase in localisation on the oxygen ions is significant, as is the reduction in An-O delocalisation, but the localisation on the actinide centres themselves also increases, meaning the localisation on the actinyl as a whole is greater than 108. This would seem consistent with a spontaneous change in oxidation state of the plutonium atom, from Pu^{6+} to Pu^{5+}. This would have the effect of removing an electron from the ligand, resulting in a system with four unpaired electrons in total, three on the plutonyl unit and one on the ligand. This is borne out by the expectation values $\langle S^2 \rangle$ and spin population analysis in Table 6.7.

		U		Np		Pu	
PBE	*xc*-functional	complex	Δ	complex	Δ	complex	Δ
λ(O)	Unconstrained	7.66	0.31	7.58	0.34	7.54	0.41
	Constrained	-	-	7.57	0.33	7.51	0.38
λ(An)	Unconstrained	86.15	-0.37	87.23	-0.43	88.43	-0.34
	Constrained	-	-	87.22	-0.44	88.33	-0.43
δ(An-O)	Unconstrained	1.98	-0.34	2.01	-0.33	2.03	-0.34
	Constrained	-	-	2.02	-0.33	2.06	-0.32
δ(O_1-O_2)	Unconstrained	0.1	-0.03	0.13	-0.04	0.14	-0.06
	Constrained	-	-	0.13	-0.04	0.15	-0.06
λ(AnO_2)	Unconstrained	105.52	-0.48	106.54	-0.46	107.74	-0.26
	Constrained	-	-	106.53	-0.47	107.63	-0.37

Table 6.38: Localisation and delocalisation indices in a.u. obtained using the PBE *xc*-functional with both the spin-constrained and spin unconstrained approach for AnO_2-rubyrin(1.1.1.1.0.0) alongside Δ, the differences from values for uncoordinated actinyls given in Table 6.6.

		U		Np		Pu	
B3LYP	*xc*-functional	complex	Δ	complex	Δ	complex	Δ
λ(O)	Unconstrained	7.73	0.28	7.64	0.31	7.8	0.56
	Constrained	-	-	7.64	0.40	7.58	0.35
λ(An)	Unconstrained	86.11	-0.33	87.21	-0.37	89.05	0.37
	Constrained	-	-	87.20	-0.44	88.37	-0.29
δ(An-O)	Unconstrained	1.95	-0.32	2.00, 1.99	-0.31	1.91	-0.42
	Constrained	-	-	2.00	-0.35	2.03	-0.31
δ(O_1-O_2)	Unconstrained	0.1	-0.01	0.12	-0.03	0.11	-0.06
	Constrained	-	-	0.12	-0.05	0.14	-0.04
λ(AnO_2)	Unconstrained	105.57	-0.43	106.59	-0.41	108.58	0.58
	Constrained	-	-	106.60	-0.40	107.75	-0.25

Table 6.39: Localisation and delocalisation indices in a.u. obtained using the B3LYP *xc*-functional with both the spin-constrained and spin unconstrained approach for AnO_2-rubyrin(1.1.1.1.0.0) alongside Δ, the differences from values for uncoordinated actinyls given in Table 6.6.

Application of spin constraint again makes only very minor differences to values of the localisation and delocalisation in the neptunyl complexes, and by far the most significant change is induced in the PuO_2-rubyrin(1.1.1.1.0.0) complex when the B3LYP *xc*-functional is employed, with the result being that the spontaneous reduction of the plutonium ion seen when the constraint is absent disappears. It would appear in this case, that the significant spin contamination issue faced by PuO_2-rubyrin(1.1.1.1.0.0) is resolved by the application of spin constraint at the single-point energy calculation level.

6.3.5.3. Electron Density Difference Distributions

Figure 6.11 shows electron density difference distributions for uranyl, neptunyl and plutonyl rubyrin complexes optimised with the PBE *xc*-functional without spin constraint. Due to there being a significant difference in topological and integrated parameters in the plutonyl complex induced by use of the B3LYP *xc*-functional, the electron density difference distribution for PuO_2-rubyrin(1.1.1.1.0.0) optimised with the B3LYP *xc*-functional is given in Figure 6.12. Looking first at the distributions generated using the PBE *xc*-functional in the gas phase, it is apparent that as with the cyclo[6]pyrrole and isoamethyrin(1.0.1.0.0.0)′ complexes, the three complexes display strongly similar behaviour upon complexation.

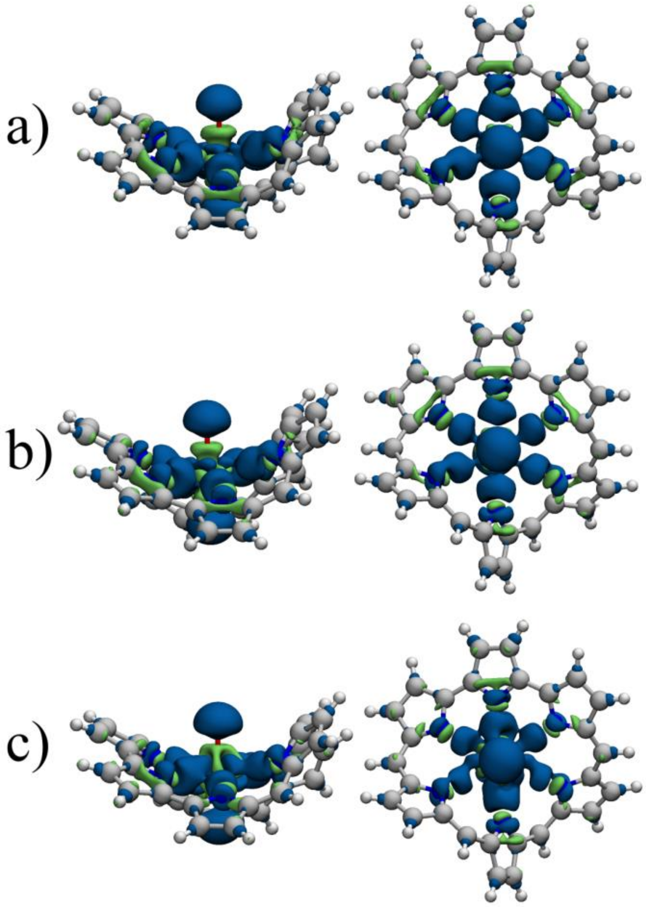

Figure 6.11: Electron density difference distributions for a) UO_2-rubyrin(1.1.1.1.0.0); b) NpO_2-rubyrin(1.1.1.1.0.0); c) PuO_2-rubyrin(1.1.1.1.0.0); generated from data obtained using the PBE *xc*-functional in the gas phase, isosurface value = 0.005 a.u.

There are blue teardrop-shaped regions of accumulation in the An-N bonding region for all three complexes. These differ slightly in magnitude, with the difference between the uranyl and plutonyl complex being reduced donation from the ligand (the green isosurfaces immediately behind the pyrrolic nitrogen centres) in the plutonyl complex alongside the accumulation in the An-N bonding region, which are both smaller in magnitude and more diffuse in the plutonyl complex, with the exception of the ‘top’ and ‘bottom’ Pu-N bonds which display significant, if diffuse, accumulation. Considering the An-O interaction, as before, there are strong similarities between the three complexes with the major difference being the perturbation of the region of depletion on the Pu-O bond caused by a change of f-occupation upon complexation. Accumulation of charge is apparent on all oxygen ions and this, along with the depletion present on all An-O bonds, indicates an interaction which becomes more ionic upon complexation, as has been seen before in Chapters 3-5.

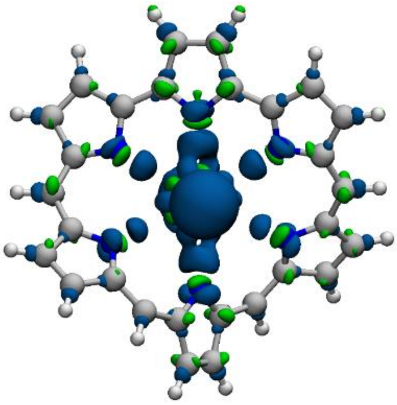

Figure 6.12: Electron density difference distribution for PuO_2-rubyrin(1.1.1.1.0.0) generated from data obtained using the B3LYP *xc*-functional in the gas phase without spin constraint, isosurface value = 0.005 a.u

Figure 6.12 shows the electron density difference distribution for the plutonyl complex with rubyrin(1.1.1.1.0.0) generated from data obtained using the B3LYP *xc*-functional without spin constraint. The differences induced by change of *xc*-functional in the plutonyl complex are significant. The distribution in Figure 6.12 shows that depletion from the pyrrolic nitrogen centres is almost non-existent at this isosurface, although small regions indicating depletion appear on several pyrrolic carbon atoms. The regions of accumulation indicative of electron sharing are significantly diminished compared to those generated from the data obtained using the PBE *xc*-functional.

The Pu-N bonds with extremely small regions of accumulation correspond to bonds with QTAIM parameters indicating interactions with no significant electron sharing. It must be questioned how meaningful it is to generate an electron density difference distribution by subtracting the densities of a dianionic ligand and dicationic plutonyl unit from that of the neutral complex, when the integrated QTAIM properties and spin-density data suggest that the fragments ought to be an anionic ligand and cationic plutonyl.

One possibility would be to re-visualise the distribution using differently charged fragments, but where An(V) expanded porphyrin complexes are reported experimentally, either there is an additional coordination of one O_{yl} ion, or the complex as a whole is anionic rather than neutral[21,133,190], and without reoptimising the entire system with an additional electron, the complex remains unrealistic.

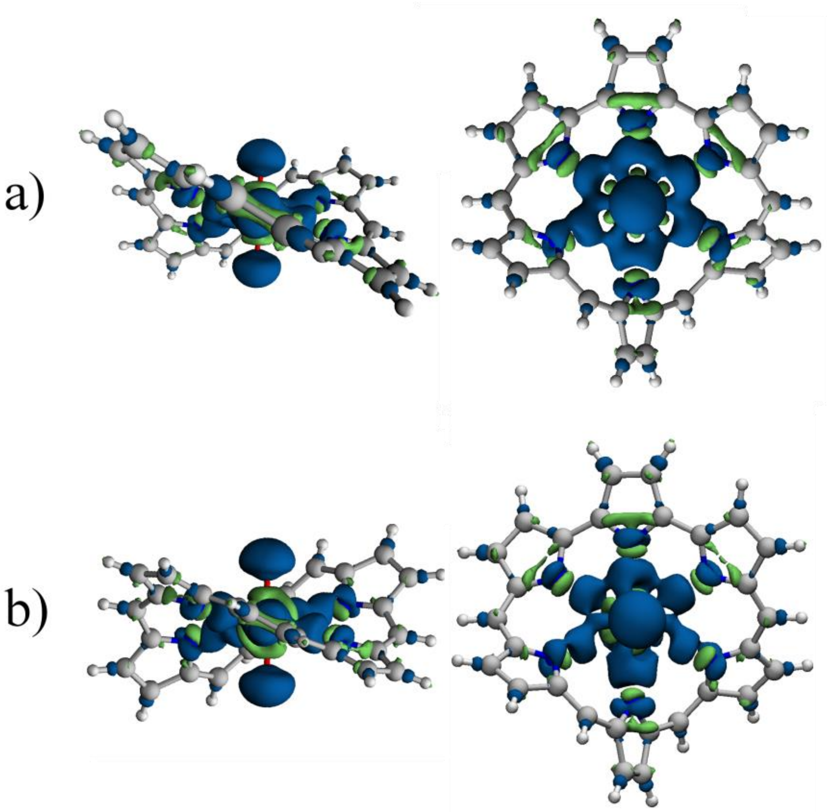

Figure 6.13: Electron density difference distribution generated from data obtained using the PBE *xc*-functional in the gas phase, with spin constraint, isosurface value = 0.005 a.u. a) NpO_2-rubyrin(1.1.1.1.0.0) and b) PuO_2-rubyrin(1.1.1.1.0.0).

When the complexes are revisualised from the data obtained from the single point energy calculations utilising the spin constraint (Figure 6.13), it can be seen that for the data obtained using the PBE *xc*-functional in the gas phase, as with the isoamethyrin and cyclo[6]pyrrole complexes, the distributions are qualitatively very similar to those obtained without the use of constraint.

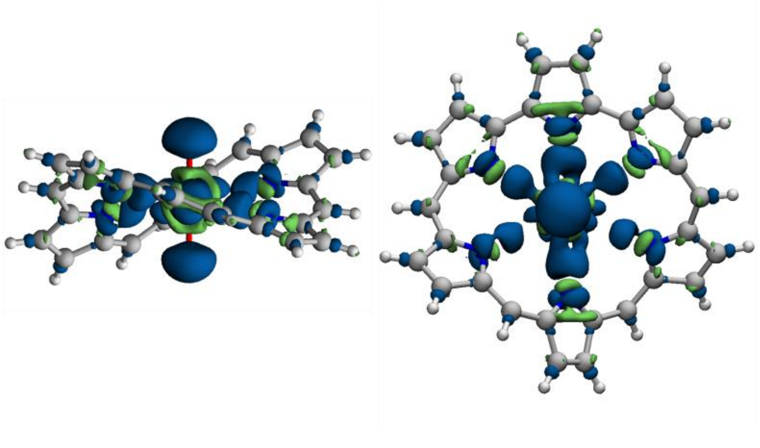

Figure 6.14: Electron density difference distribution for PuO_2-rubyrin(1.1.1.1.0.0) generated from data obtained using the B3LYP *xc*-functional in the gas phase with spin constraint, isosurface value = 0.005 a.u.

When the same distribution is visualised for the data obtained from the spin constrained calculation on the plutonyl complex using the B3LYP *xc*-functional, as in Figure 6.14, it can be seen that the plutonyl complex resemble more closely other density difference distributions obtained using a dicationic actinyl and dianionic ligand, for example, those in Chapter 5.

6.3.5.4. Spin Density and Spin Population Analysis for AnO2-rubyrin(1.1.1.1.0.0); An = Np, Pu.

Table 6.40 contains the spin analysis for the neptunyl and plutonyl complexes with rubyrin(1.1.1.1.0.0). First, it is desirable to use the expectation value $\langle S^2 \rangle$ to confirm the assertion that the Pu ion in the PuO$_2$-rubyrin(1.1.1.1.0.0) complex optimised with the B3LYP *xc*-functional has indeed undergone spontaneous reduction. A $\langle S^2 \rangle$ value of 3.05 is calculated for this complex. This can be rationalised by considering the spins of the ligand and the Pu ion. For the Pu^{5+} ion, formally the expectation value $\langle S^2 \rangle$ is now 3.75, and for the ligand, $\langle S^2 \rangle$ is now 0.75. It appears that we can subtract this number from the expectation value $\langle S^2 \rangle$ for the plutonyl unit, as the unpaired electron on the ligand will be of opposite spin, giving a $\langle S^2 \rangle$ of 3.00. In addition, Atomic Electronic Spin Population analysis reveals that in this complex, the plutonium atom has a spin population of 3.22, when the B3LYP *xc*-functional is used.

		xc-functional	$\langle S^2 \rangle$	$N_s(A)$	$\Delta N_s(A)$
Unconstrained	Np	PBE	0.88	1.29	0.29 (29%)
		B3LYP	1.76	1.10	0.10 (10%)
	Pu	PBE	2.43	2.68	0.68 (34%)
		B3LYP	3.05	3.22	1.22 (61%)
Constrained	Np	PBE	0.75	0.97	-0.03 (3%)
		B3LYP	0.75	0.98	-0.02 (2%)
	Pu	PBE	2.00	1.96	-0.04 (2%)
		B3LYP	2.00	1.98	-0.02 (1%)

Table 6.40: The expectation value $\langle S^2 \rangle$, atomic spin population of atom A ($N_s(A)$), the difference between the atomic spin population and formal spin ($\Delta N_s(A)$) and this difference expressed as a percentage of the formal spin.

For comparison, the spin population for the plutonium atom in the PBE-optimised complex without the spin constraint is 2.68, greater than the formal spin, and still consistent with significant spin contamination, but not such that an entire electron can be said to have delocalised to the ligand. The topological parameters indicating significantly reduced covalency in the equatorial bonds of the complex optimised with the B3LYP *xc*-functional without spin constraint are then consistent with a decrease in covalency with lower oxidation states, as has been seen previously[27].

As seen in Table 6.40, application of spin constraint completely resolves spin contamination issues in these complexes, although particularly for the PuO2-rubyrin(1.1.1.1.0.0) complex optimised with the B3LYP *xc*-functional, the possibility that the molecular geometry is not correct must be strong, particularly considering the rather anomalous An-N and An-O bond lengths in this complex. However, now that it can be seen that at least for the rubyrin(1.1.1.1.0.0) complexes spin contamination may be resolved by the application of spin constraint, a complete reoptimisation may not be considered a waste of resources.

Further evidence that application of spin constraint resolves spin contamination in these complexes can be seen in Figure 6.15. Looking first at Figure 6.15 a), it can be seen that for the neptunyl complex optimised using PBE *xc*-functional without spin constraint has spin density concentrated around the metal centre, consistent with the one unpaired f-electron present, as well as a small amount of negative spin density associated with the oxygen ions. This, which is present in the cyclo[6]pyrrole and isoamethyrin complexes too, is resolved by the application of spin constraint (Figure 6.15 b)), and explains the differences found in the integrated and topological properties of the An-O bond induced by the application of spin constraint.

Figure 6.15 c) shows that for the unconstrained plutonyl complex optimised using the PBE *xc*-functional, spin contamination is more significant than for the neptunyl complex. This is reflected in the topological and integrated properties, and as with the neptunyl complex, is resolved by the application of spin constraint (Figure 6.15 d)) The plutonyl complex optimised using the B3LYP *xc*-functional not only demonstrates a somewhat larger region of spin density on the metal centre, consistent with three unpaired electrons rather than two, but also demonstrates significant spin density of the opposite sign on the ligand. In order to hypothesise why this spontaneous reduction may have occurred, there are several factors to consider. Firstly, one must consider the size of the conjugated ring system. As conjugated rings grow larger, the HOMO-LUMO gap decreases, meaning that removing an electron requires less energy. This is observed as a redshift in UV-vis absorption bands.

Secondly, it is well known that in many coordination environments, Pu(V) is more stable than Pu(VI), accounting for the prevalence of the former in experimental chemistry[415].

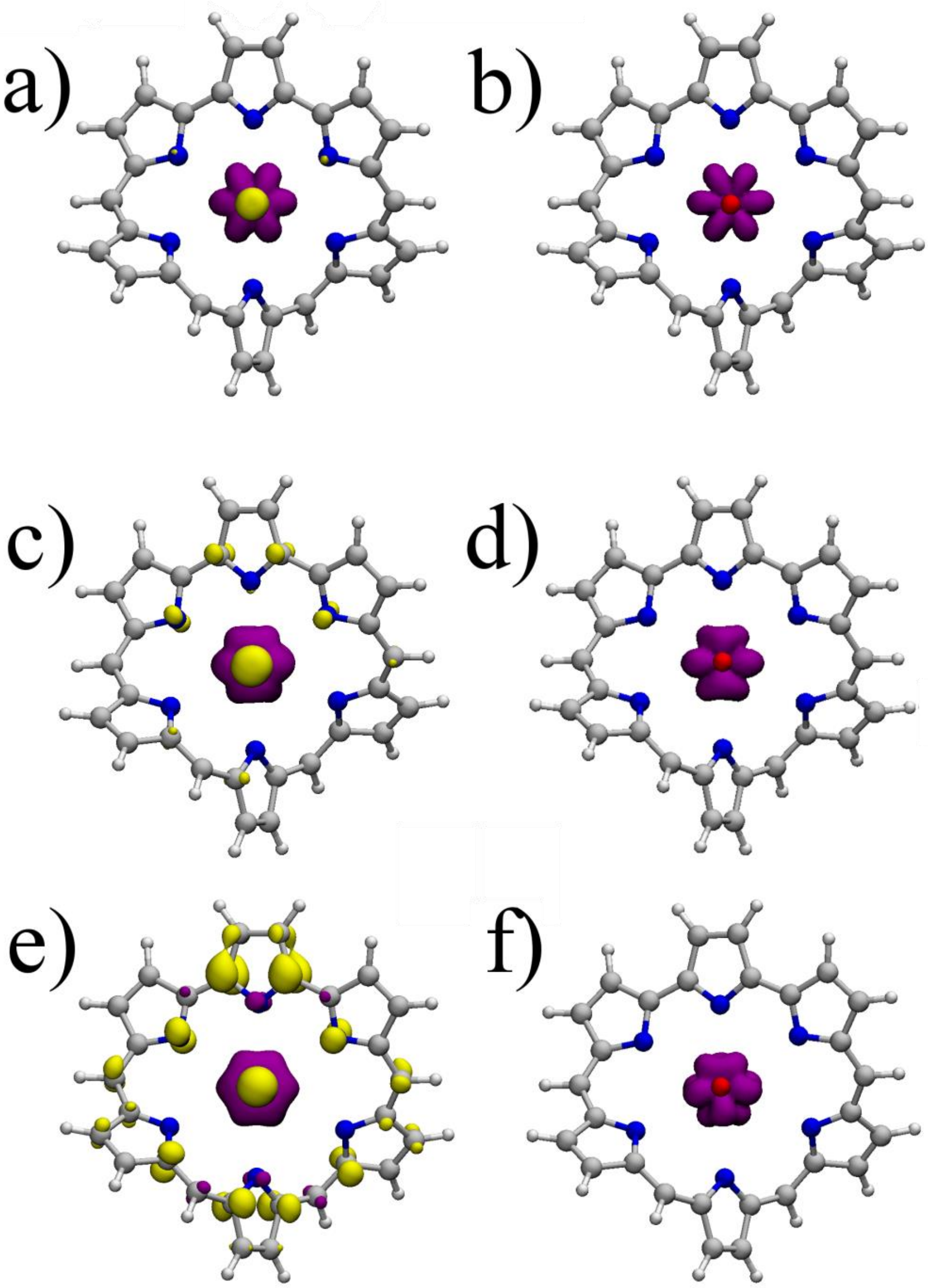

Figure 6.15: Spin-densities of the NpO_2- and PuO_2-rubyrin(1.1.1.1.0.0) complexes rendered at an isosurface of 0.005 a.u., with positive spin density in purple and negative spin density in yellow. a) NpO_2-rubyrin(1.1.1.1.0.0) optimised with the PBE *xc*-functional without spin-constraint; b) NpO_2-rubyrin(1.1.1.1.0.0) optimised with the PBE *xc*-functional with spin-constraint; c) PuO_2-rubyrin(1.1.1.1.0.0) optimised with the PBE *xc*-functional without spin-constraint; d) PuO_2-rubyrin(1.1.1.1.0.0) optimised with the PBE *xc*-functional with spin-constraint; e) PuO_2-rubyrin(1.1.1.1.0.0) optimised with the B3LYP *xc*-functional without spin-constraint; f) PuO_2-rubyrin(1.1.1.1.0.0) optimised with the B3LYP *xc*-functional with spin-constraint.

Figure 6.15 e) shows that the application of spin constraint not only resolves the spin contamination associated with the plutonyl oxygen ions, but also act to prevent the spontaneous reduction of the Pu ion. The question then is how reliable is the geometry, particularly for this complex? Based on bond length data in Table 6.31, a full reoptimisation of particularly the plutonyl complexes with rubyrin(1.1.1.1.0.0) considering the effects of spin constraint is recommended.

6.3.5.5. AnO$_2$-rubyrin(1.1.1.1.0.0) Conclusions.

The AnO$_2$-rubyrin(1.1.1.1.0.0) complexes are the first complexes examined in this thesis where the choice of *xc*-functional has a significant effect on the character of An-N and An-O bonding. As one moves from the uranyl complexes with rubyrin to neptunyl and plutonyl complexes, there is an increase in average An-N bond length and a decrease in An-O bond length in the order U > Np > Pu when the PBE *xc*-functional is used (although An-O bonds are all lengthened compared to the uncoordinated actinyls). Use of the B3LYP functional results in an unusual Pu-O lengthening. A decrease in equatorial covalency as defined by QTAIM is apparent as the central ion is changed from U to Pu, with both *xc*-functionals when spin constraint are neglected. When optimised with the B3LYP *xc*-functional, the plutonyl complex demonstrates very little equatorial covalent character, and a significant reduction in equatorial An-N delocalisation compared to the uranyl/neptunyl complexes. The differences induced by change of *xc*-functional here are of importance, particularly considering the B3LYP *xc*-functional, with its inclusion of exact exchange which has been shown to partially cancel the self-interaction error[343], giving good results for heavy element systems[61]. Again focussing on the spin constraint free calculations, analysis of the integrated properties and density difference distributions obtained using the B3LYP *xc*-functional, as well as analysis of atomic spin populations and visualisation of spin densities all support a change of oxidation state in the plutonyl complex, from Pu(VI) to Pu(V), accounting for the increased An-O bond lengths and large relative shifts of the actinyl stretching modes in these complexes. This is an interesting result, inadvertently replicating the experimentally observed spontaneous reduction of plutonyl seen upon complexation with isoamethyrin(1.0.1.0.0.0)′[133,190], but bringing into question the robustness of these model chemistries, at least without the application of spin constraint, for performing calculations on plutonyl. The application of spin constraint appears, based on analysis of the spin densities and spin population the actinide ions, to resolve the significant spin contamination which was present in the unconstrained systems. Further investigations are however necessary to ascertain the effect of this contamination on molecular geometries.

6.3.6 Summary and Conclusions

In summary, only the data obtained for the complexes with the isoamethyrin ligand was judged to be sufficiently reliable due to significant spin contamination in the other systems when the neptunyl and plutonyl complexes are investigated. This ligand is calculated to bind uranyl with the greatest degree of equatorial covalency and also the greatest stability, followed by neptunyl, followed by plutonyl. The effects of the application of spin constraint in the isoamethyrin complex are mostly small, with the energy density in the An-N bonds increasing quite significantly. Investigation of integrated properties reveals minimal changes are induced by the inclusion of spin constraint.

The anomalous spin data for cyclo[6]pyrrole and rubyrin complexes with neptunyl and plutonyl without spin constraint casts doubt on the reliability of these calculations. Application of spin constraint had largely successful results in eliminating the spin contamination itself, but it remains to be seen the effect of this on the geometry and other molecular properties. Additionally, in the NpO_2-cyclo[6]pyrrole complex optimised using the PBE *xc*-functional, although the application of spin constraint resulted in a complex with a single unpaired electron, as desired, this was not located on the Np centre, rather the ligand had one unpaired electron while the neptunium centre had spontaneously oxidised to Np(VII). This problem was not, however, present when the spin constraint were applied to the NpO_2-cyclo[6]pyrrole complex optimised using the B3LYP *xc*-functional, perhaps unsurprisingly since spin constraint as a method for resolving spin contamination has previously been more effective with hybrid functionals, rather than GGAs[61]. The spin contamination and spontaneous reduction of the Pu ion in the PuO_2-rubyrin(1.1.1.1.0.0) complex are also resolved by the application of spin constraint, although the significance of the spin contamination, particularly as far as the PuO_2-rubyrin(1.1.1.1.0.0) complex optimised with the B3LYP *xc*-functional is concerned, mean that a full geometry reoptimisation is needed in order to be sure of what is happening. It may be interesting to repeat these calculations with Np(V) and Pu(V) (with the associated coordinating species on one oxygen centre), as although crystallographic data exists only for the Np(V) complex with isoamethyrin(1.0.1.0.0.0)′, both the Np(V) and Pu(V) isoamethyrin(1.0.1.0.0.0)′ complexes have been synthesised. Additionally, the anomalous results reported here illustrate the importance of using more than one model chemistry and investigating the consequences of incorporating exact exchange, particularly when dealing with unpaired f-electrons.

It is likely that multiconfigurational calculations are necessary for accurate treatment of systems such as these. Based on the size of the systems, this may be currently beyond the reach of what is possible, but bears consideration for the future.

Based on the uranyl and neptunyl isoamethyrin data, it can be concluded that there is some evidence for selective behaviour exhibited by these ligands, although this must be considered in the knowledge that the Np(VI) and Pu(VI) complexes of isoamethyrin are not known experimentally, as instantaneous reduction of the actinide centre and corresponding oxidation of the ring cause the complexes to be of Np(V) and Pu(V). The other important implication of this is that in reality, the neptunyl and plutonyl complexes form instantaneously[133,190], while the uranyl complex takes either time or the application of heat to form. Studies of Np(V) and Pu(V) will be of interest here.

7. Conclusions

The aim of this thesis was to explore the interaction between actinyl (chiefly uranyl) dications with expanded porphyrin ligands using quantum chemical calculations and analysis of the electron density.

Chapter 3 began by examining a series of simple complexes of uranyl with monodentate first row ligands. Strong correlations were found between equatorial covalent character (based on the values of QTAIM descriptors at the equatorial bond critical points) and the frequencies of the distinctive (and readily experimentally measurable) uranyl stretching vibrational modes. The electron density of the complexes was analysed in detail. Integrated properties of the electron density showed a significant redistribution of charge within the uranyl unit upon complexation: accumulation of charge on the uranyl oxygen ions and depletion from the U-O_{yl} bond indicating that the U-O_{yl} interaction becomes more ionic upon complexation, with the magnitude of this correlating with equatorial covalency. This was supported by electron density difference distributions. Analysis of the reduced density gradient showed equatorial interactions becoming more directed with increasing binding strength. The well-known weakening of the U-O_{yl} bond upon equatorial complexation was thus attributed to a reduction in the covalent component of the U-O_{yl} interaction due to competing interactions equatorial plane. The strength of the correlations allowed the conclusion that the electron density based analytical tools employed in this chapter would be suitable for investigating more complicated systems.

The density based analytical tools utilised in Chapter 3 were subsequently turned to three complexes of uranyl with multidentate ligands: $[UO_2(BTP)_2]^{2+}$, a complex with two industrially relevant bis-triazinyl-pyridine ligands, which are known to selectively complex actinides over lanthanides, and UO_2-isoamethyrin(1.0.1.0.0.0), a complex of uranyl with the hexadentate macrocyclic expanded porphyrin ligand isoamethyrin, with the ligand in its simplified and peripherally substituted (UO_2-isoamethyrin(1.0.1.0.0.0)′) form. Good agreement with crystallographic data was found for the U-N and U-O bond lengths of the $[UO_2(BTP)_2]^{2+}$ and UO_2-isoamethyrin(1.0.1.0.0.0)′ complexes. U-N bond lengths in the peripherally simplified isoamethyrin complex were found to be badly overestimated, and the twisted conformation of the ligand observed experimentally could not be replicated, as had been shown previously, demonstrating the importance of the inclusion of peripheral alkyl groups for this complex. Strong similarities were found in the U-N and U-O bonding character of $[UO_2(BTP)_2]^{2+}$ and UO_2-isoamethyrin(1.0.1.0.0.0)′, with integrated charge data and density difference distributions showing that complexation by these ligands affected the uranyl unit in the same way. Based on this, it was concluded that isoamethyrin(1.0.1.0.0.0)′ and similar ligands were suitable complexes for investigating the U-N and U-O interaction, with a view to better understanding the factors which drive the selectivity shown by ligands like BTP.

Next, having shown that the expanded porphyrin ligand isoamethyrin(1.0.1.0.0.0)′ complexes uranyl with bonds of similar character to those in a complex with an industrially useful selective separation ligand, a series of complexes of uranyl with ligands from the hexaphyrin family were investigated. The size of the ligands depended upon the number of meso-carbon atoms (zero, two, four or six) between their pyrollic subunits. First, the effects of omitting peripheral alkyl substituents were investigated. These were only found to cause significant differences in bond length and overall geometry in complexes with two meso-carbon atoms. A weak linear relationship was found between the frequencies of the uranyl stretching modes and the binding energy. This relationship was significantly improved by omitting an anomalous complex with the large hexaphyrin(1.1.1.1.1.1) ligand, which had six meso-carbons. Justification for treating this complex separately was subsequently found in the analysis of the electron density. A representative sample of four complexes were selected for in-depth study: UO_2-cyclo[6]pyrrole (zero meso-carbons), UO_2-isoamethyrin(1.0.1.0.0.0)′ (two meso-carbons), UO_2-rubyrin(1.1.1.1.0.0) (four meso-carbons) and UO_2-hexaphyrin(1.1.1.1.1.1) (six meso-carbons). Analysis of the topological parameters for the U-N bonds showed that equatorial covalency was greatest for the smallest complex, UO_2-cyclo[6]pyrrole, which was also the most stable, followed by the UO_2-isoamethyrin(1.0.1.0.0.0)′ complex. Stability and equatorial covalency decreased again for the UO_2-rubyrin(1.1.1.1.0.0) and UO_2-hexaphyrin(1.1.1.1.1.1) complexes, which were more similar to one another. However, the topological data for the U-O_{yl} bonds, the frequencies of the uranyl stretching modes and the integrated charge data for the UO_2-hexaphyrin(1.1.1.1.1.1) complex were anomalous. Analysis of the reduced density gradient showed that in this complex, additional interactions are present between the uranyl oxygen ions and carbon/nitrogen atoms from the ligand. This is because the large hexaphyrin(1.1.1.1.1.1) ligand is folded almost completely around the uranyl unit, enclosing the oxygen ions. Two conclusions were possible here: firstly that smaller ligands, perhaps unsurprisingly, form U-N bonds with a greater degree of covalency. This is because, as evidenced by distortion in the ligands, the cavity of the isoamethyrin(1.0.1.0.0.0)′, rubyrin(1.1.1.1.0.0), hexaphyrin(1.1.1.1.1.1) ligands are somewhat too large for the uranyl dication. Secondly, the difficulties in characterising the U-N and U-O interactions in the UO_2-hexaphyrin(1.1.1.1.1.1) complex caused by the presence of additional ligand-actinyl interactions suggests that systems with a degree of equatorial planarity may be the best choice for investigating these interactions.

Chapter 6 broadened the previous study to include cyclo[6]pyrrole, isoamethyrin(1.0.1.0.0.0)′, rubyrin(1.1.1.1.0.0) complexes of NpO_2^{2+} and PuO_2^{2+}. Initial calculations on neptunyl and plutonyl complexes using unrestricted DFT were revealed to suffer from significant spin contamination. Only the isoamethyrin complexes were found to behave reasonably in this manner. Some evidence for selective behaviour was found, with the uranyl being preferentially bound by isoamethyrin, perhaps unsurprising given the smaller ionic radius U > Np > Pu and the conclusion from Chapter 5 that even uranyl is somewhat too small for the cavities of these ligands. However numerous problems with spin contamination and, in one case, the spontaneous reduction of Pu(VI) to Pu(V) in the PuO_2-rubyrin(1.1.1.1.0.0) complex, casts serious doubt on the validity of the data obtained for the cyclo[6]pyrrole and rubyrin(1.1.1.1.0.0) complexes. There was a dependence on model chemistry found, with use of a hybrid *xc*-functional perhaps offering a slight improvement, but in general, it must be concluded that unrestricted DFT is insufficient for modelling open shell actinide complexes with conjugated ligands. A preliminary investigation was subsequently carried out into the effects of using restricted DFT *via* the means of single-point energy calculations performed on the neptunyl and plutonyl complexes at the geometries optimised using unrestricted DFT. This was found to help with spin contamination, although in the NpO_2-cyclo[6]pyrrole complex, caused spontaneous oxidation of the neptunium ion from Np(VI) to Np(VII), and the unpaired electron was localised on the ligand. The spontaneous reduction of plutonium in the PuO_2-rubyrin(1.1.1.1.0.0) complex was, however, resolved, although it is likely that a full geometry reoptimisation is needed to fully assess the effects on the electronic structure of this method. It must also be stated that despite the fact that it is beyond current capabilities, multiconfigurational calculations may be the best way to perform reliable calculations on these systems. The other conclusion that can be gleaned from this chapter is a reaffirmation of that from Chapter 5: if maximising equatorial covalency and stability is desirable, smaller ligands, for example, those from the pentaphyrin family, may be a suitable choice.

Overall, it can be concluded that DFT calculations and density based analyses on uranyl complexes with hexaphyrin ligands are useful for assessing equatorial covalency and the effect on the U-O_{yl} interaction. Results point to the hexaphyrins being slightly too large for the uranyl cation. The distinctive U-O_{yl} stretching vibrations are a useful probe of the coordination environment but this relies upon a degree of planarity of the ligand around the uranium atom.

References

(1) http://www.nei.org/Knowledge-Center/Nuclear-Statistics/World-Statistics.

(2) http://www.nei.org/Knowledge-Center/Nuclear-Statistics/On-Site-Storage-of-Nuclear-Waste.

(3) Baisden, P. A.; Choppin, G. R. *Nuclear Waste Management And the Nuclear Fuel Cycle*; EOLSS, 2007.

(4) Barros, G.; Velasquez, C.; Pereira, C.; Auxiliadora, M.; Costa, A. *Int. J. Hydrogen Energy* **2016**, *41*, 7132–7138.

(5) Mincher, B. J.; Schmitt, N. C.; Case, M. E.; Mincher, B. J.; Schmitt, N. C.; Truex-based, M. E. C. A.; Mincher, B. J.; Schmitt, N. C.; Case, M. E. *Solvent Extr. Ion Exch. ISSN* **2011**, *29*, 247–259.

(6) Berthon, L.; Morel, J. M.; Zorz, N.; Nicol, C.; Virelizier, H.; Madic, C. *Sep. Sci. Technol.* **2001**, *6395*, 709–728.

(7) Romanovskiy, V. N.; Smirnov, I. V; Babain, V. A.; Todd, T. A.; Herbst, S.; Law, J. D.; Brewer, K. N. *Solvent Extr. Ion Exch.* **2001**, *19*, 1–21.

(8) Koch, L. *J. Less-Common Met.* **1986**, *122*, 371–382.

(9) Alstad, J. *J. Inorg. Nucl. Chem.* **1967**, *29*, 2155–2160.

(10) Lewis, F. W.; Harwood, L. M.; Hudson, M. J.; Drew, M. G. B.; Wilden, A.; Sypula, M.; Modolo, G.; Vu, T.; Vidick, G.; Bouslimani, N.; Desreux, J. F. *Procedia Chem.* **2012**, *7*, 231–238.

(11) Lewis, F. W.; Hudson, M. J.; Harwood, L. M. *Synlett* **2011**, 2609–2632.

(12) Dam, H. H.; Reinhoudt, D. N.; Verboom, W. *Chem. Soc. Rev.* **2007**, *36*, 367–377.

(13) Kolarik, Z. *Solvent Extr. Ion Exch.* **2003**, *21*, 381–397.

(14) Drew, M. G. B.; Foreman, M. R. S. J.; Hill, C.; Hudson, M. J.; Madic, C. *Inorg. Chem. Commun.* **2005**, *8*, 239–241.

(15) Lewis, F.; Harwood, L.; Hudson, M. J.; Drew, M. G. B.; Desreux, J.; Vidick, G.; Bouslimani, N.; Modolo, G.; Wilden, A.; Sypula, M.; Vu, T.-H.; Simonin, J.-P. *J. Am. Chem. Soc.* **2011**, *133*, 13093–13102.

(16) Petit, L.; Adamo, C.; Maldivi, P. *Inorg. Chem.* **2006**, *45*, 8517–8522.

(17) Retegan, T.; Ekberg, C.; Dubois, I.; Fermvik, A.; Skarnemark, G.; Wass, T. J. *Solvent Extr. Ion Exch.* **2007**, *25*, 417–431.

(18) Sahb, C. De; Watson, L. A.; Nadas, J.; Hay, B. P. *Inorg. Chem.* **2013**, *52*, 10632–10642.

(19) Trumm, M.; Schimmelpfennig, B. *Mol. Phys.* **2016**, *114*, 876–883.

(20) Lan, J.; Shi, W.; Yuan, L.; Zhao, Y.; Li, J.; Chai, Z. *Inorg. Chem.* **2011**, *50*, 9230–9237.

(21) Sessler, J. L.; Vivian, A. E.; Seidel, D.; Burrell, A. K.; Hoehner, M.; Mody, T. D.; Gebauer, A.; Weghorn, S. J.; Lynch, V. *Coord. Chem. Rev.* **2001**, *216–217*, 411–434.

(22) Arnold, P. L.; Love, J. B.; Patel, D. *Coord. Chem. Rev.* **2009**, *253*, 1973–1978.

(23) Sessler, J.; Melfi, P.; Pantos, G. *Coord. Chem. Rev.* **2006**, *250*, 816–843.

(24) Alexander, V. *Chem. Rev.* **1995**, *95*, 273–342.

(25) Hnatejko, Z.; Lis, S.; Starynowicz, P.; Stryła, Z. *Polyhedron* **2011**, *30*, 880–885.

(26) Berthet, J.-C.; Nierlich, M.; Miquel, Y.; Madic, C.; Ephritikhine, M. *Dalt. Trans.* **2005**, *3*, 369–379.

(27) Beekmeyer, R.; Kerridge, A. *Inorganics* **2015**, *3*, 482–499.

(28) Agrawal, Y. K.; Shrivastav, P.; Menon, S. K. *Sep. Purif. Technol.* **2000**, *20*, 177–183.

(29) Love, J. B. *Chem. Commun.* **2009**, *22*, 3154–65.

(30) Fortier, S.; Hayton, T. W. *Coord. Chem. Rev.* **2010**, *254*, 197–214.

(31) Berthet, J.-C.; Thuéry, P.; Dognon, J.-P.; Guillaneux, D.; Ephritikhine, M. *Inorg. Chem.* **2008**, *47*, 6850–62.

(32) Berthet, J.-C.; Thuéry, P.; Ephritikhine, M. *Chem. Commun. (Camb).* **2007**, *2*, 604–606.

(33) Pierloot, K.; van Besien, E. *J. Chem. Phys.* **2005**, *123*, 2043091–2043099.

(34) Pan, Q.-J.; Odoh, S. O.; Schreckenbach, G.; Arnold, P. L.; Love, J. B. *Dalton Trans.* **2012**, *41*, 8878–8885.

(35) Sessler, J. L.; Gorden, A. E. .; Seidel, D.; Hannah, S.; Lynch, V.; Gordon, P. L.; Donohoe, R. J.; Drew Tait, C.; Webster Keogh, D. *Inorganica Chim. Acta* **2002**, *341*, 54–70.

(36) Sessler, J. L.; Vivian, A. E.; Seidel, D.; Burrell, A. K.; Hoehner, M.; Mody, T. .; Gebauer, A.; Weghorn, S. J.; Lynch, V. *Coord. Chem. Rev.* **2001**, *216–217*, 411–434.

(37) Seth, M.; Dolg, M.; Fulde, P.; Schwerdtfeger, P. *J. Am. Chem. Soc.* **1995**, *117*, 6597–6598.

(38) Dolg, M. In *Encyclopedia of Computational Chemistry*; Schaefer, H. F., Ed.; Wiley: Chichester, 2002.

(39) Söderlind, P.; Gonis, A. *Phys. Rev. B - Condens. Matter Mater. Phys.* **2010**, *82*, 1–4.

(40) Schreckenbach, G.; Shamov, G. a *Acc. Chem. Res.* **2010**, *43*, 19–29.

(41) Wang, D.; van Gunsteren, W. F.; Chai, Z. *Chem. Soc. Rev.* **2012**, *41*, 5836.

(42) Dognon, J. *Coord. Chem. Rev.* **2014**, *266–267*, 110–122.

(43) Kaltsoyannis, N. *Chem. Soc. Rev.* **2003**, *32*, 9–16.

(44) Söderlind, P.; Kotliar, G.; Haule, K.; Oppeneer, P. M.; Guillaumont, D. *MRS Bull.* **2010**, *35*, 883–888.

(45) Choppin, G. R. *J. Alloys Compd.* **1995**, *223*, 174–179.

(46) Choppin, G. R. *J. Alloys Compd.* **1995**, *225*, 242–245.

(47) Odoh, S. O.; Schreckenbach, G. *J. Phys. Chem. A* **2011**, *115*, 14110–14119.

(48) Kirker, I.; Kaltsoyannis, N. *Dalton Trans.* **2011**, *40*, 124–31.

(49) Kaltsoyannis, N. *Inorg. Chem.* **2013**, *52*, 3407–3413.

(50) Lan, J.-H.; Shi, W.-Q.; Yuan, L.-Y.; Li, J.; Zhao, Y.-L.; Chai, Z.-F. *Coord. Chem. Rev.* **2012**, *256*, 1406–1417.

(51) Roy, L. E.; Bridges, N. J.; Martin, L. R. *Dalton Trans.* **2013**, *42*, 2636–42.

(52) Neidig, M. L.; Clark, D. L.; Martin, R. L. *Coord. Chem. Rev.* **2013**, *257*, 394–406.

(53) Kerridge, A. *RSC Adv.* **2014**, *4*, 12078–12086.

(54) Ingram, K. I. M.; Tassell, M. J.; Gaunt, A. J.; Kaltsoyannis, N. *Inorg. Chem.* **2008**, *47*, 7824–7833.

(55) Lewis, F. W.; Harwood, L. M.; Hudson, M. J.; Drew, M. G. B.; Sypula, M.; Modolo, G.; Whittaker, D.; Sharrad, C. A.; Videva, V.; Hubscher-bruder, V. *Dalt. Trans.* **2012**, *41*, 9209–9219.

(56) Vallet, V.; Wahlgren, U.; Grenthe, I. *J. Phys. Chem. A* **2012**, *116*, 12373–12380.

(57) Liddle, S. T. *Angew. Chemie - Int. Ed.* **2015**, *54*, 8604–8641.

(58) Kozimor, S. A.; Yang, P.; Batista, E. R.; Boland, K. S.; Burns, C. J.; Clark, D. L.; Conradson, S. D.; Martin, R. L.; Wilkerson, M. P.; Wolfsberg, L. E. *J. Am. Chem. Soc.* **2009**, *131*, 12125–36.

(59) Tassell, M. J.; Kaltsoyannis, N. *Dalt. Trans.* **2010**, *39*, 6576–88.

(60) Kerridge, A. *Dalton Trans.* **2013**, *42*, 16428–16436.

(61) Fryer-kanssen, I.; Austin, J.; Kerridge, A. *Inorg. Chem.* **2016**, *55*, 10034–10042.

(62) Mazzanti, M.; Wietzke, R.; Pécaut, J.; Latour, J.-M.; Maldivi, P.; Remy, M. *Inorg. Chem.* **2002**, *41*, 2389–99.

(63) Guillaumont, D. *J. Phys. Chem. A* **2004**, *108*, 6893–6900.

(64) Guillaumont, D. *J. Mol. Struct. THEOCHEM* **2006**, *771*, 105–110.

(65) Denecke, M. a.; Panak, P. J.; Burdet, F.; Weigl, M.; Geist, A.; Klenze, R.; Mazzanti, M.; Gompper, K. *Comptes Rendus Chim.* **2007**, *10*, 872–882.

(66) Gorden, A. E. V; DeVore, M. a.; Maynard, B. a. *Inorg. Chem.* **2013**, *52*, 3445–3458.

(67) Patel, D.; Liddle, S. T. *Rev. Inorg. Chem.* **2012**, *32*, 1–22.

(68) Moore, K. T.; van der Laan, G. *Rev. Mod. Phys.* **2009**, *81*, 235–298.

(69) Gagliardi, L. *Rev. Comput. Chem.* **2007**, *25*, 249–284.

(70) Berthet, J.-C.; Thuéry, P.; Ephritikhine, M. *Dalt. Trans.* **2015**, 7727–7742.

(71) Denning, R. G. *J. Phys. Chem. A* **2007**, *111*, 4125–4143.

(72) Maurya, M. R.; Maurya, R. C. *Rev. Inorg. Chem.* **1995**, *15*, 1–107.

(73) Ephritikhine, M. *Dalt. Trans.* **2006**, *2516*, 2501–2516.

(74) Loiseau, T.; Mihalcea, I.; Henry, N.; Volkringer, C. *Coord. Chem. Rev.* **2014**, *266–267*, 69–109.

(75) Vallet, V.; Maron, L.; Schimmelpfennig, B.; Leininger, T.; Teichteil, C.; Gropen, O.; Grenthe, I.; Wahlgren, U. *J. Phys. Chem. A* **1999**, *103*, 9285–9289.

(76) Edelstein, N. M. *J. Phys. Chem. A* **2015**, *119*, 11146–11153.

(77) Gendron, F.; Paez-Hernandez, D.; Notter, F. P.; Pritchard, B.; Bolvin, H.; Autschbach, J. *Chem. - A Eur. J.* **2014**, *20*, 7994–8011.

(78) Wilkerson, M. P.; Berg, J. M. *J. Phys. Chem. A* **2008**, *112*, 2515–2518.

(79) Chaudhuri, D.; Balasubramanian, K. *Chem. Phys. Lett.* **2004**, *399*, 67–72.

(80) Allen, P. G.; Bucher, J. J.; Shuh, D. K.; Edelstein, N. M.; Reich, T. *Inorg. Chem.* **1997**, *36*, 4676–4683.

(81) Wahlgren, U.; Moll, H.; Grenthe, I.; Schimmelpfennig, B.; Maron, L.; Vallet, V.; Gropen, O. *J. Phys. Chem. A* **1999**, *103*, 8257–8264.

(82) Allen, P. G.; Bucher, J. J.; Shuh, D. K.; Edelstein, N. M.; Reich, T.; Division, C. S.; Berkeley, L.; Dresden, D.-; May, R. V **1997**, *1669*, 4676–4683.

(83) Spencer, S.; Gagliardi, L.; Handy, N. C.; Ioannou, A. G.; Skylaris, C.; Willetts, A.; Simper, A. M. *J. Phys. Chem. A* **1999**, *103*, 1831–1837.

(84) Jones; Penneman *J. Phys. Chem.* **1953**, *21*, 542–544.

(85) Nguyen-Trung, C.; Palmer, D. A.; Begun, G. M.; Peiffert, C.; Mesmer, R. E. *J. Solution Chem.* **2000**, *29*, 101–129.

(86) Spencer, S.; Gagliardi, L.; Handy, N. C.; Ioannou, A. G.; Skylaris, C.; Willetts, A.; Simper, A. M. *J. Phys. Chem. A* **1999**, *103*, 1831–1837.

(87) Quilès, F.; Burneau, A. *Vib. Spectrosc.* **2000**, *23*, 231–241.

(88) Hay, P. J.; Martin, R. L.; Schreckenbach, G. *J. Phys. Chem. A* **2000**, *104*, 6259–6270.

(89) Ingram, K. I. M.; Häller, L. J. L.; Kaltsoyannis, N. *Dalton Trans.* **2006**, *2*, 2403–2414.

(90) Austin, J. P.; Sundararajan, M.; Vincent, M. A.; Hillier, I. H. *Dalt. Trans.* **2009**, 5902–5909.

(91) Sonnenberg, J. L.; Hay, P. J.; Martin, R. L.; Bursten, B. E. *Inorg. Chem.* **2005**, *44*, 2255–62.

(92) Vallet, V.; Wahlgren, U.; Schimmelpfennig, B.; Moll, H.; Szabó, Z.; Grenthe, I. *Inorg. Chem.* **2001**, *40*, 3516–25.

(93) Iché-Tarrat, N.; Barros, N.; Marsden, C. J.; Maron, L. *Chem. - A Eur. J.* **2008**, *14*, 2093–2099.

(94) Fillaux, C.; Guillaumont, D.; Berthet, J.-C.; Copping, R.; Shuh, D. K.; Tyliszczak, T.; Den Auwer, C. *Phys. Chem. Chem. Phys.* **2010**, *12*, 14253–14262.

(95) Quilès, F.; Nguyen-Trung, C.; Carteret, C.; Humbert, B. *Inorg. Chem.* **2011**, *50*, 2811–2823.

(96) Tsushima, S. *Dalton Trans.* **2011**, *40*, 6732–6737.

(97) Odoh, S. O.; Schreckenbach, G. *Inorg. Chem.* **2013**, *52*, 5590–5602.

(98) Maya, L.; Begun, G. M.; Division, C.; Ridge, O.; Ridge, O. **1981**, *43*, 2827–2832.

(99) Clark, D. L.; Hobart, D. E.; Palmer, P. D.; Sullivan, J. C.; Stout, B. E. *J. Alloys Compd.* **1993**, *193*, 94–97.

(100) Rowland, C. E.; Kanatzidis, M. G.; Soderholm, L. *Inorg. Chem.* **2012**, *51*, 11798–11804.

(101) Clark, D. L.; Conradson, S. D.; Donohoe, R. J.; Keogh, D. W.; Morris, D. E.; Palmer, P. D.; Rogers, R. D.; Tait, C. D. *Inorg. Chem.* **1999**, *103*, 1456–1466.

(102) Takao, K.; Takao, S.; Ikeda, Y.; Bernhard, G.; Hennig, C. *Dalt. Trans.* **2013**, *42*, 13101.

(103) Schnaars, D. D.; Wilson, R. E. *Inorg. Chem.* **2013**, *52*, 14138–14147.

(104) Straka, M.; Dyall, K. G.; Pyykkö, P. *Theor. Chem. Acc.* **2001**, *106*, 393–403.

(105) Basile, L. J. .; Sullivan, J. C. .; Ferraro, J. R. .; LaBonville, P. *Appl. Spectrosc.* **1974**, *28*, 142–145.

(106) Hayes, C. E.; Leznoff, D. B. *Coord. Chem. Rev.* **2014**, *266–267*, 155–170.

(107) Shamov, G. A.; Schreckenbach, G.; Martin, R. L.; Hay, P. J. *Inorg. Chem.* **2008**, *47*,

1465–1475.

(108) Maynadié, J.; Berthet, J.-C.; Thuéry, P.; Ephritikhine, M. *Chem. Commun. (Camb).* **2007**, *2*, 486–488.

(109) Berthet, J.-C.; Siffredi, G.; Thuéry, P.; Ephritikhine, M. *Dalton Trans.* **2009**, *18*, 3478–3494.

(110) Kiegiel, K.; Steczek, L.; Zakrzewska-trznadel, G. *J. Chem.* **2013**, *2013*, 1–17.

(111) Battersby, A. R. *Nat. Prod. Rep.* **2000**, *17*, 507–526.

(112) Avissar, Y. J.; Moberg, P. A. *Photosynth. Res.* **1995**, *44*, 221–242.

(113) Senge, M. O.; Ryan, A. A.; Letchford, K. A.; Macgowan, S. A.; Mielke, T. *Symmetry (Basel).* **2014**, *6*, 781–843.

(114) Zhu, X.; Fu, S.; Wong, W. K.; Wong, W. Y. *Tetrahedron Lett.* **2008**, *49*, 1843–1846.

(115) Chandra, B.; Mahanta, S. P.; Pati, N. N.; Baskaran, S.; Kanaparthi, R. K.; Sivasankar, C.; Panda, P. K. *Org. Lett.* **2013**, *15*, 306–309.

(116) Chatterjee, T.; Areti, S.; Ravikanth, M. *Inorg. Chem.* **2015**, *54*, 2885–2892.

(117) Chatterjee, T.; Ghosh, A.; Madhu, S.; Ravikanth, M. *Dalt. Trans.* **2014**, *43*, 6050–6058.

(118) Takahashi, K.; Nakajima, I.; Imoto, K. *Sol. Energy Mater. Sol. Cells* **2003**, *76*, 115–124.

(119) Lin, W.; Hu, Q.; Jiang, K.; Yang, Y.; Yang, Y.; Cui, Y. *J. Solid State Chem.* **2016**, *237*, 307–312.

(120) Kaltsoyannis, N.; Scott, P. *The f elements*; Oxford University Press: Oxford, 1999.

(121) Kan, J.; Wang, H.; Sun, W.; Cao, W.; Tao, J.; Jiang, J. *Inorg. Chem.* **2013**, *52*, 8505–8510.

(122) Lodi, A.; Krull, C.; Mugarza, A.; Balashov, T.; Nistor, C.; Piquerel, R.; Klyatskaya, S.; Ruben, M.; Sheverdyaeva, P. M.; Moras, P.; Carbone, C.; Stamm, C.; Miedema, P. S.; Thakur, P. K.; Sessi, V.; Soares, M.; Yakhou-harris, F.; Cezar, J. C.; Stepanow, S.; Gambardella, P. *Surf. Sci.* **2014**, *630*, 361–374.

(123) Cao, W.; Gao, C.; Zhang, Y.; Qi, D.; Liu, T.; Wang, K. *Chem. Sci.* **2015**, *6*, 5947–5954.

(124) Boroujerdi, R. *J. Fluoresc.* **2016**, *2*, 781–790.

(125) Sekhosana, K. E.; Nyokong, T. *Opt. Mater. (Amst).* **2015**, *47*, 211–218.

(126) Sekhosana, K. E.; Manyeruke, M. H.; Nyokong, T. *J. Mol. Struct.* **2016**, *1121*, 111–118.

(127) Kadish, K. M.; Moninot, G.; Hu, Y.; Dubois, D.; Barbe, A. I. J.; Guilard, R. *J. Am. Chem. Soc.* **1993**, *115*, 8153–8166.

(128) Pushkarev, V. E.; Tolbin, Y.; Zhurkin, F. E.; Borisova, N. E.; Trashin, S. A.; Tomilova, L. G. *Chem. - A Eur. J.* **2012**, *18*, 9046–9055.

(129) Sessler, J. L.; Weghorn, S. J. *Expanded, Contracted & Isomeric Porphyrins*; Pergamon, 1997.

(130) Sessler, J. L.; Hemmi, G.; Mody, T. D.; Murai, T.; Burrell, A.; Young, S. W. *Acc. Chem. Res.* **1994**, *27*, 43–50.

(131) Sessler, J. L.; Miller, R. a *Biochem. Pharmacol.* **2000**, *59*, 733–9.

(132) Osuka, A.; Saito, S. *Chem. Commun. (Camb).* **2011**, *47*, 4330–9.

(133) Sessler, J. L.; Melfi, P. J.; Seidel, D.; Gorden, A. E. V.; Ford, D. K.; Palmer, P. D.; Tait, C. D. *Tetrahedron* **2004**, *60*, 11089–11097.

(134) Melfi, P. J.; Camiolo, S.; Lee, J. T.; Ali, M. F.; McDevitt, J. T.; Lynch, V. M.; Sessler, J. L. *Dalton Trans.* **2008**, 1538–40.

(135) Josefsen, L. B.; Boyle, R. W. *Met. Based. Drugs* **2008**, *2008*, 1–24.

(136) Gouterman, M. *J. Mol. Spectrosc.* **1961**, *6*, 138–163.

(137) Gouterman, M.; Wagnière, G. H.; Snyder, L. C. *J. Mol. Spectrosc.* **1963**, *11*, 108–127.

(138) Shkirman, S. F.; Solov’ev, K. N.; Kachura, T. F.; Arabei, S. A.; Skakovskii, E. D. *Journel Appl. Spectrosc.* **1999**, *66*, 65–72.

(139) Sessler, J. L.; Seidel, D. *Angew. Chem. Int. Ed. Engl.* **2003**, *42*, 5134–5175.

(140) Roznyatovskiy, V. V; Lee, C.-H.; Sessler, J. L. *Chem. Soc. Rev.* **2013**, *42*, 1921–

1933.
(141) Misra, R.; Chandrashekar, T. K. *Acc. Chem. Res.* **2008**, *41*, 265–279.
(142) Sessler, J. L.; Tomat, E. *Acc. Chem. Res.* **2007**, *40*, 371–379.
(143) Hannah, S.; Lynch, V.; Guldi, D. M.; Gerasimchuk, N.; MacDonald, C. L. B.; Magda, D.; Sessler, J. L. *J. Am. Chem. Soc.* **2002**, *124*, 8416–27.
(144) Bauer, V. J.; Clive, D. L. J.; Dolphin, D.; Paine, J. B.; Harris, F. L.; King, M. M.; Loder, J.; Wang, S. W. C.; Woodward, R. B. *J. Am. Chem. Soc.* **1983**, *105*, 6429–6436.
(145) Sessler, J. L.; Callaway, W. B.; Dudek, S. P.; Date, R. W.; Bruce, D. W. *Inorg. Chem.* **2004**, *43*, 249–251.
(146) Sessler, J. L.; Seidel, D.; Bucher, C.; Lynch, V. *Chem. Commun.* **2000**, *2000*, 1473–1474.
(147) Gupta, A. K.; Chandrashekar, T. K. *Tetrahedron Lett.* **2001**, *42*, 3391–3394.
(148) Anand, V. G.; Pushpan, S. K. *J. Am. Chem. Soc.* **2001**, *123*, 8620–8621.
(149) Kumar, R.; Misra, R.; Chandrashekar, T. K.; Nag, A.; Goswami, D.; Suresh, E.; Suresh, C. H. *European J. Org. Chem.* **2007**, *27*, 4552–4562.
(150) Shamov, G. A.; Schreckenbach, G. *Inorg. Chem.* **2008**, *47*, 805–811.
(151) Krivokapic, A.; Cowley, A. R.; Anderson, H. L. *J. Org. Chem.* **2003**, *68*, 1089–1096.
(152) Shimizu, S.; Anand, V. G.; Taniguchi, R.; Furukawa, K.; Kato, T.; Yokoyama, T.; Osuka, A. *J. Am. Chem. Soc.* **2004**, *126*, 12280–12281.
(153) Vogel, E.; Jux, N.; Dörr, J.; Pelster, T.; Berg, T.; Böhm, H.; Behrens, F.; Lex, J.; Bremm, D.; Hohlneicher, G. *Angew. Chem. Int. Ed. Engl.* **2000**, *39*, 1101–1105.
(154) Ho, I. T.; Zhang, Z.; Ishida, M.; Lynch, V. M.; Cha, W. Y.; Sung, Y. M.; Kim, D.; Sessler, J. L. *J. Am. Chem. Soc.* **2014**, *136*, 4281–4286.
(155) Sessler, J. L.; Davis, J. M.; Lynch, V. *J. Org. Chem.* **1998**, *63*, 7062–7065.
(156) Melfi, P. J. Isoamethyrin analogues and cyclo [n] pyrrole as sensors for cations and anions, ProQuest, 2007.
(157) Zhu, X.; Fu, S.; Wong, W.-K.; Wong, W.-Y. *Tetrahedron Lett.* **2008**, *49*, 1843–1846.
(158) Rambo, B. M.; Sessler, J. L. *Chem. - A Eur. J.* **2011**, *17*, 4946–4959.
(159) Young, S. W.; Qing, F.; Harriman, A.; Sessler, J. L.; Dow, W. C.; Mody, T. D.; Hemmi, G. W.; Hao, Y.; Miller, R. A. *Proc. Natl. Acad. Sci. U. S. A.* **1996**, *93*, 6610–6615.
(160) Mody, T. D.; Sessler, J. L. *J. Porphyrins Phthalocyanines* **2001**, *5*, 134–142.
(161) Gerasimchuk, N. N.; Gerges, A.; Clifford, T.; Danby, A.; Bowman-James, K. *Inorg. Chem.* **1999**, *38*, 5633–5636.
(162) Yoon, Z. S.; Kwon, J. H.; Yoon, M.-C.; Koh, M. K.; Noh, S. B.; Sessler, J. L.; Lee, J. T.; Seidel, D.; Aguilar, A.; Shimizu, S.; Suzuki, M.; Osuka, A.; Kim, D. *J. Am. Chem. Soc.* **2006**, *128*, 14128–14134.
(163) Rath, H.; Sankar, J.; Prabhuraja, V.; Chandrashekar, T. K.; Nag, A.; Goswami, D. *J. Am. Chem. Soc.* **2005**, *127*, 11608–11609.
(164) Liu, C.-G.; Guan, X.-H. *Mol. Phys.* **2011**, *109*, 2625–2632.
(165) Chandrashekar, T. K.; Venkatraman, S. *Acc. Chem. Res.* **2003**, *36*, 676–691.
(166) Jasat, A.; Dolphin, D. *Chem. Rev.* **1997**, *97*, 2267–2340.
(167) Shin, J.-Y.; Kim, K. S.; Yoon, M.-C.; Lim, J. M.; Yoon, Z. S.; Osuka, A.; Kim, D. *Chem. Soc. Rev.* **2010**, *39*, 2751–67.
(168) Johnson, A. W.; Kay, I. T. *Proc. R. Soc. London. Ser. A Math. Phys. Sci.* **1965**, 334–341.
(169) Broadhurst; Grigg; Johnson *J. Chem. Soc., Perkin Trans. 1* **1972**, 2111–2116.
(170) Broadhurst; Grigg; Johnson *J. Chem. Soc., Perkin Trans. 1* **1972**, 1124–1135.
(171) Marks, T. J.; Stojakovic, D. R. *J. Am. Chem. Soc.* **1978**, *100*, 1695.
(172) Silver, J. *Inorganica Chim. Acta* **1988**, *44*, 281–288.
(173) Sessler, J. L.; Weghorn, S. J.; Hiseada, Y.; Lynch, V. *Chem. - A Eur. J.* **1995**, *1842*, 56–67.
(174) Weghorn, S. J.; Lynch, V.; Sessler, J. L. *Tetrahedron Lett.* **1995**, *36*, 4713–4716.
(175) Burrell, A. K.; Hemmi, G.; Lynch, V.; Sessler, J. L. *J. Am. Chem. Soc.* **1991**, *6*,

4690–4692.

(176) Burrell, A. K.; Cyr, M. J.; Lynch, V.; Sessler, J. L. *Chem. Commun.* **1991**, *91*, 1710–1713.

(177) Sessler, J. L.; Gebauer, A.; Hoehner, M. C.; Lynch, V. *Chem. Commun.* **1998**, *3*, 1835–1836.

(178) Ballico, M.; Rapozzi, V.; Xodo, L. E.; Comuzzi, C. *Eur. J. Med. Chem.* **2011**, *46*, 712–20.

(179) O'Connor, A. E.; Gallagher, W. M.; Byrne, A. T. *Photochem. Photobiol.* **2009**, *85*, 1053–74.

(180) Ali, H.; Lier, J. E. Van *Chem. Rev.* **1999**, *99*, 2379–2450.

(181) Anand, V. G.; Saito, S.; Shimizu, S.; Osuka, A. *Angew. Chem. Int. Ed. Engl.* **2005**, *44*, 7244–7248.

(182) Shimizu, S.; Osuka, A. *Eur. J. Inorg. Chem.* **2006**, *2006*, 1319–1335.

(183) Alonso, M.; Geerlings, P.; De Proft, F. *Chemistry* **2013**, *19*, 1617–28.

(184) Mori, H.; Sung, Y. M.; Lee, B. S.; Kim, D.; Osuka, A. *Angew. Chem. Int. Ed. Engl.* **2012**, *51*, 12459–63.

(185) Köhler, T.; Seidel, D.; Lynch, V.; Arp, F. O.; Ou, Z.; Kadish, K. M.; Sessler, J. L. *J. Am. Chem. Soc.* **2003**, *125*, 6872–3.

(186) Baker, E. S.; Lee, J. T.; Sessler, J. L.; Bowers, M. T. *J. Am. Chem. Soc.* **2006**, *128*, 2641–2648.

(187) Melfi, P. J.; Kim, S. K.; Lee, J. T.; Bolze, F.; Seidel, D.; Lynch, V. M.; Veauthier, J. M.; Gaunt, A. J.; Neu, M. P.; Ou, Z.; Kadish, K. M.; Fukuzumi, S.; Ohkubo, K.; Sessler, J. L. *Inorg. Chem.* **2007**, *46*, 5143–5.

(188) Hannah, S.; Seidel, D.; Sessler, J. L.; Lynch, V. *Inorganica Chim. Acta* **2001**, *317*, 211–217.

(189) Weghorn, S. J.; Sessler, J. L.; Lynch, V.; Baumann, T. F.; Sibert, J. W. *Inorg. Chem.* **1996**, *35*, 1089–1090.

(190) Sessler, J. L.; Seidel, D.; Vivian, A. E.; Lynch, V.; Scott, B. L.; Keogh, D. W. *Angew. Chemie Int. Ed.* **2001**, *40*, 591–594.

(191) Sessler, J. L.; Melfi, P. J.; Tomat, E.; Lynch, V. M. *Dalton Trans.* **2007**, *744*, 629–32.

(192) Sessler, J. L.; Weghorn, S. J.; Morishima, T.; Rosingana, M.; Lynch, V.; Lee, V. *J. Am. Chem. Soc.* **1992**, *114*, 8306–8307.

(193) Shimizu, S.; Cho, W. S.; Sessler, J. L.; Shinokubo, H.; Osuka, A. *Chem. - A Eur. J.* **2008**, *14*, 2668–2678.

(194) Kim, D.; Kwon, J. H.; Ahn, T. K.; Yoon, M. C.; Kim, D. Y.; Koh, M. K.; Furuta, H.; Suzuki, M.; Osuka, A. *J. Phys. Chem. B* **2006**, *110*, 11683–11690.

(195) Mori, S.; Shimizu, S.; Shin, J. Y.; Osuka, A. *Inorg. Chem.* **2007**, *46*, 4374–4376.

(196) Mori, S.; Kim, K. S.; Yoon, Z. S.; Noh, S. B.; Kim, D.; Osuka, A. *J. Am. Chem. Soc.* **2007**, *129*, 11344–11345.

(197) Stępień, M.; Sprutta, N.; Latos-Grażyński, L. *Angew. Chem. Int. Ed. Engl.* **2011**, *50*, 4288–340.

(198) Bucher, C.; Seidel, D.; Lynch, V.; Sessler, J. L. *Chem. Commun.* **2002**, *2*, 328–329.

(199) Sessler, J. L.; Seidel, D.; Gebauer, A.; Lynch, V.; Abboud, K. A. *j. Heterocycl. Chem* **2001**, *38*, 1419–1424.

(200) Shimizu, S.; Tanaka, Y.; Youfu, K.; Osuka, A. *Angew. Chem. Int. Ed. Engl.* **2005**, *44*, 3726–9.

(201) Kamimura, Y.; Shimizu, S.; Osuka, A. *Chem. - A Eur. J.* **2007**, *13*, 1620–1628.

(202) Sessler, J. L.; Weghorn, S. J.; Lynch, V.; Johnson, M. R. *Angew. Chemie, Int. Ed. English* **1994**, *33*, 1509–1512.

(203) Shimizu, S.; Aratani, N.; Osuka, A. *Chem. - A Eur. J.* **2006**, *12*, 4909–4918.

(204) Soya, T.; Kim, W.; Kim, D.; Osuka, A. *Chem. - A Eur. J.* **2015**, *21*, 8341–8346.

(205) Tanaka, Y.; Shin, J.-Y.; Osuka, A. *European J. Org. Chem.* **2008**, *2008*, 1341–1349.

(206) Sessler, J. L.; Mody, T. D.; Dulay, M. T.; Espinoza, R.; Lynch, V. *Inorganica Chim. Acta* **1996**, *246*, 23–30.

(207) Setsune, J.; Katakami, Y.; Iizuna, N. *J. Am. Chem. Soc.* **1999**, *121*, 8957–8958.

(208) Sessler, J. L.; Melfi, P. J.; Tomat, E.; Callaway, W.; Huggins, M. T.; Gordon, P. L.; Webster Keogh, D.; Date, R. W.; Bruce, D. W.; Donnio, B. *J. Alloys Compd.* **2006**, *418*, 171–177.
(209) Preihs, C.; Arambula, J. F.; Magda, D.; Jeong, H.; Yoo, D.; Cheon, J.; Siddik, Z. H.; Sessler, J. L. *Inorg. Chem.* **2013**, *52*, 12184–12192.
(210) Sessler, J. L.; Tvermoes, N. a.; Guldi, D. M.; Mody, T. D. *J. Porphyrins Phthalocyanines* **2001**, *5*, 593–599.
(211) Lan, J. H.; Wang, C. Z.; Wu, Q. Y.; Wang, S. A.; Feng, Y. X.; Zhao, Y. L.; Chai, Z. F.; Shi, W. Q. *J. Phys. Chem. A* **2015**, *119(1) Lan*, 9178–9188.
(212) Ho, I.-T.; Sessler, J. L.; Gambhir, S. S.; Jokerst, J. V. *Analyst* **2015**, *140*, 3731–3737.
(213) Zhang, Z.; Lim, J. M.; Ishida, M.; Roznyatovskiy, V. V.; Lynch, V. M.; Gong, H. Y.; Yang, X.; Kim, D.; Sessler, J. L. *J. Am. Chem. Soc.* **2012**, *134*, 4076–4079.
(214) Arnold, P. L.; Patel, D.; Blake, A. J.; Wilson, C.; Love, J. B. *J. Am. Chem. Soc.* **2006**, *128*, 9610–1.
(215) Givaja, G.; Volpe, M.; Leeland, J. W.; Edwards, M. a; Young, T. K.; Darby, S. B.; Reid, S. D.; Blake, A. J.; Wilson, C.; Wolowska, J.; McInnes, E. J. L.; Schröder, M.; Love, J. B. *Chemistry* **2007**, *13*, 3707–23.
(216) Yahia, A.; Arnold, P. L.; Love, J. B.; Maron, L. *Chem. - A Eur. J.* **2010**, *16*, 4881–4888.
(217) Pan, Q. J.; Shamov, G. A.; Schreckenbach, G. *Chem. - A Eur. J.* **2010**, *16*, 2282–2290.
(218) Jones, G. M.; Arnold, P. L.; Love, J. B. *Chem. - A Eur. J.* **2013**, *19*, 10287–10294.
(219) Arnold, P. L.; Patel, D.; Pécharman, A.-F.; Wilson, C.; Love, J. B. *Dalton Trans.* **2010**, *39*, 3501–3508.
(220) Arnold, P. L.; Patel, D.; Pécharman, A.-F.; Wilson, C.; Love, J. B. *Dalton Trans.* **2010**, *39*, 3501–8.
(221) Yahia, A.; Arnold, P. L.; Love, J. B.; Maron, L. *Chem. Commun.* **2009**, *17*, 2402–4.
(222) Love, J. B. *Chem. Commun.* **2009**, *22*, 3154–3165.
(223) Arnold, P. L.; Patel, D.; Wilson, C.; Love, J. B. *Nature* **2008**, *451*, 315–7.
(224) Jensen, F. *Introduction to Computational Chemistry*; 2nd ed.; Wiley, 2007.
(225) Atkins, P.; Friendman, R. *Molecular Quantum Mechanics*; 5th ed.; Oxford University Press, 2011.
(226) Bader, R. *Atoms in Molecules: A Quantum Theory*; Clarendon Press, 1995.
(227) Kaltsoyannis, N.; Scott, P. *The F Elements - Oxford Chemistry Primers*; Oxford University Press, 1999.
(228) Burke, K. *The ABC of DFT*; 2004.
(229) Burke, K. *J. Chem. Phys.* **2012**, *136*, 150901.
(230) Burke, K.; Wagner, L. O. *Int. J. Quantum Chem.* **2013**, *113*, 96–101.
(231) Szabo, A.; Ostlund, N. S. *Modern Quantum Chemistry - Introduction to Advanced Electronic Structure Theory*; 1st ed.; Macmillan Publishing Co, 1982.
(232) Kaltsoyannis, N. *Dalt. Trans.* **1996**, 1–11.
(233) García-Hernández, M.; Lauterbach, C.; Krüger, S.; Matveev, A.; Rösch, N. *J. Comput. Chem.* **2002**, *23*, 834–46.
(234) Pyykko, P. *Chem. Rev.* **1988**, *88*, 563–594.
(235) Pyykko, P. *Annu. Rev. Phys. Chem.* **2012**, *63*, 45–64.
(236) Basch, H.; Topiol, S. *J. Chem. Phys.* **1979**, *71*, 802–814.
(237) Hong, G.; Schautz, F.; Dolg, M. *J. Am. Chem. Soc.* **1999**, *121*, 1502–1512.
(238) Gagliardi, L.; Roos *Nature* **2005**, *433*, 848–851.
(239) Kerridge, A.; Coates, R.; Kaltsoyannis, N. *J. Phys. Chem. A* **2009**, *113*, 2896–905.
(240) Kerridge, A.; Kaltsoyannis, N. *J. Phys. Chem. A* **2009**, *113*, 8737–45.
(241) Schreckenbach, G.; Hay, P. J.; Martin, R. L. *J. Comput. Chem.* **1999**, *20*, 70–90.
(242) Gagliardi, L.; Roos, B. O. *Chem. Soc. Rev.* **2007**, *36*, 893–903.
(243) Wang, D.; Su, J.; Wu, J.; Li, J.; Chai, Z. *Radiochim. Acta* **2014**, *102*, 13–25.
(244) Shamov, G. A. *J. Am. Chem. Soc.* **2011**, *133*, 4316–4329.
(245) Laikov, D. N. Priroda Code **2004**.

(246) Laikov, D. N. In *DFT2000 Conference*; Menton, France, 2000.
(247) Fortes, F.; Sousa, R.; Quartarolo, A. D.; Sicilia, E.; Russo, N.; Chimica, D.; Prestazioni, A.; Eccellenza, D.; Calabria, U.; Rende, I.-A. *J. Phys. Chem. B* **2012**, *116*, 10816–10823.
(248) Cao, X.; Dolg, M. *Mol. Phys.* **2003**, *101*, 2427–2435.
(249) Cao, X.; Li, Q.; Moritz, A.; Xie, Z.; Dolg, M.; Chen, X. *Inorg. Chem.* **2006**, *45*, 43–50.
(250) Shamov, G. A.; Schreckenbach, G. *J. Phys. Chem. A* **2006**, *110*, 9486–9499.
(251) Liao, M.; Kar, T.; Scheiner, S. *J. Phys. Chem. A* **2004**, *108*, 3056–3063.
(252) Su, D. M.; Zheng, X. J.; Schreckenbach, G.; Pan, Q. J. *Organometallics* **2015**, *34*, 5225–5232.
(253) Qu, N.; Xi, Y.; Georg, Z.; Qing, S.; Pan, J. *Theor. Chem. Acc.* **2016**, *135*, 1–9.
(254) Yang, M.; Ding, W.; Wang, D. *New J. Chem.* **2016**.
(255) Furuta, H.; Maeda, H.; Osuka, a *J. Org. Chem.* **2001**, *66*, 8563–72.
(256) Earles, J. C.; Gordon, K. C.; Stephenson, A. W. I.; Partridge, A. C.; Officer, D. L. *Phys. Chem. Chem. Phys.* **2011**, *13*, 1597–605.
(257) Sundholm, D. *Chem. Phys. Lett.* **2000**, *317*, 392–399.
(258) Toganoh, M.; Furuta, H. *J. Org. Chem.* **2010**, *75*, 8213–23.
(259) Sun, G.; Lei, E.; Liu, X.; Yu, C.; Duan, X.; Liu, C. *Comput. Theor. Chem.* **2016**, *1087*, 18–25.
(260) Chatterjee, T.; Theophall, G. G.; Silva, K. I.; Lakshmi, K. V; Ravikanth, M. *Inorg. Chem.* **2016**, *55*, 6873–6881.
(261) Sun, G.; Li, H.; Jiang, S.; Wang, X.; Liu, C.; Fu, Q. *Computa* **2011**, *976*, 68–75.
(262) Augusto, S.; Jannuzzi, V.; Phung, Q. M.; Domingo, A.; Formiga, A. L. B.; Pierloot, K. *Inorg. Chem.* **2016**, *55*, 5168–5179.
(263) Seda, J.; Burda, J. V.; Leszczynski, J. *J. Comput. Chem.* **2004**, *23*, 294–303.
(264) Jensen, K. P.; Roos, O.; Ryde, U. *J. Inorg. Biochem.* **2005**, *99*, 45–54.
(265) Choe, Y.; Hashimoto, T.; Nakano, H.; Hirao, K. *Chem. Phys. Lett.* **1998**, *295*, 380–388.
(266) Choe, Y.; Nakajima, T.; Hirao, K.; Lindh, R. *J. Chem. Phys.* **1999**, *111*, 3837–3845.
(267) Serrano-andres, L.; Merchan, M.; Rubio, M.; Roos, O. *Chem. Phys. Lett.* **1998**, *295*, 195–203.
(268) Merchan, M.; Orti, E.; Roos, B. *Chem. Phys. Lett.* **1994**, *226*, 27–36.
(269) Rubio, M.; Roos, B. O.; Serrano-andrés, L.; Merchán, M.; Serrano-andre, L. *J. Chem. Phys.* **2009**, *110*, 7202–7209.
(270) Merchan, M.; Orti, E.; Roos, B. *Chem. Phys. Lett.* **1994**, *221*, 136–144.
(271) Ghosh, A.; Persson, Æ. B. J.; Taylor, Æ. P. R. *J. Biol. Inorg. Chem.* **2003**, *8*, 507–511.
(272) Kerridge, A. *Phys. Chem. Chem. Phys.* **2013**, *15*, 2197–2209.
(273) Roos, B. O.; Taylor, P. R. *Chem. Phys.* **1980**, *48*, 157–173.
(274) Veryazov, V.; Malmqvist, P. Å.; Roos, B. O. *Int. J. Quantum Chem.* **2000**, *111*, 3329–3338.
(275) Errol Lewars *Computational Chemistry: Introduction to the Theory and Applications of Molecular and Quantum Mechanics*; Kluwer Academic Publishers, 2004.
(276) Kerridge, A. In *Computational Methods in Lanthanide and Actinide Chemistry*; Dolg, M., Ed.; Wiley, 2015; pp. 121–146.
(277) Karplus, M. *J. Phys. Chem.* **1990**, *94*, 5435–5436.
(278) Mulliken, R. S. *Rev. Mod. Phys.* **1960**, *32*, 232–238.
(279) Chaney, R. C.; Tung, T. K.; Lin, C. C.; Lafon, E. E. *J. Chem. Phys.* **1970**, *52*, 361–365.
(280) Woon, D. E.; Dunning, T. H. *J. Chem. Phys.* **1993**, *98*, 1358.
(281) Hehre, W. J. *J. Chem. Phys.* **1969**, *51*, 2657.
(282) HOSTEW, R. P.; GILMAN, R. R.; DUNNING, T. H.; PIPANO, A. *Chem. Phys. Lett.* **1970**, *7*, 325–328.
(283) Teichteil, C.; Maron, L. 1–74.

(284) Weigand, A.; Cao, X.; Vallet, V.; Flament, J.-P.; Dolg, M. *J. Phys. Chem. A* **2009**, *113*, 11509–16.

(285) Küchle, W.; Dolg, M.; Stoll, H.; Preuss, H. *J. Chem. Phys.* **1994**, *100*, 7535.

(286) Giannozzi, P.; Scalar-relativistic, A. **2012**.

(287) Cao, X.; Weigand, A. In *Lanthanide and Actinide Chemistry*; Dolg, M., Ed.; Wiley, 2015; pp. 147–179.

(288) Ehlers, A. W.; Biihme, M.; Dapprich, S.; Gobbi, A.; Hijllwarth, A.; Jonas, V.; Kiihler, K. F.; Stegmann, R.; Veldkamp, A.; Frenking, G. *Chem. Phys. Lett.* **1993**, *208*, 111–114.

(289) Hgllwarth, A.; Biihme, M.; Dapprich, S.; Ehlers, A. W.; Gobbi, A.; Jonas, V.; Kijhler, K. F.; Stegmann, R.; Veldkamp, A.; Frenking, G. *Chem. Phys. Lett.* **1993**, *208*, 237–240.

(290) Fowles, G. R. *Am. J. Phys.* **1962**, *30*, 308.

(291) Liehr, A. *Ann. Phys. (N. Y).* **1957**, *1*, 221–232.

(292) Roos, B. O.; Siegbahn, P. E. M. *Int. J. Quantum Chem.* **1980**, *17*, 485–500.

(293) Malmqvist, P.-Å.; Rendell, A.; Roos, B. O. *J. Phys. Chem.* **1990**, *94*, 5477–5482.

(294) Garza, A. J.; Sousa Alencar, A. G.; Scuseria, G. E. *J. Chem. Phys.* **2015**, *143*, 244106.

(295) Laerdahl, J. K.; Fægri, K.; Visscher, L.; Saue, T. *J. Chem. Phys.* **1998**, *109*, 10806–10817.

(296) Widmark, P.-O.; Malmqvist, P.-A.; Roos, B. O. *Theor. Chim. Acta* **1990**, *77*, 291–306.

(297) Andersson, K.; Roos, B. *Int. J. Hydrogen Energy* **1993**, *45*.

(298) Pulay, P. *Int. J. Quantum Chem.* **2011**, *111*, 3273–3279.

(299) Angeli, C.; Cimiraglia, R.; Evangelisti, S.; Leininger, T.; Malrieu, J.; Angeli, C.; Cimiraglia, R. *J. Chem. Phys.* **2001**, *114*, 10252–10264.

(300) Angeli, C.; Cimiraglia, R.; Malrieu, J. *J. Chem. Phys.* **2002**, *117*, 9138–9153.

(301) Angeli, C.; Cimiraglia, R. *Chem. Phys. Lett.* **2001**, *350*, 297–305.

(302) Havenith, R. W. A.; Taylor, P. R.; Angeli, C.; Cimiraglia, R.; Ruud, K.; Havenith, R. W. A.; Taylor, P. R. *J. Chem. Phys.* **2014**, *120*, 4619–4625.

(303) Schapiro, I.; Sivalingam, K.; Neese, F. **2013**.

(304) Dirac, P. a. M. *Proc. R. Soc. A Math. Phys. Eng. Sci.* **1929**, *123*, 714–733.

(305) Breit, G. *Proc. Natl. Acad. Sci. U. S. A.* **1928**, *14*, 553–559.

(306) Dyall, K. G. *J. Chem. Phys.* **1994**, *100*, 2118.

(307) Lenthe, E. Van; Baerends, E. J.; Snijders, J. G.; Lenthe, E. Van; Baerends, E. J.; Snijders, J. G. *J. Chem. Phys.* **1993**, *99*, 4597–4610.

(308) Heully, J.-L.; Lindgren, I.; Lindroth, E.; Martensson-Pendrill, A.-M. *Phys. Rev. A* **1986**, *33*, 4426–4429.

(309) Heully, J.-L.; Lindgren, I.; Lindroth, E.; Lundqvist, S.; Martensson-Pendrill, A.-M. *J. Phys. B At. Mol. Phys.* **1986**, *19*, 2799–2815.

(310) Chang, C.; Pelissier, M.; Durand, P. **1986**, *394*.

(311) Lenthe, E. Van; Snijders, J. G.; Baerends, E. J.; Introduction, I. **1996**, *105*.

(312) van Lenthe, E.; Snijders, J. G.; Baerends, E. J. *J. Chem. Phys.* **1996**, *105*, 6505.

(313) Kroll, N. M.; Douglas, M. *Ann. Phys. (N. Y).* **1974**, *83*, 89–155.

(314) Hess, B. A. *Phys. Rev. A* **1986**, *33*, 3742–3748.

(315) Reiher, M.; Wolf, A. *J. Chem. Phys.* **2004**, *121*, 2037.

(316) Hong, G.; Dolg, M.; Li, L. **2001**, *334*, 396–402.

(317) Lodi, L.; Tennyson, J. *J. Phys. B At. Mol. Opt. Phys.* **2010**, *43*, 133001.

(318) Cao, X.; Dolg, M. *J. Chem. Phys.* **2001**, *115*, 7348.

(319) Heinz, N.; Zhang, J.; Dolg, M. *J. Chem. Theory Comput.* **2014**, *10*, 5593–5598.

(320) Weigand, A.; Cao, X.; Hangele, T.; Dolg, M. *J. Phys. Chem. A* **2014**, *118*, 2519–2530.

(321) Hulsen, M.; Dolg, M.; Link, P.; Ruschewitz, U. *Theor. Chem. Acc.* **2011**, *129*, 367–379.

(322) Fujiwara, T.; Mori, H.; Mochizuki, Y.; Osanai, Y.; Miyoshi, E. *Chem. Phys. Lett.*

2011, *510*, 261–266.
(323) Dirac, P. A. M. *Proc. R. Soc. A Math. Phys. Eng. Sci.* **1930**, *126*, 360–365.
(324) Hohenberg, P.; Kohn, W. *Phys. Rev.* **1964**, *136*, 864–871.
(325) Kohn, W.; Sham, L. J. *Phys. Rev.* **1965**, *140*, 1133–1138.
(326) Kohn, W.; Sham, L. J. *Phys. Rev.* **1965**, *137*, 1697–1705.
(327) Sham, L. J.; Kohn, W. *Phys. Rev.* **1966**, *145*, 561–567.
(328) Perdew, J. P.; Schmidt, K. In *AIP Conference Proceedings*; 2001; Vol. 577.
(329) Leeuwen, R. Van; Baerends, E. J. *Int. J. Quantum Chem.* **1994**, *52*, 711–730.
(330) Gugelchuk, M. M.; Cui, Y. *J. Mol. Struct. THEOCHEM* **1996**, *365*, 111–117.
(331) Becke, A. D. *Phys. Rev. A* **1988**, *38*, 3098–3100.
(332) Lee, C.; Yang, W.; Parr, R. *Phys. Rev. B* **1988**, *37*, 785–789.
(333) Perdew, J.; Burke, K.; Ernzerhof, M. *Phys. Rev. Lett.* **1996**, *77*, 3865–3868.
(334) Adamo, C.; Barone, V. *J. Chem. Phys.* **1999**, *110*, 6158.
(335) Xu, X.; Goddard, W. A. *J. Chem. Phys.* **2004**, *121*, 4068.
(336) Tao, J.; Perdew, J. P.; Staroverov, V. N.; Scuseria, G. E. *Phys. Rev. Lett.* **2003**, *91*, 146401.
(337) Becke, A. D. *J. Chem. Phys.* **1993**, *98*, 1372.
(338) Elliott, P.; Burke, K. *Can. J. Chem.* **2009**, *1491*, 8.
(339) Runge, E.; Gross, E. K. U. *Phys. Rev. Lett.* **1984**, *52*, 997–1000.
(340) Marques, M. A. L.; Gross, E. K. U. *Annu. Rev. Phys. Chem.* **2004**, *55*, 427–455.
(341) Marom, N.; Tkatchenko, A.; Rossi, M.; Gobre, V. V; Hod, O.; Sche, M.; Kronik, L. *J. Chem. Theory Comput.* **2011**, *7*, 3944–3951.
(342) Kim, M.; Sim, E.; Burke, K.; Kim, M.; Sim, E.; Burke, K. **2011**, *171103*.
(343) Polo, V.; Kraka, E.; Cremer, D. **2002**, *8976*, 1771–1790.
(344) Wåhlin, P.; Danilo, C.; Vallet, V.; Réal, F.; Flament, J.-P.; Wahlgren, U. *J. Chem. Theory Comput.* **2008**, *4*, 569–577.
(345) Bader, R. F. W.; Essén, H. *J. Chem. Phys.* **1984**, *80*, 1943.
(346) Bader, R. F. W. *J. Phys. Chem. A* **2009**, *113*, 10391–6.
(347) Matta, C. F.; Boyd, R. J. *An Introduction to the Quantum Theory of Atoms in Molecules*; 2007.
(348) Bader, R. F. W. *Atoms in Molecules: A Quantum Theory*; Oxford University Press: Oxford, 1990.
(349) Poater, J.; Duran, M.; Sola, M.; Silvi, B. *Chem. Rev.* **2005**, *105*, 3911–3947.
(350) Becke, a. D.; Edgecombe, K. E. *J. Chem. Phys.* **1990**, *92*, 5397.
(351) Silvi, B.; Savin, A. *Nature* **1994**, *371*, 683–686.
(352) Kohout, M.; Savin, A. *Int. J. Quantum Chem.* **1996**, *60*, 875–882.
(353) Savin, A.; Nesper, R.; Wengert, S.; Fassler, T. E. *Angew. Chem. Int. Ed. Engl.* **1997**, *36*, 1808–1832.
(354) Savin, A. *J. Mol. Struct. THEOCHEM* **2005**, *727*, 127–131.
(355) Savin, A.; Silvi, B.; Colonna, F. *Can. J. Chem.* **1996**, *74*, 1088–1096.
(356) Alikhani, M. E.; Fuster, F.; Silvi, B. *Struct. Chem.* **2005**, *16*, 203–210.
(357) Savin, A.; Silvi, B.; Colonna, F. *Can. J. Chem.* **1996**, *74*, 1088–1096.
(358) Johnson, E. R.; Keinan, S.; Mori-Sánchez, P.; Contreras-García, J.; Cohen, A. J.; Yang, W. *J. Am. Chem. Soc.* **2010**, *132*, 6498–506.
(359) Ahlrichs, R.; Bär, M.; Häser, M.; Horn, H.; Kölmel, C. *Chem. Phys. Lett.* **1989**, *162*, 165–169.
(360) Klamt, A.; Schüürmann, G. *Perkin Trans. 2* **1993**, *2*, 799–805.
(361) Roos, O.; Ryde, U.; Veryazov, V.; Widmark, P.; Cossi, M.; Schimmelpfennig, B.; Neogrady, P.; Seijo, L. *Comput. Mater. Sci.* **2003**, *28*, 222–239.
(362) Aquilante, F.; Autschbach, J.; Carlson, R. K.; Chibotaru, L. F.; Delcey, G.; Vico, L. De; Galv, F.; Ferr, N.; Frutos, L. M.; Gagliardi, L.; Garavelli, M.; Giussani, A.; Hoyer, C. E.; Manni, L.; Lischka, H.; Ma, D.; Thomas, M.; Nenov, A.; Olivucci, M.; Pedersen, T. B.; Peng, D.; Plasser, F.; Pritchard, B.; Reiher, M.; Rivalta, I.; Schapiro, I.; Segarra-mart, J.; Stenrup, M.; Truhlar, D. G.; Ungur, L.; Valentini, A.; Vancoillie, S.; Veryazov, V.; Vysotskiy, V. P.; Weingart, O.; Zapata, F.; Lindh, R. *J. Comput.*

Chem. **2016**, *37*, 506–541.
(363) Lu, T.; Chen, F. *J. Comput. Chem.* **2012**, *33*, 580–92.
(364) Keith, T. A. *AIMAll (Version 14.11.23), TK Gristmill Software, Overl. Park KS, USA* **2014**.
(365) Humphrey, W.; Dalke, A.; Schulten, K. *J. Mol. Graph.* **1996**, *14*, 33–38.
(366) Frisch, M. J.; Trucks, G. W.; Schlegel, H. B.; Scuseria, G. E.; Robb, M. A.; Cheeseman, J. R.; Scalmani, G.; Barone, V.; Mennucci, B.; Petersson, G. A.; Nakatsuji, H.; Caricato, M.; Li, X.; Hratchian, H. P.; Izmaylov, A. F.; Bloino, J.; Zheng, G.; Sonnenberg, J. L.; Hada, M.; Ehara, M.; Toyota, K.; Fukuda, R.; Hasegawa, J.; Ishida, M.; Nakajima, T.; Honda, Y.; Kitao, O.; Nakai, H.; Vreven, T.; Montgomery, J. A.; Peralta, J. E.; Ogliaro, F.; Bearpark, M.; Heyd, J. J.; Brothers, E.; Kudin, K. N.; Staroverov, V. N.; Kobayashi, R.; Normand, J.; Raghavachari, K.; Rendell, A.; Burant, J. C.; Iyengar, S. S.; Tomasi, J.; Cossi, M.; Rega, N.; Millam, J. M.; Klene, M.; Knox, J. E.; Cross, J. B.; Bakken, V.; Adamo, C.; Jaramillo, J.; Gomperts, R.; Stratmann, R. E.; Yazyev, O.; Austin, A. J.; Cammi, R.; C. Pomelli, J.; Ochterski, . W.; Martin, R. L.; Morokuma, K.; Zakrzewski, V. G.; Voth, G. A.; Salvador, P.; Dannenberg, J. J.; Dapprich, S.; Daniels, A. D.; Farkas, Ö.; Foresman, J. B.; Ortiz, J. V.; Cioslowski, J.; Fox, D. J. Gaussian 09 **2009**.
(367) Baerends, E. J.; Autschbach, J.; Bérces, A.; Bickelhaupt, F. M.; Bo, C.; Boerrigter, P. M.; Cavallo, L.; Chong, D. P.; Deng, L.; Dickson, R. M.; Ellis, D. E.; Van Faassen, M.; Fan, L.; Fischer, T. H.; Guerra, C. F.; Van Gisbergen, S. J. A.; Götz, A. W.; Groeneveld, J. A.; Gritsenko, O. V.; Grüning, M.; Harris, F. E.; Van den Hoek, P.; C. R. Jacob, H.; Jacobsen, .; Jensen, L.; Kessel, G. van; Kootstra, F.; Krykunov, M. V.; Van Lenthe, E.; McCormack, D. A.; Michalak, A.; Neugebauer, J.; Nicu, V. P.; Osinga, V. P.; Patchkovskii, S.; Philipsen, P. H. T.; Post, D.; Pye, C. C.; Ravenek, W.; Rodríguez, I. P.; Ros, P.; Schipper, P. R. T.; Schreckenbach, G.; Snijders, J. G.; Solà, M.; Swart, M.; Swerhone, D.; Velde, G. te; Vernooijs, P.; Versluis, L.; Visscher, L.; Visser, O.; Wang, F.; Wesolowski, T. A.; Van Wezenbeek, E. M.; Wiesenekker, G.; Wolff, S. K.; Woo, T. K.; Yakovlev, A. L.; Ziegler, T. ADF **2008**.
(368) Tsushima, S. *Dalton Trans.* **2011**, *40*, 6732–6737.
(369) Weigend, F.; Ahlrichs, R. *Phys. Chem. Chem. Phys.* **2005**, *7*, 3297–305.
(370) Pantazis, D. A.; Neese, F. *J. Chem. Theory Comput.* **2011**, *7*, 677–684.
(371) Douglas, M.; Kroll, N. *Ann. Phys. (N. Y).* **1974**, *155*, 89–155.
(372) Hess, B. *Phys. Rev. A* **1986**, *33*, 3742–3748.
(373) Becke, A. D. *J. Chem. Phys.* **1993**, *98*, 5648.
(374) Stephens, P.; Devlin, F.; Chabalowski, C.; Frisch, M. *J. Phys. Chem.* **1994**, *98*, 11623–11627.
(375) Song, H. X.; Geng, H. Y.; Wu, Q. *Phys. Rev. B* **2012**, *85*, 64110–64120.
(376) Jong, W. A. De; Apra, E.; Windus, T. L.; Nichols, J. A.; Harrison, R. J.; Gutowski, K. E.; Dixon, D. A. *J. Phys. Chem. A* **2005**, *2*, 11568–11577.
(377) Yang, Y.; Hu, S.; Fang, Y.; Wei, H.; Hu, S.; Wang, D.; Yang, L.; Zhang, H.; Luo, S. *Polyhedron* **2015**, *95*, 86–90.
(378) Prodan, I.; Scuseria, G.; Martin, R. *Phys. Rev. B* **2006**, *73*, 45104.
(379) Kerridge, A.; Kaltsoyannis, N. *Chemistry* **2011**, *17*, 5060–7.
(380) Staroverov, V. N.; Scuseria, G. E.; Tao, J.; Perdew, J. P. *J. Chem. Phys.* **2003**, *119*, 12129.
(381) Di Pietro, P.; Kerridge, A. *Inorg. Chem.* **2016**, *55*, 573–583.
(382) Görller-Walrand, C.; Houwer, S. De; Fluyt, L.; Binnemans, K. *Phys. Chem. Chem. Phys.* **2004**, *6*, 3292–3298.
(383) Serezhkin, V. . In *Structural Chemistry of Inorganic Actinide Compounds*; Krivovichev, S. V.; Burns, P. C.; Tananaev, I. G., Eds.; Elsevier B.V.: Amsterdam, 2007.
(384) Lychev, A. A.; Mashirov, L. G.; Smolin, Y. I.; Shepelev, Y. . *Sov. Radiochem.* **1986**, *28*, 622–625.
(385) Ricks, A. M.; Gagliardi, L.; Duncan, M. a *J. Am. Chem. Soc.* **2010**, *132*, 15905–7.

(386) Clavaguéra-Sarrio, C.; Brenner, V.; Hoyau, S.; Marsden, C. J.; Millie, P.; Dognon, J. P. *J. Phys. Chem. B* **2003**, *107*, 3051–3060.
(387) Schreckenbach, G.; Hay, P. J.; Martin, R. L. *Inorg. Chem.* **1998**, *37*, 4442–4451.
(388) Tsushima, S.; Reich, T. *Chem. Phys. Lett.* **2001**, *347*, 127–132.
(389) Odoh, S. O.; Walker, S. M.; Meier, M.; Stetefeld, J.; Schreckenbach, G. *Inorg. Chem.* **2011**, *50*, 3141–3152.
(390) Ruipérez, F.; Wahlgren, U. *J. Phys. Chem. A* **2010**, *114*, 3615–21.
(391) Hashem, E.; Platts, J. A.; Lorusso, G.; Evangelisti, M.; Schulzke, C.; Baker, R. J. *Inorg. Chem.* **2014**, *53*, 8624–8637.
(392) Bullock, J. I. *J. Chem. Soc. A* **1969**, 781–784.
(393) Toth, L. M.; Begun, G. M. *J. Phys. Chem.* **1981**, *85*, 547–549.
(394) Clark, A. E.; Sonnenberg, J. L.; Hay, P. J.; Martin, R. L. *J. Chem. Phys.* **2004**, *121*, 2563–70.
(395) Silvi, B.; Savin, A. *Nature* **1994**.
(396) Di Pietro, P.; Kerridge, A. *Inorg. Chem.* **2015**.
(397) Savin, A.; Becke, A. D.; Flad, J.; Nesper, R.; Preuss, H.; von Schnering, H. G. *Angew. Chemie Int. Ed. English* **1991**, *30*, 409–412.
(398) Sessler, J. L.; Weghorn, S. J. *Expanded, Contracted & Isomeric Porphyrins*; Elsevier, 1997.
(399) Kumar, M. R.; Chandrashekar, T. K. *J. Incl. Phenom. Macrocycl. Chem.* **1999**, *35*, 553–582.
(400) Rath, H.; Aratani, N.; Lim, J. M.; Lee, J. S.; Kim, D.; Shinokubo, H.; Osuka, A. *Chem. Commun. (Camb).* **2009**, 3762–4.
(401) Kee, S.-Y.; Lim, J. M.; Kim, S.-J.; Yoo, J.; Park, J.-S.; Sarma, T.; Lynch, V. M.; Panda, P. K.; Sessler, J. L.; Kim, D.; Lee, C.-H. *Chem. Commun. (Camb).* **2011**, *47*, 6813–5.
(402) Chmielewski, P. J.; Latos-Grażyński, L. *Coord. Chem. Rev.* **2005**, *249*, 2510–2533.
(403) Saito, S.; Osuka, A. *Angew. Chem. Int. Ed. Engl.* **2011**, *50*, 4342–73.
(404) Di Pietro, P.; Kerridge, A. *PCCP* **2016**, *18*, 16830–16839.
(405) Ismail, N.; Heully, J.-L.; Saue, T.; Daudey, J.-P.; Marsden, C. J. *Chem. Phys. Lett.* **1999**, *300*, 296–302.
(406) Day, V. W.; Marks, T. J.; Wachter, W. A. *J. Am. Chem. Soc.* **1975**, *505*, 4519–4527.
(407) Di Pietro, Poppy; Kerridge, A. *Phys. Chem. Chem. Phys.* **2017**.
(408) Dyall, K. G.; Dyall, K. G. **2016**, *8976*.
(409) Berg, J. M.; Gaunt, A. J.; May, I.; Pugmire, A. L.; Reilly, S. D.; Scott, B. L.; Wilkerson, M. P. **2015**.
(410) Andrews, J. S.; Jayatilaka, D.; Bone, R. G. A.; Handy, N. C.; Amos, R. D. *Chem. Phys. Lett.* **1991**, *183*, 423–431.
(411) Küchle, W.; Dolg, M.; Stoll, H. *J. Phys. Chem. A* **1997**, *101*, 7128–7133.
(412) Kaltsoyannis, N. *Dalt. Trans.* **2016**, *45*, 3158–3162.
(413) Swart, M.; Gruden, M. *Acc. Chem. Res.* **2016**, *49*, 2690–2697.
(414) Jacob, C. R.; Reiher, M. *Int. J. Quantum Chem.* **2012**, *112*, 3661–3684.
(415) Clark, D. L. *Los Alamos Sci.* **2000**, *26*, 364–381.

Appendix I

Appendix I contains additional data obtained using the TPSS and TPSSh *xc*-functionals from Chapter 3. All figures in appendix I were reproduced from Di Pietro and Kerridge, “U−O yl Stretching Vibrations as a Quantitative Measure of the Equatorial Bond Covalency in Uranyl Complexes: A Quantum-Chemical Investigation”, *Inorg. Chem.*, January 2016.

Complex	U-O$_{yl}$			U-X/U-L		
	ρ_{BCP}	$\nabla^2\rho_{BCP}$	H	ρ_{BCP}	$\nabla^2\rho_{BCP}$	H
$[UO_2]^{2+}$	0.351	0.344	-0.364	-	-	-
$[UO_2(CO)_6]^{2+}$	0.325	0.333	-0.315	0.042	0.105	-0.003
$[UO_2(H_2O)_5]^{2+}$	0.305	0.333	-0.279	0.061	0.218	-0.005
$[UO_2(NC)_5]^{3-}$	0.283	0.337	-0.243	0.064	0.183	-0.008
$[UO_2(NCS)_5]^{3-}$	0.294	0.301	-0.263	0.064	0.207	-0.007
$[UO_2(CN)_5]^{3-}$	0.284	0.343	-0.243	0.061	0.119	-0.009
$[UO_2(F)_5]^{3-}$	0.244	0.348	-0.180	0.084	0.323	-0.014
$[UO_2(OH)_4]^{2-}$	0.242	0.356	-0.176	0.095	0.287	-0.022

Table AI.1: Topological parameters associated with all uranium bonds, obtained *via* QTAIM analysis of TPSS-derived densities. ρ_{BCP} is the magnitude of the electron density at the bond critical point (BCP), $\nabla^2\rho_{BCP}$ it’s Laplacian, and H the energy density at the BCP.

Complex	U-O$_{yl}$			U-X/U-L		
	ρ_{BCP}	$\nabla^2\rho_{BCP}$	H	ρ_{BCP}	$\nabla^2\rho_{BCP}$	H
$[UO_2]^{2+}$	0.364	0.309	-0.393	-	-	-
$[UO_2(CO)_6]^{2+}$	0.339	0.300	-0.344	0.042	0.105	-0.003
$[UO_2(H_2O)_5]^{2+}$	0.319	0.300	-0.307	0.061	0.222	-0.006
$[UO_2(NC)_5]^{3-}$	0.298	0.305	-0.270	0.064	0.186	-0.008
$[UO_2(NCS)_5]^{3-}$	0.294	0.301	-0.263	0.064	0.207	-0.007
$[UO_2(CN)_5]^{3-}$	0.298	0.311	-0.270	0.061	0.120	-0.009
$[UO_2(F)_5]^{3-}$	0.259	0.317	-0.204	0.084	0.328	-0.014
$[UO_2(OH)_4]^{2-}$	0.255	0.328	-0.199	0.096	0.293	-0.023

Table AI.2: Topological parameters associated with all uranium bonds, obtained *via* QTAIM analysis of TPSSh-derived densities. ρ_{BCP} is the magnitude of the electron density at the bond critical point (BCP), $\nabla^2\rho_{BCP}$ its Laplacian, and H the energy density at the BCP.

Complex	$N(\mathrm{U})$ (q_{U})	$N(\mathrm{O})$ ($q_{\mathrm{O}_{yl}}$)	$N(\mathrm{UO_2})$ ($q_{\mathrm{UO_2}}$)
$[UO_2]^{2+}$	88.63 (+3.37)	8.68 (-0.68)	106 (+2.0)
$[UO_2(CO)_6]^{2+}$	89.16 (+2.84)	8.74 (-0.74)	106.64 (+1.36)
$[UO_2(H_2O)_5]^{2+}$	88.98 (+3.02)	8.83 (-0.83)	106.66 (+1.36)
$[UO_2(NC)_5]^{3-}$	89.03 (+2.97)	8.91 (-0.91)	106.85 (+1.15)
$[UO_2(NCS)_5]^{3-}$	89.06 (+2.94)	8.93 (-0.93)	106.92 (+1.08)
$[UO_2(CN)_5]^{3-}$	89.18 (+2.82)	8.91 (-0.91)	107.00 (+1.00)
$[UO_2(F)_5]^{3-}$	88.94 (+3.06)	9.04 (-1.04)	107.02 (+0.98)
$[UO_2(OH)_4]^{2-}$	89.10 (+2.90)	9.05 (-1.05)	107.19 (+0.80)

Table AI.3: One-electron integrated QTAIM parameters for uranyl in a.u., obtained *via* analysis of TPSS-derived densities. *n* and *q* are electronic populations and overall charges, respectively.

Complex	$N(\mathrm{U})$ (q_{U})	$N(\mathrm{O})$ ($q_{\mathrm{O}_{yl}}$)	$N(\mathrm{UO_2})$ ($q_{\mathrm{UO_2}}$)
$[UO_2]^{2+}$	88.57 (+3.43)	8.72 (-0.72)	106 (+2)
$[UO_2(CO)_6]^{2+}$	89.07 (+2.93)	8.77 (-0.77)	106.61 (+1.39)
$[UO_2(H_2O)_5]^{2+}$	88.89 (+3.11)	8.85 (-0.85)	106.59 (+1.59)
$[UO_2(NC)_5]^{3-}$	88.94 (+3.06)	8.93 (-0.93)	106.80 (+1.20)
$[UO_2(NCS)_5]^{3-}$	88.96 (+3.04)	8.94 (-0.94)	106.84 (+1.14)
$[UO_2(CN)_5]^{3-}$	89.09 (+2.91)	8.93 (-0.93)	106.95 (+1.05)
$[UO_2(F)_5]^{3-}$	88.84 (+3.16)	9.05 (-1.05)	106.94 (+1.06)
$[UO_2(OH)_4]^{2-}$	89.00 (+3.00)	9.06 (-1.06)	107.12 (+0.88)

Table AI.4: One-electron integrated QTAIM parameters of uranyl and complexing ligands, obtained *via* analysis of TPSSh-derived densities. *n* and *q* are electronic populations and overall charges, respectively.

Complex	$\lambda(\mathrm{U})$	$\lambda(\mathrm{O}_{yl})$	$\lambda(\mathrm{UO_2})$	$\delta(\mathrm{U},\mathrm{O}_{yl})$	$\delta(\mathrm{O}_{yl1},\mathrm{O}_{yl2})$	$\delta(\mathrm{U},\mathrm{L})*$	$(n-\lambda)_{\mathrm{UO_2}}$
$[UO_2]^{2+}$	86.42	7.52	106.00	2.21	0.12	-	0.00
$[UO_2(CO)_6]^{2+}$	86.14	7.55	105.39	2.07	0.11	0.29	+1.25
$[UO_2(H_2O)_5]^{2+}$	86.05	7.70	105.51	1.98	0.10	0.37	+1.15
$[UO_2(NC)_5]^{3-}$	86.02	7.79	105.47	1.88	0.09	0.41	+1.38
$[UO_2(NCS)_5]^{3-}$	85.98	7.82	105.42	1.86	0.09	0.41	+1.49
$[UO_2(CN)_5]^{3-}$	86.10	7.78	105.52	1.89	0.09	0.41	+1.48
$[UO_2(F)_5]^{3-}$	85.90	8.01	105.43	1.72	0.08	0.53	+1.59
$[UO_2(OH)_4]^{2-}$	85.95	8.02	105.49	1.71	0.07	0.7	+1.71

Table AI.5: Two-electron integrated QTAIM parameters of uranyl and complexing ligands, obtained *via* analysis of TPSS-derived densities. †delocalisation indices between uranium and coordinating species of the ligand, averaged over all ligands.

Complex	$\lambda(\mathrm{U})$	$\lambda(\mathrm{O}_{yl})$	$\lambda(\mathrm{UO_2})$	$\delta(\mathrm{U},\mathrm{O}_{yl})$	$\delta(\mathrm{O}_{yl1},\mathrm{O}_{yl2})$	$\delta(\mathrm{U},\mathrm{L})*$	$(n-\lambda)_{\mathrm{UO_2}}$
$[UO_2]^{2+}$	86.38	7.56	106.00	2.19	0.11	-	0.00
$[UO_2(CO)_6]^{2+}$	86.12	7.59	105.33	2.06	0.11	0.27	+1.08
$[UO_2(H_2O)_5]^{2+}$	86.02	7.73	105.52	1.97	0.10	0.35	+1.07
$[UO_2(NC)_5]^{3-}$	86.00	7.82	105.49	1.88	0.09	0.39	+1.31
$[UO_2(NCS)_5]^{3-}$	85.97	7.83	105.44	1.86	0.09	0.39	+1.40
$[UO_2(CN)_5]^{3-}$	86.07	7.80	105.52	1.88	0.09	0.40	+1.43
$[UO_2(F)_5]^{3-}$	85.88	8.02	105.42	1.71	0.08	0.50	+1.52
$[UO_2(OH)_4]^{2-}$	85.92	8.04	105.47	1.70	0.07	0.67	+1.65

Table AI.6: Two-electron integrated QTAIM parameters of uranyl and complexing ligands, obtained *via* analysis of TPSSh-derived densities. †delocalisation indices between uranium and coordinating species of the ligand, averaged over all ligands.

Complex	$n^{c}_{\mathrm{UO}_{yl}}$	n^{c}_{UL}
$[UO_2]^{2+}$	0.376	-
$[UO_2(CO)_6]^{2+}$	0.384	0.175
$[UO_2(H_2O)_5]^{2+}$	0.387	0.165
$[UO_2(NC)_5]^{3-}$	0.383	0.214
$[UO_2(NCS)_5]^{3-}$	0.386	0.190
$[UO_2(CN)_5]^{3-}$	0.378	0.279
$[UO_2(F)_5]^{3-}$	0.323	0.188
$[UO_2(OH)_4]^{2-}$	0.378	0.262

Table AI.7: Values of $n(\boldsymbol{r})$ at the (3,-1) critical points of the electron localisation function associated with axial and equatorial bonding to the uranium centre in all complexes studied, obtained *via* analysis of TPSS-derived densities.

Complex	$n^{c}_{\mathrm{UO}_{yl}}$	n^{c}_{UL}
$[UO_2]^{2+}$	0.378	-
$[UO_2(CO)_6]^{2+}$	0.385	0.168
$[UO_2(H_2O)_5]^{2+}$	0.388	0.160
$[UO_2(NC)_5]^{3-}$	0.384	0.210
$[UO_2(NCS)_5]^{3-}$	0.386	0.190
$[UO_2(CN)_5]^{3-}$	0.379	0.274
$[UO_2(F)_5]^{3-}$	0.384	0.185
$[UO_2(OH)_4]^{2-}$	0.379	0.258

Table AI.9: Values of $n(\boldsymbol{r})$ at the (3,-1) critical points of the electron localisation function associated with axial and equatorial bonding to the uranium centre in all complexes studied, obtained *via* analysis of TPSSh-derived densities.

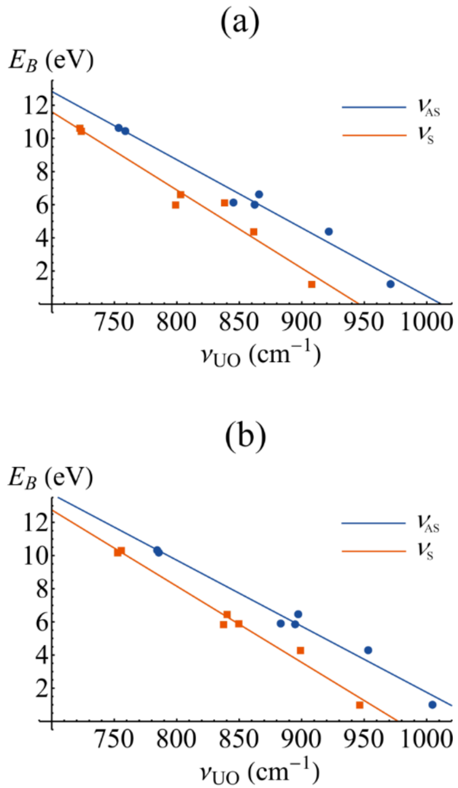

Figure AI.1: Linear fitting of calculated U-O$_{yl}$ vibrational frequencies to binding energies. a) TPSS data: R^2 = 0.98 and 0.96 for antisymmetric and symmetric stretch modes, respectively. b) TPSSh data: R^2 = 0.98 for both antisymmetric and symmetric stretch modes, respectively.

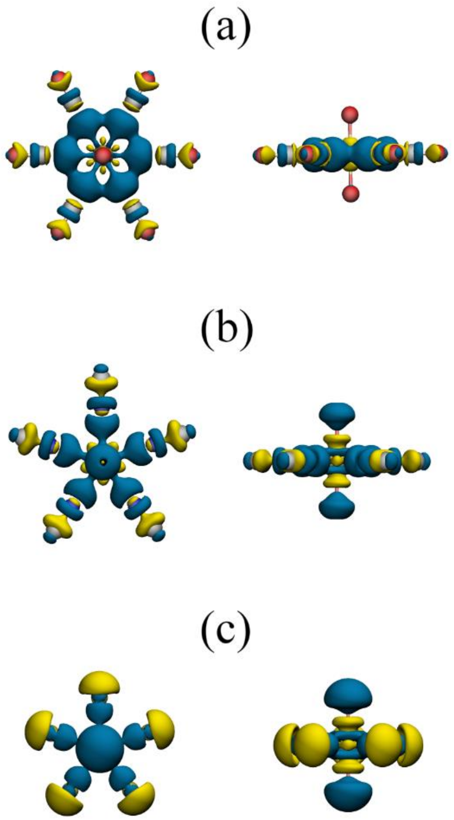

Figure AI.2: Density difference plots of the a) carbonyl, b) isocyano and c) fluoro complexes of uranyl, calculated by subtracting the TPSSh-calculated electron densities of the uranyl and ligand fragments from that of the full complexes. Blue regions indicates areas of electronic charge accumulation and yellow regions charge depletion. Molecular structures drawn to same scale. All isosurfaces rendered at a value of 0.005 a.u.

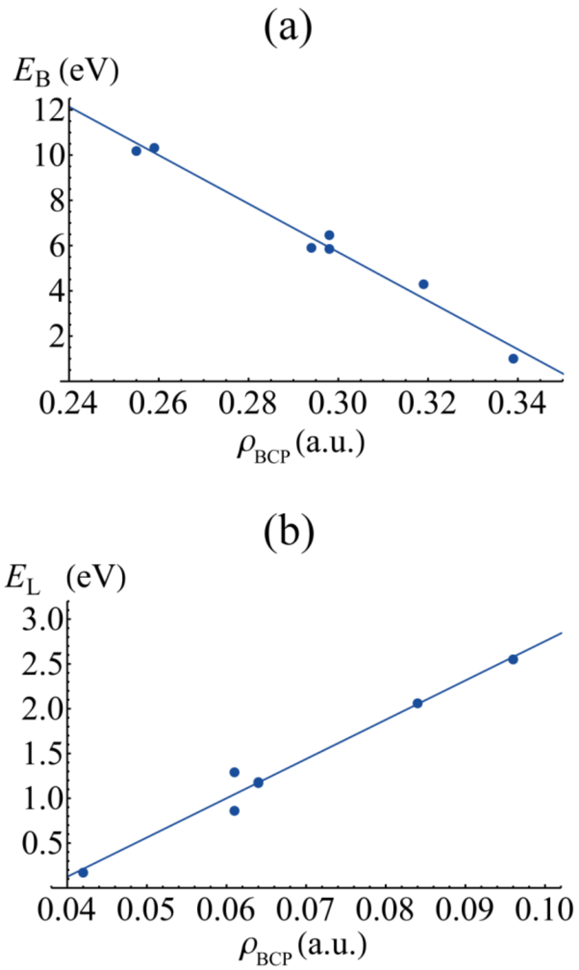

Figure AI.3: Correlation of a) total binding energy (E_B) with U-O$_{yl}$ ρ_{BCP} values and b) per ligand binding energy (E_B) with U-L ρ_{BCP} values.

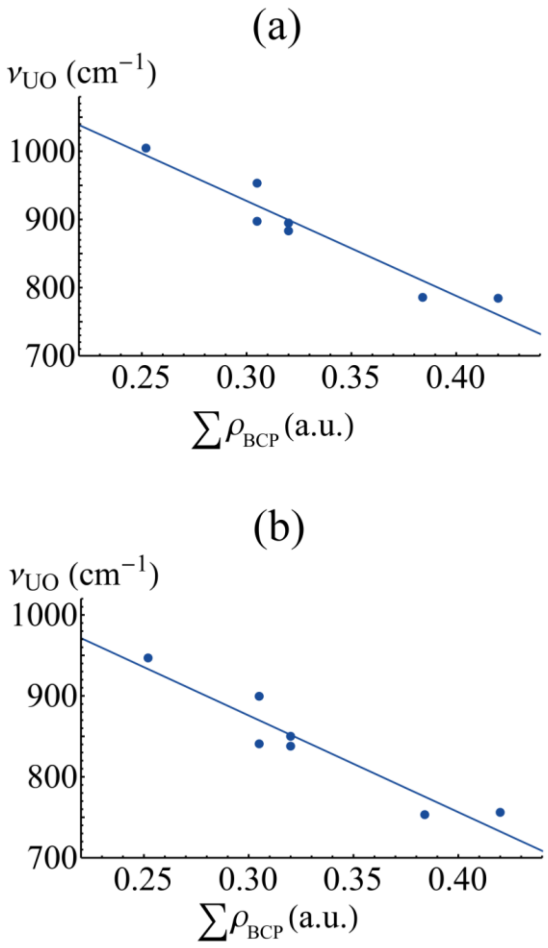

Figure AI.4: Correlation of a) U-O$_{yl}$ antisymmetric and b) symmetric stretch vibrational frequencies with the sum of electron densities at the equatorial ligand BCPs.

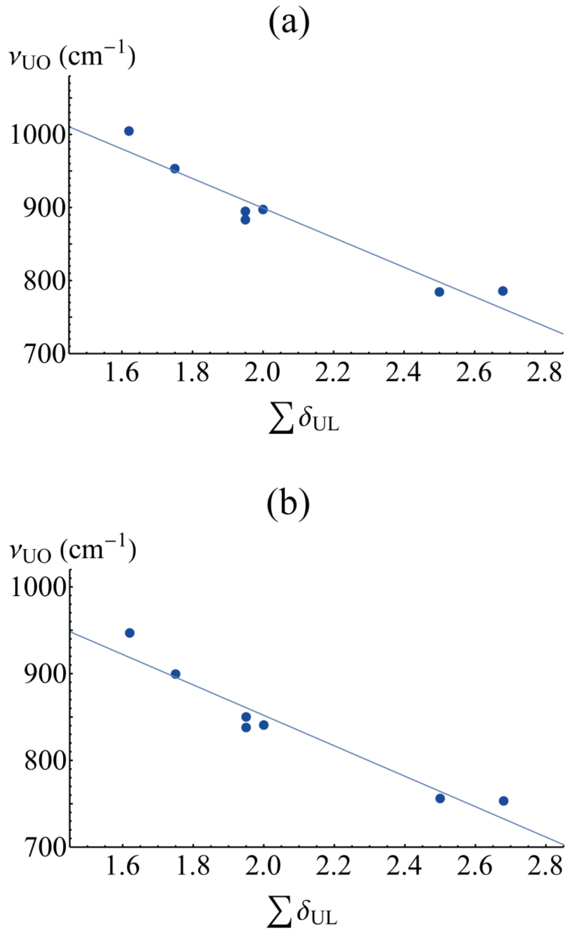

Figure AI.5: Correlation of a) U-O$_{yl}$ antisymmetric and b) symmetric stretch vibrational frequencies with the sum of uranium-ligand delocalisation indices.

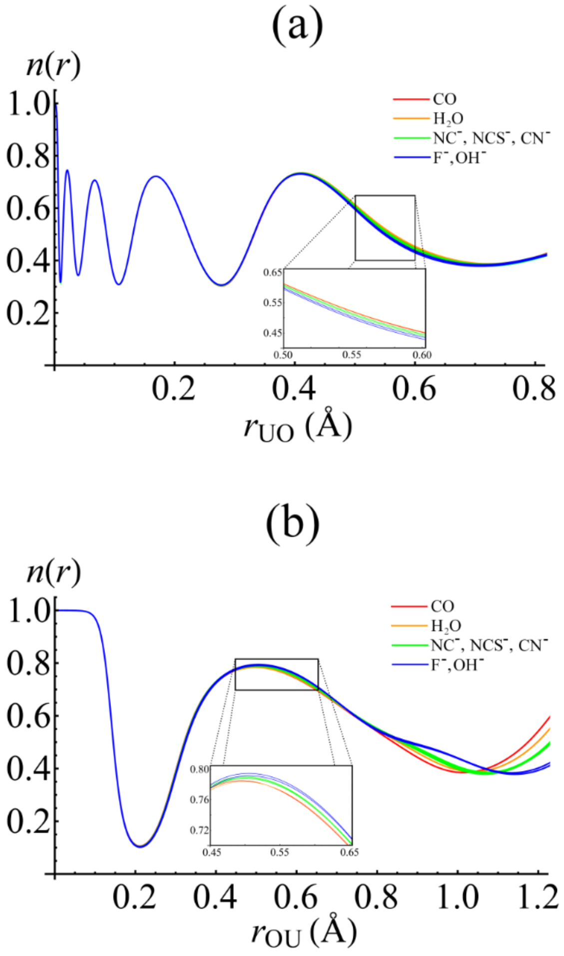

Figure AI.6: Behaviour of the electron localisation function, $n(\mathbf{r})$, along the U-O$_{yl}$ bond. (a) $n(\boldsymbol{r})$ between the uranium centre and (3,-1) CP; (b) $n(\mathbf{r})$ between the oxygen centre and the (3,-1) CP.

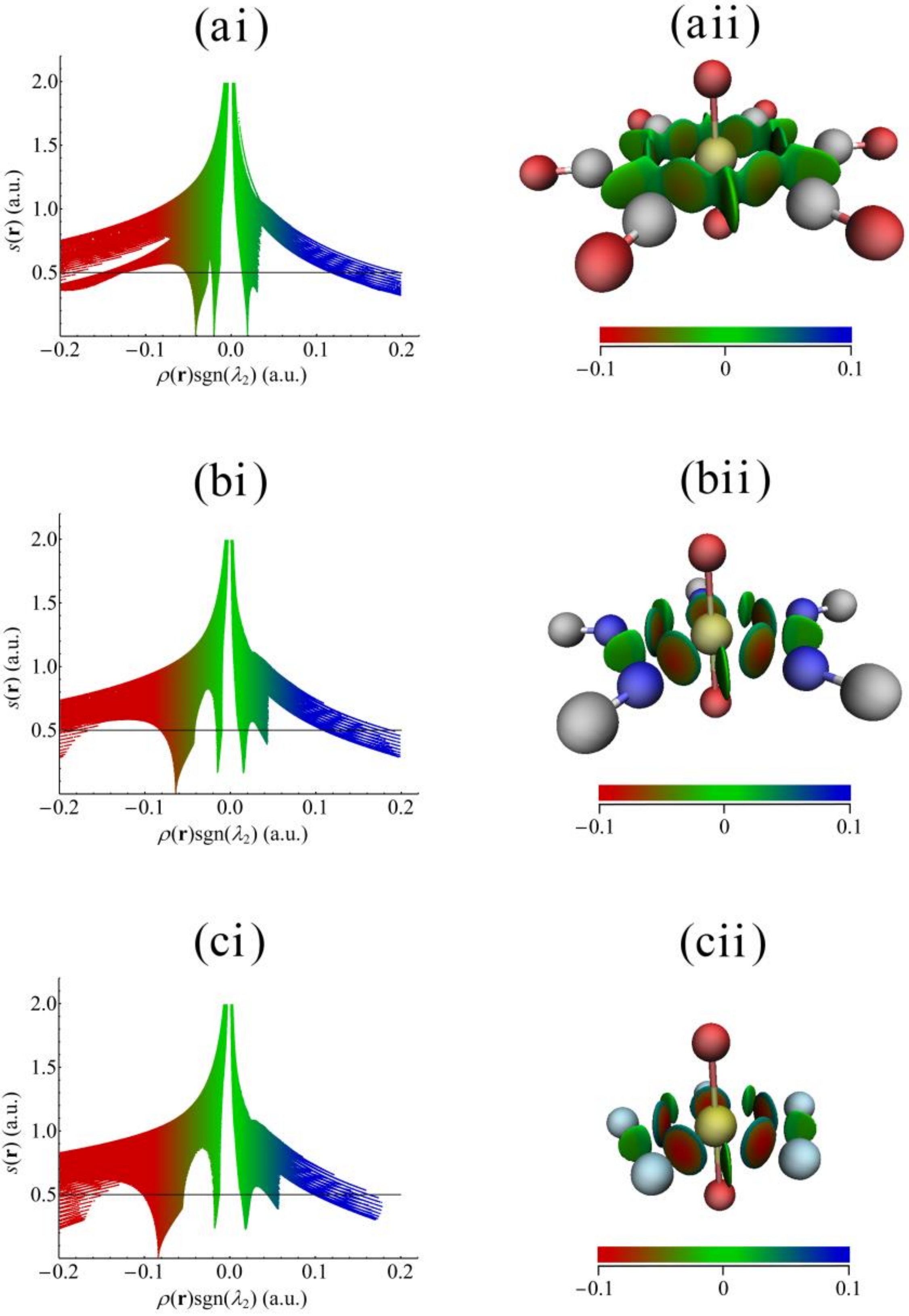

Figure AI.7: Analysis of the reduced density gradient (RDG) for a) $[UO_2(CO)_6]^{2+}$ b) $[UO_2(NC)_5]^{3-}$ and c) $[UO_2F_5]^{3-}$. Colour mapping is identical in all plots. Isosurfaces are rendered at $s(\boldsymbol{r})$ = 0.5 a.u., corresponding to the horizontal lines in the left hand panes.

Appendix II

Appendix II contains additional data from calculations performed for Chapter 5. Data is from calculations using the PBE *xc*-functional with the COSMO continuum solvation model to simulate solvation in DCM, and from calculations using the B3LYP *xc*-functional both in the gas phase, and with the COSMO continuum solvation model to simulate solvation in DCM.

	$r_{\mathrm{U-N1}}$	$r_{\mathrm{U-N2}}$	$r_{\mathrm{U-N3}}$	$r_{\mathrm{U-N4}}$	$r_{\mathrm{U-N5}}$	$r_{\mathrm{U-N6}}$	$\overline{r_{\mathrm{U-N}}}$
C_0	2.538/ *2.534*	2.538/ *2.534*	2.530/ *2.523*	2.538/ *2.534*	2.538/ *2.534*	2.530/ *2.523*	2.535/ *2.530*
C_2b′	2.602/ *2.586*	2.601/ *2.586*	2.790/ *2.773*	2.785/ *2.766*	2.726/ *2.716*	2.724/ *2.710*	2.704/ *2.689*
C_4a	2.615/ *2.599*	2.859/ *2.842*	2.788/ *2.777*	2.546/ *2.539*	2.788/ *2.777*	2.859/ *2.842*	2.742/ *2.723*
C_6	2.854/ *2.817*	2.661/ *2.637*	2.661/ *2.637*	2.854/ *2.817*	2.661/ *2.637*	2.661/ *2.637*	2.725/ *2.697*

Table AII.1: U-N bond lengths in Angstrom for complexes optimised using the B3LYP exchange-correlation functional in the gas phase/*DCM*.

	$r_{\mathrm{U\text{-}O1}}$	$r_{\mathrm{U\text{-}O2}}$
C_0	1.781/*1.794*	1.871/*1.794*
C_2b′	1.766/*1.777*	1.766/*1.777*
C_4a	1.762/*1.770*	1.762/*1.770*
C_6	1.764/*1.796*	1.761/*1.790*

Table AII.2: U-O bond lengths in Angstrom for complexes optimised using the B3LYP exchange-correlation functional in the gas phase/*DCM*.

	ΔE (eV)	ΔE_{DA} (eV)	E_{DL} (eV)	$E_{\mathbf{DU}}$ (eV)
C_0	-29.13	-30.23	0.69	0.40
C_2b′	-27.78	-29.02	0.96	0.28
C_4a	-26.00	-28.18	1.93	0.25
C_6	-25.76	-27.84	1.83	0.25

Table AII.3: Molecular binding energies and deformation adjusted binding energies, with deformation energies of the UO_2^{2+} unit and the ligands, all given in eV. Data was obtained using the B3LYP *xc*-functional, and due to the simple COSMO solvation model being a rather poor approximation for solvated uncoordinated UO_2^{2+}, are given in the gas phase only.

	C_0	C_2b'	C_4a	C_6
$\sum \rho_{\mathrm{U-N}}$	0.356	0.264	0.251	0.251
$\overline{\nabla^2\rho_{\mathrm{U-N}}}$	0.148	0.108	0.102	0.103
$\sum H_{\mathrm{U-N}}$	-0.044	-0.022	-0.019	-0.019
$\sum \delta(\mathrm{U,N})$	2.226	1.922	1.838	1.820

Table AII.4: various topological parameters measured at the bond critical points of the U-N bonds, measured in atomic units (a.u) given as total or average values, and total indices of delocalisation between the U-N atomic basins given as a proportion of a pair of electrons. Data is from structures calculated using the PBE functional including the effects of solvation in DCM using COSMO.

	C_0	C_2b'	C_4a	C_6	
				U-O_1	U-O_2
$\rho_{\mathrm{U-O}}$	0.281	0.290	0.294	0.295	0.292
$\nabla^2\rho_{\mathrm{U-O}}$	0.323	0.254	0.316	0.325	0.310
$H_{\mathrm{U-O}}$	-0.238	-0.316	-0.261	-0.263	-0.259
$\delta(\mathrm{U,O})$	1.872	1.928	1.946	1.934	1.935

Table AII.5: Various topological parameters measured at the bond critical points of the U-O bond measured in atomic units (a.u). Data is from structures calculated using the PBE *xc*-functional including the effects of solvation in DCM using COSMO.

	C_0	C_2b'	C_4a	C_6
$\sum \rho_{\mathrm{U-N}}$	0.344/*0.352*	0.244/*0.255*	0.230/*0.238*	0.234/*0.248*
$\overline{\nabla^2\rho_{\mathrm{U-N}}}$	0.152/*0.151*	0.105/*0.107*	0.098/*0.100*	0.101/*0.106*
$\sum H_{\mathrm{U-N}}$	-0.040/*-0.043*	-0.017/*-0.020*	-0.016/*-0.018*	-0.016/*-0.019*
$\sum \delta(\mathrm{U,N})$	1.970/*2.053*	1.629/*1.740*	1.558/*1.627*	1.561/*1.665*

Table AII.6: various topological parameters measured at the bond critical points of the U-N bonds, measured in atomic units (a.u) given as total or average values, and total indices of delocalisation between the U-N atomic basins given as a proportion of a pair of electrons. Data is from structures calculated using the B3LYP functional in the gas phase/DCM.

	C_0	C_2b'	C_4a	C_6	
				U-O_1	U-O_2
$\rho_{\mathrm{U-O}}$	0.304/*0.295*	0.317/*0.308*	0.320/*0.313*	0.320/*0.299*	0.319/*0.295*
$\nabla^2\rho_{\mathrm{U-O}}$	0.274/*0.278*	0.265/*0.267*	0.264/*0.266*	0.273/*0.281*	0.257/*0.265*
$H_{\mathrm{U-O}}$	-0.281/*-0.265*	-0.303/*-0.287*	-0.309/*-0.297*	-0.309/*-0.271*	-0.307/*-0.265*
$\delta(\mathrm{U,O})$	1.872/*1.831*	1.936/*1.897*	1.945/*1.915*	1.936/*1.890*	1.926/*1.887*

Table AII.7: Various topological parameters measured at the bond critical points of the U-O bond measured in atomic units (a.u). Data is from structures calculated using the B3LYP xc-functional in the gas phase/DCM.

C_6	PBE, DCM	B3LYP, gas phase	B3LYP, DCM
$\rho_{\mathrm{O-Cm}}$	0.009	0.008	0.009
$\nabla^2\rho_{\mathrm{O-Cm}}$	0.038	0.035	0.038
$H_{\mathrm{O-Cm}}$	0.002	0.002	0.002
$\delta(\mathrm{O_1,Cm})$	0.034	0.029	0.033
$\delta(\mathrm{O_2,N})$	0.092	0.087	0.092

Table AII.8: Various topological parameters measured at the bond critical points of the O-C_m interactions of C_6, given as average values. Measured in atomic units (a.u). Data is from structures calculated using the PBE *xc*-functional including the effects of solvation in DCM with COSMO and the B3LYP *xc*-functional both in the gas phase and including the effects of solvation in DCM with COSMO.

	UO_2^{2+}	C_0	C_2b'	C_4a	C_6
$N(\mathrm{U})$	88.70	89.19	89.18	89.17	89.18
$N(\mathrm{O_1})$	8.65	8.90	8.89	8.87	8.87,8.86
$\lambda(\mathrm{U})$	86.45	86.04	86.11	86.13	86.14
$\lambda(\mathrm{O})$	7.47	7.77	7.75,7.74	7.70	7.67,7.64
$\delta(\mathrm{U,O})$	2.24	1.87	1.93	1.94	1.94,1.93
$\delta(\mathrm{O_1,O_2})$	0.13	0.10	0.10	0.10	0.10
$N(\mathrm{UO_2})$	106.00	106.99	106.95	106.91	106.90
$\lambda(\mathrm{UO_2})$	106.00	105.43	105.56	105.53	105.42
$N(\mathrm{UO_2})$- $\lambda(\mathrm{UO_2})$	0.00	1.56	1.39	1.39	1.49

Table AII.9: Integrated properties associated with the uranyl ions of each complex given to 2 decimal places. Data from complexes optimised using the PBE *xc*-functional including the effects of solvation in DCM with COSMO.

	UO_2^{2+}	C_0	C_2b'	C_4a	C_6
$N(U)$	88.71	88.98	88.96	88.95	88.96
$N(O)$	8.65	8.91	8.89	8.88	8.88
$\lambda(U)$	86.44	86.01	86.09	86.11	86.12
$\lambda(O_2)$	7.45	7.80	7.76	7.73	7.71,7.69
$\delta(U,O)$	2.27	1.87	1.94	1.95	1.94,1.93
$\delta(O_1,O_2)$	0.11	0.09	0.10	0.10	0.09
$N(UO_2)$	106.00	106.81	106.74	106.72	106.72
$\lambda(UO_2)$	106.00	105.44	105.59	105.57	105.47
$N(UO_2)$- $\lambda(UO_2)$	0.00	1.37	1.15	1.15	1.26

Table AII.10: Integrated properties associated with the uranyl ions of each complex given to 2 decimal places. Data from complexes optimised using the B3LYP *xc*-functional in the gas phase.

	UO_2^{2+}	C_0	C_2b'	C_4a	C_6
$N(U)$	88.56	88.98	88.96	88.95	88.98
$N(O)$	8.72	8.95	8.92	8.91	8.91,8.90
$\lambda(U)$	86.37	86.00	86.08	86.10	86.11
$\lambda(O)$	7.57	7.86	7.81	7.77	7.74,7.71
$\delta(U,O_1)$	2.19	1.83	1.90	1.91	1.89
$\delta(O_1,O_2)$	0.11	0.09	0.09	0.09	0.09
$N(UO_2)$	106.00	106.88	106.81	106.77	106.79
$\lambda(UO_2)$	106.00	105.46	105.59	105.56	105.43
$N(UO_2)$- $\lambda(UO_2)$	0.00	1.42	1.22	1.21	1.36

Table AII.11: Integrated properties associated with the uranyl ions of each complex given to 2 decimal places. Data from complexes optimised using the B3LYP *xc*-functional including the effects of solvation in DCM with COSMO.